UNIVERSITEIT VAN PRETORIA
UNIVERSITY OF PRETORIA
YUNIBESITHI YA PRETORIA

DEVELOPMENT OF A PRACTICAL METHODOLOGY FOR THE ANALYSIS OF GRAVITY DAMS USING THE NON-LINEAR FINITE ELEMENT METHOD

by

JOHAN HENDRIK DURIEUX

A dissertation submitted in the partial fulfilment of the requirements for the degree of

MASTER OF ENGINEERING (STRUCTURAL ENGINEERING)

in the

FACULTY OF ENGINEERING, BUILT ENVIRONMENT AND INFORMATION TECHNOLOGY

UNIVERSITY OF PRETORIA

DECEMBER 2008

UNIVERSITEIT VAN PRETORIA
UNIVERSITY OF PRETORIA
YUNIBESITHI YA PRETORIA

SUMMARY OF DISSERTATION

Development of a practical methodology for the analysis of gravity dams using the non-linear finite element method

Supervisor: Professor BWJ van Rensburg

Department: Civil Engineering

University: University of Pretoria

Degree: MEng. (Structural Engineering)

In the classical design method for gravity dams, the designs are conducted in the linear elastic isotropic material domain. For many decades the so-called 'classical method' (or conventional method) was used to design gravity dams. This method is based on the Bernoulli shallow beam theory. Despite much criticism expressed by academics regarding the basis of the theory, dam design engineers are still using the classical method to design gravity dams. Currently, in most dam building countries the various codes of practice are standardised and based on this method, and engineers have confidence in these codes. This state of affairs will probably continue until structural engineers come up with a viable alternative for designing gravity dams more precisely. The perception of increased risk is always a critical aspect to overcome when introducing an alternative design method, especially when the established, well-known methodology has proved to be safe.

However, when so-called 'back analyses' are performed on existing dams, it is not so straightforward to assess the safety margin of these structures. Material properties and their yielding or failure characteristics are now becoming important in evaluating these structures accurately in the non-linear domain.

With the growing popularity of roller compacted concrete as a dam building material, the attractiveness of gravity dams has also increased and the author is of the opinion that the finite element method could be utilised more efficiently to optimise gravity dams. But, as with any new or alternative design method, the parameters and means of evaluation should be developed to establish a workable and reliable technique.

The objective of this dissertation is to develop a practical methodology for the non-linear analysis of gravity dams by means of the non-linear finite element method. A further aspect of this dissertation is the inclusion of a broad guideline on the application of the latest dam design standards used in South Africa for both the classical and finite element methods.

In order to gain a better understanding of the basic design criteria, a literature survey was conducted on the evolution of dams and the various theories developed in the past to design and optimise gravity dams. The literature survey included the examination of gravity dam

safety criteria and some available statistics on dam failures. The International Committee on Large Dams (ICOLD) has interesting statistics on dam failures and their causes. A few typical dam failures are presented to illustrate what can go wrong.

During this literature research, a thorough study was done on the non-linear material theory, with special reference to the Mohr-Coulomb and Drucker Prager material models. The findings of the study are used to illustrate how the non-linear material models are incorporated into the finite element method and in what manner the different material parameters have an influence on the accuracy of the results.

As already mentioned, currently the classical method is still a recognised design standard and for this reason a summary is presented of the South African Department of Water Affairs and Forestry's practice for designing gravity dams. This includes the latest concepts on load combinations and factors of safety for these load conditions. This summary of current practice is used as a stepping stone for the proposed load combinations that could be used for the finite element method as these are not always compatible. However, this dissertation does not deal with the full spectrum of load combinations and the scope is limited to hydrostatic loads.

Although the finite element method is a very powerful structural engineering tool, it has some serious potential deficiencies when used for dam design. The most serious problem concerns the singularities and mesh density, which develop high stress peaks at the heel of the dam wall. This problem is illustrated and some practical finite element examples are given. Some solutions for addressing this problem are also presented. It is concluded that an effective method for overcoming the singularity problem is to use the non-linear material yielding model.

In order to calibrate the non-linear Drucker Prager model, several finite element benchmarks were conducted, based on work done by other researchers in the fracture mechanics field. Although the theory of the Drucker Prager model is not based on fracture mechanics principles, this model simulates the failure of the concrete material very well. To demonstrate this, various benchmarks were conducted, such as a pure tension specimen, a beam in pure bending, a beam combined with bending and shear, the flow models of Chen (1982), a model of a gravity dam and, finally, a full-size gravity dam.

The next step in the study was to calibrate the Drucker Prager model with the concrete material properties used in existing dams of different construction methods and ages. The material strength of the concrete was statistically analysed and the average strength was calculated.

The important ratio of tensile strength to compression strength (f_t/f_c) was also examined and the findings are presented. This ratio is important to get accurate results from the Drucker Prager model. The normal input parameters for the Drucker Prager model are the internal friction angle of the material (φ) and the cohesion (c). Scrutiny of the work done by Chen (1982) helped to find a useful solution to obtaining the parameters for the non-linear finite element method without determining the φ and c values, but by using the material tensile and compression strengths instead. The formulation is demonstrated in the chapter on theory.

To illustrate the usefulness of the non-linear yielding model a few case studies were conducted. A hypothetical triangular gravity dam structure was analysed because it was widely used in other literature studies and a useful comparison could be made. Then, a case study of an 80-year-old concrete gravity dam was performed. The uniqueness of this dam lies in the fact that it was designed before the theory of underdrainage was used in South Africa and the dam has a characteristic shape due to its relatively steep downstream slopes compared with today's standards. A study of material strength sensitivity was also done on this dam to evaluate its stability under severe load conditions.

The last case study presented is on a recently designed 75-m-high roller compacted concrete gravity dam, optimised primarily by the classical method. The non-linear Drucker Prager yield model was used to evaluate this structure, with the actual material strengths taken from the laboratory design mix results. Although the finite element method was used during the design stage of this dam, it was used mainly to check the results of the classical method. The finite element method was also used to do studies on this dam where the classical method could not be used, such as studies of temperature and earthquake load conditions (not included in this research). The factor of safety against sliding was also determined using the results obtained from the finite element method and compared with the results obtained from the classical method. This case study gives an approximate comparison between the classical method and the finite element method.

Finally, a methodology is proposed for analysing a gravity dam. Procedural steps are given to describe the methodology.

With regard to the future, the advantage of the non-linear finite element method is that it can easily be extended to contemporary 3-D analysis, still using the same concept. Many dams can only be accurately evaluated by a full 3-D analysis. There is a modern tendency to design gravity dams in 3-D as well so as to evaluate their stability against sliding in the longitudinal direction. The non-linear 3-D finite element method is also used for arch dams, for which very few alternative numerical analysis methods are available. Moreover, the non-linear finite element method can be extended to earth and rock-fill embankments.

ACKNOWLEDGEMENTS

Firstly, like to thank my Heavenly Father who opened a door for me to undertake the study. I experienced that He challenged me to understand that one is never too old to develope in life.

Prof Ben van Rensburg who guided me in making this dissertation a reality. His in-depth knowledge of structural engineering helped to solve many of the engineering challenges we came across.

Dr Chris Oosthuizen of DWAF, who at all times assisted me with useful ideas and who invited me to do the research. This enabled me to obtain a better understanding of the state of the art of dam building engineering from an academic view and provide a document that could be used as a guide for the younger generation in dam design engineering.

Personnel of MSC for support I received in getting the Marc finite element software working for the specific problems we had to solve.

Beverlie Davies for reviewing the language at short notice.

My wife Carli and the children, Jean and Elmien, for their sacrifice and being so patient with me during this time and accepting my late regular home coming to enable me to do the necessary research for this task.

CONTENTS

LIST OF FIGURES

LIST OF TABLES

LIST OF SYMBOLS

ΣV	Summation of the normal vertical forces acting on the dam [MN or kN]
ΣH	Summation of the normal horizontal forces acting on the dam [MN or kN]
ΣU	Summation of the normal uplift forces acting on the dam [MN]
ΣM_S	Sum of stabilising moment about the downstream or the upstream end of the joint considered [MN.m or kN.m]
ΣM_O	Sum of destabilising (overturning) moments [MN.m or kNm]
φ	Angle of internal friction (sometimes also given as tanφ)
A	Cross-sectional area. For a dam it is the area of the uncracked base section [m²]
$[A]$	Coefficient matrix associated with displacement function
$[B]$	Matrix relating element strains to element nodal displacement
$[D]$	Elasticity matrix
$c` =$	Cohesion or ultimate shear resistance of concrete or rock in Equation 3-3 [kPa]
c	Cohesion from Section 3.6.5
d	Lateral dimensions of cross-sections
d_1	Lateral dimensions of cross-sections, in formula of BS 1881
d_2	Lateral dimensions of cross-sections, in formula of BS 1881
^oC	Degrees Celsius
E	Modulus of elasticity [MPa]
f	Material strength [MPa]
f_{ct}	Flexural strength in formula of BS 1881 [MPa]
f_t	Tensile strength of concrete [MPa]
f_c	Compressive strength of concrete [MPa]
F	Force on structure [MN or kN]
F_x, F_y, F_z	Force in directions
$\{F\}$	Vector nodal forces
g	Gravity (9,81 m/s^2)
G	Shear modulus
H	Hour(s)
$[H]$	Stress-displacement matrix
I	Second moment of area
I	Moment of inertia of the uncracked base section [m^4] in Equation 3-1 and Equation 3-2
K	Stiffness
l	Distance between the supporting rollers in formula of BS 1881
K_{ij}	Term in [K] located in row i and column j
[K]	Stiffness matrix
L	Length
L_1, L_2, L_3	Area co-ordinates
M	Bending moments [MN.m or kNm]
N_s, N_y	Shape functions
R_y	Vertical reaction force
$S1$	Maximum principal stress [MPa]
$S3$	Minimum principal stress [MPa]
S_x, S_y, S_z	Normal stresses from the FE program in the x, y and z directions.

U_r	Resultant displacement [m]
t	Thickness
$[T]$	Transformation matrix
u, v, w	Displacements along the x, y and z axes
U_x	Used to quantify the boundary condition in the x direction.
U_y	Used to quantify the boundary condition in y direction.
x, y, z	Rectangular Cartesian co-ordinate system
α_1, α_1	Constants used in displacement function
$\gamma_{xy}, \gamma_{yz}, \gamma_{zx}$	Shear strain
δ	Displacement
$\{\delta\}$	Vector nodal displacements
Δ	Area of element
ε	Strain
$\varepsilon_x, \varepsilon_y, \varepsilon_z$	Direct stains
$\theta_x, \theta_y, \theta_z,$	Rotations about the x, y and z axes
$\Phi, \Phi_{x\bar{x}}, \Phi_{x\bar{y}}$	Angles between local and global axis systems
ρ	Density [kg/m³]. Dependent on the units used in FEA
σ	Stress
σ_D	Deviatory stress
$\sigma_1, \sigma_2, \sigma_3$	Maximum, intermediate and minimum principal stresses
$\sigma_x, \sigma_y, \sigma_z,$	Direct stress
τ_{oct}	Octahedral shear stress
$\tau_{xy}, \tau_{yz}, \tau_{zx}$	Shear stress
υ	Poisson's ratio
$[\ ]$	Indicates a matrix
$\{\ \}$	Indicates a one-dimensional array, row or column vector
$[^e], \{^e\}$	Matrix, vector relating to a single element
$\bar{x}, \bar{u}$	Global quantities
$[\ ]^T$	Transpose of matrix
$\{_i\}$, x_i	Indicates quantities associated with node i
(x, y)	Indicates quantities are functions of x and y
$[\ ]^{-1}$	Inverse matrix

LIST OF ABBREVIATIONS

AAR	Alkali-aggregate reaction
APP	Approved professional person
CM	Classical method
CMOD	Crack mouth displacement
CRCM	Coaxial rotating crack model
DP	Drucker Prager
DSO	Dam Safety Office
DWAF	Department of Water Affairs and Forestry
ECSA	Engineering Council of South Africa

EQPS	Equivalent plastic strain
EQPS	Equivalent plastic strain
FCM-VSRF	Fixed crack model with variable shear resistance factor
FE	Finite element
FEA	Finite element analysis
FEM	Finite element method
FM	Fracture mechanics
FOS	Factor of safety
FSL	Full supply level
HFL	High flood level
ICOLD	International Committee on Large Dams
L	Linear
LEFM	Linear elastic fracture mechanics
LVDT	Linear variable differential transformer
MCE	Maximum credible earthquake
MOL	Minimum operation level
NL	Non-linear
NLFEM	Non-linear finite element method
NLFM	Non-linear fracture mechanics
NOC	Non overspill crest
OBE	Operational-based earthquake
OSF	Overturning safety factor
RCC	Roller-compacted concrete
RCD	
RDF	Regional design flood
RDM	Recommended design memorandum
RL	Reduced level
SEF	Safety evaluation flood
TW	Tail water

1 INTRODUCTION

1.1 Background

Gravity dams as we know them today originated in the 7th century BC, although the shape of the gravity dam as we are acquainted with it today was developed much later, in the second half of the 19th century (Fahlbusch, 2001). Through the ages many theories were developed to design these dams. For many decades the popular *classical* or *conventional* method was used; this method became virtually a design standard and is still used by many engineers. It is based on the formulation of Bernoulli's 'shallow beam theory'. Despite its popularity, the method has many limitations. Its popularity can be attributed to its straightforward approach and the fact that manual calculations can be done. The method has proved to be a conservative standard and many gravity dams were designed and optimised by means of the classical method.

With the development of modern computers and high-speed numerical processing, the finite element (FE) method has become a popular tool for analysing complex structures. Although the geometry of a gravity dam is very basic, the structural analysis of such a mass concrete structure is relatively complex due to the many design considerations to be accounted for.
Failure of a dam is usually a disastrous event due to the high hazard potential of the stored water. Risk assessment of dams has now become an integral part of the analysis and design process. Through the ages many lessons were learned from design mistakes and these lessons have now been incorporated into the modern design criteria and codes. The aim of the science of dam building is to optimise the total life cycle cost (including construction and maintenance) at acceptably low levels of risk.

In this dissertation the finite element method (FEM) is investigated as a design tool for analysing gravity dams. Although the FEM is already widely used in the design process of gravity dams, there are still some serious deficiencies that have to be addressed. These uncertainties in the FEM are the main reason why many dam engineers still use the classical method to design gravity dams. In many instances FEM is only utilised to deal with those design issues that the classical method cannot address. The author is of the opinion that more accurate dam analysis and cost savings could be achieved by utilising the FEM on larger gravity dams correctly.

In several countries legislation requires that dams should be inspected and validated by a professional team on a regular time basis. Back analyses of existing dams should be done with the latest state-of-the-art methods. In many cases older dams were not designed to incorporate all the latest design criteria. The correct utilisation of the FEM will enable dam engineers to make assessments regarding safety considerations and also essential rehabilitation and refurbishment. This more powerful design tool will enable engineers to make better economic optimisations for dam rehabilitation.

The motivation for this research was to develop an enhanced design tool for analysing gravity dams to overcome the limitations of the classical method. The FEM should be correctly

validated to overcome the negative mindset in the problematic areas in order that it can be utilised as a fully recognised tool for designing gravity dams.

One of the objects of this research is to put a methodology in place for analysing gravity dams by means of the non-linear FE yield model.

The importance of this research is firstly that an accurate calibration will be achieved and the problem areas of the FEM will be benchmarked. Secondly, it will illustrate that the obstacles can be overcome. Finally, a methodology will be proposed that can be trusted by engineers to guarantee safety while cost-optimising gravity dams.

Using the classical method, the stability of a gravity dam is determined by calculating the tensile stress at the heel of the wall and then assessing this stress against the allowable tensile stress for a given load condition. This norm is based on many years of engineering judgement by various dam-building organisations. However, it is very difficult to assess the stability of a gravity dam by means of the linear FEM using a similar approach. The major limitation of the linear elastic FEM in the analysis of gravity dams is the problem of predicting stress peaks caused by singularities and their association with the mesh density.

In this dissertation it will be illustrated that the mesh density plays a determining role in the outcome of tensile stress at points where stress singularities occur.

Several approximate methods are presented to overcome the singularities in a linear elastic FEM, but it will be illustrated that a more accurate method for overcoming the singularity problem is by utilising the non-linear FEM yield model. To utilise the non-linear yield model for gravity dams properly, the accuracy of the input parameters in relation to the materials used is of great importance.

The advantage of the non-linear FEM yield model is that it can simulate the mass concrete failure criterion fairly accurately without using complex fracture mechanics techniques. The aim of this study is to determine the load condition for a given yield-stress in the material and, to a lesser degree, to predict accurately the actual crack path. Accurate determination of crack propagation is best done by modern non-linear fracture mechanics (NLFM) techniques. However, this topic falls beyond the scope of this dissertation.

A big advantage of the Drucker Prager non-linear FE material yield model is that it is relatively straightforward to use and can easily be extended to a full 3-D analysis because the material parameters are exactly the same in 2-D and 3-D yield models.

A limit on the scope of this dissertation is that only gravity dams will be considered. However, this non-linear FEM yield model can be utilised on all types of dams.

An implication of this research is that the limitations of the linear FEM can be overcome and that a methodology can be put in place to minimise risk in the optimisation process of gravity dams.

1.2 Objectives of the Study

The objectives of the dissertation can be summarised as follow:

- To outline the limitations and advantages of the classical method
- To illustrate the application of linear elastic FEM and to demonstrate the effect of stress peaks caused by singularities at points of sharp edges and re-entrant corners
- To conduct a literature study on the non-linear finite element model (NL FEM)
- To establish a method to determine appropriate parameters for the NL FEM Drucker Prager yield model, i.e. the material yield stress ($\overline{\sigma}$) and constant (α).
- To establish a method for determining appropriate c and φ values for the non-linear finite element model (NLFEM) Drucker Prager yield model
- To establish a strategy for applying the Drucker Prager (DP) model in a non-linear finite element analysis (FEA) for gravity dams
- To conduct a benchmark comparison with published results
- To determine realistic concrete properties from existing dams
- To compare the results of the of non-linear DP method with those of the classical method and the proposed LEFM method of Chemaly (1995)
- To do a parameter study on the sensitivity of relative concrete/foundation stiffness
- To do a case history study of the Van Ryneveld's Pass Dam – both a sensitivity study and an evaluation of its stability
- To do a case study of the proposed new De Hoop Dam.

1.3 Scope of Study

Although the aim of this research is to examine the non-linear FEM yield model, the scope of the work is limited to:

- Gravity dams
- 2-D plane strain FE models
- Static loads
- Static load combinations
- The non-linear, perfect plastic DP model.

The following aspects are not considered:

- Seismic loads
- Temperature, creep and contact
- Fracture mechanics.

1.4 Methodology

1.4.1 Literature study

The following aspects were investigated in the literature study:

- The theory of the classical method
- The theory of the plane strain FEM
- The basic steps to put together an FE stiffness matrix
- The different types of elastic plastic yield models
- 3-D space diagonal illustrating the hydrostatic and deviatoric stress tensors
- The basic formulation of the Mohr-Coulomb and DP yield models
- The input parameters for the DP method in terms of the concrete properties
- The singularity phenomenon.

1.4.1 Analytical work

The analytical work was based on benchmarks/comparisons of published results.

The following benchmarks studies were performed:

- Pure tension specimen
- 2-D beam in bending
- DP flow rules
- Shear beam
- Scale model of a gravity dam
- Full-scale gravity dam

1.5 Organisation of the Dissertation

This dissertation consists of the following chapters and appendices:

- Chapter 1 serves as an introduction to the report.

- Chapter 2 discusses the design considerations and practice of dam engineering, which serves as practical background for understanding the dissertation.

- Chapter 3 contains the technical introduction based on the literature study on dam engineering.

- Chapter 4 addresses the problems encountered with finite element analysis (FEA). A selection of NLFEM benchmarks taken from recognised researchers is used to calibrate the DP yield model.

- Chapter 5 contains three case studies. These are included to illustrate the functionality of the DP yield model.

- Chapter 6 presents a proposed methodology that could be followed to perform non-linear FEA.

- Chapter 7 contains the conclusions and recommendations.

- Chapter 8 presents some concluding remarks.

- Chapter 9 is the list of references.

- Appendix A summarises the South African dam safety legislation concerned dam classification on the basis of its size and hazard potential.

- Appendix B contains useful information on the evolution of gravity dams as background to progress in structural dam engineering.

- Appendix C contains figures of the triangular dam analysed by the classical method.

- Appendix D presents contour plots of the finite element method (FEM).

- Appendix E gives the basic theory of the stiffness matrix of a rectangular element for plane elasticity (seven steps).

- Appendix F gives the basic theory of linearisation for minimising singularity effects.

- Appendix G presents the factors of safety (FOS) calculated for a triangular dam with using a finite element analysis (FEA).

2 DESIGN CONSIDERATIONS AND PRACTICE FOR GRAVITY DAMS

2.1 Object of this Chapter

The object of this chapter is to elucidate dam-building considerations and practice and to lay a basis for motivating the research done in this dissertation. In dam-building engineering, no formal or standard design code is available as practised in general civil engineering design. Each dam is usually so unique that it is designed to its characteristic shape, load conditions and functionality. However, before an engineer can design or alter a category II of III dam in South Africa, he first has to be approved by the Minster of the Department: Water Affairs and Forestry in consultations with the Engineering Council of South Africa (ECSA) as an 'Approved Professional Person' (APP).

Depending on the size and category of the dam that is being considered, there is legislation on the procedure that should be followed. For a large category III dam, the APP should be assisted by an approved professional team. This professional team will then set up a design criterion memorandum. This memorandum will be forwarded to the client for his approval. In situations where the client is not in a position to evaluate the memorandum, the client can appoint an external review panel to evaluate the memorandum on his behalf. Before construction can commence, the design criterion memorandum and design report should be forwarded to the Dam Safety Office (DSO) for their approval.

In this dissertation the focus is on gravity dams.

Dam building is an ancient art and through the ages many design methods have been developed to analyse various types of dams. Some general aspects of the analysis of dams are presented and the development of gravity dams is illustrated, leading to a discussion of the well-known, so-called *classical method*. The object of this dissertation is to investigate the advantages of the non-linear finite element method (NLFEM) and how this method can be utilised to deliver an improved gravity dam design. The importance of a cost-effective design is highlighted in terms of longevity of dams, and dam safety regulations and risk are discussed in the light of some International Committee on Large Dams (ICOLD) statistics on gravity dam failures.

The evolution of gravity dam analysis is discussed, as well as the development of gravity dam design in South Africa. Relevant earlier dissertations on this subject are briefly reviewed.

The design criteria used for modern dams have an important influence on the costs used in the tender in order to be competitive in the engineering environment. The challenge is to present the client with an optimally economic design and still maintain acceptably low risk on structural safety, i.e. the well-known principle of weighing quality against cost.

Simultaneously, dam owners are required to comply with the latest dam safety standards and regulations on both new and existing dams. With old existing dams, the design criteria play an important role in determining the cost of rehabilitating and maintaining a dam.

Many of our well-known South African dams are becoming older and the important question that arises is when and how should structures be judged to be serviceable? At what stage do dam structures become unsafe and need to be rehabilitated, abandoned or replaced?

One of the objectives of this dissertation is to do fresh research on the analysis of gravity dams by using the FEM and to do a comparative evaluation on the classical stability design method.

2.2 Longevity of Dams

This section is based on some ideas of Herman, R (1988). In the previous section, the question of the longevity of dams was mentioned. This is an important aspect for South African dams because a large number of these structures were built during the 1960s and 1970s. Many dams around the world have served long, useful lives, while others have needed drastic repairs and sometimes undergone dramatic terminations. By and large, dam building has progressed tremendously and major advances have often been triggered by experience gained from catastrophic failures. The progress in technology, especially with the advent of widespread use of computers and improved computational ability, has made a big impact on the type of dams and size of structures that can be constructed. Laboratory methods and material quality have also played a major role in improving the quality of structures that can be built today. Although the oldest dam was built nearly 5 000 years ago, the actual understanding of dam engineering was not complete until the beginning of the 19th century when the industrial era in Europe began. Older dams were based largely on an empirical design process and the failures were numerous, e.g. the Bouzey Dam and Habra Dam which are well documented in literature

In most countries dam safety legislation has been introduced and likewise in South Africa the Act on Dam Safety, Act 1956 of 25 July 1986, was approved in Parliament. Unlike in Europe, South African dams are not so old and the oldest dams in South Africa were constructed during the 1920s. South Africa is fortunate not to have had catastrophic dam failures with loss of life as experienced in other countries, e.g. the failure of the Teton Dam in Idaho, USA, a 91-metre-high modern structure completed in 1975 which failed during the initial filling. South Africa had a very similar dam failure in 1993 when the 40-metre-high Zoeknog Dam in Limpopo Province, which was nearing completion, breached during its initial filling in the early morning. The dam had reached only about 30% of its full water capacity when it suddenly breached; fortunately, nobody was injured and relatively little damage occurred downstream. Until today this dam has never been rebuilt due to the high cost of replacing it and making it economically viable again.

There are many considerations that determine the longevity of dams and their infrastructure. Some of these are listed below:

- *Deterioration*. This can be of civil, as well as of mechanical and electrical, components. The dam safety legislation and regulations regulate these issues and accurate state-of-the-art analyses of the dams are necessary to make proper decisions which are both risk-based and financially based.

- *Too expensive operation and maintenance*. In many older dams it is not economical to replace large and expensive parts such as large radial gates, turbines, etc.

- *Outdated technology*. This is mostly applicable at dams utilised to generate power and where the use of more up-to-date technology would be more economical for maintaining the dam.

- *Silting up of the dam basin*. In South Africa this is a major problem and many South African dams silt up with time. For example, the Welbedacht Dam silted up to 94% of its capacity. This dam was augmented by an off-channel dam, Knellpoort Dam, to solve the silting problem.

- *Competing systems*. In some instances water could be supplied to the consumer via an alternative scheme.

- *Ecological legislation*. This is becoming more likely these days and can be a costly business to comply with.

Due to the high construction cost of dams, they are normally built to have a long lifespan of, say, a century and more.

Water percolation through a wall is the main cause of ageing as the water dissolves the cementitious components of the mortar, masonry, lime or concrete. Ageing should be considered as a basic design issue.

The results of ageing recorded in the literature are:

- Diminishing mechanical strength of the material (pervious dams tend to age more quickly)
- Diminishing water tightness
- Decrease in relative density of the material
- Deterioration of alkaline concrete aggregate.

Here one can also mention that South Africa's dam safety legislation stipulates strict procedures on how to abandon a dam and that the regulations are such that the abandonment of a dam must be managed in such a way that it will not be a safety or an environmental threat to the region.

Dams are expensive to construct and thus their expected efficient lifespan is usually very long. In most cases a micro-economy system develops around a dam, e.g. Hartebeespoort Dam where prestige residential development started on the perimeter of the dam basin. At Loskop Dam a prosperous farming community developed and uplifted a large region that was previously poverty stricken.

Rehabilitation of dams in South Africa has now become an important issue and is a costly exercise. Many of the dams were built in the 1960s and 1970s and are now 40 years old and

older. These dams were also constructed in an era in which there was no formal dam safety legislation in place and each dam was designed and constructed uniquely to the design engineer's standards. Needless to say, the standards differ hugely from dam to dam.

It is time for a new design concept to be employed for the accurate design of gravity dams. The cost of a modern roller-compacted concrete (RCC) gravity dam is such that a more sophisticated design method should be used to optimise these dams.

2.3 Dam Safety: Evaluation of Dams

This section deals briefly with dam safety legislation. The aim is to catalogue the various organisations involved with dam safety. Dam size criteria are reviewed to point out the dams in different countries that have to comply with dam safety legislation.

International standards on dam safety are strongly influenced by the International Committee on Large Dams (ICOLD) standards, although individual countries have their unique legislation on dam safety that suits their unique circumstances. Some of the major role-players are:

- IALAD (Integrity Assessment of Large Concrete Dams) – This is the European dam safety group which represents Austria, Bulgaria, France, Germany, Greece, Italy, Romania, Slovenia, Spain, Switzerland and Turkey
- ANCOLD representing Australia
- ASDSO (Association of State Dam Safety Officers) International
- B.C. Hydro and C.D.S.A. representing Canada
- SANCOLD representing South Africa
- CHINCOLD representing China
- USCOLD representing the USA
- USBR representing the United States Bureau of Reclamation: 'Design of small dams'.

Useful information on these organisations is available on the Internet. This information can help the design engineer to compare his design criteria with international standards and practices.

A summary of some of the countries' dam safety standards, and when structures should begin to comply with legislation, is given in Table 2-1 (from Herman, 1988).

Table 2-1: Minimum values of height and volume that imply safety measures

Source	Height of wall [m]	Volume in dam basin [m³]
Austria	15	500 000
ICOLD	15	1 000 000
Portugal	-	100 000
Switzerland	10	50 000
Zimbabwe	8	-
USA	7.6	62 000
Canada	7.6	62 000
South Africa	5	50 000
Sweden	5	50 000
Norway	4	500 000
Finland	3	-
Canada	2.5	30 000
United Kingdom	-	25 000

2.3.1 Summary of the South Africa Dam Safety legislation

This section is included to document the standards used in South Africa to classify dams. This classification will be used later to help define load cases for the different categories of dams. For example, the load conditions for a category III dam will be much stricter than for a category I dam.

The 'Safety of Dams in South Africa' was written into South African law for the first time in the Water Act, 1956, on 25 July 1956, as published in the Government Gazette No.10366. Regulations in terms of Section 9C of the Water Act, 1956, relate to dams with a safety risk. This legislation was later superseded by Chapter 12 of the new National Water Act, No. 36 of 1998.

The South African dam safety legislation is based on three classifications that are summarised in the SA Water Act of 1998.

An extract from the regulations is attached as Appendix A.

Dam safety legislation also has an impact on the cost of maintaining dams and new standards are laid down from time to time by authorities on international best practices. It is thus important to evaluate the safety of existing dams accurately. Engineers who still use the classical method do not always reach the optimum solution for rehabilitation. Here the FEM is a more accurate means of reaching an optimum solution.

2.3.2 Safety of gravity dams

In the previous sections, the dam safety regulations were summarised and the question arose as to the actual safety of gravity dams and the risks involved in dam failures. A few typical

examples of dam failures will be given to illustrate failure mechanisms, the risk of gravity dam failures and the lessons to be learned from these events.

The ICOLD statistics on dam failures give some background to historical failure events. The aim of this section in relation to the object of the dissertation is to illustrate the importance of accurate structural analyses of dams to prevent serious dam failures. It will also help to identify the types of failure that can be expected from gravity dams.

2.3.2.1 ICOLD statistics

ICOLD statistics on gravity dam failures from *ICOLD Bulletin 117* (2000) are quoted below and give an indication of lessons to be learned from failures and the ageing of dams, which will help the dam designer to consider the risks involved in gravity dams.

Out of some 4 000 gravity dams (excluding China), 23 failures have been reported of which only 2 happened after 1950 and 18 were masonry dams.

- *9 of the dams were recorded to have failed during the first filling.*
- *3 dams failed due to piping in the clay or gravel under the dam, but the wall itself did not fail.*
- *9 dams failed due to foundation problems, generally sliding. (6 were masonry and 3 concrete dams.)*
- *9 dams had failures in the wall itself. All 9 were masonry walls. Some failures were due to poor-quality masonry (4 cases), but floods, thin profiles, cracks due to bombing and poor grouting were the causes of the other failures.*

General summary of failures:

- *3% of masonry gravity dams built before 1930 and 0.3% of the more recent dams have failed.*
- *More than 1% of concrete gravity dams built before 1930 have failed, but none of the 2 500 more recent ones have failed.*
- *30% of failures were due to poor foundations.*
- *15% of failures were due to poor masonry.*
- *20% of failures were due to very high reservoir levels.*
- *Others were due to a variety of causes, including a too-thin profile.*
- *Concrete quality or joints in concrete have never caused any failure in 3 000 dams.*

- *The 3-dimensional arching effects have saved some dams from breeching, but this was not effective in cases where poor foundations existed.*

Most cases of failure of the breeching section were between 10 and 30 metres deep and the length was usually close to 100 metres, so the theory of failure being limited to one or two blocks seems to be unjustified. Failures in general were sudden, which explains the high mortality figures recorded during dam failure events.

The ICOLD Bulletin also mentions the importance of good disaster management and quick response to save lives in the event of a dam failure.

2.3.2.2 Examples of gravity dam failures found on the Internet

A search on dam failures revealed that worldwide, very few gravity dams have failed during the past few years. The only report on the failure of a gravity dam was from Brazil, but unfortunately very little technical information was made available and it was only reported in certain news bulletins. The following information was gathered from the literature study and the photographs were taken from the photo gallery of Geoengineer (2007).

Camara Dam in Brazil: Failed on 21 June 2004

The Australian dated 21 June 2004, reported *'The Camara Dam on the Mamanguate River in north-eastern Brazil burst on the night of 21 June 2004, flooding the towns of Alagoa Grande and Mulungu, in the state of Paraiba. More than 3 500 people were evacuated from their homes, and dozens are still missing. Hundreds of homes were destroyed. Paraiba's Water Resources Department blamed faulty construction for the failure.'*

Later news bulletins reported that 6 people had been killed, 250 homes destroyed and close to 800 families had been left homeless, 300 of which were living in public buildings. Heavy rain preceded the dam failure, which seems to have been caused by a slip on the foundation contact surface on the left flank of the wall. The dam was only 2 years old and was constructed at a cost of US$6.5 million. Some press reports stated that cracks had been detected in the wall prior to the failure. Unfortunately, no technical information could be gathered from the Internet search.

Figure 2-1 and Figure 2-2 are photos of the failure of the Camara Dam in Brazil seen from the upstream and downstream sides.

Figure 2-1: Photos of Camara Dam illustrating the portion of the wall that slipped on the foundation surface

Figure 2-2: Photos of Camara Dam illustrating the collapse of the concrete section

Historical dam failure: Austin Dam in Pennsylvania, USA: Failed on 30 September 1911
Information found on the website: Austin Dam (2005).

The Austin Dam was built by Bayless Pulp and Paper Company to supply water to their paper mill. Construction began on 8 May 1909 and the dam was completed on 9 December 1909. The dam stood 15.25 metres high and was more than 168 metres long. It held approximately 650 000 m³ of water at a depth of 12.2 metres and was, at the time, the largest concrete dam in Pennsylvania. The dam failed on 30 September 1911 as a result of which 78 people died. It cost US$88,000 to build and the flood caused US$14 million in damage. The flood was the second-worst disaster for an impoundment structure in Pennsylvania at that time. It was owing to the Austin flood that the first Federal and State regulations and inspection laws were passed.

Figure 2-3 to Figure 2-5 show photos of the Austin Dam before and after the failure. The dam stood for less than 2 years before it breached, causing major destruction to the villages below.

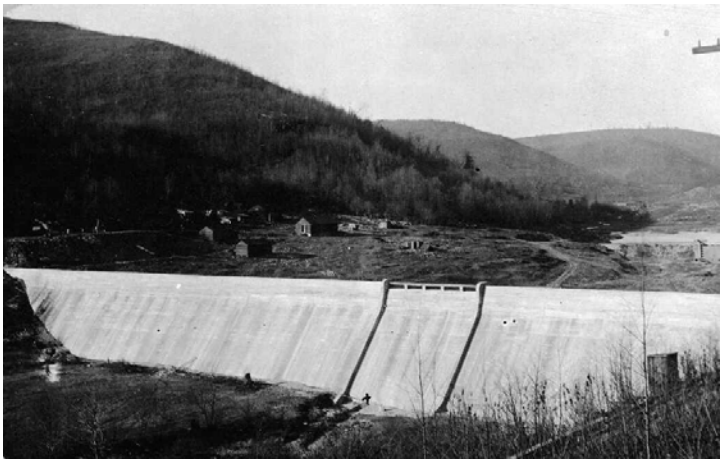

Figure 2-3: Austin Dam as it appeared shortly after completion (Austin Dam, 2005)

Figure 2-4: Photo taken shortly after the Austin Dam burst, destroying almost everything in its path (Austin Dam, 2005)

Figure 2-5: Photo of Austin Dam taken recently, illustrating the high concrete erosion that occurred (Austin Dam, 2005)

Figure 2-5 is a photo that was taken a few years ago and the author was amazed to see the enormous amount of concrete erosion that took place over a period of more or less 80 years. The question arises: Was the material of good standard?

Historical dam failure: St Francis Dam, California: Failed on 12 March 1928

The following dam failure was found on the website of the University of California, Berkeley, (St Francis Dam, 2006). A detailed PowerPoint presentation is available on the website referred to on the failure of the St Francis Dam, which breached on 12 March 1928 and is one of America's worst dam catastrophes, killing at least 420 people. Details are given on the website, along with a detailed geological report on the failure mechanism.
Figure 2-6 illustrates the remains of St Francis Dam shortly after it failed.

Figure 2-6: Photo of the failed St Francis Dam, California

Dam failures during the 18th century that influenced the design approach of gravity dams in Europe (Schnitter, 1994 and Chemaly, 1995)

Other older dams that failed and were recorded in the literature were the Bouzey Dam, which failed twice (15 March 1884 and 27 April 1895), and the Habra Dam, which was constructed in Algeria by the French, completed in 1865 and failed during 1881. The geometries of these dams are available from the literature and they have interesting shapes from a structural point of view.

2.3.3 Evolution of gravity dams

Before starting research in the dam engineering field, it is enlightening to study the history of the subject. Dam engineering is a very old field of study and some interesting books are available, for example Smith (1971), Schnitter (1994) and Fahlbusch (2001).
A summary of the history of gravity dams is given in Appendix B.

2.3.4 The question of stability and risk

Lately, many dams have been designed with slopes of 1:0.8 due to the stricter regulations on design standards set by authorities. Brian Forbes, Manager, GHD (Pty) Ltd, Australia (2006) mentioned in his discussion with engineers from the Department of Water Affairs and Forestry

that designers of gravity dams are being challenged more and more nowadays by engineering review panels on the stability, risk and cost of gravity dam structures. The latest earthquake magnitudes specified for seismic load conditions are the main reason for the conservative 1:0.8 downstream slope in order to comply with the prescribed factors of safety. Economic comparisons with other dam types tend now to make the gravity dam a less attractive option.

A question still to be answered is: Are the earthquake load conditions as specified by the pseudo-static method used in the classical design method still relevant today? More sophisticated design tools, such as the finite element method (FEM), are now available but it seems as if in many cases these tools are only used to check the integrity of the dam geometry calculated with the classical method. If the downstream slope of a gravity dam could be made steeper, this could result in significant cost savings on concrete volumes.
The other bone of contention in the design of gravity dams is uncertainty about the efficiency of the under-drainage of ageing dams. It is well known that calcification in concrete gravity dams seals off water leakages in the galleries after a certain time. This also implies that in the long run the drainage system can also be sealed off and the pore pressure under the dam will gradually build up to an undrained pressure condition. Many design engineers prefer to build in a safety factor for these conditions and the familiar 1:0.8 slope helps to achieve a low risk condition.

Later in this dissertation (Section 3.1) the advantages and limitations classical method will be briefly discussed

History of Dams in the South African Department of Water Affairs and Forestry (DWAF)

The DWAF is the organisation that developed and owns most large dams in South Africa. Gravity dams were developed and designed in South Africa using approaches very similar to those used in the rest of the world. Historically there was a close association between the previous Department of Irrigation and the American Bureau of Reclamation (USBR). During July and August 1948 two design engineers, J.M. Jordaan and J.F. Oldfield, visited the USA on a study tour to investigate a number of multi-purpose water projects constructed over the period 1930 to 1948. Great works of the Boulder Canyon, Central Valley, Columbia Basin and Missouri Basin Development Projects were visited and studied. A very comprehensive report was published in December 1949 on *Water Control and Utilisation in the United States of America* (Jordaan, 1949). Because these were senior officials in the Department of Water Affairs, the information gathered during this visit had a large impact on the development of South African water projects and obviously also on the type and shape of dams constructed in South Africa.

Later visits by W. Croucamp in 1973 and H. Elges in 1974 to the USBR, and other engineers who studied and visited abroad, had a significant influence on the development of dam design in the DWAF. The gravity dam has been a popular type of dam in South Africa and to date approximately 55 gravity dams have been built by the DWAF or by consulting engineers and contractors for the Department.

One of the oldest dams in the Dam Safety Record is the Gwaba Dam which was built in 1884. A number of dams, such as the Bulshoek Dam and the Clan William Dam, were built in the

Olifants River during 1923 and 1935. At the foot of Table Mountain are also two very old dams built by the Municipality of Cape Town called the Hely-Hutchinson and Woodhead Reservoirs, which are probably South Africa's oldest gravity dams.

The latest gravity dam to be constructed is the De Hoop Dam, a roller-compacted concrete (RCC) gravity dam on the Steelpoort River in Mpumalanga province. The wall is 75 metres high and is currently designed for a 1: 0.8 downstream slope. The spillway width is 110 metres and the total length of the RCC wall is 1 015 metres. This dam is chosen to be one of the case studies for this dissertation and will be analysed in Chapter 5.

The DWAF has a long dam-building history and engineers in the Department have served nationally and internationally on dam engineering committees. Some of these design engineers have also written post-graduate dissertations that are relevant to this study and these are listed below with a brief account of the contents.

Kroon's (1985) dissertation on gravity dam structures is basically a general design guide (and to a certain extent also includes standards) for gravity structures in South Africa. In this document the classical method was for the first time officially documented in the DWAF and load conditions and factors of safety were recommended. This dissertation helped to set a broad standard in the DWAF to achieve better continuity in the design office.

Van den Berg (1985) dealt with the application of the FEM to concrete gravity dams. A strong argument was given for the use of the FEM in the design of concrete dams. This dissertation illustrates how the FEM can be utilised as a design tool to calculate stresses in a gravity dam, with the emphasis on temperature flow and temperature load conditions. It served as a guideline for utilising the DWAF's in-house FEM programs for gravity dam analysis.

Chemaly (1995) covered the subject of gravity dams and fracture mechanics. The purpose of this research project was to investigate the application of fracture mechanics as an alternative method for the assessment of the sliding stability of gravity dams. He gave a historical background on the evolution of gravity dam design. His focus was on the theory of linear fracture mechanics in concrete dams and on gaining a better understanding of the stability of gravity dams by introducing fracture mechanics.

O'Connor's (1985) PhD thesis was based on developing in-house FE software for the DWAF. The no-tension theory was used to develop software for analysing arch dams. The software could be utilised to model hydrostatic, temperature and seismic load conditions. O'Connor's dissertation was different from the other studies in as far as the Limtension and Jntarch FE programs were developed for the DWAF on a special assignment. The programs developed in house were utilised in the DWAF for many years and quite a number of international papers were published on analyses performed with these FE programs.

Cai's (2007) dissertation is a follow-up of work done by Chemaly (1984), but based on the FEM. The literature study presents the theory of fracture mechanics constitutive models. Cai uses some benchmarks from the literature by well-known researchers to calibrate his model,

which is based on a bilinear strain softening model. A subroutine was developed for the MSC Marc FE program.

The aim of this dissertation is to take a step forward in the analysis of gravity dams utilising modern FE programs with the emphasis on the Drucker Prager (DP) material yield model. An attempt is made to benchmark and calibrate the DP yield model in order to be able to use this model with more confidence in the optimisation and back-analysis of gravity dams. A methodology is also proposed for conducting non-linear FE analysis with the information given in this dissertation.

2.4 Relationship between the Classical Method of Analysis and the 2-D Finite Element Method (FEM)

The finite element method is based on the continuum mechanics theory, whereas the classical method is based on the shallow beam theory of Euler-Bernoulli. See Sections 3.1.2 and 3.5 for a theoretical overview of the two methods.

Because the two methods differ significantly in their basic theoretical approaches, it is difficult to find a direct correlation between the results of the two methods. The FEM considers the full geometry of the structure modelled, whereas the classical method is derived from the basic, Bernoulli, shallow beam theory. This theory is then used to approximate a triangular dam shape. The stresses calculated by means of the classical method are limited to the theory of shallow beams. The shear stress or resistance against sliding is calculated from the coulomb friction equations.

However, if only the normal vertical stresses (S_y) at the heel of the wall are considered, a rough correlation could be found between the two methods if a relative coarse FE mesh is used. Usually the stress calculated by the FEM is higher than that calculated by the classical method and this is also directly related to the mesh density, with the complication of the singularity problem of an L-shaped structure. The singularity problem will be dealt with in Section 4.4.

It is important to observe that the high tensile stresses are highly localised at the heel of the wall and then fade away in the downstream direction.

To conclude, the argument was made that it is important to develop analysis methods that will enhance the economics of dam design, but within the standards for acceptable risk.

2.5 Concluding Remarks

In this chapter the design considerations for gravity dams were discussed. Dam design is a unique process and differs from standard civil engineering practices in that no prescribed and standardised design code exists. It was illustrated that dams are categorised into different classes of risk and size. Each country has its own legislation and standards for designing and maintaining dams and Table 2-1 gives some international standards. South African dam safety standards were summarised.

A summary of the development of gravity dams in South Africa was given to illustrate the progress made with design over the years, using examples taken from previous academic dissertations written by engineers in the DWAF.

The evaluation of the stability of the wall versus risk was discussed and that the FEM can be a useful design tool to analyse gravity dams if it can be utilised with more confidence, i.e. if the problem of stress peaks at the heel of the dam due to the mesh density and the singularity problems can be resolved.

3 LITERATURE STUDY

In this chapter the basic theories used to analyse a gravity dam are studied. The classical method and its failure mechanisms are discussed only briefly as this method is well documented in the literature. The advantages and disadvantages of the classical method are pointed out to draw attention to the importance of utilising the finite element method (FEM) in dam design. The importance of the load combinations and the allowable stresses for the range of load combinations is illustrated in table format. It should be kept in mind that these standards can change from one design panel to the next on each dam. No design criterion is universal and this criterion can only serve as a guideline.

The FEM is summarised, the principles of plane strain are explained and, finally, the theory of the Mohr-Coulomb and Drucker Prager non-linear models is presented. The input parameters for a non-linear plasticity analysis are discussed and how they can be implemented in the FE model.

3.1 Classical Method

For the purpose of this dissertation only the main failure mechanisms and different load conditions with their factors of safety will be discussed. Later chapter 5 these same failure mechanisms will be used to evaluate the FEM analysis of gravity dams.

3.1.1 Failure mechanisms

In the CADAM User's Manual (2001) a figure is used to illustrate the failure mechanisms of gravity dams (see Figure 3-1). The failure mechanisms are for gravity dams in general and not exclusively for use with the classical method.

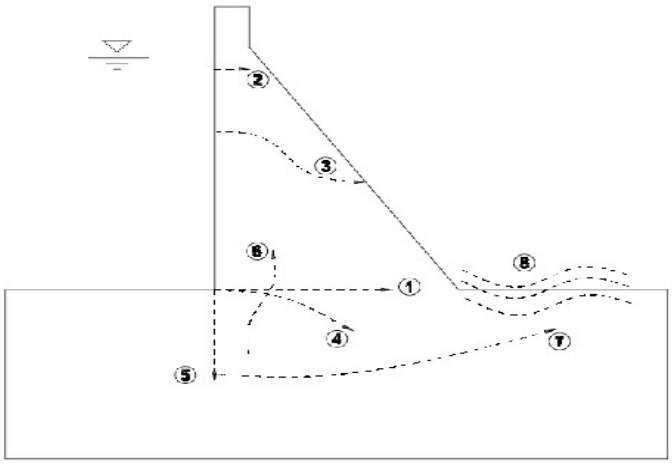

Figure 3-1: Failure mechanisms of gravity dams (CADAM, 2001, p. 64)

The following failure mechanisms are identified:

Horizontal cracks (1 and 2)
Curvilinear cracks (3 and 4)
Vertical foundation cracks (5)
Extension of existing foundation discontinuities in wall (6)
Sliding in foundation (7)
Buckling failure of thin bedded strata (8)

3.1.2 Theoretical background

In the 19th century gravity dam design was based on the theory of *profiles of equal resistance.* Appendix B illustrates the German and French dam profiles of the 19th century, with a general trend towards thickening the lower profile.

Later the so-called *classical method* was developed. This is based on the shallow beam Bernoulli-Euler theory developed in 1750 and on the elastic theory of materials. Still later the 'middle third rule' was adopted, which stipulates that no tension should occur in the body of the structure.

The theory of the classical method is well documented in, among others, the following references: Design of Gravity Dams USBR (1976), CADAM User's Manual (2001), Chemaly (1995) and Van der Berg (1985).

3.1.3 Formulation of the classical method

(Reference: CADAM User's Manual 1.4.3, 2001)

Calculation of the normal stresses from the Euler-Bernoulli theory:

$$\text{Normal stress } \sigma = \frac{P}{A} \pm \frac{M.c}{I} \qquad \textbf{Equation 3-1}$$

where:
P = the summation of the vertical forces, including uplift forces
M = the moment about the centre of gravity, including uplift forces
I = the moment of inertia
A = area of the uncracked portion of the base
c = distance from the centre of gravity of the uncracked base section.

This can also be formulated for a gravity dam as follows:

$$\sigma = \frac{\sum V}{A} \pm \frac{\sum M.c}{I}$$ **Equation 3-2**

Stability against sliding from the familiar Coulomb friction equation for a horizontal base:

$$FOS = \frac{c`.A + (\sum \overline{V} - U).\tan\varphi}{\sum H}$$ **Equation 3-3**

where:
ΣV = sum of all vertical loads, including uplift pressures
$\Sigma\overline{V}$ = sum of vertical loads, excluding uplift pressures
U = uplift pressures
A = area of uncracked ligament
ΣM = moment about the centre of gravity of the uncracked ligament of all loads, including uplift pressures
ΣH= sum of all horizontal loads, including tail-water pressures
I = moment of inertia of the uncracked ligament
c = distance from the centre of gravity of the uncracked ligament to the location where the stresses are computed
c` = cohesion (apparent or real, for apparent cohesion a minimum value of compressive stress, σ_n, to determine the compressed area upon which cohesion could be mobilised could be specified)
φ = friction angle (peak value or residual value).

Overturning safety factor:
As an additional indicator of overturning stability, the overturning safety factor (OSF) is computed as:

$$OSF = \frac{\sum M_s}{\sum M_o}$$ **Equation 3-4**

where:
ΣM_S = sum of stabilising moment about the downstream point considered
ΣM_O = sum of destabilising (overturning) moments.

Uplift or 'floating' safety factor:

$$OSF = \frac{\sum \overline{V}}{\sum U}$$ **Equation 3-5**

where:
$\sum \overline{V}$ = sum of vertical loads, excluding uplift pressures (but including the weight of water above the submerged components)
$\sum U$ = uplift forces due to uplift pressures.

Table 3-1 and Table 3-2 in Section 0 show the safety factors and maximum stresses allowed for given load combinations.
It should be noted that the classical method can also include seismic load conditions called the *pseudo-static* (rigid body) response and *pseudo-dynamic* (simplified) response, which are used for spectra analyses.

The seismic loads can be incorporated into the above formulations. However, the seismic load conditions fall outside the scope of this dissertation and are thus not discussed here.

3.1.4 Assumptions and approximation of the classical method

Firstly, the formulation is based on the Euler-Bernoulli shallow beam theory which is reasonably accurate for beams where the length/depth ratio is larger than 5 (Chemaly, 1995). The theory is also derived for a beam with a uniform cross-section and the neutral axis is near the centre of the cross-section. In applying the theory for a gravity dam, which basically has a triangular shape, the limitations of this formulation have to be understood. Fortunately, this method has been used for many decades and has proved to be quite a conservative method if used within its limitations.

The Bernoulli formulation of the classical method calculates the vertical stress. Formulation to calculate the vertical and horizontal shear is given in Jansen (1988). The factor of safety against sliding is calculated with the coulomb friction theory on different elevations and is given in Equation 3-3.

Furthermore, the classical method uses only the geometry of the wall to calculate the weight and centre of gravity of the wall, but ignores geometric irregularities which can significantly influence the stress in the wall. For example, if the cross-section of wall incorporates large shafts, hydro-electric equipment chambers or a hollow gravity section, care should be taken when using this method to correctly calculate stresses.

The method is restricted to a 2-D analysis.

3.1.5 Limitation on temperature loading

A disadvantage of this method is that it cannot simulate temperature loadings. In many instances temperature plays a dominant role in generating stresses throughout the body of the wall, e.g. the hydration heat created by the curing of the concrete, as well as the cyclic seasonal temperature fluctuations, which influence the stress condition in the outer zone of the wall. In modern design methods for large mass concrete structures, temperature analysis is an important design consideration to determine if concrete cracking is a problem. Mass concrete mixtures are specially designed to lower hydration temperatures in order to minimise cracking through the wall structure.

3.1.6 Material limitations

The method can only model a homogeneous cross-section and the effects of skin concrete, which is commonly used in the roller-compacted concrete (RCC) process, are not considered. The variation in material elasticity and strength in zoned cross-sections is thus not accounted for. Serious cracking and failure of the skin concrete can cause hazardous and undesirable structural instability of the wall.

Material properties such as chemical reactions and alkali aggregate reaction (AAR) cannot be analysed because the effect of swelling of concrete cannot be incorporated into the formulation. The effect of these reactions is usually small but can still be important when movement behaviour of the dam is monitored and interpreted.

Foundation material conditions cannot be modelled. However, a sloped foundation line and the passive resistance of downstream material at the toe of the wall can be included.

3.1.7 Limitation on the seismic loading

Although seismic load conditions fall outside the scope of this dissertation, it should be noted that the pseudo-static and pseudo-dynamic analyses, as mentioned in Section 3.1.3, should be considered as approximate methods for simulating seismic load conditions. The structural response to a random dynamic loading and the complex interaction between natural mode frequencies (Eigen values) and the frequencies of earthquake loads are not accounted for.

3.1.8 The advantages of the classical method

The main advantage of the classical method is that it is straightforward and the calculations are easy, even without a computer. It is also logical and the results can be easily interpreted by the design engineer. This method was used successfully over many years and historically it has been proved that very few gravity dams have failed due to stability design errors. However, it has also been proved to be a conservative design method for hydrostatic loads, excluding seismic, material and temperature loads.

The method can take into account a great variety of load conditions, such as hydrostatic pressure, tail-water pressure, uplift pressures, drainage, self-weight, silt, cable forces, gate forces, overtopping, additional forces acting on the structure, etc. These loads can be used in combination with each other to simulate extreme load conditions.

Although the classical method is a straightforward method sound engineering judgement by an experienced dam engineer of the results of this method is essential.

Due to the relative basic approach of the classical method it is a relative cheap method to use and can thus be economically used for relative small dams where design cost is a critical factor. The design refinement is usually in relation to the information available, associated risk and cost involved of the project.

3.2 Static Load Combinations for the Classical Method

The criteria accepted for load magnitudes coupled with probability and load combinations are very much a matter of personal preference of the approved professional person (APP) at this stage. The literature study (Section 2.3) revealed that most countries and organisations have their unique criteria for risk and factors of safety. In South Africa no specific standard is prescribed and it is left to the (APP) and the review panel to decide on such criteria. In the DWAF the first design criteria for gravity dams were documented in 1970 by Hollingworth (1970) and during 1984 these were incorporated into the dissertation by Kroon (1984). The load combinations were grouped in terms of service loads and abnormal load conditions.

To determine the load conditions and load combinations, it is important to study other international standards for dam design and dam safety. Section 2.3, together with the references (Section 9) at the end of this dissertation, gives a useful list of dam organisations that can be consulted to compare the international criteria and standards used for load cases on dams.

3.2.1 Load combinations for the classical method

Table 3-1 is an example of the typical load combinations used for South Africa conditions. It should be noted that no design code exists for gravity dams and that this table can alter at the engineering discretion of the project APP and his panel.

Table 3-1: typical load combinations used for the classical method to design gravity dams

Load combination	Hydrostatic loads							Other loads			
	MOL	FSL	RDF	SEF	TW	Silt	Gravity	Pore pressure		Earthquake	
								Partial	Full	OBE	MCE
Service – 1			X		X	X	X	X			
Service – 2	X					X	X	X			
Abnormal – 1		X			X	X	X	X		X	
Abnormal – 2			X		X	X	X		X		
Extreme – 1		X			X	X	X	X			X
Extreme – 2				X	X	X	X	X			

Loads considered with the classical method:

MOL	Minimum Operation Level
FSL	Full Supply Level
RDF	Recommended Design Flood
SEF	Safety Evaluation Flood (see SANCOLD, 1991)
TW	Tail Water
OBE	Operational-based Earthquake
MCE	Maximum Credible Earthquake
Partial uplift	Drainage gallery is present and drainage criteria are specified
Full uplift	Uplift pressure is equal to FSL level in the reservoir and tail-water conditions
Silt load	Usually for 100-year silt accumulation or existing silt level.

3.3 Criteria, Acceptable Stresses and Factors of Safety

In the previous section it was mentioned that no standardised code of practice exists for dam design and that acceptable standards for factors of safety are left to the assessment of the APP and his professional panel.

Guidelines on acceptable stresses and safety factors used in the DWAF's structural analyses are presented in Table 3-2. For service load combinations, **no tensile stress** is permitted, while small tensile stresses are permitted for the load combinations of the abnormal and extreme load cases.

Calculating the overturning safety factor (OSF) is, in most circumstances, unnecessary because the limits set on the tensile stress are usually sufficient to cover the OSF case. However, some APPs do still prefer to lay down an overturning safety factor of, say 1.5, to check the general stability of the wall.

In circumstances where a dam is significantly submerged in water it may also be necessary to perform safety check on the floating failure mechanism.

3.3.1 Typical stress values and factors of safety (FOS) for the design of gravity dams for the classical method.

Table 3-2 are typical stress values and FOS for gravity dams used in the Department: Water Affairs and Forestry engineering services, Oosthuizen (2006).

It should be noted that the values given in Table 3-2 are for the classical method and are given simply to serve as a **guideline**.

Table 3-2: Typical stress ranges and safety factors used for concrete sections

Load combination	Tensile stress (MPa)	Compressive stress (MPa)	Factor of safety against sliding		Factor of safety against overturning
			Peak	Residual	
Service – 1	0.0	3.0	3.0	1.5	1.5
Service – 2	0.0	3.0	3.0	1.5	1.5
Abnormal – 1	0 – 0.5	3.0	1.5	1.1	1.2
Abnormal – 2	0 – 0.5	3.0	1.5	1.1	1.2
Extreme – 1	0.2 – 1.0	3.0	1.3	1.0	1.1
Extreme – 2	0.3 – 1.0	3.0	1.3	1.0	1.1

A typical range of the tensile stresses are given to provide the design engineer some flexibility in his design for the abnormal and extreme static and dynamic load conditions.

Factors of safety against sliding for peak and residual concrete strength are related to the material strength parameters and the friction angle specified for short- and long-time duration. Usually, the peak shear strength value is used for earthquake conditions and the residual shear strength value for long-term concrete strength, i.e. weathered concrete.

3.3.2 Hydrostatic pressure and pore pressures

Table 3-1 represents a list of load conditions that could be used for a typical analysis of a gravity dam using the classical method. These combinations include risk conditions where the drainage system is malfunctioning and pore pressure will rise to a linear 'triangular shape', varying from a maximum of the full supply head to the tail-water head. It is also important to use the correct combinations in order not to overestimate the actual risk to which the dam is subjected. For example, it is unrealistic to have a load combination of high flood conditions and an earthquake load condition acting simultaneously on the dam. The probability that these two load conditions will occur at the same time is very small. However, it is possible that a high flood condition could occur simultaneously with a blocked drainage condition and such a load combination should be investigated as an abnormal load condition.

3.3.2.1 Stability at the horizontal construction joints

Dams with unique geometry which diverge from the traditional triangular shape or have no vertical drainage system above the gallery should be analysed at the different joint levels. Many dams are stable at base level but have tensile stress at higher levels.

3.3.2.2 Crack analysis

A condition that should also be examined for extreme flood load conditions is the possibility that cracks could propagate through the structure. The theory of cracks and fracture mechanics on gravity dams is thoroughly dealt with in the CADAM User's Manual (2001) and by the US Army Corps (1995), the USBR (1987) and Chemaly (1995). In conditions where cracking is an important factor to be considered, it is advisable to include it in the analysis. In the author's experience, however, the cracking analysis in the classical method (CADAM) is very sensitive and crack propagation progresses rapidly from the point of crack initiation. The parameters required are not readily available and are critical for achieving a stable analysis. The crack analysis is usually utilised to evaluate the effect of cracks and the sensitivity at different levels of the gravity section.

Example of a crack analysis of the Van Ryneveld's Pass Dam using the CADAM program

The geometry and dimensions of this dam are given in Section 5.2. Graphical illustrations of the Van Ryneveld's Pass Dam analysis are given in Appendix C.

The purpose of this exercise was to illustrate the sensitivity of crack propagation when using the classical method.

For this exercise plane load conditions were applied with varying upstream hydrostatic pressure, full uplift pressure on the base of the wall and a 20 m silt pressure on the upstream face in order to simplify the analysis for easy interpretation of the results.

The hydrostatic load was ramped up iteratively until a crack would propagate in the model.

The author found that no cracking occurred at level 40.90 m but, on the other hand, a full crack propagated at level 40.98 m. See Figure 10-8 and Figure 10-9 in Appendix C.

3.3.3 Additional load conditions

- **Cable forces**
  In certain dams cables are used to stabilise the wall against sliding and overturning. The resultant forces can be applied to the wall in a 2-D layout.

- **Sluice gates, *Hydroplus*-type gates, etc.**
  The forces created by these structures can be applied on the structure.

- **Debris**
  In afforested areas this load condition may be applicable.

- **Overtopping**
  This load case is applicable where an analysis is performed on an existing dam with insufficient spillway capacity.

- **Ice**
  Not applicable in South Africa.

3.4 Raising of a Gravity Dam

3.4.1 Theory of thickening and raising a gravity dam (R Sigg method)

During the last SANCOLD (2007) short course, Muller mentioned that in South Africa the main shortcoming (80% of dams to be rehabilitated) is insufficient spillway capacity. In circumstances where the spillway length of a dam cannot be widened, the non overspill crest (NOC) of the wall has to be raised in order to increase the spillway capacity. A design method is presented to calculate the stress of raising a gravity dam with the proposed load steps. The method can be applied to both the classical method and the FEM.

Changing safety standards, increasing water demands and strengthening the structure are some of the reasons that gravity dams have to be thickened or raised from time to time.

As mentioned previously, one of the disadvantages of the classical method is that it cannot simulate temperature load conditions. In the DWAF a method was developed by Mr R Sigg, during the late 1970s which simulates a stepped load condition of thickening or raising a gravity dam by means of the classical method. This method is included because the approach could be effectively utilised with the finite element method and furthermore it was never documented.

Improved standards and techniques of dam safety have led to the need to make up for shortcomings in the original designs. The main problem in raising or thickening an existing dam is that construction is usually undertaken with water loading on the wall. The existing dam is thus deformed and in a state of stress. By adding new concrete on the downstream face, the old structure is still inclined to retain the previous built-in stresses. Furthermore, the shrinkage of the new concrete can induce unfavourable pre-stressing on the old concrete, which in turn causes stresses in the new concrete. Lastly, it is essential to ensure monolithism of the complete structure.

The main cause of shrinkage in the new concrete is the temperature variation caused by the hydration heat of the cement. To compensate for this shrinkage, an open joint or 'soft joint' is constructed between the old and new concrete. The construction process is such that the first stage is constructed with a bonded joint. The next phase is then constructed with an open joint where free sliding can occur to accommodate the concrete shrinkage. The final stage is a fixed joint again to secure the last segment of the spillway. Combinations of the considered loadings are then summarised to calculate the stress in the gravity section. Figure 3-2 illustrates the stepped procedure for calculating these stresses.

This method has also been successfully applied in the FEM by activation and de-activation ('death and birth') of the elements in the FE mesh. The soft joint between the old and new concrete are modelled with friction contact elements. The stresses during the construction phases are then incorporated into the final stress distribution. In the more sophisticated FE programs, these analyses can also be performed with non-linear yield or fracture mechanic models.

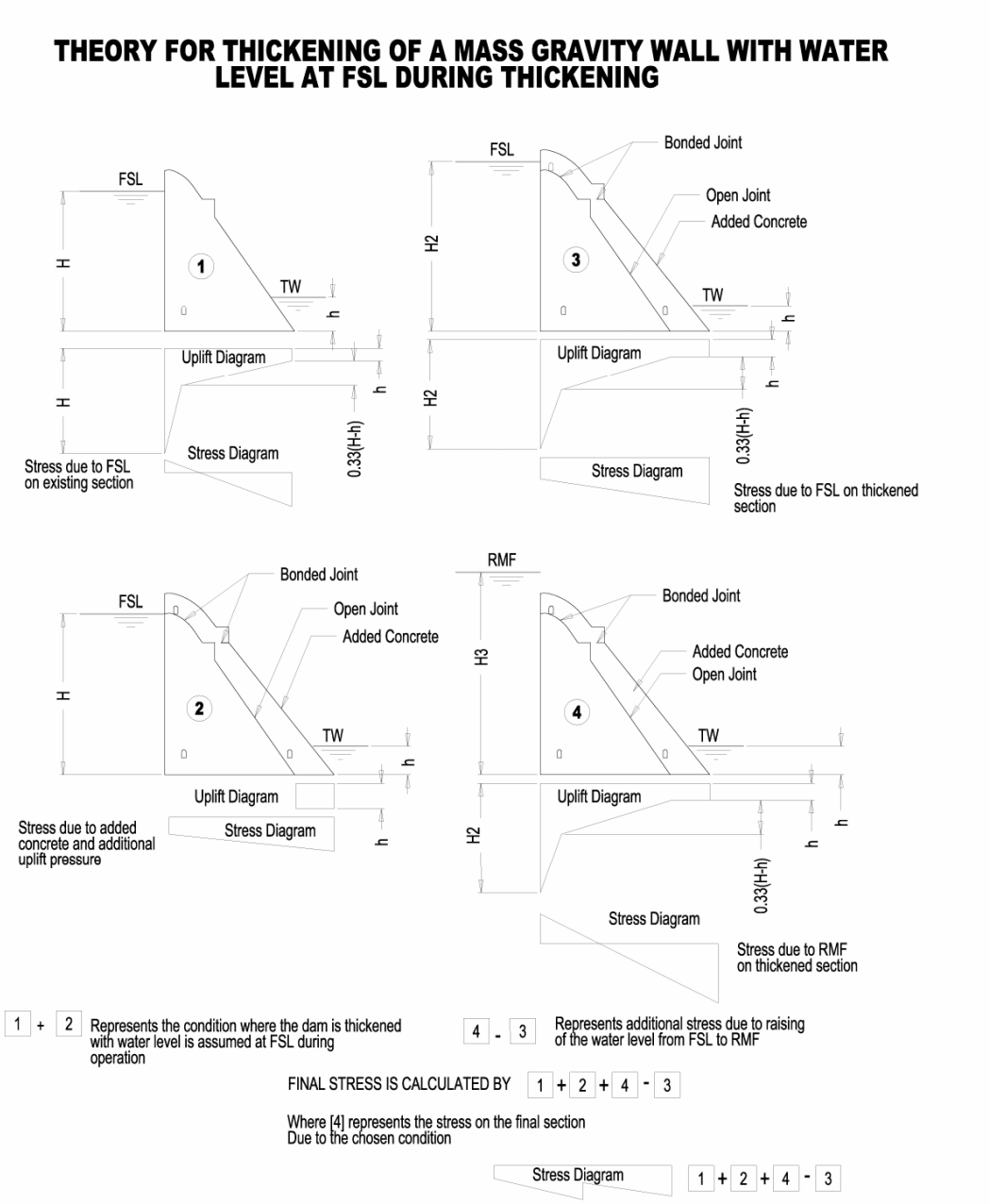

Figure 3-2: Theory for raising a mass gravity wall with the water level at FSL during construction

3.5 Development of the Finite Element Method

In this section the basic theory and methodology of the finite element method (FEM) for linear elastic analysis will be dealt with. For the purpose of this dissertation, only 2-D FE analyses will be performed and thus the discussion on the theory will be restricted to 2-D models.

Many textbooks are available on the basic theory of the FEM. For the purpose of this dissertation, the more practical issues will be addressed. For the analysis of gravity dams, certain aspects of the FEM are discussed to give an understanding of the analysis process used by the author.

3.5.1 Plane stress and plane strain models

3.5.1.1 Plane stress

(Extracts taken from Bathe, 1982 and Smith, 1971.)

When a thin plate is loaded along its edge by forces parallel to the plane of the plate and distributed uniformly over the thickness, the components σ_z, τ_{xz} *and* τ_{yz} are zero on both surfaces of the plate and they are assumed to be zero within the plate. The state of stress is then specified by σ_x, σ_y *and* τ_{xy} and is known as the 'stress state'. With plane stress the assumption is made that that σ_x, σ_y *and* τ_{xy} do not vary throughout the thickness of the plate. This stress state is applied to model thin plate structures. See Figure 3-3 taken from Bathe (1982).

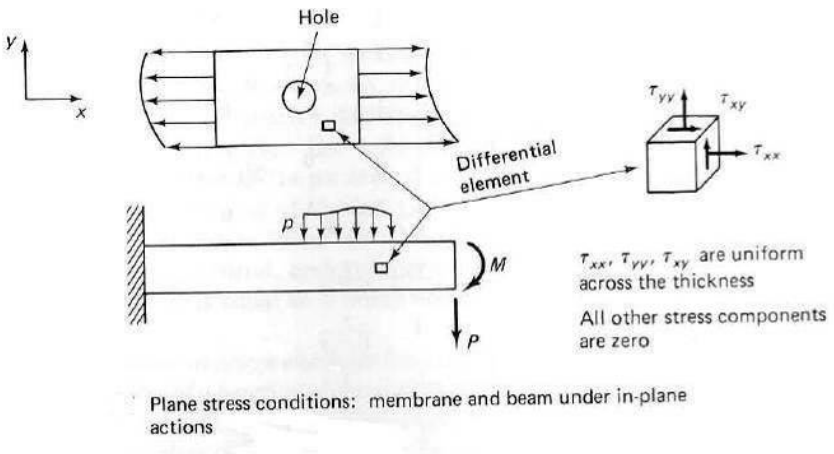

Figure 3-3: Illustration of a plane stress body (Bathe, 1982, p. 146)

3.5.1.2 Plane strain

If the dimension z of a body is very large, the opposite extreme to a plane stress model, it is assumed that the end-sections are confined between two smooth and rigid plates so that the displacement along the z-direction is prevented. In other words, plane strain elements are used

to represent a slice (of unit thickness) of a structure in which the strain components ε_z, γ_{yz} and γ_x are zero. This situation arises in the analysis of a long gravity dam, as illustrated in Figure 3-4.

In this dissertation, the plane strain model will be used by and large because gravity dams are usually analysed in only two dimensions.

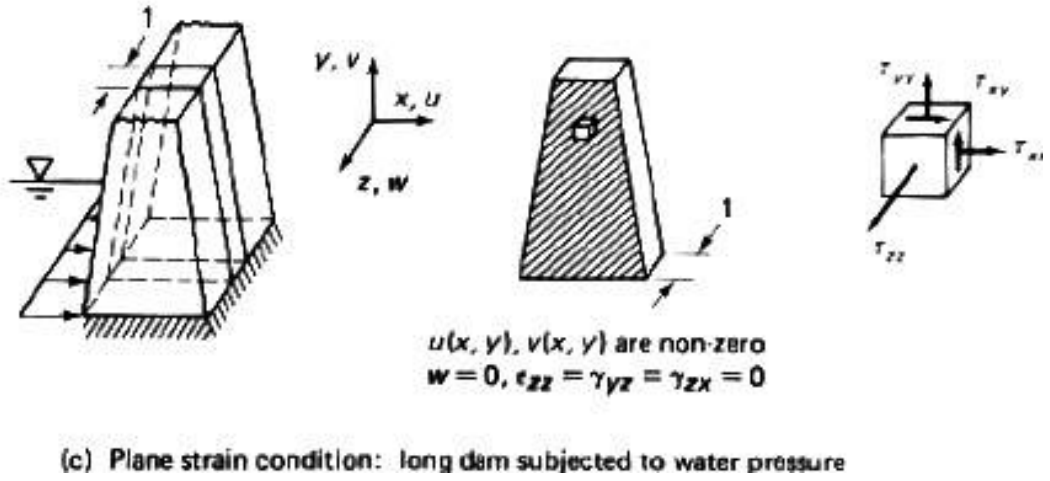

(c) Plane strain condition: long dam subjected to water pressure

Figure 3-4: Illustration of a body in plane strain (Bathe, 1982)

The elasticity matrix for plane strain can be derived from the normal principles of elasticity. Extracts taken from Smith (1971, p. 109) briefly illustrate the formulation.

Elasticity for uniaxial stress is defined as:

$$\varepsilon_x = \frac{\sigma_x}{E} \quad , \quad \varepsilon_y = -\nu\frac{\sigma_x}{E} \quad \text{and} \quad \varepsilon_z = -\nu\frac{\sigma_x}{E} \qquad \textbf{Equation 3-6}$$

For a rectangular element subjected to the action of three normal stresses σ_x , σ_y, σ_z uniformly distributed over the sides, the resultant components of strain can be obtained from the above Equation 3-6 by superposition:

$$\varepsilon_x = \frac{1}{E}\left(\sigma_x - \nu(\sigma_y + \sigma_z)\right)$$

$$\varepsilon_y = \frac{1}{E}\left(\sigma_y - \nu(\sigma_x + \sigma_z)\right) \qquad \textbf{Equation 3-7}$$

Now $\sigma_z = \nu(\sigma_x + \sigma_y)$

And $$\varepsilon_x = \frac{1}{E}(\sigma_x - \nu\sigma_y - \nu^2(\sigma_x + \sigma_y))$$

$$\varepsilon_x = \frac{1}{E}(\sigma_x(1-\nu^2) - \nu\sigma_y(1+\nu)) \qquad \textbf{Equation 3-8}$$

Similarly

$$\varepsilon_y = \frac{1}{E}(\sigma_y(1-\nu^2) - \nu\sigma_x(1+\nu)) \qquad \textbf{Equation 3-9}$$

$$\sigma_y = \frac{E\varepsilon_y + \nu\sigma_x(1+\nu)}{1-\nu^2}$$

Substituting for σ_y in Equation 3-8 eventually leads to the expression:

$$\sigma_x = \frac{E\ (1-\nu)}{(1+\nu)(1-2\nu)} \left[\varepsilon_x + \frac{\nu}{1-\nu}\varepsilon_y\right] \qquad \textbf{Equation 3-10}$$

A similar expression can be evolved for σ_y

τ_{xy} as for plane stress, is given by the expression:

$$\tau_{xy} = \frac{E}{2(1+\nu)}\ \gamma_{xy}$$

Hence the elasticity matrix for plane strain can be written as:

$$\begin{bmatrix}\sigma_x\\ \sigma_y\\ \tau_{xy}\end{bmatrix} = \frac{E(1-\nu)}{(1+\nu)(1-2\nu)} \begin{bmatrix} 1 & \frac{\nu}{1-\nu} & 0 \\ \frac{\nu}{1-\nu} & 1 & 0 \\ 0 & 0 & \frac{1-2\nu}{2(1-\nu)} \end{bmatrix} \begin{bmatrix}\varepsilon_x\\ \varepsilon_y\\ \gamma_{xy}\end{bmatrix} \qquad \textbf{Equation 3-11}$$

This can be written:

$$\overline{\sigma} = \overline{D}\overline{\varepsilon}$$

or $$\{\sigma(x,y)\} = [D]\{\varepsilon(x,y)\}$$

With $\overline{D}$ or [D] defined as the elasticity or stiffness matrix.

It is important to note that this expression becomes inoperable for incompressible material, i.e. with a $\nu = 0.5$. This is normally of little consequence but with saturated soil material, such as clays, the Poisson's ratio is very near to 0.5 and obviously a plane strain problem cannot be used for such materials. In some cases a value of, say, 0.45 could be considered but the results should be verified carefully. With concrete, the Poisson's ratio ν is approximately 0.22 and could thus be safely used.

3.5.2 Formulation of the FEM and stress analysis

Several theories have been developed to formulate the FEM. The more familiar methods are the displacement or stiffness approach and the weighted residual and variational approaches.

The displacement approach, also called the stiffness approach, for a finite element analysis of an elastic continuum will be briefly discussed. According to Rockey et al. (1975), the basis of the FEM is derived from the formulation of a simple linear spring:

Force (F) = spring stiffness (K) x displacement (δ)

For the FEM, a similar formulation can be made for linear spring stiffness:

$\{F\} = [K]\ \{\delta\}$

Where {F} and {δ} are vectors of nodal loads and nodal displacements. [K] is referred to as the stiffness of the spring structure.

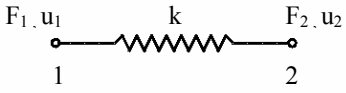

Figure 3-5: Equivalent spring element for a pin-jointed tie

Figure 3-5 illustrates the force and displacement action axially at nodal points 1 and 2.

The force vector for the spring is $\begin{Bmatrix} F_1 \\ F_2 \end{Bmatrix}$ and the displacement vector is $\begin{Bmatrix} u_1 \\ u_2 \end{Bmatrix}$

The stiffness matrix for a spring can thus be derived for a 2 x 2 order matrix and is given as:

$$\begin{Bmatrix} F_1 \\ F_2 \end{Bmatrix} = \begin{bmatrix} k_{11} & k_{12} \\ k_{21} & k_{22} \end{bmatrix} \begin{Bmatrix} u_1 \\ u_2 \end{Bmatrix} \qquad \textbf{Equation 3-12}$$

The terms in the stiffness matrix [K] are still undetermined and are solved by permitting each element to adopt an independent mode of deformation caused by the nodal forces. The normal

sign convention for the forces and displacements is accepted, i.e. positive to the right-hand (horizontal) and upwards (vertical) directions.

For a linear spring, three cases can be considered:

The first case is where node 1 can displace and node 2 is fixed; refer to Figure 3-5.

For equilibrium of the forces, action on the spring requires that

$$F_{1a} + F_{2a} = 0 \quad \text{and}$$

$$F_{2a} = -F_{1a} = -ku_1$$

Three cases are illustrated in Figure 3-6.

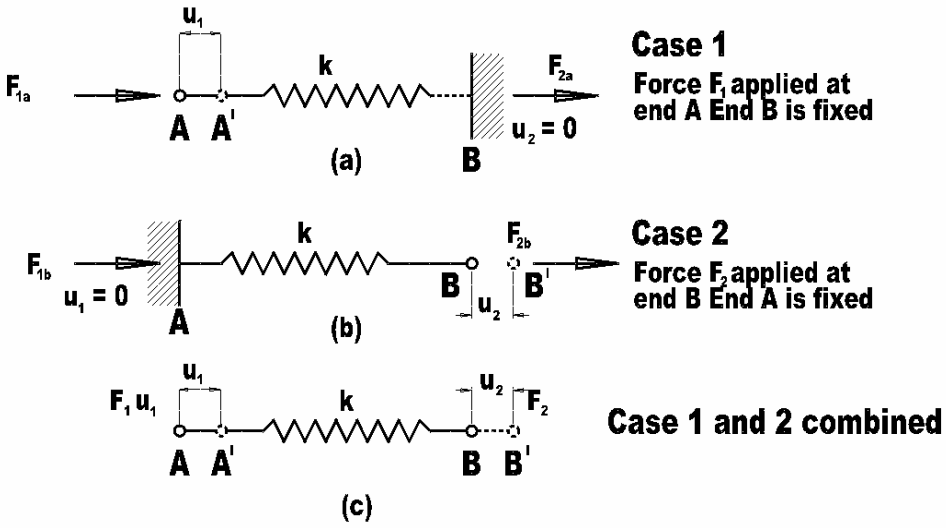

Figure 3-6: Possible deflection states for a spring AB

The inverse situation can be found by fixing node 1 and allowing node 2 to displace under the force F_2 at end B. See Figure 3-6 (b).

$$F_{2b} = ku_2 = -F_{1b}$$

Obtaining the relationship for forces F_1 and F_2 and the displacements u_1 and u_2 for the case when both ends are forced to displace, as shown in Figure 3-6 (c), the principle of superposition is used by combining the load systems shown in Figure 3-6 (a) and Figure 3-6 (b).

Total force acting at node 1: $F_1 = F_{1a} + F_{1b}$
Total force acting at node 2: $F_2 = F_{2a} + F_{2b}$

or

$$F_1 = ku_1 + ku_2$$
$$F_2 = -ku_1 + ku_2$$

In matrix format the equations can be rewritten as follows:

$$\{F\} = [K]\ \{\delta\}$$

or

$$\begin{Bmatrix} F_1 \\ F_2 \end{Bmatrix} = \begin{bmatrix} k & -k \\ -k & k \end{bmatrix} \begin{Bmatrix} u_1 \\ u_2 \end{Bmatrix} \qquad \textbf{Equation 3-13}$$

The stiffness matrix $[K^e]$ for a single spring element is given by Equation 3-14, with the suffix *e* being used to indicate that the matrix is for a single element.

$$\left[K^e\right] = \begin{bmatrix} k & -k \\ -k & k \end{bmatrix} \qquad \textbf{Equation 3-14}$$

The stiffness matrix is symmetrical, i.e. the coefficient k_{21} is equal to k_{12} .

Rockey et al. (1975) show that by using a similar procedure the stiffness matrix for an assembly of springs (or bars) and a framework can be formulated. As this dissertation is focused on the practical application of the FEM, only the basic steps in preparing a stiffness matrix will be discussed in the next section.

3.5.3 Basic steps in the derivation of the element stiffness characteristics (7 steps)

The textbook on FEM by Rockey et al. (1975) gives a useful, comprehensible method illustrating all the basic steps in deriving a finite element stiffness matrix for different types of elements. For the purpose of this dissertation, only the seven steps of the mathematical procedure for developing a finite element program are illustrated.

Step I
Identify the type of problem.
Choose a suitable co-ordinate system.
Number the nodes.

$$\{F^e\} = [K^e]\ \{\delta^e\}$$

where:
F^e = nodal load factor.
$[K^e]$ = the stiffness matrix for a individual element
δ^e = the nodal displacement vector

Step II
Choose a displacement function

$$\{\delta(x,y)\} = [f(x,y)]\{\alpha\}$$

where:
$\{\delta(x,y)\}$ = displacement at any point
$\{\alpha\}$ = column vector of the unknown coefficients of displacement of the polynomial function $[f(x,y)]$.

Step III
Obtain the state of displacements at any point in terms of the nodal displacements.

$$\{\delta(x,y)\} = [f(x,y)][A]^{-1}\{\delta^e\}$$

where:
$[A]^{-1}$ = the inverse coefficient associated with displacement.

Step IV
Relate the strain at any point to $\{\delta(x,y)\}$ and hence to $\{\delta^e\}$

$$\{\varepsilon(x,y)\} = [B]\ \{\delta^e\}$$

where:
$[B]$ = matrix relating to element strains to element nodal displacements

Step V
Relate the stresses at any point to $\{\delta(x,y)\}$ and hence to $\{\delta^e\}$

$$\{\sigma(x,y)\} = [D][\ B]\ \{\delta^e\}$$

where:
$[D]$ = elasticity matrix.

The relationship of Equation 3-11 used in this step.

Step VI
Replace $\{\sigma(x,y)\}$ by equivalent nodal loads $\{F^e\}$, thus relating $\{F^e\}$ to $\{\delta^e\}$

$$[F^e] = \int [B]^T\ [D][B]d(\text{vol})\ \{\delta^e\}$$

By comparison with the equation immediately above, the equation becomes:

$$[K^e] = \int [B]^T\ [D][B]d(\text{vol})$$

where:
$[K^e]$ = the element stiffness matrix.

Step VII
Establish a stress-displacement matrix [H]

$$\{\sigma(x,y)\} = [H]\ \{\delta^e\}$$

where from step V,

$$[H] = D][B]$$

See Appendix E for the basic theory of the stiffness matrix of a rectangular element for plane elasticity (7 Steps).

3.6 Finite Element Non-linear Analysis of a Plane Strain Model

In the previous section and Appendix E, the basic concept of the linear finite element method (LFEM) was discussed. It was assumed that the displacements of the assemblage are small and that the material is linearly elastic, i.e. that the relation of the strain and stresses was linearly proportional to the external loads applied to the body. It was further assumed that the relations between stress and strain were time-independent. In this section the non-linear finite element method (NLFEM) will be discussed. For the purpose of this dissertation, the study will be restricted to the material non-linearity analysis with conversion steps in the process.

3.6.1 Classification of non-linear analyses

Table 3-3 summarises the most important types of non-linear analyses used for structural analysis. For the analyses of dams, only the first type (material non-linear) is applicable as the displacement in a concrete gravity dam is relatively small in relation to the overall size of the structure.

Table 3-3: Classification of non-linear analyses

Type of analysis	Description
Material non-linear	Material non-linear such as concrete, soils, steel, plastic, etc. Small displacements and strains. Stress-strain relation is non-linear.
Large displacements and rotations and small strains	Large displacement and rotation of fibres and angle changes of fibres are small. Stress-strain relation can be linear or non-linear.
Large displacements, large rotations and large strains	Fibre extensions and angle changes between fibres are large. Stress-strain relation can be linear of non-linear.
Contact	With Coulomb sliding friction model, this also has damping and sticking facilities.

3.6.2 Elastic and plastic yield theories for metals and soils, including concrete

3.6.2.1 Perfect plastic

The mathematical requirements of any yield theory can be stated as follows (MSC Marc User's Guide, 2003):

- The volume of a perfectly plastic material remains constant under plastic deformation.
- Hydrostatic stress has no influence on yielding.
- Yield must be independent of the axes chosen to define the system.

Typical stress-strain relations as found in most FE programs are illustrated in Figure 3-7 (MSC Marc User's Guide, 2003):

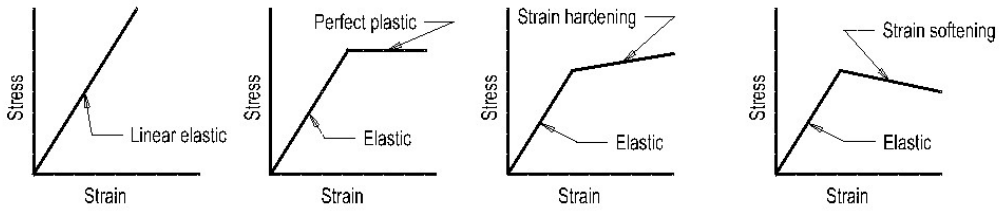

Figure 3-7: Simplified stress-strain curves for uniaxial test

The four figures represent:

- Pure linear elastic relationship
- Perfect elastic plastic relationship
- Elastic relationship with strain hardening or the so-called work hardening
- Elastic relationship with strain softening to model a low-tension strength cracking model called 'tension softening'.

There are various other non-linear models for concrete, which are based on the same basic theory of Mohr-Coulomb, e.g. the concrete model of Buyukozturk used in the Marc program. These models can be utilised to eventually get closer to realistic finite element models to evaluate the structural behaviour of a dam.

In this dissertation the research is done on the perfect elastic plastic relationship. The motivation for using only the perfect elastic plastic model is that there is very little information is available in the literature on these material models. The author's approach is to start off with a simple material model which has only a few input parameters. To get the FEM to converge correctly with the perfect elastic plastic model is relatively straightforward.

The definition of 'convergence' is when the FE analysis results for stress or deflection congregate to a single value through the prescribed time steps and iterations, and the

oscillation of the results stabilises within the given convergence tolerances. There are many different types of convergence and these are described in the Marc User's Guide (MSC, 2003).

The interpretation of the results can also be followed more accurately and conclusions can be drawn with more certainty. During the next phase the more complex models can then be calibrated based on the results obtained with the previous model. The author found that the strain softening model for simulating concrete was far more sensitive to converging correctly due to the brittleness of the material, but still provided very similar results in the near-yielding zones where the observations were done for this study. As previously mentioned, the aim of this dissertation was not to simulate fracture mechanics.

3.6.3 3-D space diagonal illustrating hydrostatic and deviatoric stress tensors

A very useful space diagram was found in the handbook by Smith (1971) which gave a better understanding of the 3-D stress configuration used in the FEM. This space diagonal will be used to explain the 3-D normal and principal stresses which are important parts of the non-linear material yield models.

Figure 3-8 represents a space diagonal illustrating all the principal stress directions (Smith, 1971).

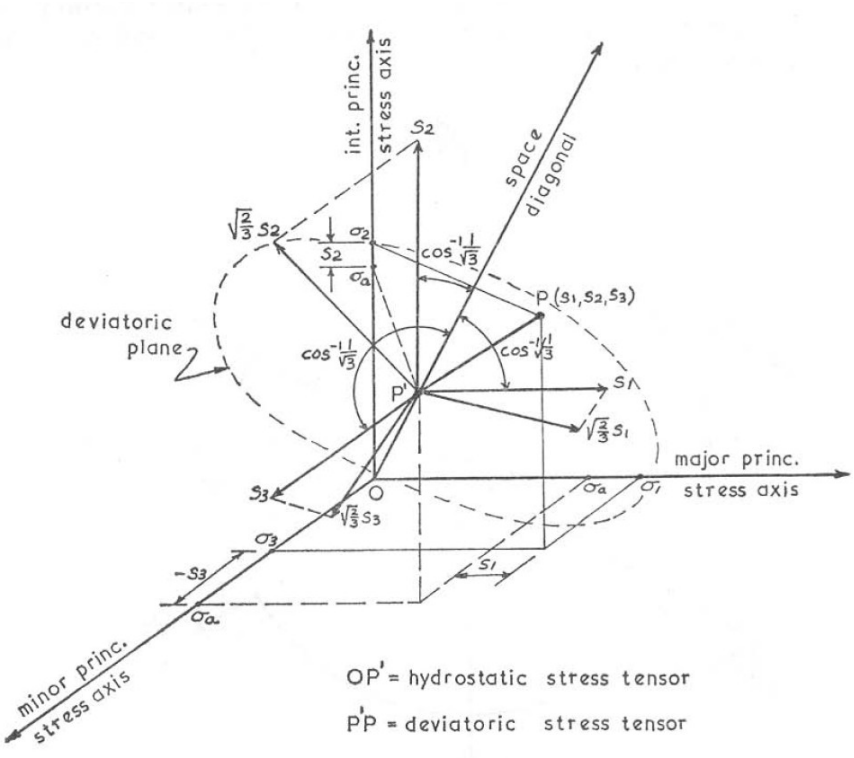

Figure 3-8: Space diagonal used to illustrate the 3-D yield criteria (from Smith, 1971)

The main features of the space diagonal are as follows. The three principal stresses are represented by the main axis, i.e. σ_1, σ_2, and σ_3. σ_1 is known as the major or maximum principal stress and in the FE notation is usually defined as the maximum tensile stress. The sign for tensile stress is positive. σ_3 is defined as the minor or minimum principal stress and represents the maximum compression stress. In a FE model the maximum and minimum principal stresses are always perpendicular to each other and the σ_2, the intermediate principal stress, is perpendicular to the σ_1 - σ_3 plane. See main axis in Figure 3-8.

OP' Represents the *hydrostatic* or *mean* stress tensor and
P'P represents the *deviatoric* or *shear* stress tensor.

Point P' represents the hydrostatic stress system (σ_a, σ_a, σ_a) where:

$$\sigma_a = \tfrac{1}{3}(\sigma_1 + \sigma_2 + \sigma_3)$$ **Equation 3-15**

and the length of OP' is $\sqrt{\sigma_a^2 + \sigma_a^2 + \sigma_a^2} = \sqrt{3}\ \sigma_a$ **Equation 3-16**

Orthogonal vectors are vectors that are at right angles to each other. An important property of orthogonal vectors is that when two are multiplied, the product is zero, i.e. if two vectors y_1 and y_2 along two reference axis 01 and 02 are orthogonal, then:

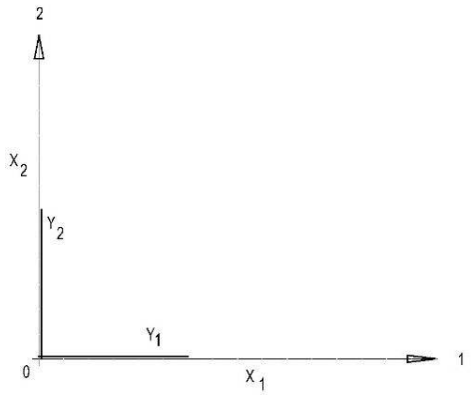

Figure 3-9: Axis for orthogonal vectors

From Smith, 1971, p. 20:

$$y_1 = \begin{bmatrix} x_1 \\ 0 \end{bmatrix} \quad and \quad y_2 = \begin{bmatrix} 0 \\ x_2 \end{bmatrix}$$

Hence $y_1 y_2 = x_1 .0 + 0 .x_2 = 0$

The argument can also be shown by the use of direction cosines. If we have three direction cosines, l_1, m_1, n_1 and l_2, m_2, n_2, then the angle θ between them is given by:

$$cos\ \theta = l_1 l_2 + m_1 m_2 + n_1 n_2 \qquad \textbf{Equation 3-17}$$

In the special case of orthogonal vectors, cos θ = cos 90º = 0. Thus, $l_1 l_2 + m_1 m_2 + n_1 n_2 = 0$, which is the set of direction cosines that are components of a unit vector (i.e. a vector of unit length).

$$cos\ \theta_1 = \frac{x_1}{l} = x_1 \text{ and } \cos\theta_2 = \frac{x_2}{l} = x_2 \qquad \textbf{Equation 3-18}$$

The hydrostatic stress σ_a is taken as having no effect on plastic yielding, which is therefore solely dependent on the magnitude of the deviatory stress tensor PP'. Considering point P' as a new origin, then the plane containing P and P', as it passes through the origin, is referred to as the *deviatoric* plane. Refer to Figure 3-9 (diagonal plane).

Smith (1971, p. 124) gives the stress vector P'P as:

$$\text{P'P} = \frac{1}{\sqrt{3}}\sqrt{\left\{(\sigma_1-\sigma_2)^2+(\sigma_2-\sigma_3)^2+(\sigma_3-\sigma_1)^2\right\}}$$

$$\sigma_D = \sqrt{(3)}\tau_{oct} \qquad \text{i.e. the deviatory stress.} \qquad \textbf{Equation 3-19}$$

$$\tau_{oct} = 1/3\sqrt{\left\{(\sigma_1-\sigma_2)^2+(\sigma_2-\sigma_3)^2+(\sigma_3-\sigma_1)^2\right\}} \qquad \textbf{Equation 3-20}$$

It can also be proved from the space diagonal that $\text{P'P}^2 = \text{OP}^2 - \text{OP'}^2$.

3.6.4 Definitions of Tresca and Von Mises stresses

The determination of the yield locus is such that for isotropic materials the assumption is made that failure (yield) occurs in a complex stress system when the maximum shear stress attained is related to the yield stress of the material when in pure tension or compression.

For the purpose of this dissertation, only the Mohr-Coulomb, Tresca and Von Mises yield theories are discussed.

The **Tresca** stress theory can be visualised as the *maximum shear stres*s. Is often used for materials that possess only cohesive strength. From the Mohr diagram for triaxial stress a maximum shear stress of $(\sigma_1-\sigma_3)/2$ can be derived. The Tresca theory states that $(\sigma_1-\sigma_3)/2 = Y/2$ or $Y = (\sigma_1-\sigma_3)$ (Smith, 1971, and Desai and Abel, 1972).

$$Y = (\sigma_1 - \sigma_3)$$ **Equation 3-21**

where:
Y = yield stress
σ_1 = maximum principal stress
σ_3 = minimum principal stress.

The **Von Mises** criterion can be visualised as the maximum shear strain energy. This is also regarded as the maximum deformation energy. This stress theory is used to examine metal structures where the tensile and compression yield stresses are similar, e.g. for steel. This gives the design engineer a quick glance at all the critical stress locations in the structure, but does not distinguish between the tensile and compression stresses.

$$Y = \frac{3\tau_{oct}}{\sqrt{2}}$$ **Equation 3-22**

Where:
Y = yield stress
τ_{oct} = octahedral shear stress.

3.6.5 Mohr-Coulomb theory

This Mohr-Coulomb theory is extensively used in the soil mechanics field to model the relationship between the maximum and minimum (major and minor) principal stresses. The theory is based on the joint theories of the Mohr circle and the Coulomb friction. Owen and Hinton's handbook (1980, p 220) gives a figure that illustrates the theory (Figure 3-10).

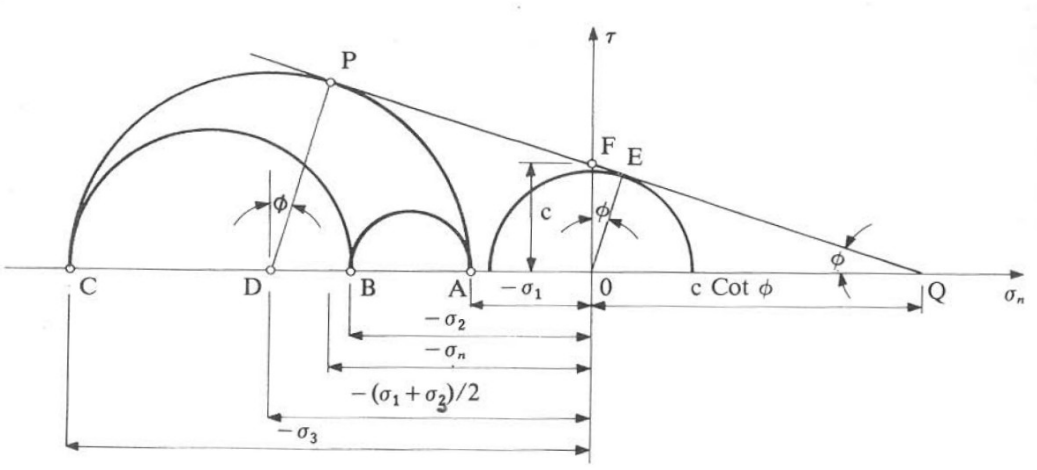

Figure 3-10: Mohr-Coulomb diagram

(Taken from Owen and Hinton, 1980)

In the theory it is assumed that the difference between the two principal stresses is a function of their summations and can therefore be expressed as:

$$(\sigma_1-\sigma_3) = f(\sigma_1+\sigma_3)$$

σ_2 is ignored in the 2-D calculations.

$$\sin\varphi = \frac{PD}{DQ} = \frac{0.5(\sigma_1-\sigma_3)}{c\cot\varphi + 0.5(\sigma_1+\sigma_3)}$$

$$(\sigma_1-\sigma_3) = 2c\cot\varphi\sin\varphi + (\sigma_1+\sigma_3)\sin\varphi$$

$$\therefore (\sigma_1-\sigma_3) = 2c\cos\varphi + (\sigma_1+\sigma_3)\sin\varphi \qquad \textbf{Equation 3-23}$$

3.6.5.1 Yield criteria of concrete material and definition of effective stress

Although in concrete dams the assumption is made that the upstream face of the dam is an impervious membrane, this is actually not true. After many years, water will slowly penetrate the concrete in a manner similar to that in which water penetrates an earth embankment dam and internal pore pressure will eventually develop. In recent FE studies, the influence of this pore water pressure has been studied in terms of the so-called 'poro-elastic' and 'poro-plastic' elements in mass concrete structures.

Smith (1971, p. 130) states that: "*In most soil shear tests a measurement of the pore water pressure within the test sample is obtained. If principal stresses are expressed in terms of* ***effective stress,*** *i.e. (total stress – pore water pressure), the effects of some variables are reduced. It is therefore often convenient to express stress analysis work in soils in terms of effective stresses. For a sandy type of soil the strength envelopes are expressed as materials with negligible cohesion and for such soils the Mohr-Coulomb expression becomes"*:

$$\therefore (\sigma_1-\sigma_3) = (\sigma_1+\sigma_3)\sin\varphi$$

This reduces the compression (σ_{1C}) and tensional stress (σ_{1T}) envelopes, which are defined by Chen (1982):

$$\sigma_{1C} = \sigma_3\frac{1+Sin\phi}{1-\sin\phi} \qquad \text{and} \quad \sigma_{1T} = \sigma_3\frac{1-Sin\phi}{1+\sin\phi}$$

For $\sigma_1 \geq \sigma_2 \geq \sigma_3$

In FE theory the Mohr-Coulomb theory is rearranged. If the yield surface (and material) is isotropic, it is convenient to express it in terms of the three stress invariants.

Zienkiewicz (1977, p. 465) gives an expression that corresponds to the formulation used in the MSC Marc User's Guide (MSC, 2003):

$$\sigma_m = \frac{J_1}{3} = \frac{(\sigma_1 + \sigma_2 + \sigma_3)}{3} \qquad \textbf{Equation 3-24}$$

$$\bar{\sigma} = J_2^{1/2} = [\frac{1}{2}(s_1^2 + s_2^2 + s_3^2) + \tau_{12}^2 + \tau_{23}^2 + \tau_{31}^2]^{\frac{1}{2}}$$

(J_2 is later also defined in Equation 3-30 in relation to the findings of Chen (1982))

$$\theta = \frac{1}{3}\sin^{-1}\left[-\frac{3\sqrt{3}}{2}\frac{J_3}{\bar{\sigma}^3}\right] \qquad \text{With} \quad -\frac{\pi}{6} \le \theta \le \frac{\pi}{6}$$

$$J_3 = s_1 s_2 s_3 + 2\tau_{12}\tau_{13}\tau_{31} - s_1\tau_{23}^2 - s_2\tau_{13}^2 - s_3\tau_{12}^2 \qquad \textbf{Equation 3-25}$$

and $s_1 = \sigma_1 - \sigma_m, \quad s_2 = \sigma_2 - \sigma_m, \quad s_3 = \sigma_3 - \sigma_m$

Where: $\tau_{12}, \tau_{13}, \tau_{31}$ etc. are the shear stresses in the respective planes.

The *Mohr-Coulomb* can now be formulated as:

$$F = \sigma_m \sin\phi + \bar{\sigma}\cos\theta - \frac{\bar{\sigma}}{\sqrt{3}}\sin\phi\sin\theta - c\cos\phi = 0 \qquad \textbf{Equation 3-26}$$

3.6.6 The Drucker-Prager theory

The Drucker-Prager (DP) theory is closely related to the Mohr-Coulomb theory. Zienkiewicz's handbook (1977) gives:

$$\mathrm{F} = 3\alpha'\sigma_m + \bar{\sigma} - K = 0 \qquad \textbf{Equation 3-27}$$

$$\alpha' = \frac{2\sin\phi}{\sqrt{3}(3 - \sin\phi)} \quad , \quad K = \frac{6c\cos\phi}{\sqrt{3}(3 - \sin\phi)}$$

These equations correspond to those given in Chen (1982, p. 216), which will be discussed in Section 3.6.7 as input data for the FE programs.

The values of c and ϕ may depend on a strain hardening parameter.

Figure 3-11, taken from Zienkiewicz (1977), gives a presentation of the yield criteria and demonstrates the relation between the Drucker Prager, Von Mises, Mohr-Coulomb and Tresca theories. The similarity between the different theories can be clearly observed.

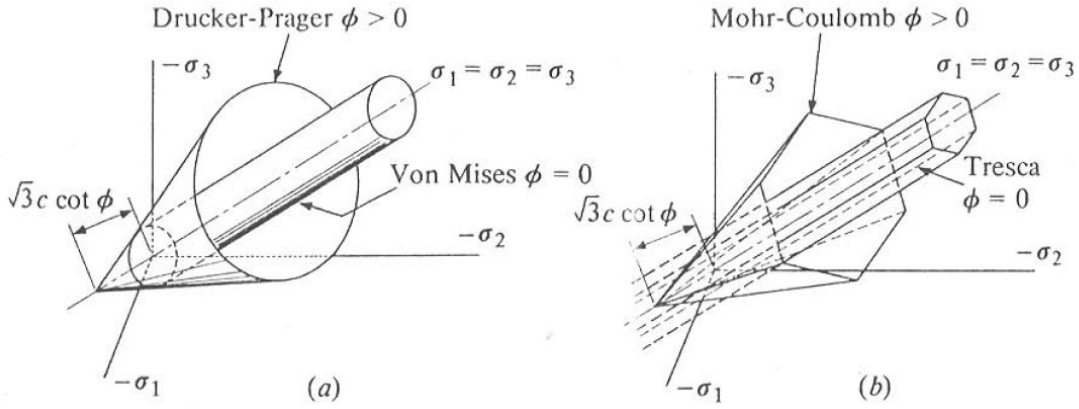

Figure 3-11: Graphical illustration of the different yield criteria (Zienkiewicz, 1977)

3.6.7 Definitions and input data for the FE programs

For the purpose of this dissertation, the MSC Marc FE program will be used for most of the analyses. From the MSC Marc User's Guide (2003), Volume A, *Theory*, and the handbook by Chen (1982), the following equations are formulated for the Mohr-Coulomb material which is hydrostatic stress-dependent.

3.6.7.1 Definitions and input parameters for the MSC Marc FE program

Two types of Mohr-Coulomb isotropic material models are incorporated into the Marc FE program, i.e. a linear and a parabolic model. The theory from the MSC Marc User's Guide (2003) gives the following formulation:

Linear Mohr-Coulomb

$$f = \alpha J_1 + J_2^{1/2} - \frac{\overline{\sigma}}{\sqrt{3}} = \quad 0 \qquad \textbf{Equation 3-28}$$

Chen (1982) gives Equation 3-28 as:

$$f(I_1, J_2) = \alpha I_1 + \sqrt{J_2} - k$$

(See Eq. 5.109 in Chen, 1982, p. 215). Note that Chen uses I_1 and Marc uses J_1 and that this is the first invariant of the stress tensor.)

Chen's formulation and the Marc formulation correspond if $k = \frac{\bar{\sigma}}{\sqrt{3}}$

Figure 3-12 illustrates the equations of the Mohr-Coulomb theory graphically.

Also from Chen (1982), J_1 is defined as $J_1=\sigma_{ii}$ (with $\sigma_{ii}= \sigma_1+ \sigma_2+ \sigma_3$ defined as the first invariant of the stress tensor, J_1).

$$J_1= \sigma_1+ \sigma_2+ \sigma_3 \qquad \textbf{Equation 3-29}$$

and

$$J_2 = \frac{1}{2}\sigma'_{ij}\sigma'_{ij}$$

Also defined as:

$$\frac{1}{2}s_{ij}s_{ij} = \frac{1}{6}\left[(\sigma_x-\sigma_y)^2+(\sigma_y-\sigma_z)^2+(\sigma_z-\sigma_x)^2\right]+\tau_{xy}^2+\tau_{yz}^2+\tau_{zx}^2 \qquad \textbf{Equation 3-30}$$

(J_2 is defined as the second invariant of the stress deviator tensor and σ_x, σ_y, σ_z are the normal stresses in the x, y, and z directions. τ_{xy}, τ_{yz}, and τ_{zx} are the normal shear stresses.)

In the MSC Marc User's Guide (2003) the constants for α and $\bar{\sigma}$ are given in terms of c and ϕ:

$$c = \frac{\bar{\sigma}}{\left[3\left(1-12\alpha^2\right)\right]^{1/2}} \quad ; \quad \frac{3\alpha}{\left(1-3\alpha^2\right)^{1/2}} = \sin\phi \qquad \textbf{Equation 3-31}$$

Where c is the cohesion and ϕ is the angle of friction.

Chen (1982, p. 216) gives an important approximation for linking the Mohr-Coulomb equations to the Drucker Prager equations:

$$\alpha = \frac{2Sin\,\phi}{\sqrt{3}(3-Sin\,\phi)} \quad ; \quad \bar{\sigma} = \frac{6cCos\,\phi}{(3-Sin\,\phi)}$$ For the outer bound of the hexagon

and

$$\alpha = \frac{2Sin\phi}{\sqrt{3}(3+Sin\phi)} \quad ; \quad \bar{\sigma} = \frac{6cCos\phi}{(3+Sin\phi)}$$ for the inner bound of the hexagon

See Equations 5.111 and 5.112 in Chen (1982, p. 216).

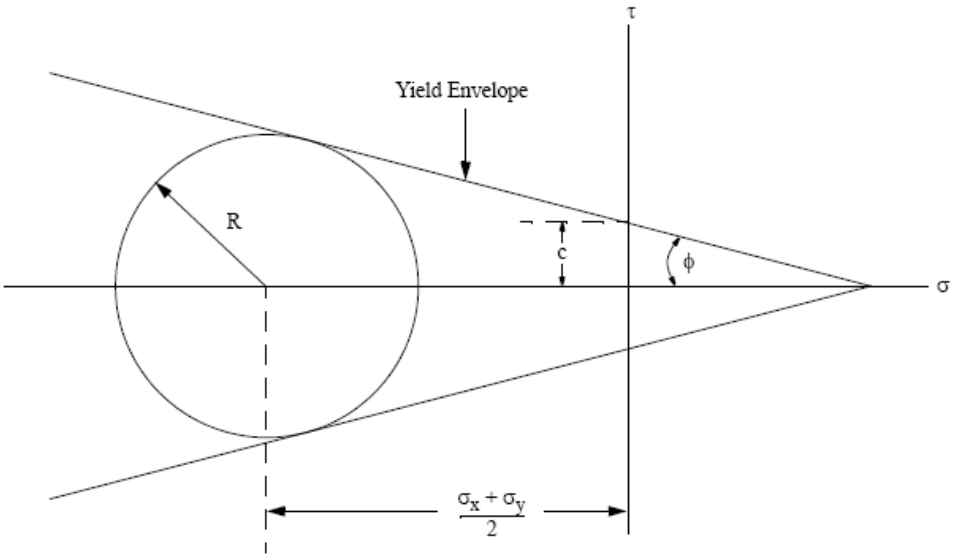

Figure 3-12: Yield envelope of plane strain linear Mohr-Coulomb material

(From MSC Marc, 2003)

3.6.7.2 Introducing the compressive strength (f_c) and tensile strength (f_t) as input parameters

By studying the formulations in Chen (1982) a set of equations could be derived very easily.

Equations 9.46 and 9.47 are:

$$\alpha = \frac{2Sin\phi}{\sqrt{3}(3-Sin\phi)} \text{ and } k = \frac{6c\cos\phi}{\sqrt{3}(3-Sin\phi)} \text{ or } \overline{\sigma} = \frac{6c\cos\phi}{(3-Sin\phi)}$$

with ($k = \frac{\overline{\sigma}}{\sqrt{3}}$) from the definitions by MSC Marc (2003) and Chen (1982)

The basic three flow models given by Chen (1982, p. 216) are as follows:

$$\alpha = \frac{2\sin\phi}{\sqrt{3}(3-\sin\phi)} \qquad k = \frac{6c\cos\phi}{\sqrt{3}(3-\sin\phi)}$$ **Equation 3-34**

$$\alpha = \frac{2\sin\phi}{\sqrt{3}(3+\sin\phi)} \qquad k = \frac{6c\cos\phi}{\sqrt{3}(3+\sin\phi)}$$ **Equation 3-35**

$$\alpha = \frac{\tan\phi}{\sqrt{9+12\tan^2\phi}} \quad k = \frac{3c}{\sqrt{9+\tan^2\phi}}$$ **Equation 3-36**

and from Chen (1982, p. 409) is given:

$$Sin\phi = \frac{f_c - f_t}{f_c + f_t} \text{ and } c = \frac{f_c f_t}{f_c - f_t} Tan\phi$$ **Equation 3-37**

where:
f_t = tensile strength of material (MPa)
f_c = compressive strength of material (MPa)
ϕ = internal friction angle of material
c = cohesion of material (MPa)

From the values of f_t and f_c, ϕ and c can be derived. These values can be used to calculate the input parameters for the FE program from the flow models given in Equation 3-34 to Equation 3-36

A spreadsheet was developed to calculate $\bar{\sigma}$ and α by inserting the values of ϕ and c from Equation 3-37 and then substituting them in Marc Equation 3-31.

From these equations it can be seen that $F(f_t/f_c) = F(\phi)$ and $F(c) = F(f_c, F_t, \phi)$

Above equations thus imply that for a certain ratio of f_t/f_c, ϕ stays constant.

For example, if the ratio of $f_t/f_c = 0.1$, then ϕ is constant = 54.9º and the yield stress $\bar{\sigma}$ is dependent only on the change in the cohesion *c*.

This will be illustrated in Chapter 4 for typical concrete models.

The following two figures illustrate the relationship between α and f_t/f_c, as well as between $\bar{\sigma}$ and f_t/f_c. In the previous equations it was shown that the value for α is constant and $\bar{\sigma}$ is thus dependent only on α and f_c. The figures show the linear relationship between the parameters.

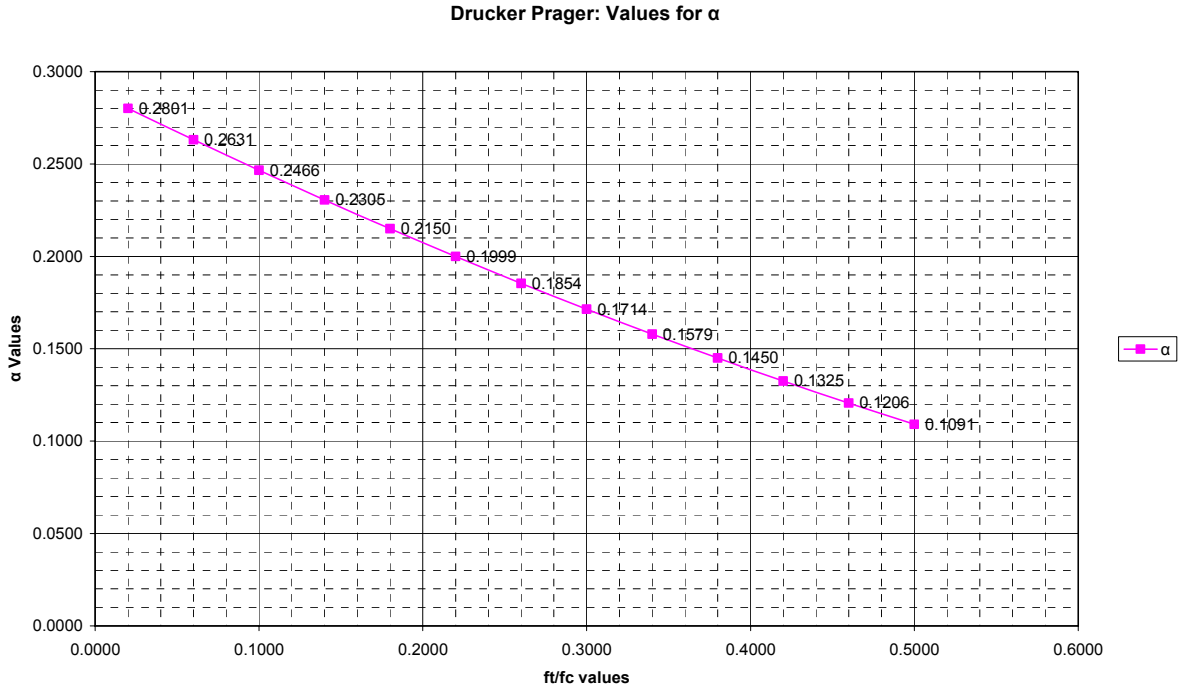

Figure 3-13: Graph illustrating the relationship for α versus f_t/f_c

The same exercise can be done to make a family of graphs to display the relationship between f_t/f_c and the calculated yield stress $\bar{\sigma}$ from the previous equations.

Figure 3-14 illustrates the linear relation of $f_t/f_c = 0.1$ and the values of the yield stress can be read of directly from the graph if the compression stress is available.

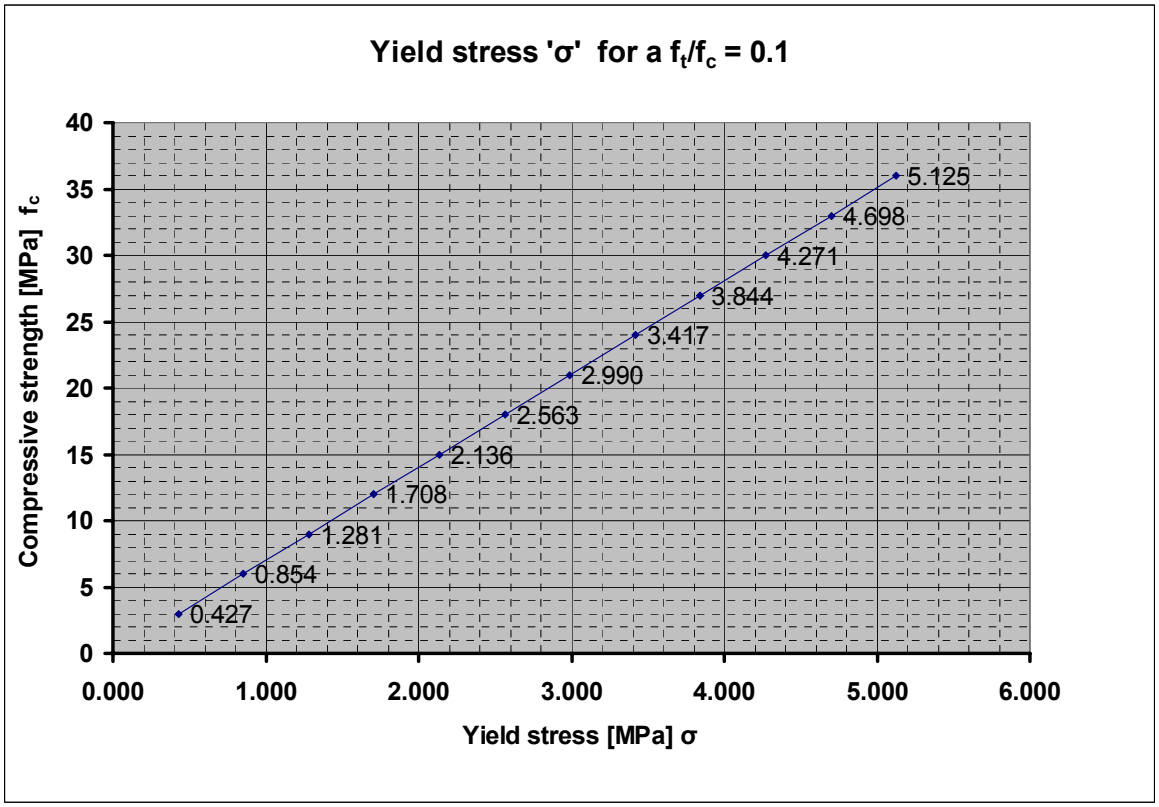

Figure 3-14: Graph illustrating the relationship of compressive stress (f_c) and yield stress ($\bar{\sigma}$) for values of $f_t/f_c = 0.1$

The FEM program input data vary from program to program. Some programs use the cohesion c and friction angle φ as input parameters. The FEM program used in this dissertation, MSC Marc, uses the Drucker Prager constant α and yield stress $\bar{\sigma}$ as input parameters. However, the different programs and their input parameters should give the same results. The important aspect is that the parameters for the FE Drucker Prager yield model can be derived from the tension and compression yield strength for a given concrete. As illustrated from the theory given by Chen (1982), the α and $\bar{\sigma}$ parameters can be easily derived from the tensile and compressive stress of concrete.

3.6.8 Work done by other researchers

The technique of using the Drucker Prager (DP) method in concrete analysis has been practised by engineers for many years. Reference has been made to plastic methods (NW-IALAT, 2001 and Nisar, A et al., 2008). Little useful information could be found on benchmark gravity dam problems or details of numerical analysis using the DP method on dams. Also, relatively little research could be traced in which the tensile and compressive stress were used to determine the DP NL FE parameters, as illustrated in Chen (1982).

Other references were studied to see what the state of the art is in the non-linear FEM field combined with the problems of singularity in dam analyses. Some of these references are briefly discussed below.

Jefferson (2003) analysed a concrete gravity dam using the LUSAS program. This was an NL FEM but only the linear FEM stresses were published and the crack propagation in the dam calculated by fracture mechanics. However, limited information was available and the research could not be used in the benchmarks for this dissertation.

Oliver et al. (2004) published on the European research network (NW-IALAT) and this research team supplied useful information on a gravity arch dam. A 3-D parabolic DP model was also used in the benchmark exercise.

An interesting article was written by Wieland (2005) on the management of high stress concentrations caused by singularities in FEM. He suggested 10 ways of dealing with high tensile stresses in linear elastic FEM, some of which he mentioned were questionable. Wieland is well known for specialising in dynamic analyses and some of these methods are related to linear dynamic FEM analysis:

- Use of FE models with coarse mesh in corner regions
- Calculation of stress in stress points of FEM rather than on element surfaces
- Use of beam models to analyse arch dams (trial load method)
- Use of high static and dynamic tensile strength values
- Use of mean values of tensile strength
- Taking into account strength increase due to ageing of concrete
- Reduction of the return period of design earthquakes
- Use of high damping values for seismic analysis
- Use of pseudo-static seismic analysis
- The high tensile stresses at stress singularities (‘negative corners’) are considered as purely theoretical in nature with no engineering relevance for dams.

Guanglun et al. (2000) wrote an article on the seismic fracture mechanics analysis of Koyna Dam using an idealised bilinear softening curve for the fracture energy G_f. It is interesting to compare this with the work of Cai (2007) who also used the bilinear softening curve to analyse the Koyna Dam. (In this dissertation the DP results were compared with the results of the FM.)

Köksal et al. (2005) did research on concrete masonry blocks utilising the DP yield criterion and compared the material failure with laboratory experimental results. They found that the DP model could predict the bearing capacity of the hollow blocks with reasonable accuracy.

Wang et al. (2004) presented an analysis of a gravity dam modelled on a foundation block with characteristic foundation conditions which were analysed with the DP FEM. The focus of this study was on stresses in the foundation. The analysis was extended to a 3-D FEM of the dam and the foundation block.

3.6.9 Maximum and minimum (major and minor) principal stresses

To conclude the chapter, the equations for the different principal stresses are discussed. The principal stresses are derived from the Mohr circle and are explained in Smith (1971).

It is useful to have the equations for the principal stresses available so that they can be calculated from the normal stress. The equation is for a 2-D stress model:

$$\begin{matrix} S_1 \\ S_2 \end{matrix} = \frac{\sigma_x + \sigma_y}{2} \pm \sqrt{\left\{ \left(\frac{\sigma_x - \sigma_y}{2} \right)^2 + \tau_{xy}^2 \right\}} \qquad \text{Equation 3-38}$$

3.6.10 Equivalent plastic strain contour plots

In this dissertation the equivalent plastic strain is a contour plot used to a great extent and it is therefore appropriate to explain it here. The equivalent plastic strain is a scalar measure of the strain in the region where plastic yielding occurs. It can be defined as the tool for measuring the strain that occurs above the line of a conventional stress-strain curve. It can be regarded as similar to the Von Mises stress, which represents a scalar measure of shear stress in a region of the FE model.

The equivalent plastic strain contour plot is thus a very useful outline that represents the region where failure or yielding of the material occurs. To a certain extent, the equivalent plastic strain can be seen as the area where material cracking can be expected for a brittle material.

3.6.11 Closure and summary

The aim of Chapter 3 was to do a literature study of the theories used in gravity dam analyses. The theory used by the so-called *classical method* was discussed, along with the advantages and limitations of this method as a design tool for gravity dams. It was pointed out that the classical method is based on the Bernoulli-Euler theory for a shallow beam. A case was also made for the FEM being a more accurate method for doing a structural analysis of gravity dams but that it is a more complex method.

The typical load conditions and load combinations were illustrated with typical factors of safety (FOS) for the classical method. These conditions can also be used as a basis for establishing the load conditions for the FEM, but it was pointed out that the classical method and the FEM are not readily compatible due to the difference in theory.

The seven steps used by Rockey et al. (1975) to develop a 2-D plane strain FE program were briefly discussed to illustrate the FEM utilised in this dissertation.

The theory of the plane strain FEM was explained and it was shown how the non-linear material model of Mohr-Coulomb and Drucker Prager are formulated. By using the formulas given in the MSC Marc FE User's Guide (2003) and Chen's handbook (1982), a technique

was presented for calculating the input parameters for the FEM program by simply using the concrete tensile and compressive strength.

The linear relationships between the parameters were also illustrated in two graphs, Figure 3-13 and Figure 3-14).

Some references were also made to other researchers using the Drucker Prager yield model.

In Chapter 4 these relationships will be used to calculate the input data for the Drucker Prager non-linear material yield model and to verify the results from the models of other researchers.

4 ADDRESSING THE PROBLEMS EXPERIENCED WITH FINITE ELEMENT ANALYSES

4.1 Introduction

The object of this chapter is firstly to illustrate the problems experienced with the FEM in analysing a gravity dam. An attempt will be made to address some of the major problems restricting the FEM from being a trusted design tool for gravity dams. The problems that will be addressed are the stress singularities and evaluating the results of the FEM.

From the proceedings of the conferences on Roller Compacted Concrete (Hansen, 1988 and Hansen 1992) can be seen that the classical method is still a popular method used by dam building organisations to design gravity dams. The author got the same impression when different design codes of dam building countries were studied via. the internet.

Some of the aspects that make the FEM unfavourable are the high price of the software, the complexity of the software and the related training necessary. Other aspects are the problems encountered with the analysis itself, such as the problems with singularities related to mesh density, the convergence sensitivity of non-linear analysis and the input parameters which are not readily available.

The FEM is certainly used in South Africa, but usually only to study certain aspects of the gravity dam which the classical method is unable to address, such as temperature loading, seismic loadings and special material studies.

The problem of the stress singularities is illustrated by a simple structure of a vertical beam and a triangular gravity dam, by using different mesh densities. Graphs were prepared illustrating the stress peak at positions of sharp edges, i.e. at the heel and toe of the wall.

To deal with these problems the following two methods were considered. The first one is recommended for a normal linear elastic analysis and basically involves changing the toe geometry at the heel of the wall with a fillet to redistribute the tensile stress at this point. The second method for dealing with the stress peak is to alter the material properties, to permit material yielding and to redistribute the tensile stress to compressive stress. This is accomplished by doing a non-linear FE analysis with material yielding. The Drucker Prager yield model is recommended.

In the next part of the chapter the aim is to verify that the Drucker Prager method simulates the correct material behaviour and that the results correctly simulate the stress distribution. Six benchmarks are done of typical FE models taken from other researchers to calibrate the parameters of the non-linear FE program using the Chen (1982) formulation.

4.2 Preparation of the FEM and the Analysis of Gravity Dams

Before a finite element analysis is conducted, it is essential to consider a few important aspects of modelling:

- The analyst should understand the engineering problem of the dam that he is going to analyse and what it involves. It is necessary to understand the structure and its structural behaviour and to be able to visualise what can be expected of the dam.

- Visualise how the dam structure can be solved and what assumptions, approximations and simplifications could be made to utilise the available FEM tools. Dams can have complex interior geometry and in many cases this can be cut down by manipulating the material properties, such as the stiffness. In many instances a very simple mathematical model may be sufficient. The FEM is a mathematical design tool and it is not always necessary to model all the details. For example, a complex tapered beam with offset can be represented by a single line in space. Beginners tend to create models that look geometrically very impressive, but are mathematical disasters in the finite element solvers and give inaccurate results.

- Decide on a finite element model and the type of elements to be used, e.g. 2-D or 3-D models, plane strain, plane stress elements, axisymmetric solid elements, plate and beam elements, etc. (Modern programs have a great variety of elements and it is important to understand what the element type was programmed for, e.g. a gravity dam can in most cases be analysed in a 2-D plane strain model.)

- Decide on a mesh type, element size, mesh density and the shape of the elements (triangle, quadrilateral, wedge, etc.). With gravity dam analyses the 2-D quadrilateral eight-node element is popular for its flexibility and accuracy.

- Choose the correct element order considering shape, function and accuracy.

- It is good practice to benchmark the elements that are to be used to verify the performance and accuracy of the element in the mesh configuration. Some of the benchmarks used in this dissertation can be used to calibrate the gravity dam model.

- Use the correct boundary conditions because the incorrect choice of boundary conditions can lead to misleading results, e.g. symmetric and anti-symmetric models. Beginners tend to over-restrict the FE model. It is also important to see that the model is fixed in all the necessary degrees of freedom and that it is stable. For gravity dams it is usually only necessary to constrain the bottom and sides of the foundation block.

- Decide on the method that is to be used to apply forces, moments, pressures, temperatures, etc. Water loading on a gravity dam is applied as variable distributed pressure loading. Avoid single-point forces, moments, displacements, etc. as they cause singularities which result in incorrect answers. (Singularities are discussed in Section 4.4.)

- Mixed element types should be connected correctly considering the degrees of freedom and the connection of each type of element.

- Use the correct material properties, especially when non-linear material analyses are performed. Such calibrations are illustrated in this chapter.

- Ensure that the units of force, moments, gravity and dimensions are correct and consistent (see the Section 4.3 on units). This is a common mistake made by beginners.

- Use the correct solving method. Know the different solvers and their capabilities, as well as the convergence parameters. Convergence values that are too coarse can lead to fictitious results.

- Visualise and understand the results. Structural deformation with animation is always a good first-check.

- Watch out for stress singularities and point constraint inaccuracies.

- Always do a check calculation and do not simply trust computer results. The analyst should have good judgement with regard to the structural behaviour. The classical method is a suitable alternative method to check the results of the FEM.

4.3 Units used in the Finite Element Method

It is up to the user to decide what units he prefers to use, but it is important to be consistent with the units of the dimensions, forces, mass, pressures and gravity throughout the analysis.

A useful rule is that the units should satisfy Newton's Law of motion.

$$F = M\,a$$

$$F\ [\text{force}] = M\ [\text{mass}].a\ [\text{displacement/time}^2]$$

South Africa uses the SI system. The units are based on metres for length (m), kilograms for mass (kg) and acceleration in m/s². Table 4-1 gives a set of consistent SI input and output units; these will be used in this dissertation. Because dams are large structures, the DWAF tends to use the MPa and metre units.

The most FE programs have no units built into their input data. Units can be solved by using Newton's law:

Thus 1 N force accelerates 1 kg mass x 1 m/s²

or 1 N force accelerates 1 mg x 1 mm/s²

or 1 MN force accelerates 1 kg x 10^{-6} 1 m/s²

The conversion of weight units to mass units is built into the program.

Table 4-1: Consistent FEM system of units

System of units	INPUT					OUTPUT		
	Length	**Force**	**Elastic Modulus**	**Mass**	**Mass Density**	**Displ.**	**Force**	**Stress**
SI	m	N	Pa	kg	kg/m³	m	N	Pa
SI	mm	N	GPa . 10^{-3}	kg . 10^{3}	Mg/mm³	mm	N	MPa
DWAF	m	MN	GPa . 10^{-6}	kg .10^{-6}	kg.10^{-6} /m³	m	MN	MPa

In this dissertation the SI units and DWAF units will be followed.

4.4 Singularity

The theoretical part of this section is based on a typed document on singularities, but unfortunately the original reference and author of the document could not be traced.

In this section the problem of 'singularity' and how to overcome this by using some mathematical approaches will be examined. Many design engineers identify the points where singularity occurs and then ignore the stress peaks at those specific points. This technique can be applied, but a dilemma arises when the critical design criterion is based at the points where singularities occur, as in the case of gravity dams where the maximum stresses occur at the heel and toe of the wall.

What is a singularity? In many mathematical formulations that model physical systems of processes, the analytical solution includes singular points. These are points in space or time where one or more quantities of the solution take infinite values (e.g. displacements, stresses, velocities or accelerations). These phenomena are called singularities because they concentrate on one single point. In its direct vicinity the solution is regular, i.e. the corresponding values are finite.

In structural engineering, singularities are often observed when there are certain concentrations in the problem data, e.g. concentrated forces, sharp edges or moving bodies suddenly coming into contact. In such cases, singularities are a hint at the fact that certain quantities (mostly stresses) are very high, also in reality (although, of course, not infinite). Singularities are also sometimes a result of contradictory boundary conditions.

Two- and three-dimensional elasticity stress singularities are common. In practice, singularity-free problems are the exception. Knowledge about the origin and correct interpretation of these cases is crucial for design engineers. Consider the simple case of checking a gravity dam structure subject to certain loads versus allowable maximum stresses. If singularities are present, maximum stresses are always infinite, regardless of the size and load. With the modern computer power available, there is a strong tendency towards using

refined meshes to capture more realistic geometric detail and this leads to more singularities, giving misleading results.

Obvious cases where singularities occur are at point loads or forces acting on beam-and-slab structures.

The principle of singularity is explained as follows:

$$\lim_{A \to 0} \frac{F}{A} = \infty$$

Thus $\sigma = \infty$

In reality, concentrated forces do not exist. They are merely an idealisation of forces which are distributed over a relatively small area. For this dissertation only a 2-D case is examined.

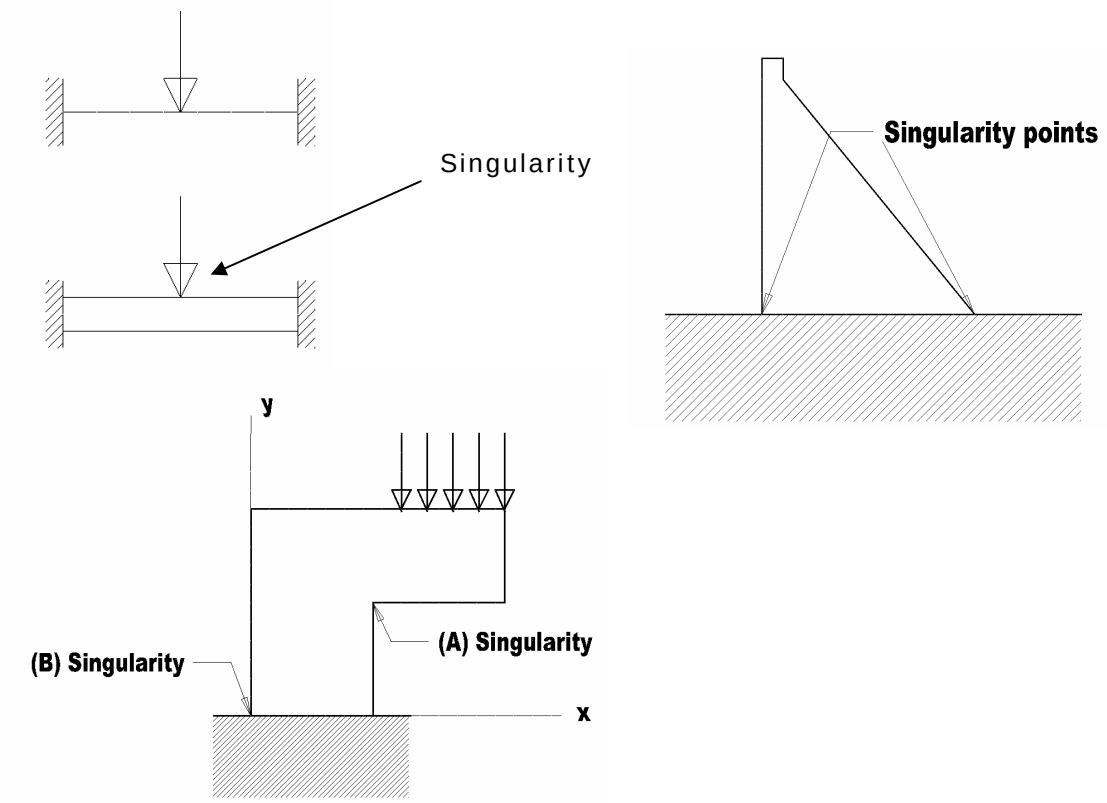

Figure 4-1: Examples of points of singularities

In gravity dam design the situations with stress singularities in linear elasticity analysis are characterised by the geometry: Sharp edges or re-entrant corners usually lead to infinite normal stresses in two or three spatial dimensions.

The mathematical origin of such similarities is not as trivial as in the case of concentrated forces. At point A in Figure 4-1 a horizontal and vertical free boundary meets. For the horizontal edge the boundary conditions are:

$$\sigma_y = 0 \qquad \sigma_{xy} = 0$$

For the vertical edge we have

$$\sigma_x = 0 \qquad \sigma_{xy} = 0$$

Singularities at point A, where both edges meet, lead to a contradiction (obviously both boundary conditions cannot be met at the same time, unless the load is zero). In both the x- and y-directions there is a jump in the corresponding stress components. It turns out that for such a situation all field equations (equilibrium, kinematics and material equations) can only be satisfied within the limit of the normal stress components becoming infinite at this point.

Singularities at point B (see Figure 4-1), where displacement boundary conditions and force boundary conditions meet, are closely related to those described in the previous section. At point B in Figure 4-1 a vertical, free edge and a horizontal, clamped edge meet. The corresponding boundary conditions are:

$$\sigma_x = 0 \qquad \sigma_{xy} = 0$$

at the vertical edge and

$$u_{x,x} = 0 \qquad u_{y,x} = 0 \text{ where } u_{x,x} = \frac{\partial u}{\partial x} \quad and \quad u_{x,y} = \frac{\partial u}{\partial y}$$

for the horizontal edge. Again, satisfying both boundary conditions at the common edge point leads to a non-physical result. From $\sigma_{xy} = 0$ it follows via the material law that $\varepsilon_{xy} = 0$. Together with the kinematics equations and the condition $u_{y,x} = 0$ at the horizontal edge. we have:

$$u_{x,y} = -u_{y,x} \Rightarrow u_{x,y} = 0 \qquad \text{where } u_{y,x} = \frac{\partial v}{\partial x}$$

Moreover, inserting the remaining two conditions into the material equation:

$$\sigma_x = \frac{E}{\left(1-\nu^2\right)} \left(\varepsilon_x + \nu\varepsilon_y\right)$$

$$\text{where } \varepsilon_x = \frac{\partial u}{\partial x} \quad , \quad \varepsilon_y = \frac{\partial v}{\partial y} \quad \text{and} \quad u_{y,y} = \frac{\partial v}{\partial y}$$

leads to

$$0 = \frac{E}{1-\nu^2}(0 + \nu\varepsilon_y) \Rightarrow \quad \varepsilon_y = 0 = \quad u_{y,y}$$

Hence, all strains and stresses ought to be zero which again is only possible for the trivial case of a vanishing load.

Similar effects occur at all points where displacement boundary conditions and force boundary conditions meet (not necessarily at edges, but also along a straight line)

To summarise, the following stress singularities are observed:

- at single forces and supports
- at sharp, 'concave' edges like re-entrant corners and crack tips, and
- at transition points from displacement boundary conditions to force boundary conditions.

With the design of a gravity dam there is a singularity problem of changing boundary conditions as described above.

4.5 Dealing with Singularities in the Structural Analysis of Dams

At first glance, stress singularities can have dramatic consequences in design situations. Typically, stresses are required to remain below certain thresholds in order to ensure structural integrity and usability. If these limits are exceeded, one has either to strengthen or reduce the allowable loads. In the case of singularities, however, neither measure helps. If there is a singularity, the values are infinite regardless of load and material properties. This will be illustrated later in this section by refining the mesh density at the singularity and demonstrating the outcome it has on the stress concentrations.

The key observation in developing corresponding strategies is that infinite values of any quantity, either measurable directly (displacement) or derived (stress and strain) do not occur in reality. They are a result of idealisations and model assumptions. Simply ignoring these phenomena, however, can be dangerous and is, of course, not advisable.

As already mentioned, 'point' forces do not exist. Loads are always distributed over a certain area. This means there is a stress concentration in reality, but the stresses do not become infinite. In the case of re-entrant corners, a similar observation can be made: There is no such thing as a sharp edge in reality, but there is always a certain round-off radius, relaxing the situation. The same discrepancy applies to the transition from displacement boundary conditions to forces boundary conditions.

On top of the fact that the 'sharpness' in geometry and loads is a result of idealisations in the structural models, there is another important factor: real materials do not withstand infinite stresses. In other words, at singular points, the limits of linear elasticity are by far exceeded. In reality, irreversible (plastic) deformations of cracks occur, limiting the stresses to certain maximum values depending on the material strength. At the same time, stress redistribution in the vicinity of the singularity ensures equilibrium, i.e. the process of cracking or plastic yielding does not necessarily propagate through the entire structure. This means that the presence of cracks or plastic zones does not mean ultimate failure of the entire structure. Often these phenomena are limited to very small regions.

To summarise, in dealing with singularities the following methods are available:

- Evaluate the possibility of a singularity and if it only occurs in a very small localised area, selection of the peak stress can be ignored.
- Use a mesh density that is coarse enough to filter out the singularity but still capture the essential geometry of the structure.
- Modify the geometry to incorporate a round-off radius, relaxing the stress concentration. In some cases a wedge-shaped chamfer could also be modelled.
- Utilise fracture mechanics to simulate a crack at the singularity point and redistribute the stress peaks.
- Linearise the stresses along the cross-section of the thin cylinder, as used in the design of pressure vessels and thin arches.
- Contact elements that follow a prescribe path and open them when specified tensile stress occurs.
- Adapted finite element methods and special hp-elements (Evergreen, 2007).
- Use a non-linear material analysis, such as the Mohr-Coulomb and Drucker Prager yield models.

In view of the scope of this dissertation, it will not be possible to do an in-depth study on all the methods and only certain methods will be dealt with that are relevant to gravity dams. The non–linear Drucker Pager method is the most important one and this will be dealt with in detail.

4.6 Effect of Mesh Density on Singularity Errors

4.6.1 Cantilever beam example

To illustrate the effect of mesh density, a few models were chosen with simple geometric shapes and they were modelled with different mesh densities. This is a well-known phenomenon and a variety of researchers have studied the effect of mesh density and element shape on FEM results. An important study on the subject was done in South Africa by Roland Prukl and this is available on his website under the subject 'Papers' (Prukl, 2007).

Two exercises were performed for this dissertation to illustrate the effect of singularities in a plane strain model. The first one was for a simple cantilever beam modelled vertically. The size of the beam is 100 m x 50 m with mesh density varying from 5, 10, 15, 25, 40, 65, 105 to 170 elements over the base length.

A varying pressure was applied to the left side of the beam with values from zero to 1 MPa. The beam was modelled on a foundation to soften the stresses at the base of the beam. The last two meshes were modelled with two-way varying mesh to save computer time. The larger middle elements have no significant influence on the stress accuracy at the boundaries of the beam structure.

A linear static FEA with second-order isotropic quadrilateral elements was used. The cantilever was modelled in a 2-D plane strain domain.

The material properties of a typical concrete were used for the beam and the base, i.e. elastic modulus E_c = 20 GPa, Poisson's ratio is 0.22 and the density is 2 400 kg/m³.

The base block was fixed on the circumference by boundary conditions $U_x = 0$ and $U_y = 0$. Figure 4-2 illustrates the different meshes used in the exercise.

Figure 4-3 illustrates the Sy (or σ_y) normal stress over the mesh density. The stress was taken on both sides, at the base, of the beam. The upstream side (left-hand side) of the beam is in tension (+) and the rear end or downstream side in compression (-). From the figure the effect of the singularity can be seen in that the tensile stress varies from 1.7 MPa to 12 MPa over the reach of mesh density.

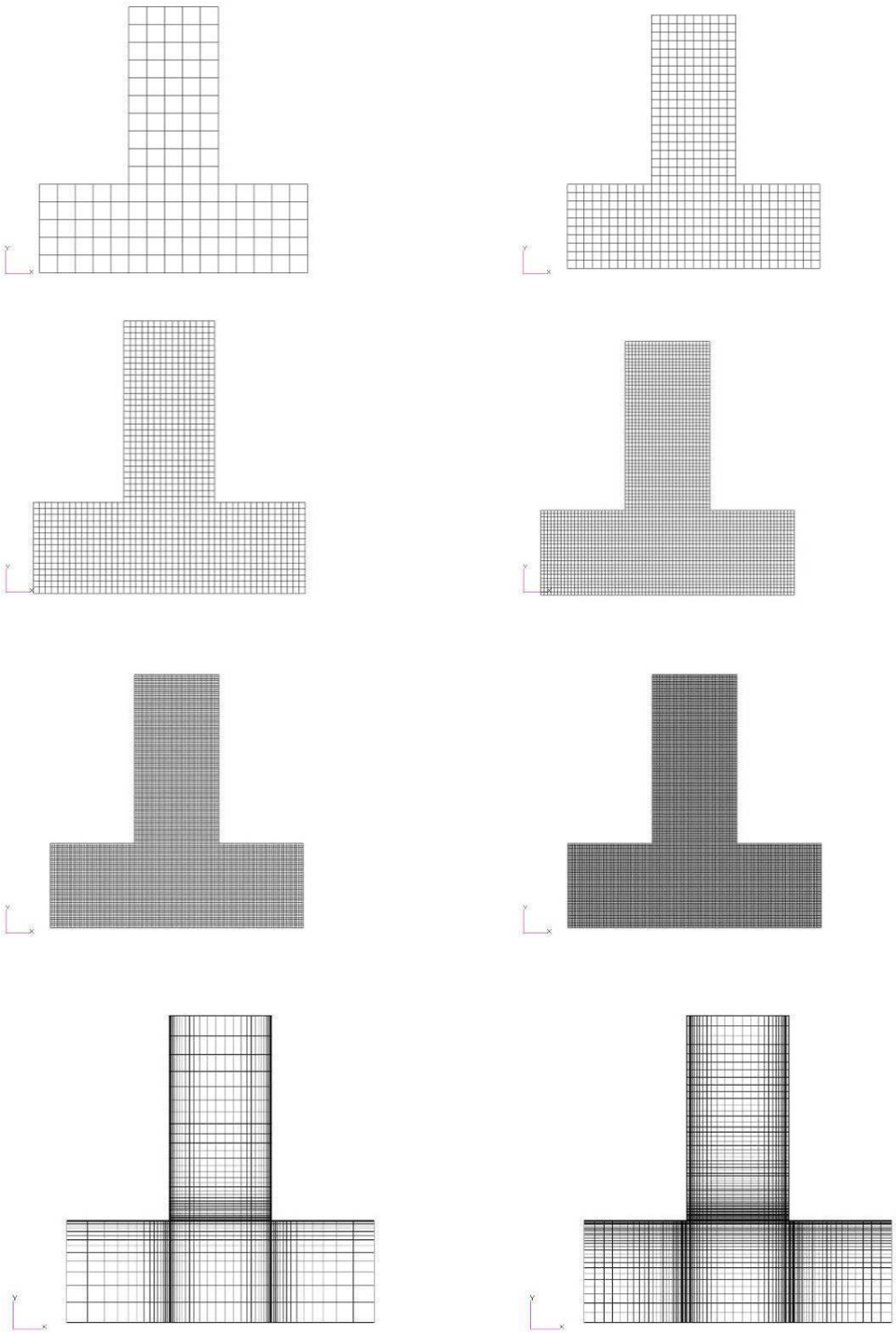

Figure 4-2: Mesh density of 5, 10, 15, 25, 40, 65, 105 and 170 elements at the base position

Note: The symbol for stress has been changed from σ to S because it is more convenient to write the S symbol into the spreadsheet graphs. US is upstream and DS is downstream.

Figure 4-3 shows the normal stress Sy of the vertical cantilever for the different mesh densities varying from 5 to 150 elements at the base of the beam.

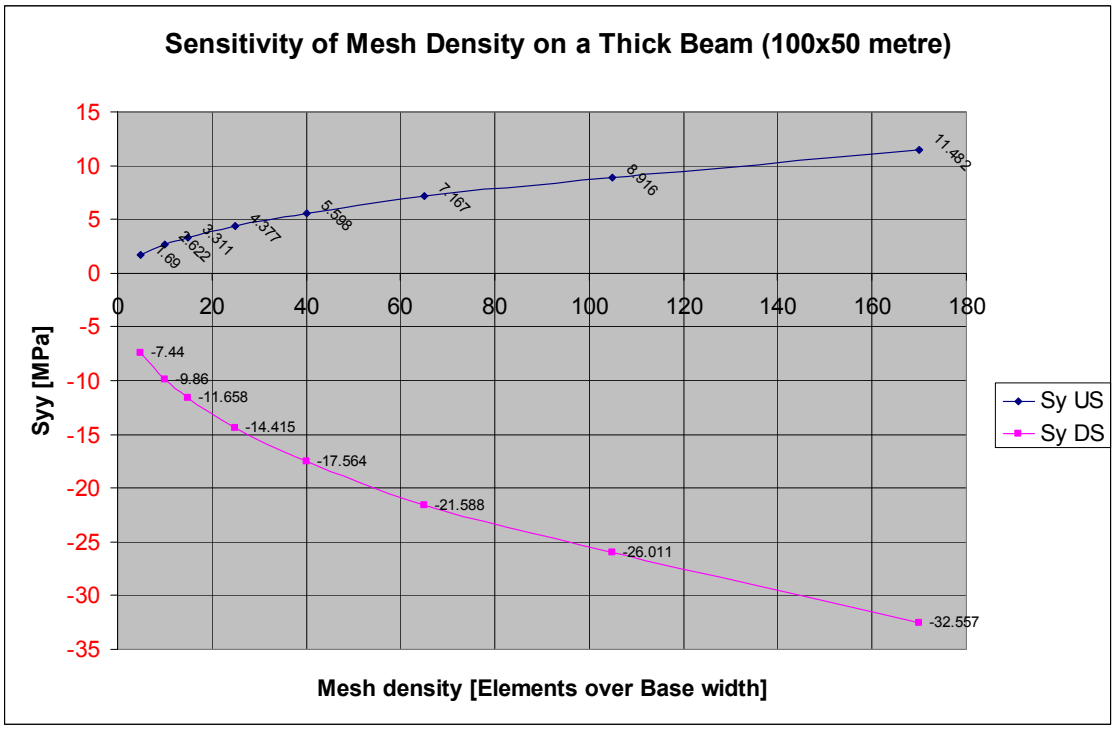

Figure 4-3: Variation of normal stress Sy with mesh density at the base of a vertical cantilever beam

The equivalent beam was also modelled with the classical method for comparison. See Appendix C for the graphical illustration. The stresses of the beam at base level are:

Table 4-2: Variation of normal stress S_y of the classical method and the FEM

	Classical Method	FEM (Mesh density=5)	FEM (Mesh density = 170)
Tensile stress U/S [MPa]	1.56	1.69	11.48
Compressive stress D/S [MPa]	-6.28	-7.44	-32.56

Table 4-2 gives the S_y stresses for the FEM and the classical method taken from Figure 4-3 and the illustration of the classical method in Appendix C.

4.6.2 Triangular gravity dam

A similar exercise to the cantilever beam was performed on a triangular shaped gravity dam comparable to the shape and size that Chemaly (1995) used in his dissertation in Section 5.8.3. The triangular shaped gravity dam is 100 m high with a base width of 80 m. The hydrostatic pressure is 100 m water and full uplift pressure is assumed, i.e. a triangle-shape uplift stress distribution varying from 1 MPa at the heel to zero at the toe of the wall.

This shape was chosen so that the results could be compared with those of the classical method and the crack analysis that Chemaly (1995) performed on this type of dam.

The linear static FE analysis was conducted with plane strain second-order isotropic quadrilateral elements.

The material properties of a typical concrete used in gravity dams were used for the wall, i.e. elastic modulus $E_c = 20$ GPa and a Poisson's ratio of 0.22. For the foundation, an $E_r = 30$ GPa, Poisson's ratio of 0.25. The density of the concrete was assumed to be 2 400 kg/m³ while no gravity effect was assumed in the foundation block.

The foundation was fixed on the circumference by boundary conditions $U_x = 0$ and $U_y = 0$

The last two meshes were one-way biased to limit the number of elements but still have the correct element size at the heel of the wall.

Figure 4-4 illustrates the triangular dam and the mesh densities used to understand the effect of the singularity.

Figure 4-5 illustrates the maximum principal stress of a 160-mesh-density triangular dam to show the limited stress concentration at the heel of the wall.

Figure 4-6 illustrates the normal stress Sy for the different mesh densities for the triangular dam at the heel of the wall. The Sy stress varies from 0.36 MPa to 5.3 MPa, i.e. a stress peak ratio of 14.72.

Figure 4-7 was compiled to illustrate the normal stress Sy distribution along the base of the wall. The mesh density varied from four elements over the width of the wall to 160 elements.

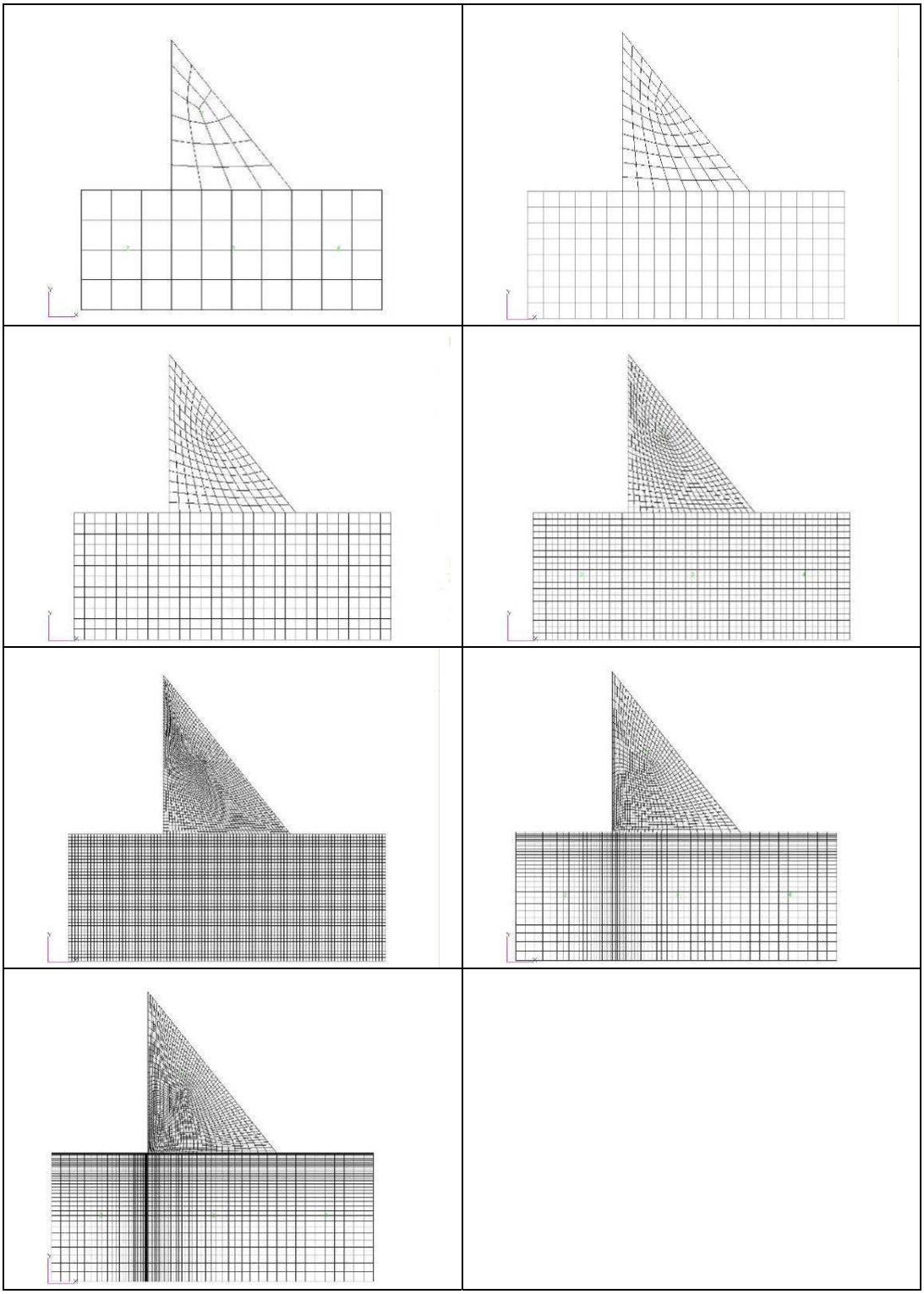

Figure 4-4: Triangular gravity dam: Mesh density with 4, 8, 12, 20, 40, 80 and 160 elements at the base

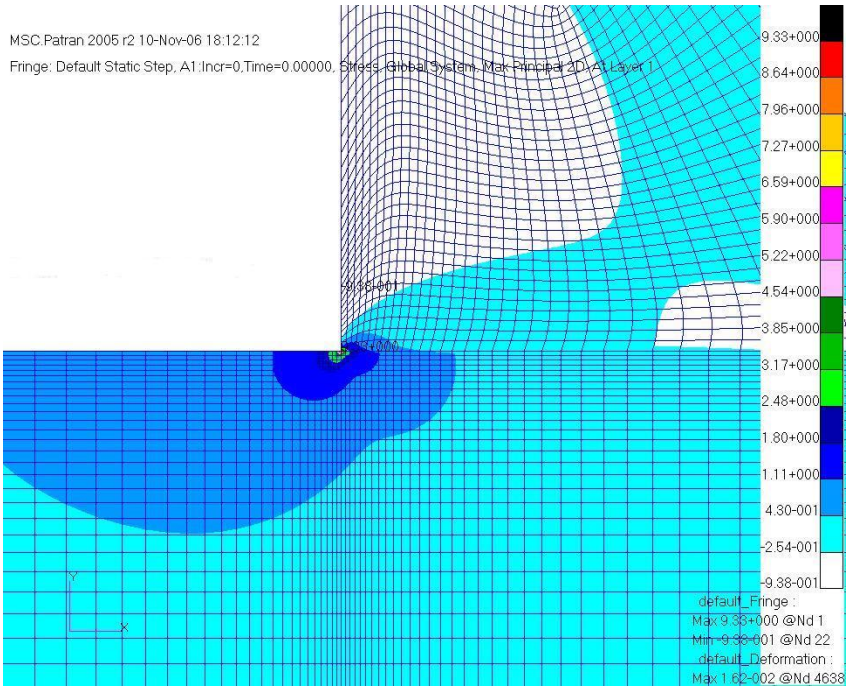

Figure 4-5: Triangular gravity dam: Mesh density = 160: Max principal stress S1 = 9.33 MPa

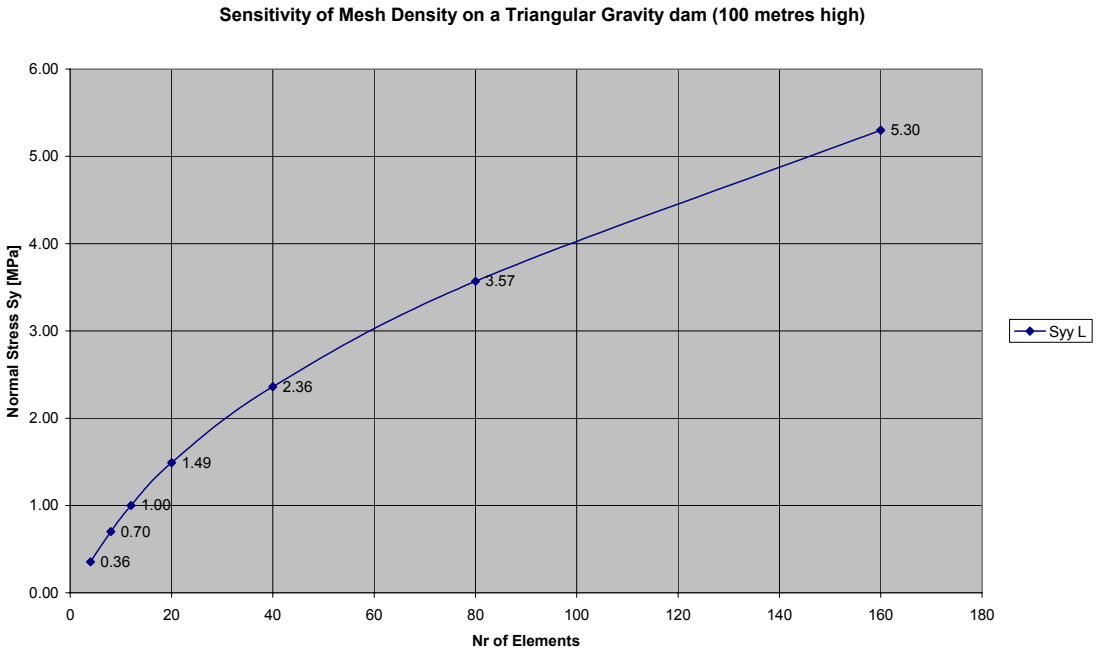

Figure 4-6: Triangular gravity dam: Normal stress S_y at the heel of the wall versus mesh density to illustrate the singularity effect

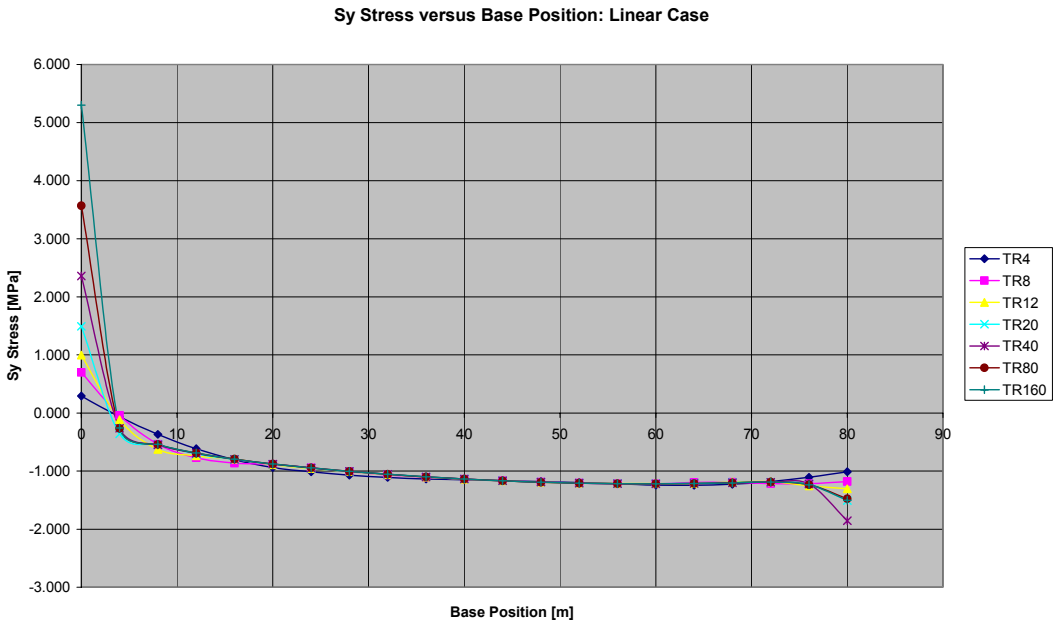

Figure 4-7: Triangular dam: Normal stress S_y versus base position for various mesh densities

Figure 4-7 illustrates the high variation in stress versus mesh density. If a design criterion is based on the stress criterion, e.g. as used in the classical method, it can be seen that it is very difficult to choose a mesh density to obtain the correct stress values.

In Figure 4-5 it can be seen that the tensile stress area at the heel of the dam represents only a very small area relative to the cross-section of the wall, which clearly illustrates the singularity effect encountered on a gravity dam.

The results of the FEM triangular dam with 160 elements on the base position were compared with those of the triangular dam used by Chemaly (1995). The crack length calculated by Chemaly (1995, Table 3, p. 89) was 32.5 m for the classical method and 24.3 m for the linear elastic fracture mechanics method (LEFM) with $K_{Ic} = 1$. From Figure 4-7 it can be seen that the position to where the tensile stress progresses to zero in the FEM is approximately 4 m from the heel of the wall. This distance gives an approximate indication of what point yielding could be expected if no tension were assumed. Even with this extreme condition, the 'virtual' crack length using the FEM is relatively small compared with Chemaly's crack length for the classical method. With a non-linear FEA, the position to where the tensile stress can extend will be illustrated later in this dissertation.

In Section 4.5 one of the solutions for overcoming the singularity problem was to use the FE non-linear material option. To be able to utilise this method it is important first to benchmark some typical non-linear examples available in the literature and to calibrate the results in order

to simulate these laboratory tests. In Section 4.7 some of these concrete laboratory tests are modelled and benchmarked with the FEM by the author.

4.6.3 Shape modification to minimise singularity effects.

In Section 4.5 a summary of some methods of dealing with singularities is given. For the purpose of this dissertation, the emphasis will be on the non-linear material properties, but other methods of dealing with singularities will be discussed briefly. In some cases it could be useful to use a combination of these methods to minimise the singularity effect.

Modifying the shape of the structure at the position where the singularity occurs can reduce the high stresses. To illustrate this on a triangular gravity dam, the dam was modelled with a fillet and a chamfer on the 80-element mesh.

The fillet and chamfer were sized to be smaller than 5% of the wall height to have a minimum impact on the stress distribution in the remainder of the wall. To illustrate the efficiency of reducing the stress peaks at the original position of the heel, Figure 4-8 was prepared.

The curves in Figure 4-8 illustrate the reduction in stress at the heel for a linear static FE model. This is an approximate technique and should only be used for preliminary studies where a quick result needs to be obtained.

Figure 4-8 illustrates the effect of a shape modification at the heel of the wall with a fillet and chamfer. It should be noted that this modification is only done *in the model* to minimise the stress peaks caused by singularity and that the prototype is not constructed as such. The fillet has resulted in the more realistic outcome of reducing the maximum Sy tensile stress from 3.57 to 1.44 MPa, but this is not exactly at the original heel position. If the stress is measured exactly along the base line, at the intersection the stresses are reduced to 0.28 MPa for the fillet.

For the chamfer, the stress at the same position at the heel of the wall is -0.1 MPa. However, the stress value for the chamfer is questionable because it is obviously too low and it is recommended that fillets rather be used.

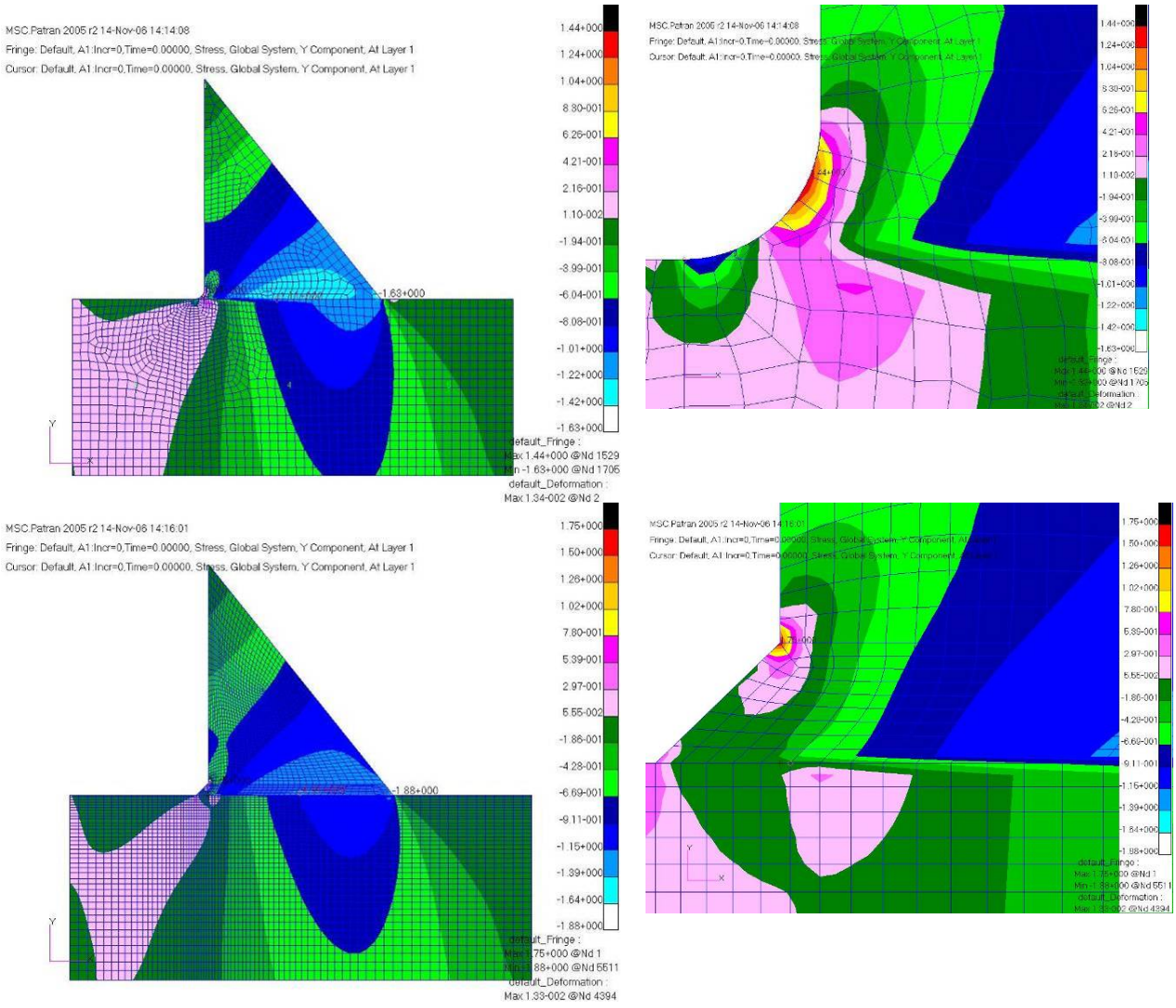

Figure 4-8: Triangular dam: 80 elements: Change in Sy stress (MPa) of a fillet and a chamfer modification at the heel of the wall

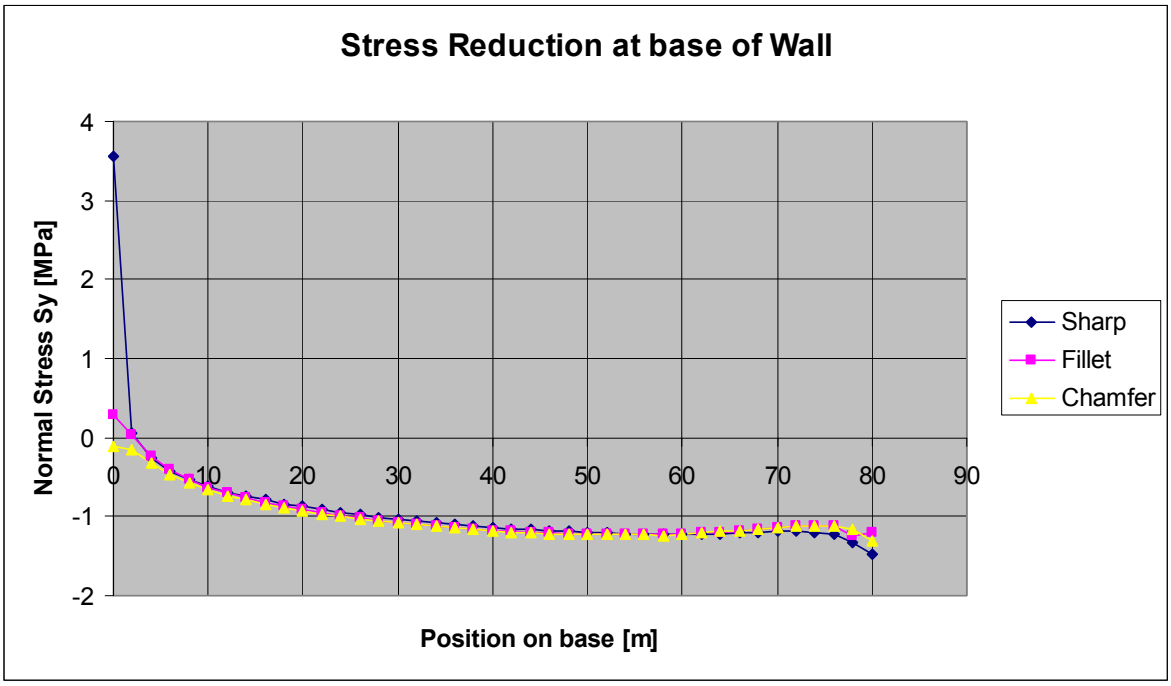

Figure 4-9: 80-element triangular dam: Graph of the normal stress Syy at the base of the wall, starting at the beginning of the heel for the fillet, and chamfer modification

Figure 4-9 illustrates the results of the shape modification of the stresses along the base line. What the shape-modification method actually accomplishes is a redistribution of the tensile stress concentration in the fillet or chamfer. In the chamfer example, there is still a singularity at a point higher up where the chamfer connects at the upstream face of the wall.

The author is of the opinion that one should be very careful when using this method on brittle materials such as concrete as this is not properly benchmarked with actual measured stresses. In the mechanical field, where ductile materials are used, this is quite generally practised.
From Figure 4-9 can be seen that the stresses from the fillet appear to be more realistic. However these results are also dependant on the size of the radius of the fillet adopted and the interpretation of the stress values should be done with good engineering judgement.

4.6.4 Non-linear Drucker Prager method for minimising the stresses caused by singularity

Figure 4-6 and Figure 4-7 illustrate the effect of high stress concentrations at the heel and base of a triangular dam for several mesh densities. It is seen that the stresses vary from 0.36 MPa to 5.3 MPa for a load condition where the hydrostatic pressure is 100 m from the upstream side. It must noted that the correct stress is somewhere in between these extreme stress values. The non-linear Drucker Prager method is now applied to the same triangular dam with the same material properties and mesh configuration as in the previous section. This is done to examine the results of the non-linear analyses and then evaluate them against the linear analyses.

The Drucker Prager non-linear parameters were for a material tensile strength f_t = 1.5 MPa and a compression strength f_c = 15 MPa, which gives α = 0.2466 and σ = 2.1356 MPa when calculated from Chen's (1982) formula (see Equation 3-37).

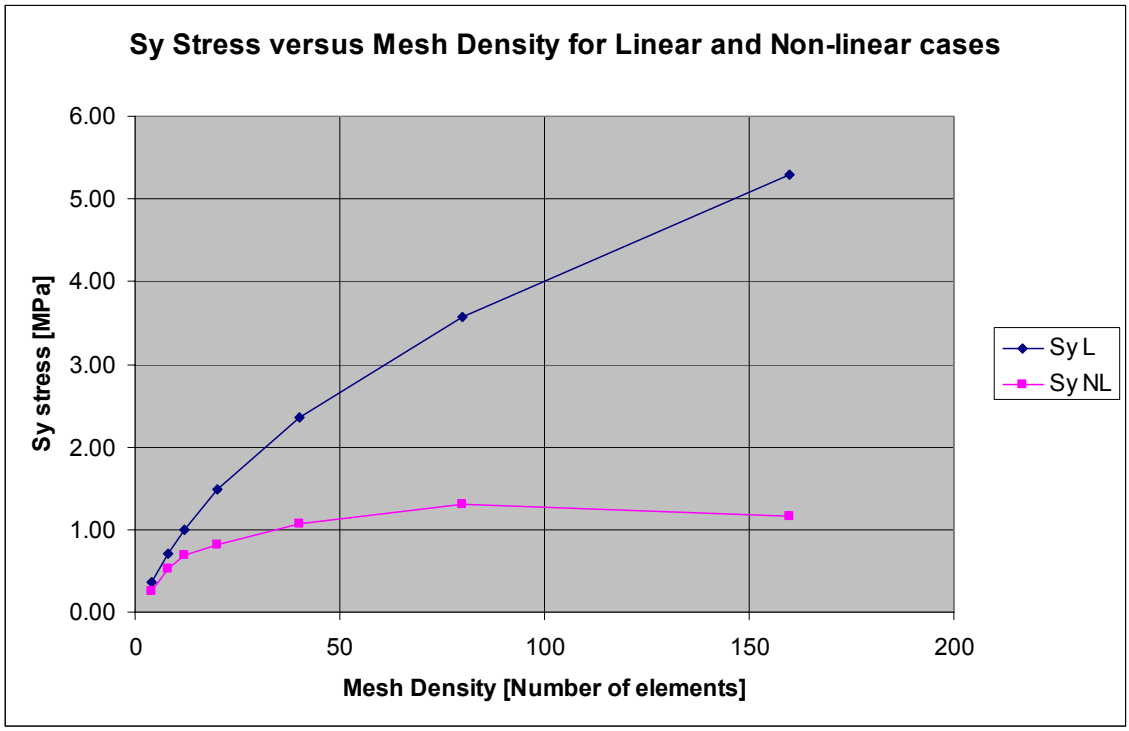

Figure 4-10: Mesh density versus Sy stress at the heel of a triangular gravity dam

Figure 4-9 illustrates the Sy stress values for the linear and non-linear analyses. It can be seen that the stress is reduced to approximately 1.5 MPa, tensile stress, at the heel of the triangular dam.

Figure 4-10 was compiled to examine the effect of mesh density along the base of a triangular wall for a static non-linear Drucker Prager model. This graph can be directly compared with the graph in Figure 4-7 .

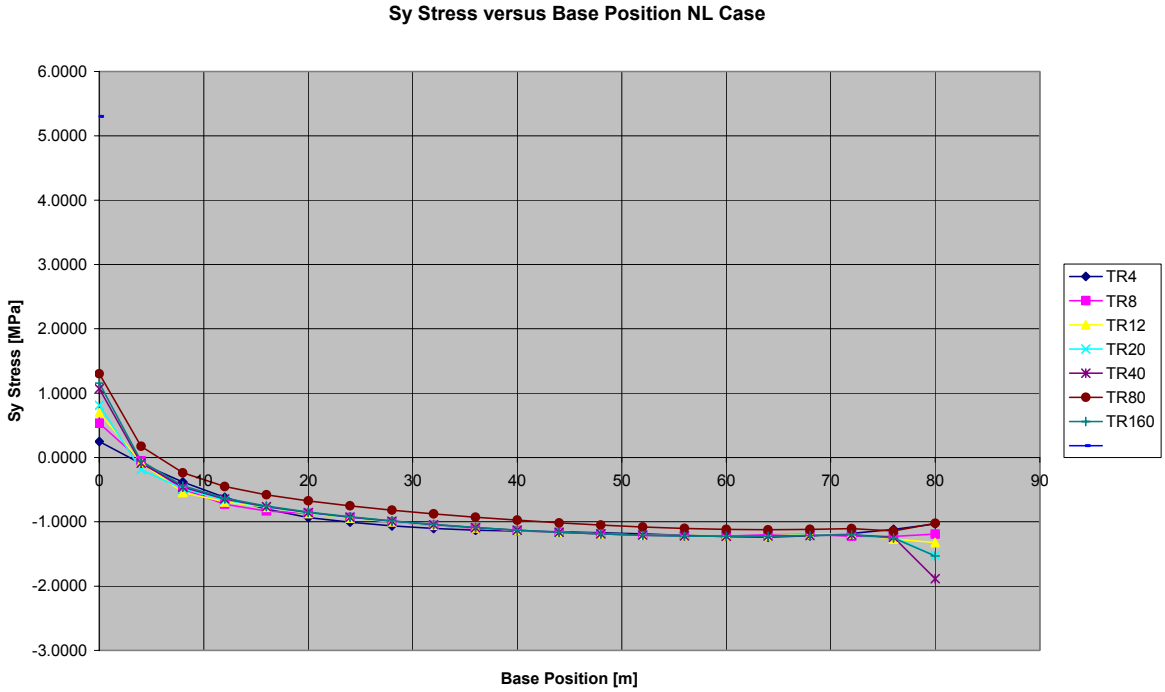

Figure 4-11: Sy stress versus mesh density at the heel of a triangular dam: Non-linear Drucker Prager method

From Figure 4-10 it can be concluded that the non-linear S_y stress distribution along the base is now restricted to the maximum allowable tensile stress f_t =1.5 MPa. The Sy stress curves are slightly more scattered along the middle section than in the linear case, but this is due to the fact that the program has to converge for the non-linear conditions and this produces some inaccuracies. If the convergence parameters are refined in the program, the results will probably be more accurate. The S_y stresses as exhibited for the coarse meshes are less that the given strength of f_t = 1.5 MPa due to the fact that a coarse mesh results in lower stresses than a fine mesh and thus no material yielding occurs. The lower stress value is thus displayed. With the finer meshes, i.e. from a mesh density of 20 elements upwards, material yielding commences and the values tend to converge to yield stress.

Figure 4-11 illustrates to what extent the Drucker Prager non-linear material analysis eliminates the high stress peaks at the heel of the wall caused by singularities. However, it should be remembered that the reduction in stress is caused by material yielding and that the yield zones should be examined to evaluate the performance of the structure. In other words, the area where yielding occurs should be within certain safety standards set by the design engineer.

The strategy for applying the Drucker Prager model in the NLFE for gravity dams is to have a relatively fine mesh in the areas where the stress peaks are expected. This is the opposite of what would be done with the linear FE. The material properties should be correctly determined for the different zones in the dam, e.g. the concrete zones in an RCC dam are an

outer skin concrete, inner concrete, dental concrete to level out the foundation and then the rock foundation material.

To be able to get the correct yielding conditions, it is important to apply the different load conditions in phases and this is done by dividing up the analysis into time steps. These time steps incorporate the self-weight, the hydrostatic pressure on the upstream face, the silt pressure, the uplift pressures, the high flood pressure conditions and the tail-water pressure.

In the case studies later in the dissertation, examples will be given to illustrate how strategy is incorporated.

4.6.5 Linearisation to minimise singularity effects

The theory of linearisation is not recommended for gravity dams but in some special cases it could be used for thin arch dams. Some of the theory as described in the pressure vessel code is given in Appendix F at the end of the dissertation.

4.7 Benchmarking of Drucker Prager Yield Model on Concrete to Calibrate the Material Properties

The aim of this section is to benchmark the non-linear Drucker Prager yield model. Examples of physical models developed by well-known researchers, obtained from the literature survey, are used. The material parameters used in the published research will also be used here as input data for the FEM to benchmark the author's FE models. Many different tests and papers are available in the literature, but only a small selection was made of those tests that would best match the aim of this dissertation.

The benchmarks were progressed in stages of complexity:

- Simple tensile specimen
- 2-D standard beam test
- 2-D standard shear beam
- Chen's flow model
- Model of a gravity dam, 2.4 m high
- Full-size concrete gravity dam.

The object of doing the benchmarks in progression is to have validated results while moving through the different phases.

In the ICOLD Bulletin 94 (1994) on benchmarking of dams, a useful guideline is given on the criteria proposed for acceptable benchmarks for dams:

- Internationally accepted standards
- Quality assurance
- Choice of test cases
- Validation of software used
- Calibration input parameters of material properties

- Accessibility of software
- Setting up an acceptable methodology
- Using the classical method as a check on standards.

4.7.1 Benchmark of a tensile specimen

The aim of this exercise is to examine a standardised tensile specimen test. The work of Reinhardt and Tassilo (1998) was found useful for benchmarking the non-linear Drucker Prager analysis. The linear elastic plastic Drucker Prager theory as given in Section 3.6.6 is used to calculate the input parameters for the FE programs (see Equation 3-37).

Reinhardt and Tassilo's (1998) paper was found useful because it gives the ratio between f_t and f_c yield strength for high-strength concrete. They also specify the type of concrete.

Figure 4-12 illustrates the FE model used by the author to model the tensile specimen with the forces and boundary conditions. A relatively fine mesh was used to represent the Drucker Prager yield model accurately.

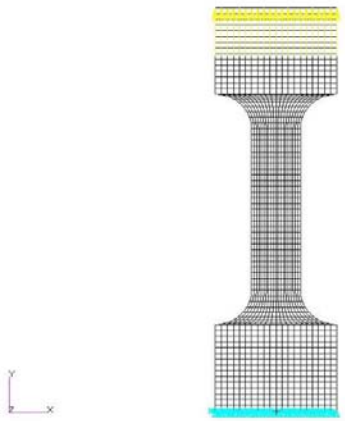

Figure 4-12: Finite element mesh of the tension specimen (from Reinhardt and Tassilo, 1998)

Boundary conditions and applied forces

The nodes at the bottom of the specimen were fixed in the x and y direction (U_x & U_y = 0) which is a minor simplification of the actual laboratory test conditions which were anchored from a central T shaped tube embedded in the concrete. The same simplification is also made attaching the forces on the top of the model.

Figure 4-13 was reproduced from Reinhardt and Tassilo (1998) and illustrated the geometry and laboratory test specimen with the two linear variable differential transformers (LVDT) installed.

Figure 4-14 is from Reinhardt and Tassilo (1998) and represents the results of the tensile creep of high strength concrete of Mix 2 with the I, II, III primary, secondary and tertiary stages.

The FEA used for this benchmark only represents the static condition of Figure 4-14, i.e. no creep and only the values of Reinhardt and Tassilo's graphs for time equal to zero is used.

One of the objects of this FEA is to examine the yield pattern at maximum tensile stress and the positions where the failure will occur at maximum yield stress.

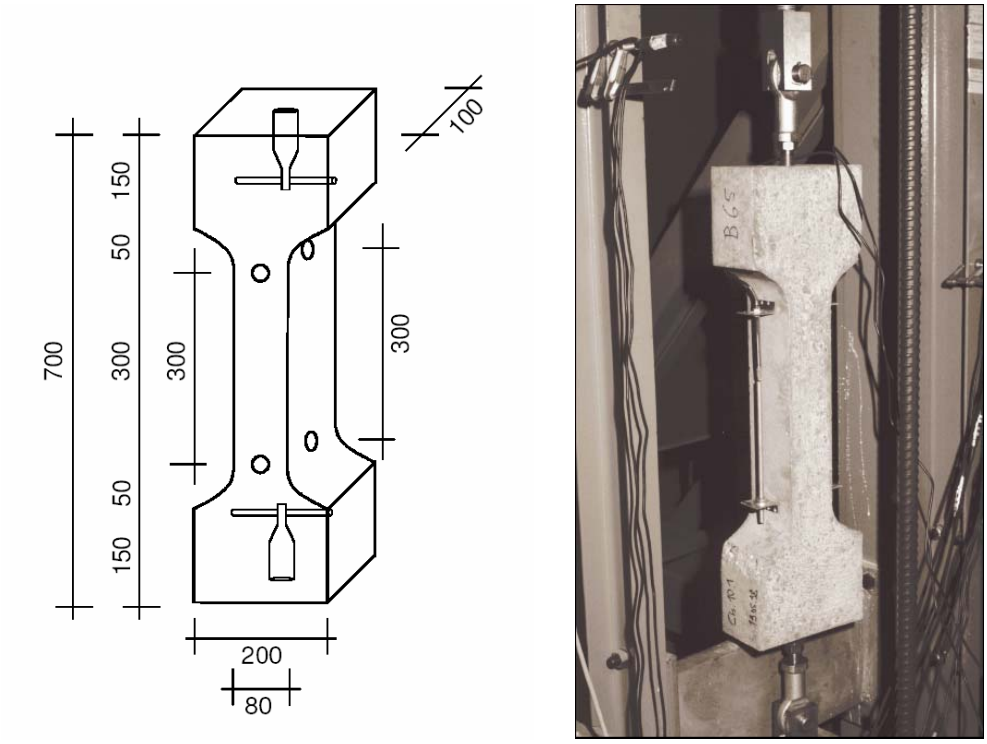

Figure 4-13: (a) Specimen geometry and anchorage (dimensions in mm); (b) Test set-up with two LVDTs (from Reinhardt and Tassilo, 1998)

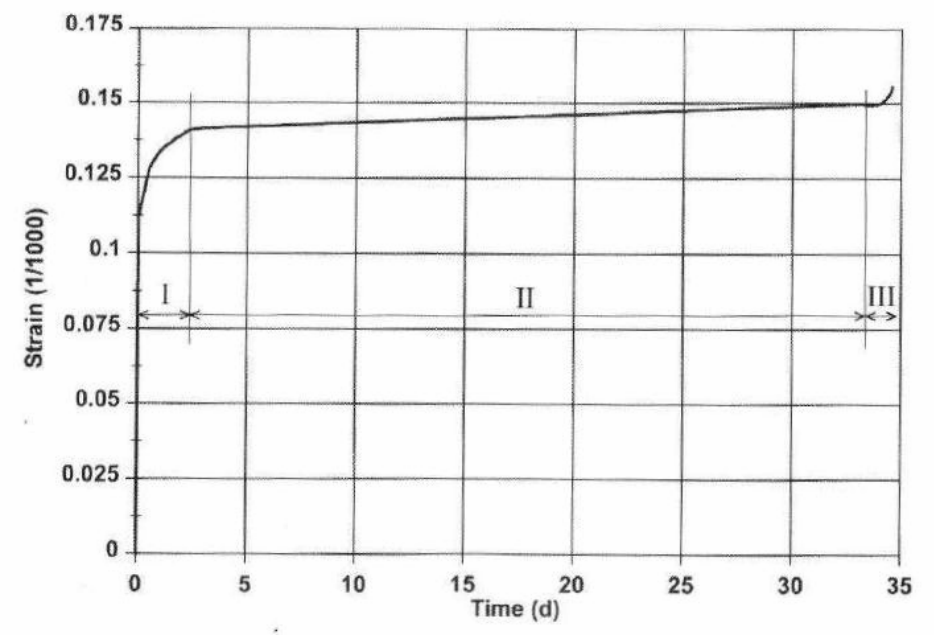

Figure 4-14: Tensile creep of high strength concrete (from Reinhardt and Tassilo, 1988)

Finite element model
The FE mesh was modelled with second-order isotropic quadrilateral elements. A plane stress model was used with a thickness of 0.1 m. A total of 1 520 elements were use to model the specimen.

The model was fixed at the bottom layer (as illustrated in Figure 4-12) in the *x*- and *y*-directions. A force of 1.8971 kN or 1.8971 x 10^{-3} MN applied on each top node (calculated from the f_t = 4.98 MPa multiplied by the area) in the *y*-direction was fixed to the 21 nodes in the upper anchorage position on all nodes along the cross-section.

Self weight was also included, although this will have a very small effect on the results.

Material properties
Material strength properties similar to those given by Reinhardt and Tassilo (1988) were used.

The elastic properties of high-strength concrete for Mix 1 and Mix 2 were:

E_{Mix1} = 41.5 GPa E_{Mix2} = 45.5 GPa

υ = 0.35 a high value was used to simulate the long-term stretching period that was used by Reinhardt and Tassilo (1988) in their laboratory test.

ρ_1 = 2 260 kg/m³ ρ_2 = 2 480 kg/m³

The material strength was:

f_{t1} = 4.98 MPa f_{t2} = 5.2 MPa
f_{C1} = 81.3 MPa f_{C2} = 94.3 MPa

where:
f_{t1} = tensile strength of concrete for specimen 1
f_{t2} = tensile strength of concrete for specimen 2
f_{C1} = compressive strength of concrete for specimen 1
f_{C2} = compressive strength of concrete for specimen 2

To determine the material properties for a linear plastic Drucker Prager model from Equation 3-37, the author calculated the parameter values for the model as follows:

α_1 = 0.2625 α_2 = 0.2652
σ_1 = 7.2384 σ_2 = 7.8525

(The subscripts 1 and 2 refer to the specimen numbers used in Reinhardt and Tassilo, 1988.)

The boundary conditions and pressure applications were tested during the first runs of the FE model. These simplifications seem to be acceptable and no singularity effects occurred at these positions (see Figure 4-12 and Figure 4-13).

Results
The results for the tensile specimen are illustrated in the graphs and contour plots of the FE model given below.

The FE program was set to use automatic time-stepping for this exercise and the maximum load occurs at step 1.0.

Figure 4-15 shows the relation between the y-displacement and the tensile stress at the node in the neck of the tensile specimen. When S_y reaches the maximum tensile strength, yielding occurs at this node and the Drucker Prager yield model keeps the stress constant according to the linear plastic rule. Figure 4-19 is included to illustrate the fracture pattern of the laboratory specimens. It will be noticed that 19 of the 24 specimens fractured near the neck of the specimen. Figure 4-18 is a contour plot of the equivalent plastic strain and indicates that yielding occurs near the neck of the FE model.

Figure 4-16 shows the relationship between the normal stress S_y and the applied load. This graph basically illustrates the same results as in Figure 4-15 because there is a direct relationship between the time steps and load increments. The total load on the specimen was chosen to be 21 multiplied by 1.897 kN, i.e. 39.8 kN, to illustrate the total force applied to the specimen.

Figure 4-17 was prepared to illustrate the relationship with the test model of Reinhardt and Tassilo (1988). It can be seen that at time step 1.0, at maximum load level, the value of strain is 0.112×10^{-3} and this corresponds to the value on Reinhardt and Tassilo's graph given in Figure 4-14 at time position zero.

Figure 4-18 illustrates the normal stress S_y and the equivalent plastic strain for mix 1 at maximum load level. This contour plot was prepared to show the tensile stress distribution and the positions where initial failure occurs. Here one of the features of the Drucker Prager model can be seen, namely that it can handle failure in different areas simultaneously. The failure positions are also correctly located for a tensile specimen if compared with Figure 4-19.

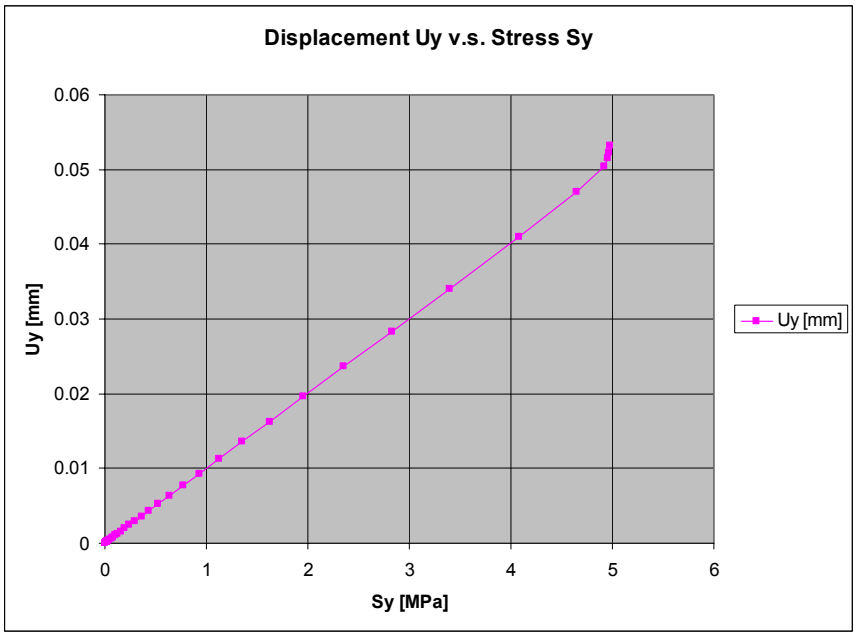

Figure 4-15: Mix 1: Resultant displacement U_y versus stress S_y increment

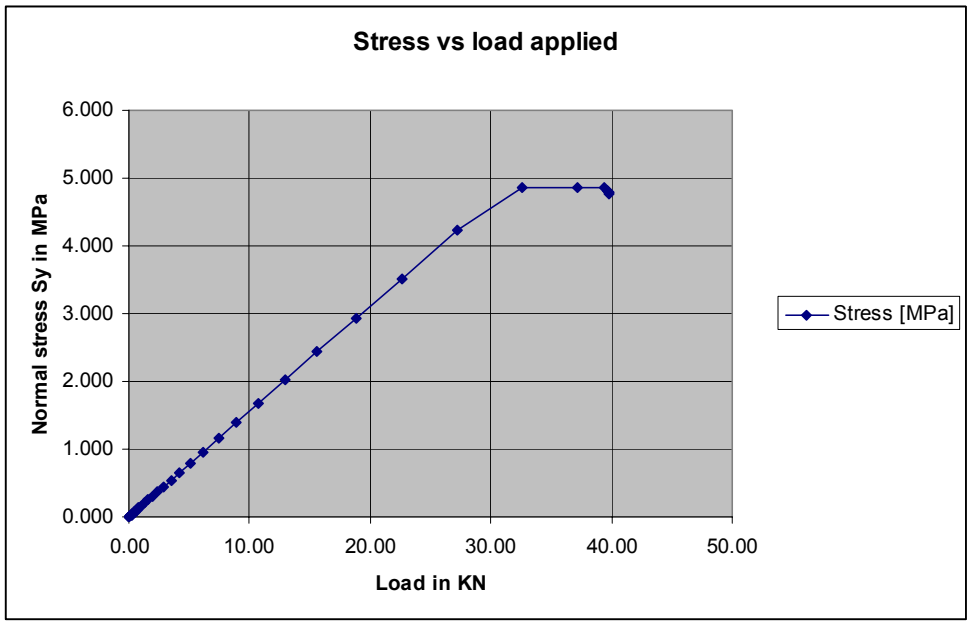

Figure 4-16: Mix 1: Normal stress S_y versus load increment in kN

(see note [1] after Figure 4-18)

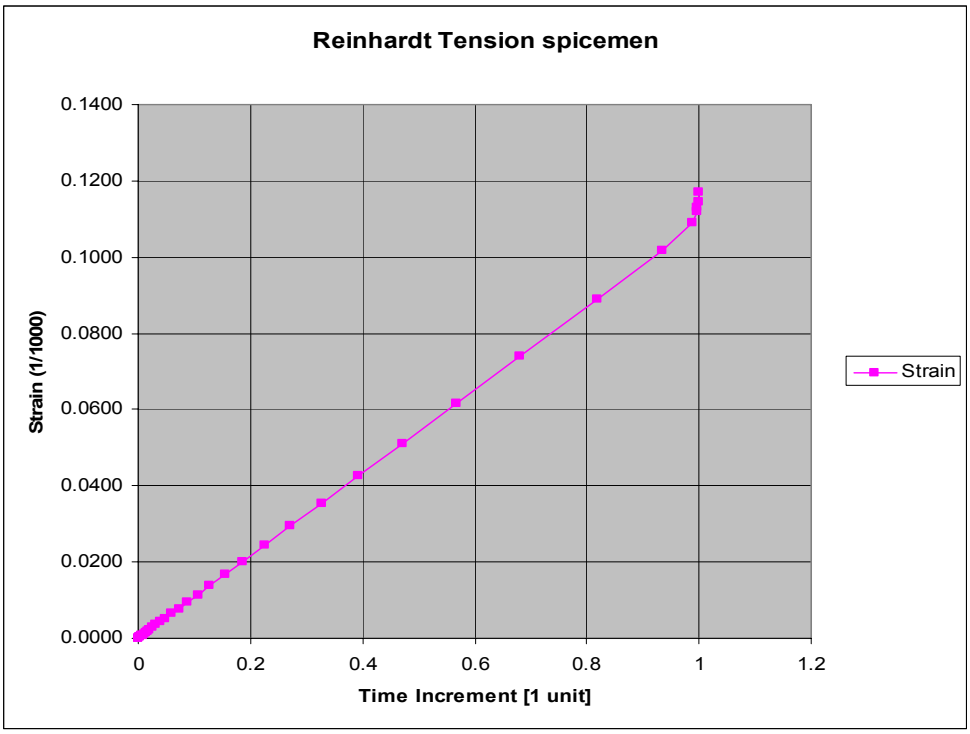

Figure 4-17: Mix 2: Strain versus time increment

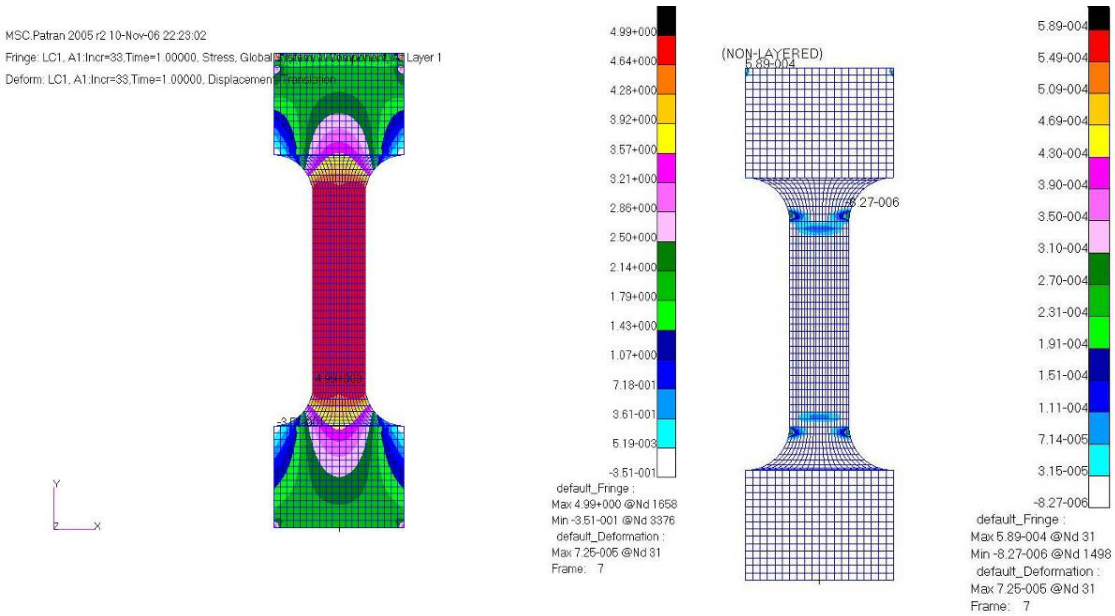

Figure 4-18: Normal stress S_y and equivalent plastic strain for Mix 1

Note 1: The stress S_y is measured at the neck of the specimen where yielding occurs (see Figure 4-18 illustrating the equivalent plastic strain). Although yielding occurs at this point the stress in the rest of the specimen is still in the linear region and the residual stress is redistributed to the adjoining elements. This is the reason why the S_y stress remains constant while the load increases.

Figure 4-15 and Figure 4-17 show the typical Drucker Prager linear elastic plastic relationship as illustrated in Figure 3-7. The program was set on 'auto time stepping' and thus the variable time steps can be seen in the graphs. For this analysis, the time increments are directly proportional to the loading force. The turning point indicates the yielding point slightly before the last time increment of 1.0. From the stress plots the S_y stress is 4.99 MPa, which corresponds to the values used as input parameters for the Drucker Prager model to compare with Reinhardt and Tassilo's (1998) values, Table 3, mix 1. The equivalent plastic strain illustrates the positions where the specimen FE model has moved into the plastic domain.

A similar analysis was done on mix 2 to compare the strain calculated from the Drucker Prager theory and the experimental values measured by Reinhardt and Tassilo (1998), Figure 5. The strain value of 0.11 (1/1 000) from Figure 4-14 at time zero corresponds to the value in Figure 4-17, namely 0.108 (1/1 000) for a 90% ratio of the applied force, i.e. at time interval 0.98, which shows good correlation of the strain values.

The model was stable and the results correlated well with the published experimental values. The behaviour expected from a linear plastic material model could be observed clearly from the graphs. The point of failure could also be identified at the stage when the equivalent plastic strain started (see Figure 4-18).

Figure 4-19 is taken from Reinhardt and Tassilo (1988) and shows the fractured specimens and where the failure occurred. As mentioned above, the fracture patterns of the laboratory test specimens tend to correspond to the Drucker Prager failure predictions and can be visualised by examining the equivalent plastic strain (EQPS) contour plot. The positions where EQPS will occur, cracking and yielding are predicted.

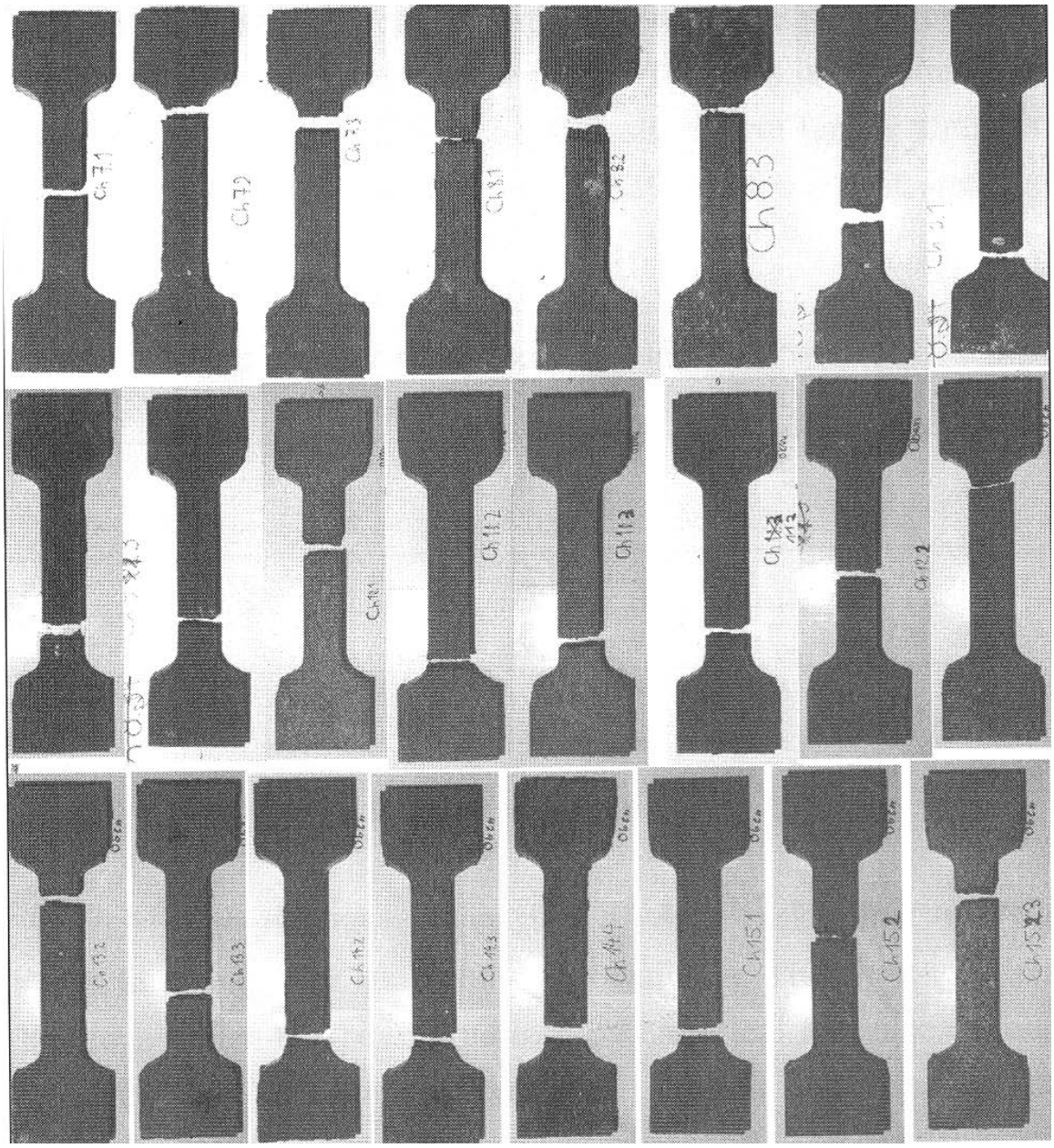

Figure 4-19: Specimens after failure of short-term and long-term tensile test (from Reinhardt and Tassilo, 1988)

The aim of this benchmarking exercise was to find the critical stress when concrete failure occurs and where it would happen within the parameters used for the non-linear yield model.

It can be concluded that this Drucker Prager benchmark FE model gave a reliable representation of a laboratory tensile specimen failure test when compared with the work done by Reinhardt and Tassilo (1988).

4.7.2 Benchmark of a beam in bending, according to BS 1881

Standardised Beam Test BS 1881

The next exercise is to benchmark a standardised beam bending test. This section has been included to illustrate how the raw data from an actual dam were prepared to determine the material properties for the Drucker Prager FE model. This is actual mass concrete used for dam construction and it is important to note the strength of the concrete.

The author wishes to thank Mr Alan Chemaly of the DWAF (Chemaly, 2006), who was willing to share information on material laboratory records from Zimbabwe, dating from the time when he was involved with the construction of the Palawan Dam. For construction quality control, prefabricated beams were tested according to BS 1881. The next challenge was to simulate and benchmark this standardised laboratory test and compare the outcome with the actual laboratory test results.

The Palawan Dam concrete mix is given in Table 4-3 for academic purposes in order that it can be compared later with other concrete mixes and the concrete strength of other dams.

Table 4-3: Mix proportions of concrete used at Palawan Dam (from Chemaly, 2006)

Cement	255 kg
80 mm aggregate	775 kg
40 mm aggregate	447 kg
20 mm aggregate	220 kg
River sand	418 kg
Fine sand	163 kg
Water (w/c = 0.55)	140 kg
Total per m³	2 418 kg

The available laboratory information was still in basic raw format and had to be processed by the author; this is given in Table 4-4. The aim of the data processing was to find the relationship between the actual tested cubic compressive strength and the tensile strength of the concrete from the laboratory tests.

Table 4-4: Summary of construction report on the concrete strength of Palawan Dam (from Chemaly, 2006)

Age	Mean strength (MPa)	Mean standard deviation (MPa)	Mean density (kg/m³)	No. of tests
7 days	19.3	2.7	2399	30
5 000 (°C.h)	18.4	2.4	2399	30
28 days	33.5	3.4	2402	30
20 000 (°C.h)	33.0	3.2	2402	30
90 days	46.4	4.2	2422	30
65 000 (°C.h)	46.5	3.9	2422	30

Note: °C.h is the measurement for the maturity of concrete (see Fulton, 1977, p. 104 and Plowman, 1951).

The samples of Palawan Dam concrete were statistically analysed to determine a relation of f_t/f_c for the concrete used on the dam.

Figure 4-20 was prepared to examine the distribution of f_t versus f_c. Figure 4-21 presents the histogram and illustrates the approximate normal distribution of f_t.

The laboratory test values were also analysed for the German $f_t = a \quad f_c^{2/3}$ relationship, (Heilmann et al., 1976), but did not correlate as this relation tends to fit only high-strength concrete stress values.

Figure 4-20 and Figure 4-21 illustrate the concrete strength distribution for the Palawan Dam with the aim of finding a statistical relationship between the tensile and compressive strength of the concrete. The classification of concrete as 260/80 represents the cement content (kg/m³) and the aggregate size (mm).

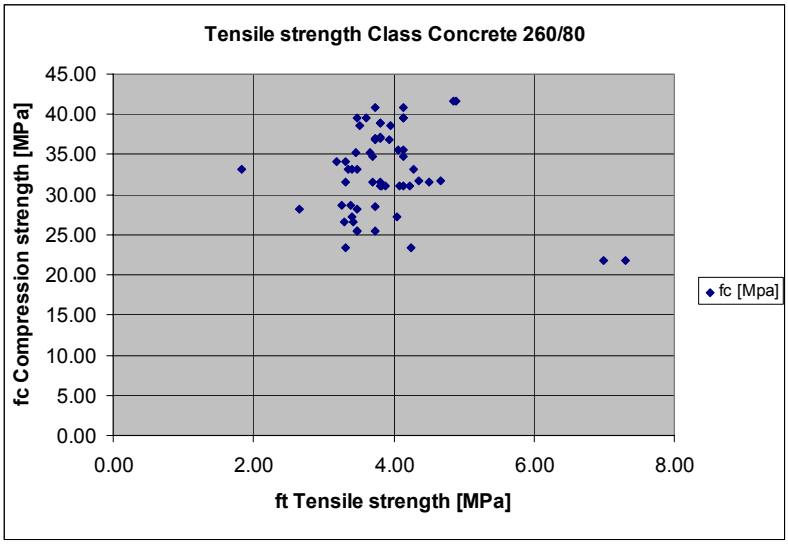

Figure 4-20: Compression yield stress versus tensile strength stress – Palawan Dam

The plotted points of concrete strength in Figure 4-20 show a random distribution and the next step is to set up a frequency histogram of the data to study the distribution.

The two outliers in Figure 4-20 were probably laboratory errors of some kind but were neglected in the calculations of the strength later.

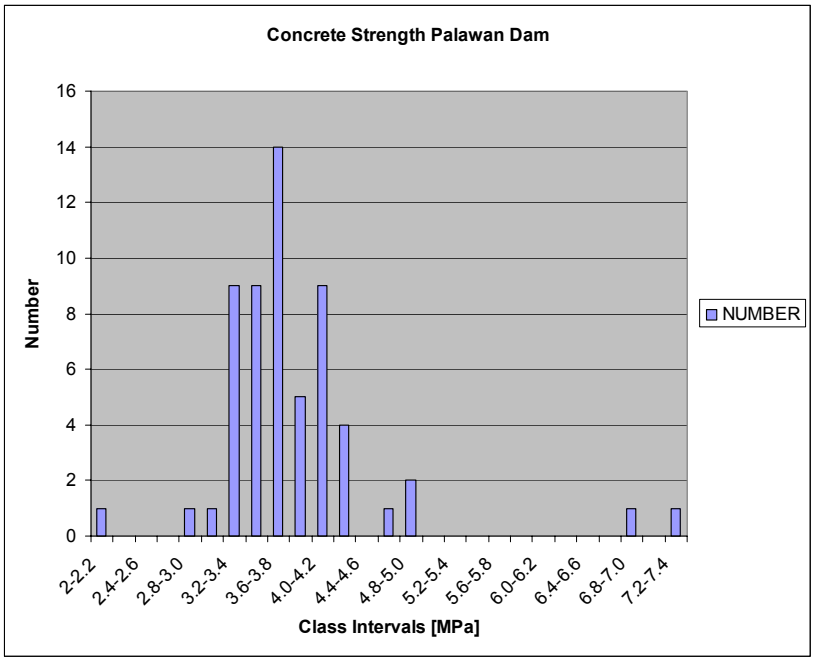

Figure 4-21: Frequency distribution histogram of test values for f_t

Table 4-5 was compiled by the author and represents the statistical values of the Palawan Dam concrete strength that will be used for the next benchmarking exercise.

The distribution tends to be a normal distribution and the average and standard deviations were calculated from the data.

Table 4-5: Statistical values for concrete strength of Palawan Dam

Item	f_c (MPa)	f_t (MPa)
Average strength	32.767	3.871
Standard deviation	5.261	0.796
Minimum value	38.03	3.07
Maximum value	27.51	4.67

Note: The value for f_t/f_c = 0.118, which agrees approximately with the well-known ratio of 10% used in the DWAF

BS1881 Concrete Test Model (see BS 1881, 1983)

The next step was to create the FE model. Figure 4-22 and Figure 4-23 illustrates the test set-up of the BS 1881 test model and was redrawn from the sketch given in the British standard.

Figure 4-24 illustrates the FE model used by the author to simulate the BS 1881 test. The mesh was modelled in the pre-processor. The FE model of the beam was modified to reduce the singularity effect, as described below.

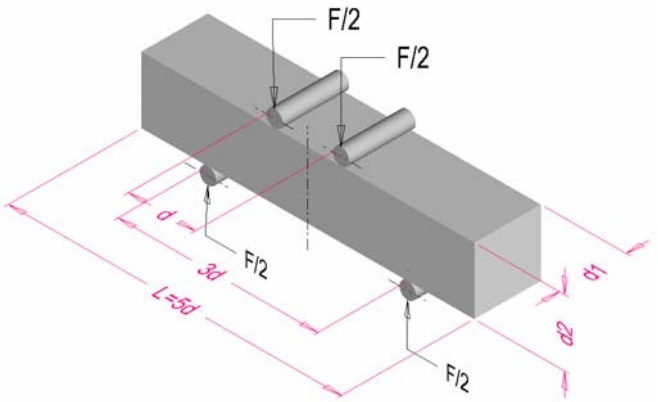

Figure 4-22: BS 1881 test specimen illustrating the symbols

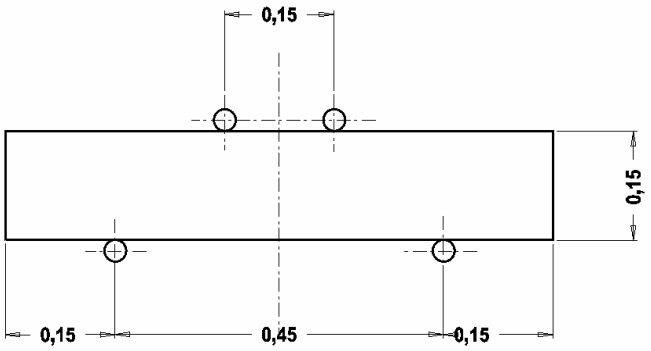

Figure 4-23: BS 1881 arrangement for loading of the test piece (two-point loading, dimensions in metres)

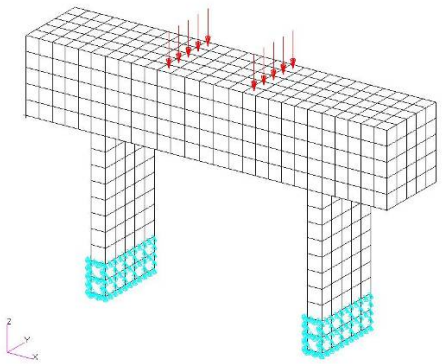

Figure 4-24: FEM of the test beam illustrating the forces and boundary conditions

The BS 1881 concrete test beam was modelled with second-order isotropic 20-node brick or hexagonal elements. The author found that the standard FE roller boundary condition caused stress peaks due to the singularity points at the roller positions. In order to overcome this problem, another model was created to simulate the support rollers as two columns with a stiff elastic modulus that would restrict the vertical movement, but be slender in the horizontal direction, to model the roller effect. This modification solved the problem of fictitious material yielding at the roller contact points without having to use contact elements.

Boundary conditions

The boundary conditions were applied on the columns in the three translation degrees of freedom (u_x, u_y and u_z), as shown in Figure 4-24.

Load applied

From BS 1881, Section 6, the flexural strength $f_{ct} = \dfrac{F.L}{d_1.d_2^2}$, from which the force F can be calculated. See Figure 4-22 for the symbols.

A pressure of 1.842 MPa was distributed over the elements. This pressure was used to eliminate the singularity problem which caused incorrect material yielding.

Material properties

The material properties were derived as previously from the Drucker Prager formulation for the ratio of tensile and compressive stresses for Palawan Dam, as given in Table 4-5.

$E_c = 28$ GPa
$\upsilon = 0.22$
$\rho = 2\ 500$ kg/m³
$\alpha = 0.2393$
$\bar{\sigma} = 5.456$ MPa

The DP NL FE analysis was conducted with the MSC Marc FE program (2003).

Results of the analysis

Figure 4-25 illustrates the normal stress S_x, i.e. the horizontal stress distribution for the DP NL FEM. The maximum S_x stress is 4.0 MPa.

Figure 4-26 represents the S_x stress for the DP NL FE analysis along the centreline of the beam. The small irregularity at the top of the curve is caused by the high pressure concentrations over the relatively small area on top of the beam which brings about some irregularities. Theoretically, this curve should be symmetrical along the centreline.

Figure 4-27 illustrates the vector plot of the major principal stress (S1) and shows the dominant direction of the vectors. Note the arching effect of the vectors. Yielding starts at $S_x = 3.64$ MPa and the analysis converged at 3.85 MPa, which is in agreement with the tensile stress of 3.84 MPa given in Table 4-5.

Figure 4-29 was compiled to illustrate the stress strain relationship of the DP NL FE analysis of the BS 1881 beam test. Two material strength are illustrated i.e for the f_t = 3.87 and f_t = 1.0 MPa.

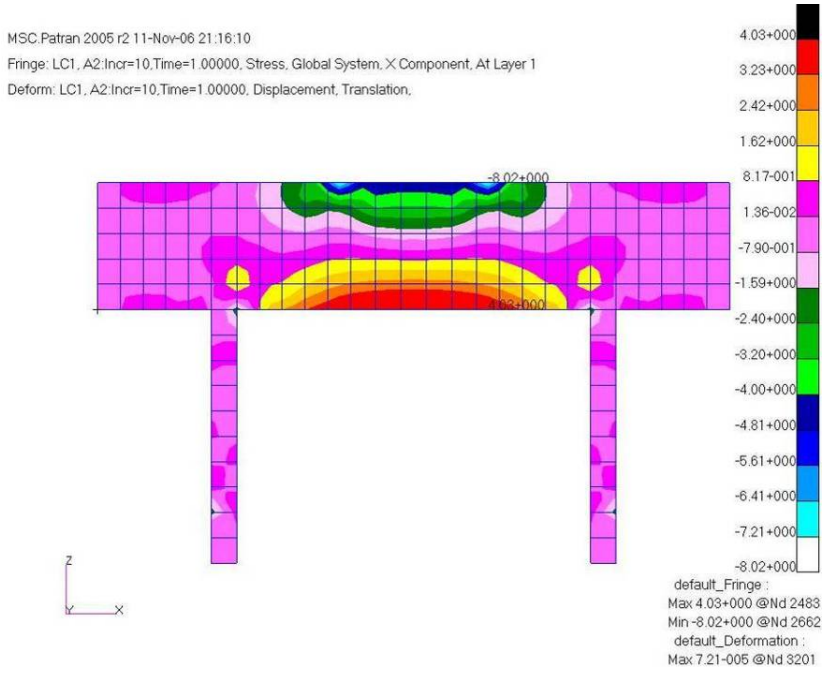

Figure 4-25: S_x stress for the NL Drucker Prager analysis

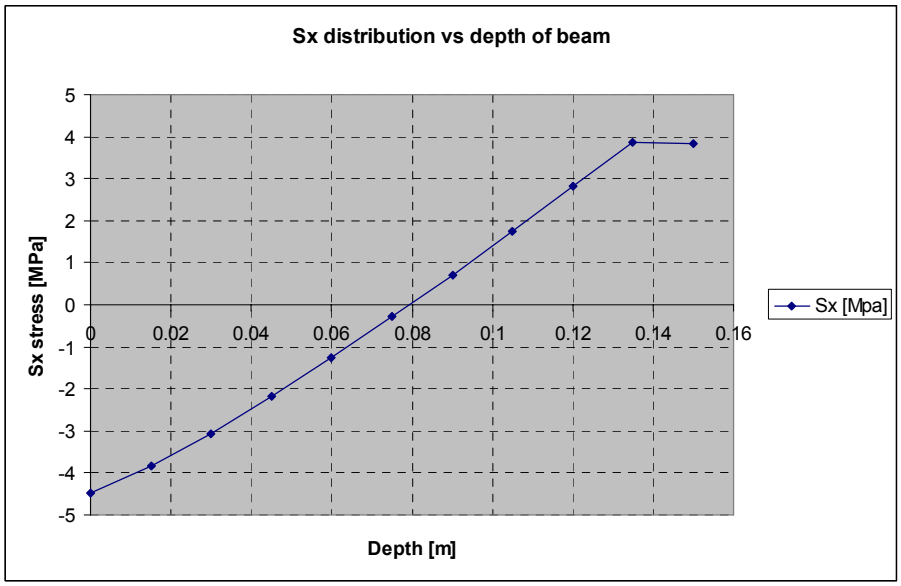

Figure 4-26: S_x distribution through the depth of the beam along the centreline for the maximum force

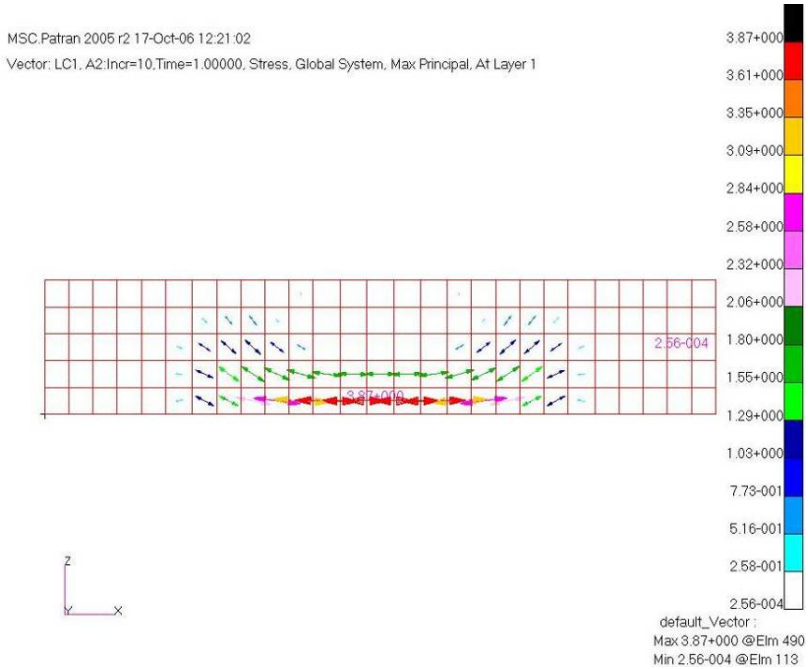

Figure 4-27: Vector plot of the maximum principal stress S1

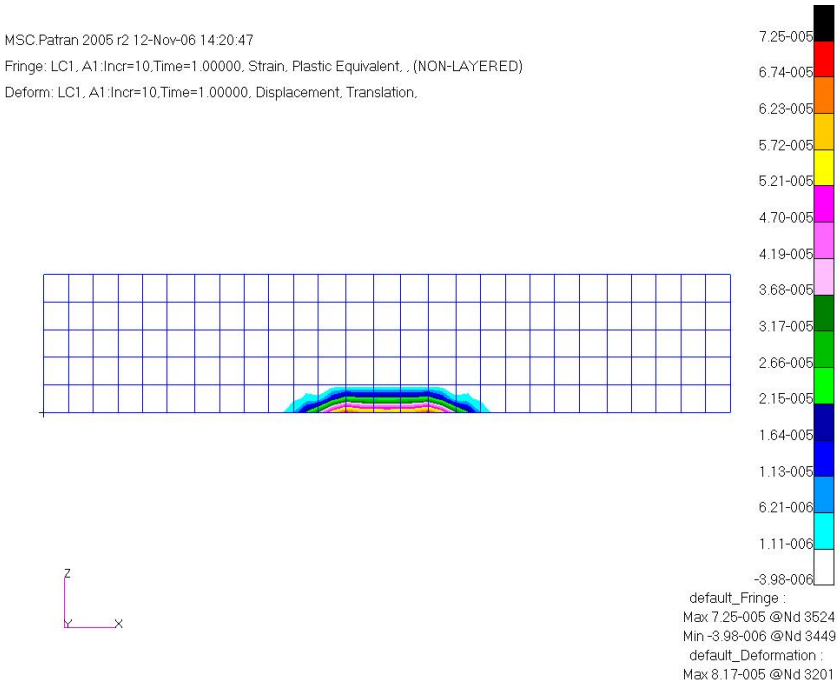

Figure 4-28: Contour plot of the equivalent plastic strain, i.e. position where yielding occurs

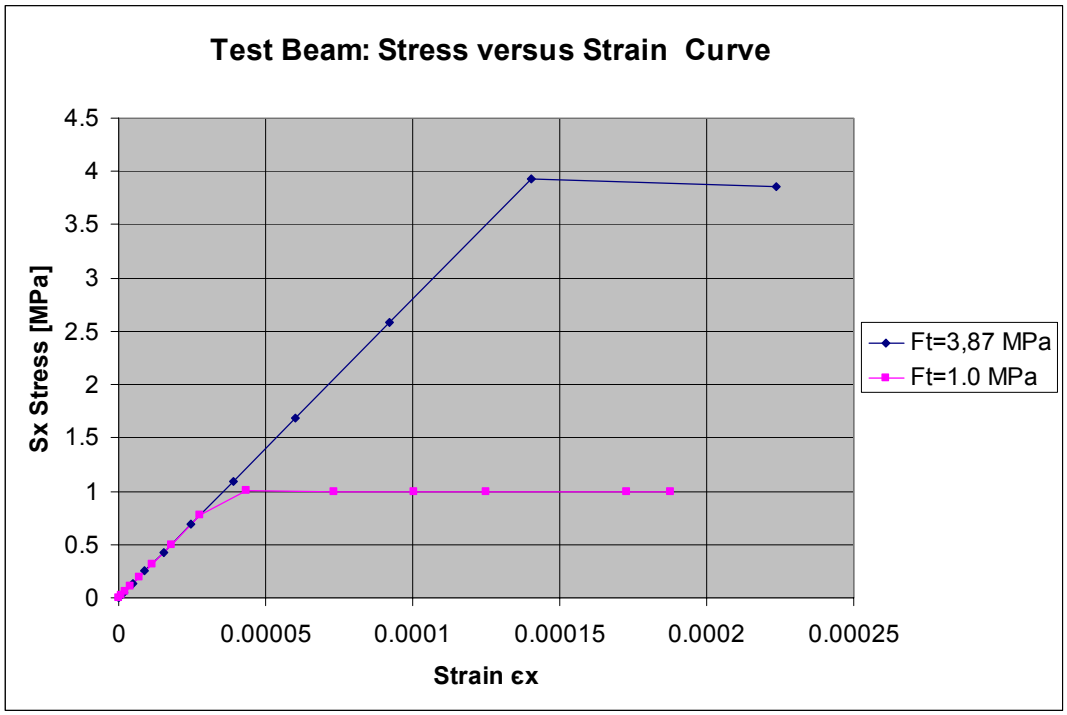

Figure 4-29: Graph of the S_x stress versus strain; yielding starts at 3.64 MPa and 1.0 MPa

The results of the Drucker Prager analysis tie up fairly well with the original yield stress values of 3.87 MPa used to calculate the input parameters of the program. The point where the stress is measured influences the maximum value. The point where the stress was measured was not exactly in the centre of the beam but at the point where the equivalent plastic strain was at its maximum value to capture the correct failure value.

A test run was also done with a lower strength concrete with properties f_t =1.0 MPa and f_c=15 MPa. This exercise was performed to illustrate the behaviour of a low strength concrete as used in mass concrete for dams. The weaker concrete also gave satisfactory results and illustrated the typical linear plastic pattern. See Figure 4-29.

4.7.3 Benchmark of Drucker Prager yield theory and flow rules

(Drucker Prager flow model from the handbook of Chen (1982))

The following benchmark was taken from handbook of Chen (1982, Section 6.7.3, p. 281) which illustrates the different types of Drucker Prager yield theory. This is an important exercise to help to understand the differences in the three flow models presented by Chen. The model was converted to the metric SI units see Table 4-1. Three different types of materials presented in Chen's handbook, i.e. Equation 3-34 to Equation 3-36, are used in the analysis with an associated flow rule.

Figure 4-30 and Figure 4-32 were created to illustrate the similarity of the FE models used by Chen and the author. Figure 4-31 was copied from Chen's handbook and graphically illustrates the three Drucker Prager flow models that will be benchmarked in this exercise.

Boundary conditions and load cases

The boundary conditions are similar to those of the Chen model in Figure 4-30, i.e. with hinges at the floor and rollers on the sides.

The pressure applied on the model was dependent on the flow model equations that were analysed. The pressures varied between 1.5 MPa and 2.75 MPa for the lower and upper cases. No gravity of density was used in the model.

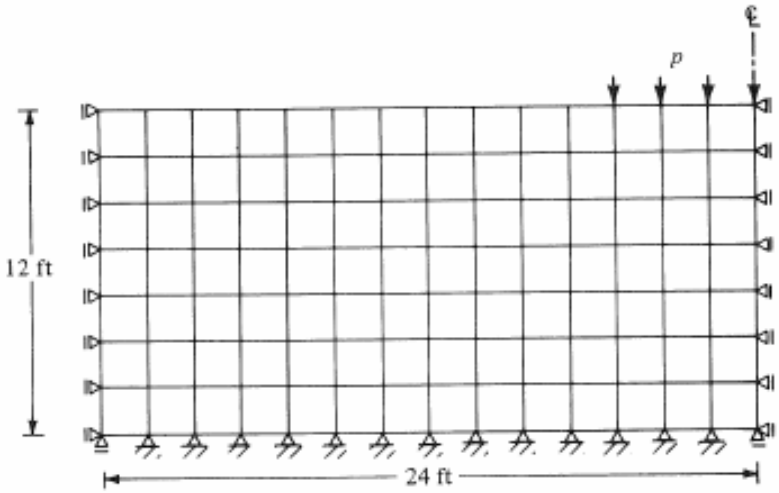

Figure 6.12 Plane-strain problem of a layer of material under a strip loading; $E = 30$ kips/in^2, $\nu = 0.3$, $\phi = 20^\circ$, $c = 10$ lb/in^2.

Figure 4-30: Plane strain problem from the handbook by Chen (1982, Figure 6.12, illustrating the FE model)

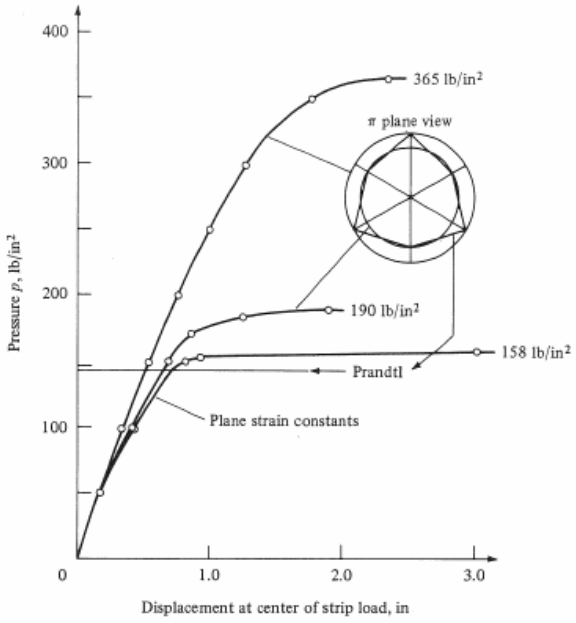

Figure 6.13 Load-displacement curve (plane-strain condition).

Figure 4-31: Graph illustrating the Drucker Prager flow rules in imperial units (from Chen, 1982)

The following equations from Chen (1982), i.e. Equation 3-34 to Equation 3-36, will be analysed and are given to differentiate the formulations: The equations are plotted in Figure 4-33 as Chen NL1, Chen NL2 and Chen NL3 respectively.

$$\alpha = \frac{2\sin\phi}{\sqrt{3}(3-\sin\phi)} \qquad k = \frac{6c\cos\phi}{\sqrt{3}(3-\sin\phi)}$$ **Equation 3-34**

$$\alpha = \frac{2\sin\phi}{\sqrt{3}(3+\sin\phi)} \qquad k = \frac{6c\cos\phi}{\sqrt{3}(3+\sin\phi)}$$ **Equation 3-35**

$$\alpha = \frac{\tan\phi}{\sqrt{9+12\tan^2\phi}} \quad k = \frac{3c}{\sqrt{9+\tan^2\phi}}$$ **Equation 3-36**

The values for the material constants as input to the FE program are given below. The values for k have been changed to $\bar{\sigma}$ by using the equation $k = \frac{\bar{\sigma}}{\sqrt{3}}$. The parameters have been converted to metric units.

$\alpha_1 = .01486$

for NL1

$\bar{\sigma}_1 = 0.1461$ (MPa)

$\alpha_2 = .011817$

for NL2

$\bar{\sigma}_2 = 0.11624$ (MPa)

$\alpha_3 = 0.011184$

for NL2

$\bar{\sigma}_3 = 0.11001$ (MPa)

The elastic material properties are from Chen and have been converted to metric units.

E = 206.7 MPa (30 Kips/in²)
υ = 0.3
c' = 6.89 MPa (10 lb/in²)
$\phi = 20^o$

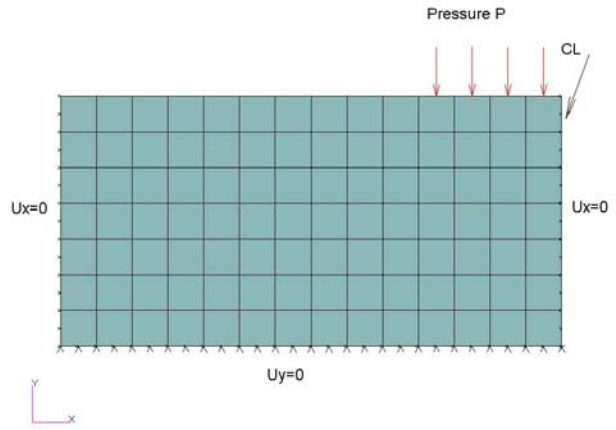

Figure 4-32: Author's finite element model for Chen's benchmark

Results

Figure 4-33 illustrates the combined results of the benchmark and the graph in Figure 4-31 taken from Chen (1982).

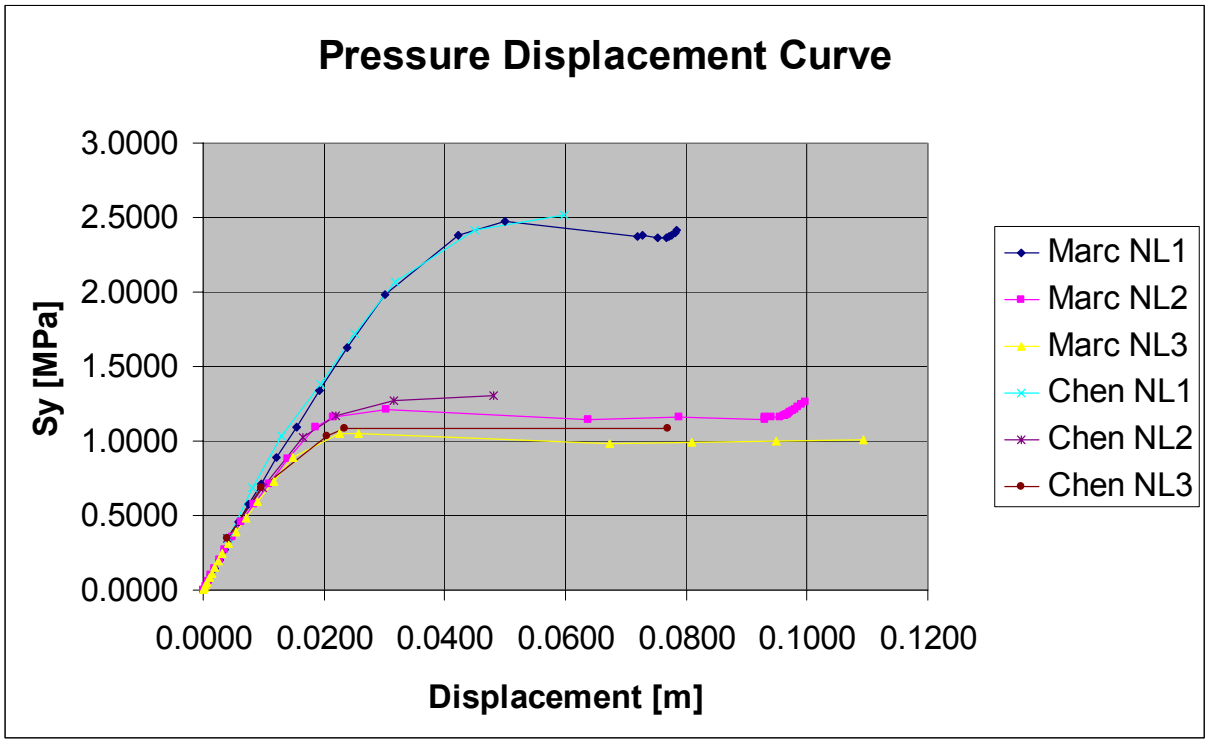

Figure 4-33: Graph of the three Drucker Prager flow models compared with Chen's curves

The legend symbols used are:
Marc NL1 represents the curve for the NL DP, flow model 1(Equation 3-34), by the author.
Chen NL1 represents the curve for the NL DP, flow model 1(Equation 3-34), by Chen.

Marc NL2 represents the curve for the NL DP, flow model 1(Equation 3-35), by the author.
Chen NL2 represents the curve for the NL DP, flow model 1(Equation 3-35), by Chen.
Marc NL3 represents the curve for the NL DP, flow model 1(Equation 3-36), by the author.
Chen NL3 represents the curve for the NL DP, flow model 1(Equation 3-36), by Chen.

Figure 4-34 was included to illustrate the vector diagrams and contour plots of the displacements which shows the flow pattern of the DP NL FEM.

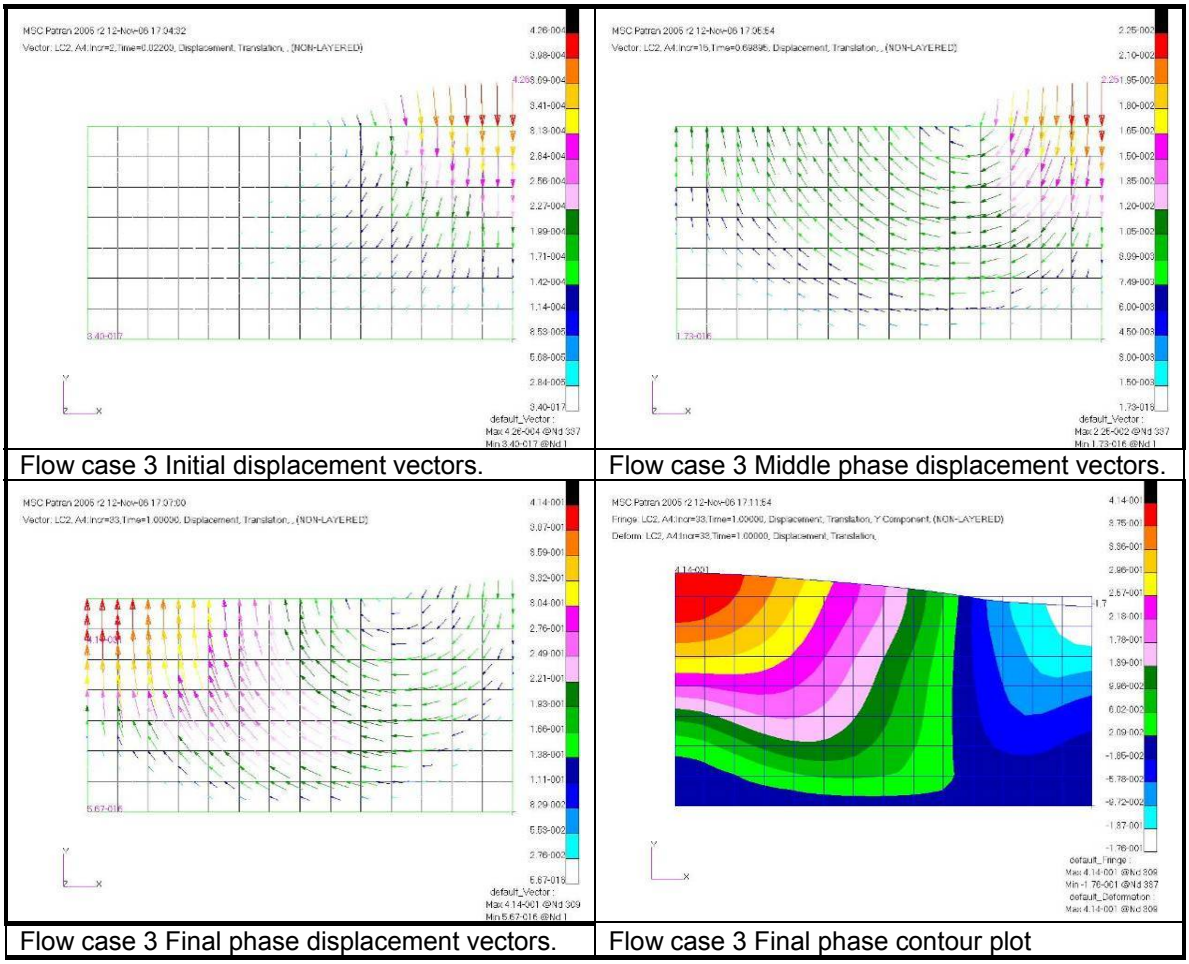

Flow case 3 Initial displacement vectors. | Flow case 3 Middle phase displacement vectors.

Flow case 3 Final phase displacement vectors. | Flow case 3 Final phase contour plot

Figure 4-34: Drucker Prager flow model: Benchmark for Chen (1982)

This is an important benchmark because it represents the three flow models of the DP NL FE flow model from Chen (1982). When the results are animated on the post-processor, a clear picture of the material movement and yielding through the time increments can be seen. An illustration of the beginning and end of the time increments is given to elucidate the yielding process – the first, middle and last flow increments are illustrated. It can be seen that all three Drucker Prager flow models have correlate very well.

The last Drucker Prager flow model (No. 3) simulates the low-strength mass concrete the best and will be more fully explored later in Chapter 5.

4.7.4 Benchmark of a shear beam

The aim of this benchmark is to model a beam with shear stress to get closer to the point where a gravity dam can be modelled. The same progression is followed as in Bhattacharjee and Léger (1994).

Although this dissertation only deals with the Drucker Prager non-linear material behaviour of concrete, useful information was gathered from Bhattacharjee and Léger (1994) for benchmarking the shear beam model. The un-reinforced single notched shear beam was originally experimentally investigated by Arrea and Ingraffea (1981).

The geometry of the model is illustrated in Figure 4-35 and the dimensions are given in mm. The force at point P is taken as 140 kN and is distributed over two elements. At point A a concentrated load of 0.13 P was applied. The first set of elements directly below point P was kept linear to reduce the crushing effect and consequent yielding of the material due to the pressure concentration.

The boundary conditions, as illustrated in Figure 4-36, were also distributed over the elements to prevent large stress concentrations caused by point supports that would cause singularity problems. As illustrated, boundary conditions of a hinge and roller were used.

The FE model was created as a plane stress model with a thickness of 156 mm and is illustrated in Figure 4-36. The mesh was modelled as a replica of the original mesh, as illustrated in Arrea and Ingraffea (1981).

The constitutive parameters were taken from Bhattacharjee and Léger (1994):

E_c = 24.8 GPa
υ = 0.18
σ_i = 2.8 MPa (assumed f_t)
f_c = 28 MPa (assumed to be 10* f_t)

Drucker Prager parameters:

α = 0.2466
$\overline{\sigma}$ = 3.986 MPa

Load conditions

The maximum load P applied at point B was 140 kN and was applied as a pressure over two elements. The pressure applied on each element was 32.693 MPa and this was increased from zero to the maximum value in 50 equal increments. For the extraction of data directly from the model, a *near point* was defined next to point P on the FEM. This point is illustrated in later figures.

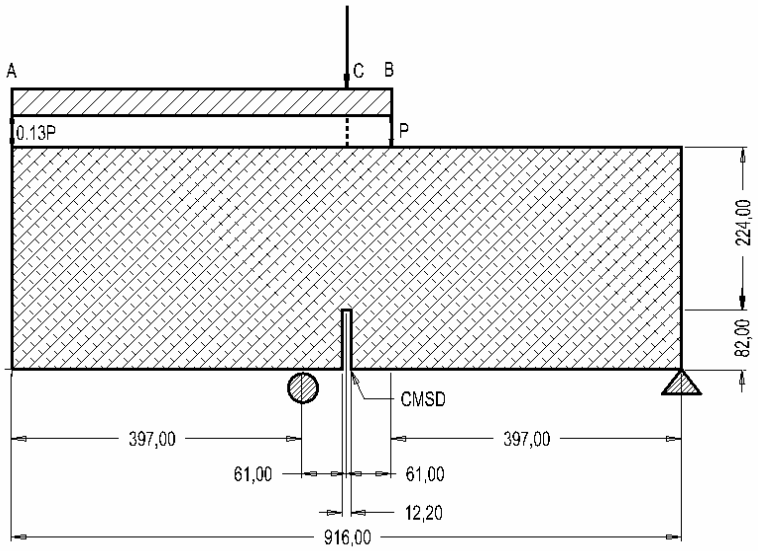

Figure 4-35: Geometry of the Arrea and Ingraffea (1981) model

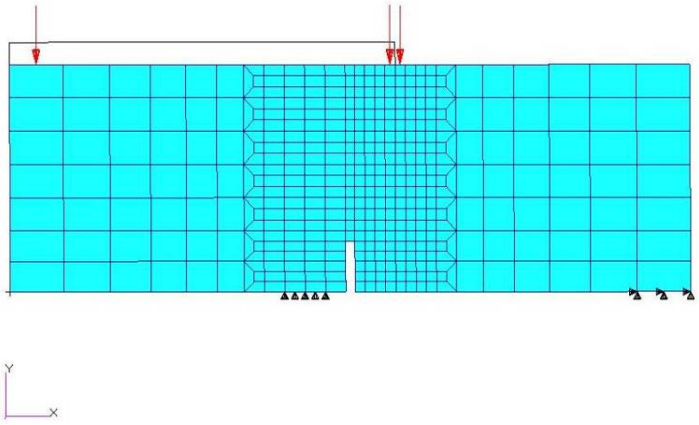

Figure 4-36: FE mesh with load and boundary conditions

Results of the FE analysis

Figure 4-37 summarises the results in graphical format. The three curves for the linear, Drucker Prager and Drucker Prager near point analyses were computed by the author and the 'fixed crack model with variable shear resistance factor' (FCN-VSRF) curve was computed by Bhattacharjee and Léger (1994).

The *near point* is a defined as a point next to the point P in Figure 4-35 to capture the correct yielding stress.

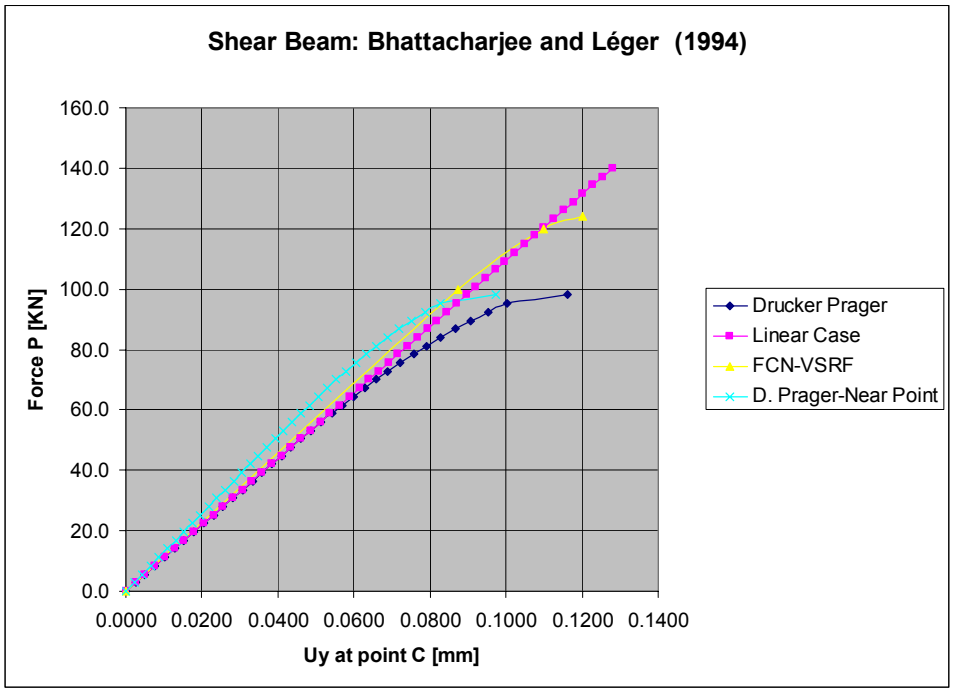

Figure 4-37: Shear beam response; displacement U_y is measured at point C on the rigid link

Figure 4-38 shows the maximum displacements of the shear beam at maximum load level and is presented in a deformed format to give a holistic picture of the performance of the structure.

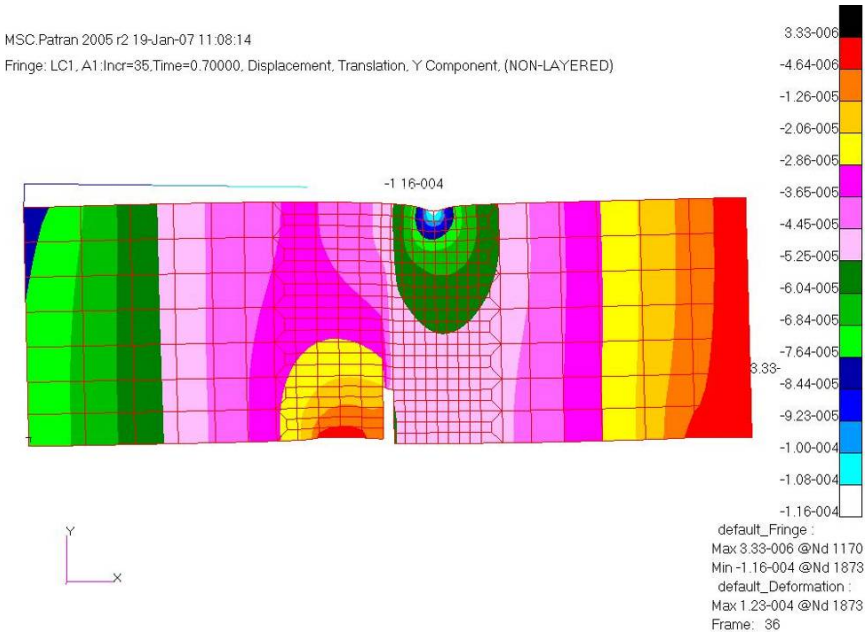

Figure 4-38: Maximum displacement U_y in metres and a deformed shape at maximum load level

Figure 4-39 shows the material yielding zones as presented by the equivalent plastic strain contour plot at maximum load level.

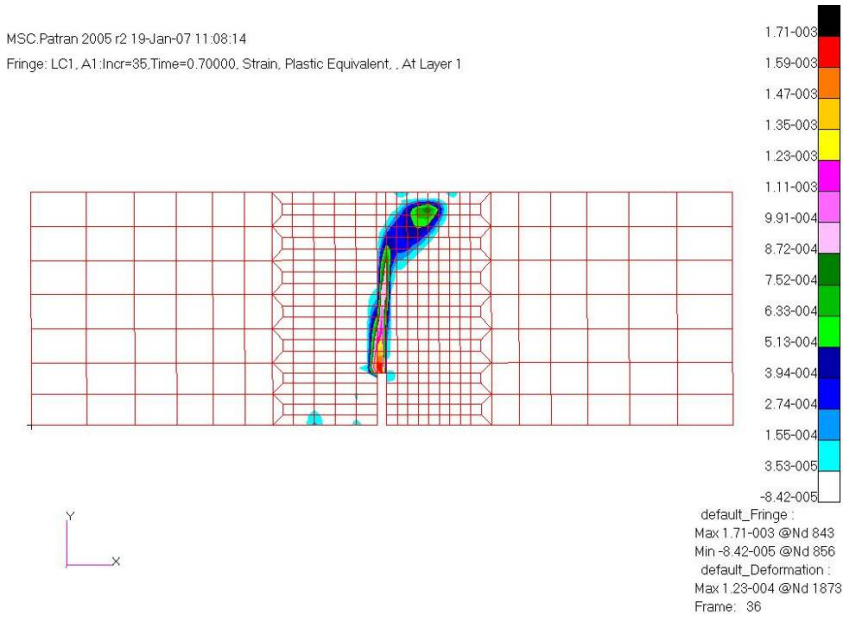

Figure 4-39: Equivalent plastic strain, illustrating the area in plastic deformation

Figure 4-40 from Bhattacharjee and Léger (1994) is included to allow the results of the Drucker Prager model to be compared with the crack profile predictions of some fracture mechanics models used by these researchers. In the Figure 4-40(a) represents the different fracture mechanics curves; (b) illustrates the experimental crack profile; and (c) and (d) show the crack profiles predicted by the CRCM and FCM-VSRF models. (See List of Abbreviations for the acronyms used in Figure 4-40.

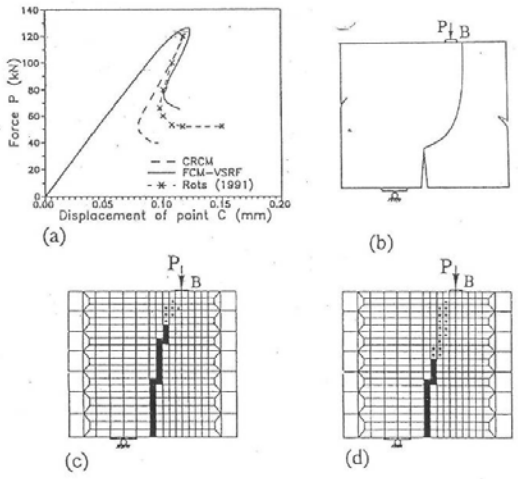

Figure 4-40: Shear beam response (from Bhattacharjee and Léger, 1994)

Discussion of results
The results given in Figure 4-37 illustrate that the shear beam yields at an earlier stage than the FCM-VSRF of Bhattacharjee and Léger (1994). The reason became clear when the results were animated. The Drucker Prager model first started yielding near the notch, but soon also started yielding near point P where there was a high pressure concentration.

The Drucker Prager model stopped to converge at a load of approximately 100 kN. Figure 4-39 illustrates the failure area at the point when the model became unstable, i.e. when the yielding area intersected the cross-section of the beam. From the results of the equivalent plastic strain plots, it is seen that the first yielding of the concrete material started in the notch at time interval 0.24, i.e. when the force reached a value of 33.6 kN. At this time interval the maximum principal stress S1 at the notch was 2.66 MPa and the maximum shear stress was 2.83 MPa.

The larger displacement of the Drucker Prager model as seen in Figure 4-37 can be ascribed to the following. During the load cycle, most of the yielding progressed from the notch area. However, during the latter load steps, yielding also occurred at the top and a larger displacement was measured at point C, on the rigid link. Figure 4-40 from Bhattacharjee and Léger (1994) indicates that no yielding took place in their analysis at their point B, which resulted in less displacement.

When the displacement was measured at a point directly on the shear beam one element to the left of point B, a new curve with different characteristics could be extracted (see curve named 'D. Prager – Near Point' in Figure 4-37.

It can be concluded that the fracture pattern was very similar to the fracture mechanics results, as can be seen from the structural response illustration (Figure 4-40) by Bhattacharjee and Léger. (1994).

The outcome of the Drucker Prager analysis indicated that the point of yielding is more conservative than in the fracture mechanics results (Bhattacharjee and Léger, 1994). Although there are small differences from the results of these researchers, the author is satisfied that the model still produced reliable results for predicting the point of yielding. This example gives an indication of the ultimate loading of a shear beam.

4.7.5 Benchmark of a 2.4-m-high model concrete dam

The following benchmark was taken from Carpinteri et al. (1992) who modelled a 1:40 scale gravity dam subjected to equivalent hydraulic loads. The same model of the gravity dam was also used in the paper by Bhattacharjee and Léger (1994) who modelled it in LEFM. The model of the dam had a pre-assigned notch on the upstream side at ¼ of the height of the wall.

The *material properties* were the same as those used by Bhattacharjee and Léger (1994):

Concrete properties used by the author:

E_c = 35.7 GPa
υ = 0.1
ρ_c = 2 400 kg/m³

The linear plastic Drucker Prager parameters were calculated from Equation 3-36 and Equation 3-37:

σ_i = 3.6 MPa (apparent tensile strength)
f_t = 3.6 MPa
f_c = 36 MPa (assumed to be 10 x f_t)

α = 0.2466
$\overline{\sigma}$ = 3.56 MPa

A plane stress FE model was created from 8-node, second-order isotropic quadrilateral elements and the mesh was shaped to be a replica of the original mesh to reproduce accurate results for comparison. The thickness of the model is 300 mm. All dimensions are in metres. Figure 4-41 gives the geometric details and the boundary conditions. The dimension of the notch is also accurately modelled to simulate the yielding point.

The FE model was created in the program's post-processor.

No foundation block was modelled because the model in the paper by Carpinteri et al. (1992) was without one. However, the first row of elements was modelled with linear elastic properties to soften the boundary condition effects at the heel in order to get the non-linear failure to start in the notch and not at the heel of the model.

Boundary conditions
The model was restricted in the *x*- and *y*- directions ($U_x = U_y = 0$) along the base of the gravity dam concrete model.

Load conditions
This model includes gravity loading and because it is a non-linear FE analysis, the load conditions were time-stepped and ramped from zero to the maximum values. The loading was stepped as shown in Table 4-6.

Table 4-6: Stepped load conditions

Time step	0	1	2	3
Self-weight	0	Ramp to full gravity	Full gravity	Full gravity
Pressure	0	0	Ramp to full pressure	Constant pressure

The load stepping was performed to induce the correct stress in the model in order to perform the Drucker Prager non-linear material analysis. The stresses at the different time steps will then produce the right yielding conditions. Premature failures with their experimental model led Bhattacharjee and Léger (1994) to conclude that the self-weight was modelled incorrectly. They continued with the experiment, but without gravity corrections. This FEM was modelled similarly in that no adjustment was made for the self-weight.

Load step 3 was included to stabilise the analysis for correct convergence and to be able to observe that the displacement and stress stay constant.

In this exercise, during the first time step the gravity loading was ramped from zero to 1.0 g (9.8 m/s²) and stayed constant for the second and the last time steps.

During the second time step, the pressure was ramped from zero to full supply level. The original experimental model of Carpinteri et al. (1992) was loaded with jacks at four different positions on the upstream face. To eliminate singularity problems, the author's model was loaded with a hydrostatic pressure on the upstream face. The fluid density was increased to provide an increased total horizontal load of 750 kN to correspond with that of the reference.

The third time step was introduced with a constant pressure to monitor the convergence in order to check whether the FEM completed correctly.

Discussion of results

The results of the model concrete gravity dam are first illustrated by a set of contour plots of the displacements and stresses for some load conditions. The combined results of all the load cases are given in graph format. The combined picture is given by including the curves from Carpinteri et al. (1992) in order to get a total impression of the study.

Figure 4-41 shows the identical FEM mesh as originally modelled by Carpinteri et al. (1992) and illustrates the dimensions, load and boundary conditions.

Figure 4-42 is a deformed shape of the displacement U_x at maximum loading F = 750 kN, which was distributed as for a hydrostatic pressure condition in the model.

The equivalent plastic strain as illustrated in Figure 4-43 gives an indication of where the material yielding can be expected. At 750 kN, all the yielding was still in the notch and no yielding occurred at the heel of the model. This indicated that the precautions taken to soften the base boundary conditions and the loads had been successful in restricting the yielding in the notch.

Figure 4-44 presents the maximum principal stress S1 and the non-linear stress distribution through the model.

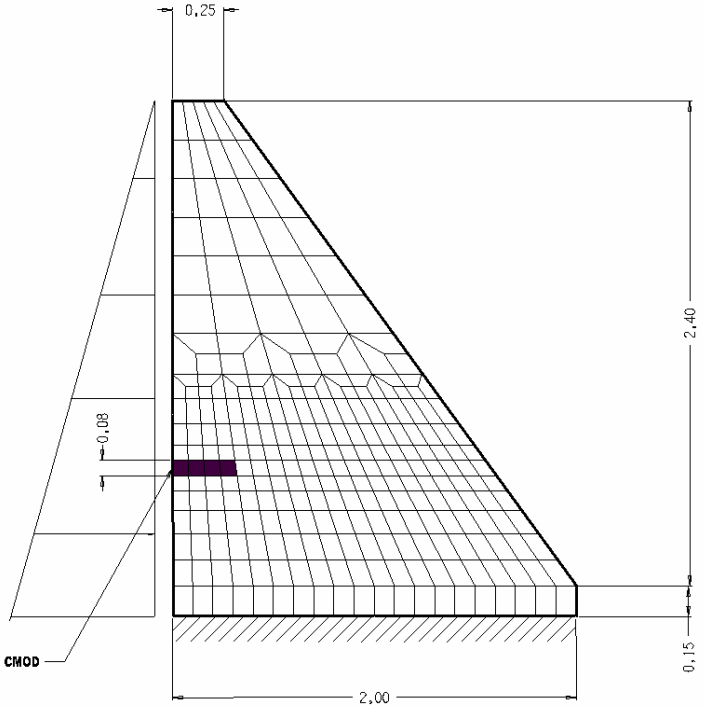

Figure 4-41: Geometry of the concrete model of a gravity dam (Bhattacharjee and Léger, 1994)

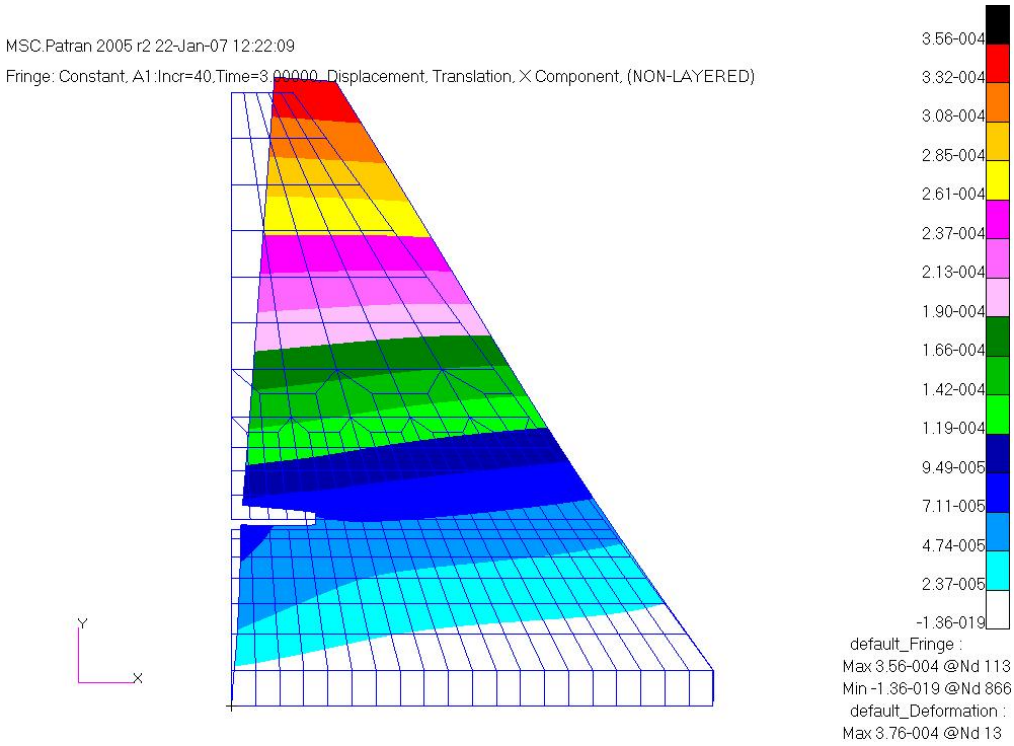

Figure 4-42: Maximum displacement U_x [m] at force = 750 kN

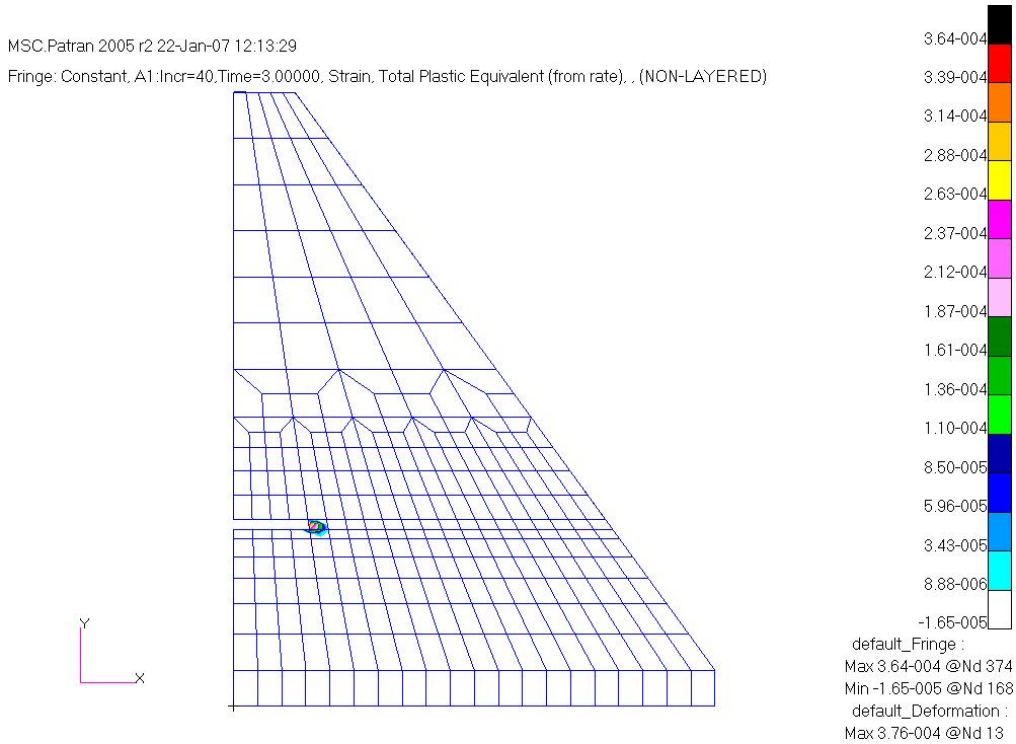

Figure 4-43: Equivalent plastic strain (m) at force = 750 kN

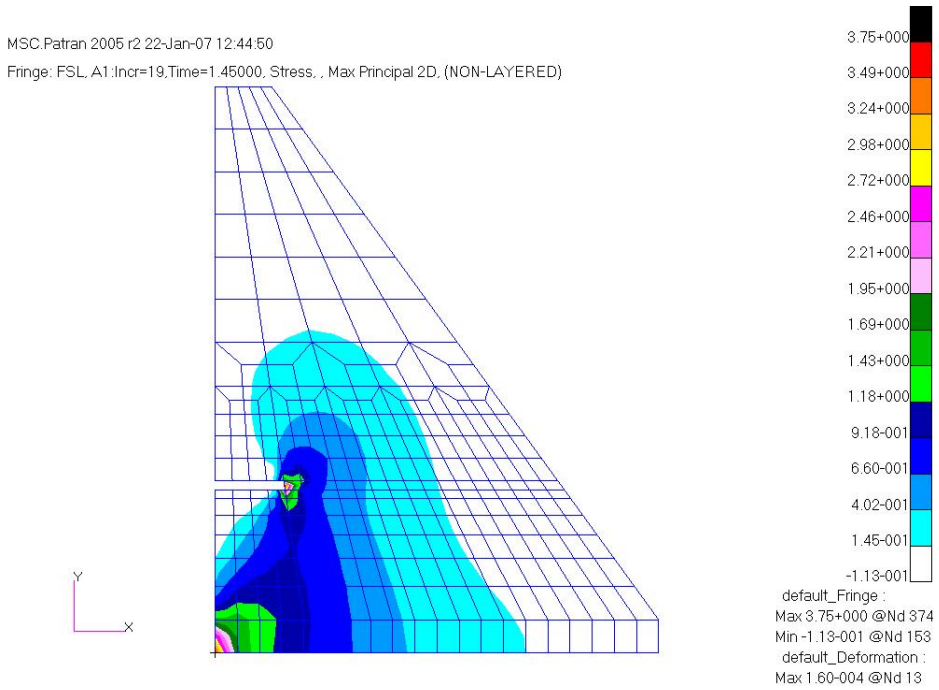

Figure 4-44: Maximum principal stress S1 at the point of first yielding of concrete, i.e. at force = 337 kN

In interpreting the results of Figure 4-44 care should be taken to remember that the first row of elements above the baseline was modelled with linear elements. Stresses in these elements will not yield and high stresses can be exhibited here. This model was created to examine the performance of the concrete material in the vicinity of the notch.

Figure 4-45 graphically illustrates the author's results in comparison with the results of the following:

- The experimental curve originally created by Carpinteri et al. (1992)
- The FCM-VSRF curve computed by Bhattacharjee and Léger (1993)
- The curve of Drucker Prager computed by the author.

The crack mouth displacement (CMOD) was derived by measuring the node displacements, in the post-processor program, at both sides of the notch. The displacements were imported into a spreadsheet to calculate the CMOD values for each load step. The difference in displacement from one time step to another will give the CMOD.

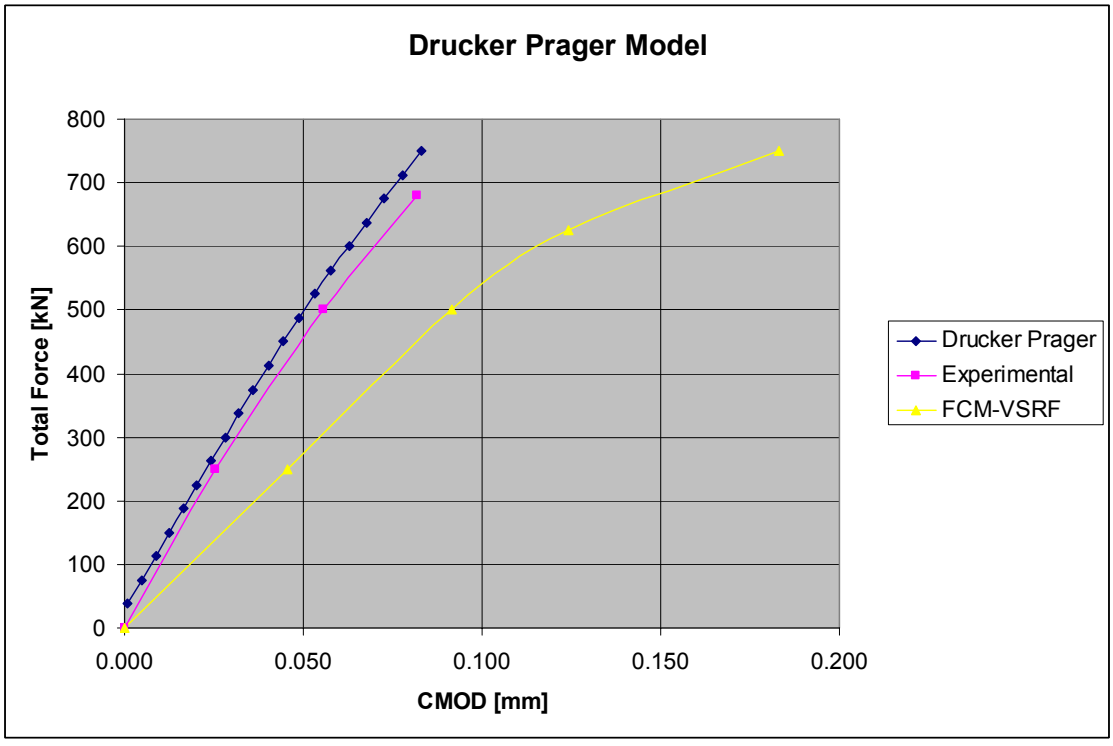

Figure 4-45: Response of the model gravity dam: (a) Drucker Prager; (b) Experimental, (c) FCM-VSRF

Discussion of results

Figure 4-42 shows the displacement of the model of the gravity dam. The maximum displacement on the crest is 0.356 mm and the deflection in the notch is clearly visible from

the deformation in the figure. The results are presented in the same formation as used by Bhattacharjee and Léger (1993), i.e. at the CMOD in the notch.

Figure 4-43 illustrates the equivalent plastic strain if a 750 kN force is applied to the model. This figure shows that the non-linear plastic deformation starts in the notch and at a force of 750 kN the analysis is still stable.

Figure 4-44 gives the maximum principal stress S1, which is approximately the yielding stress of 3.6 MPa. (The value of S1 = 3.6 lies between the time intervals of 1.4 and 1.45, i.e. a horizontal force of 337 kN.)

Figure 4-45 is a graph of the model's response and shows the curves representing the Drucker Prager, experimental and FCM models with a variable shear resistance factor (FCM-VSRF). It is worth noting that the Drucker Prager model gave the best fit with the experimental curve. However, the Drucker Prager curve continues whereas the experimental model would fracture at approximately 680 kN. The reason is that the linear plastic Drucker Prager model continues with a constant stress strain relationship.

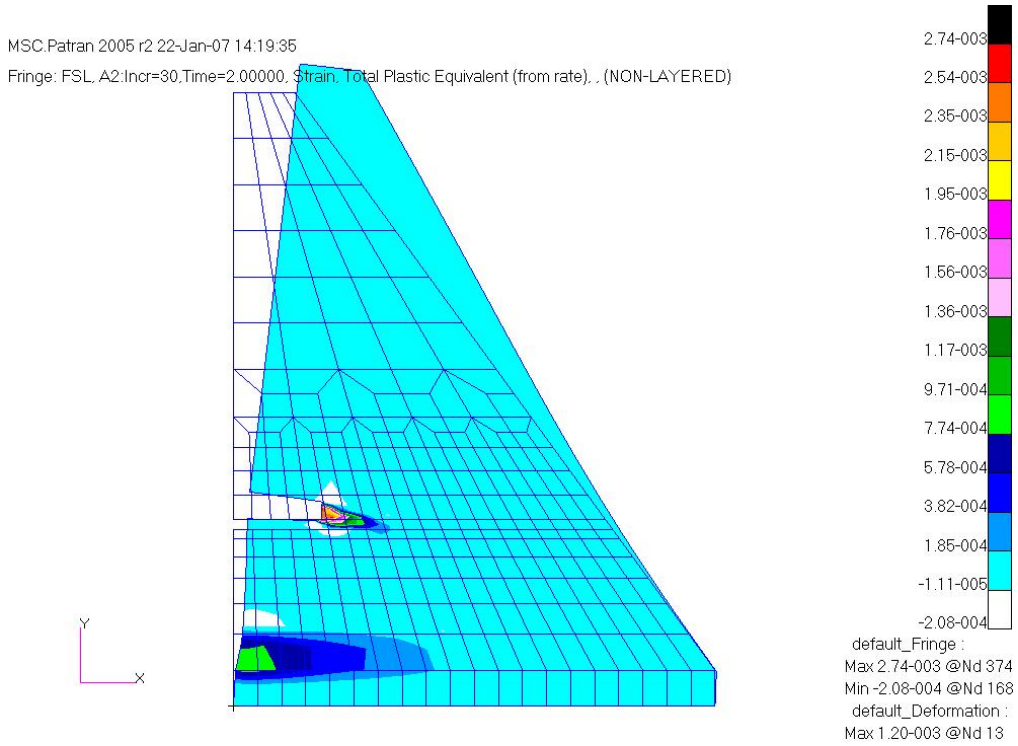

Figure 4-46: Equivalent plastic strain for the 1 500 kN load condition

The author experimented with the FE model by increasing the force up to 1 500 kN. The values of CMOD will continue because a linear elastic plastic Drucker Prager was used. Figure 4-46 illustrates the equivalent plastic strain for the 1 500 kN load condition and it can be seen that the line of yielding shows a similar pattern to the CRCM (coaxial rotating crack model) profile demonstrated by Bhattacharjee and Léger (1993).

The aim of the analysis was to benchmark the Drucker Prager yield model with a fracture mechanics model to determine the yielding point of the material. The Drucker Prager model simulated the experimental curve well, as seen in Figure 4-45. However, this model was able to handle a much higher horizontal force than the fracture mechanics and experimental models before it became unstable, as illustrated in Figure 4-46. Yielding also now occurred at the heel of the wall.

In conclusion, the Drucker Prager model provided satisfactory results for determining the failure point of the model dam as compared with the experimental model of Carpinteri et al. (1992).

4.7.6 Non-linear Drucker Prager analysis of a full-size concrete dam

Following Bhattacharjee and Léger's paper (1994), a non-linear analysis was performed on a full-size concrete gravity dam. The Koyna Dam has been analysed by several researchers and the geometry and concrete parameters are readily available.

The object of this benchmark was to study the probable failure of the concrete wall at the pre-assigned notch in the top section of the wall.

The paper by Gioia et al. (1994) was a very useful reference for obtaining benchmark solutions for the non-linear analysis. Gioia et al. (1994) use a perfectly plastic model with an associated flow rule and a yield surface as proposed for plain concrete by Ottosen (1977).

Material strength values of f_t = 0.1, 0.3 and 1.0 MPa were used in this benchmarking exercise.

The geometry was modelled from the data given in the original paper by Chopra and Chakrabarti (1972), except for the upstream face slope which was assumed to be a straight vertical line as used by Gioia et al. (1994).

FE model
Various material properties were assumed in the analysis to provide a comparative evaluation between the results of the Drucker Prager analysis and those obtained by Gioia et al. (1994).

The foundation block and dam were modelled monolithically. The mesh was refined in the area of the notch to capture the correct stresses for a non-linear yield model.

The wall was modelled as a plane strain FE model and second-order isotropic quadrilateral elements were used.

Material properties

E_c = 25.0 GPa
υ_c = 0.2
ρ_c = 2 450 kg/m³

Boundary conditions
The FE model was altered slightly from that of Bhattacharjee and Léger (1994) in that a foundation block was also modelled. The reason for this was to soften the boundary condition at the base of the wall in order to get the non-linear failure to start in the notch and not at the heel of the wall. The foundation block was restricted in the *x*- and *y*-directions ($U_x = U_y = 0$) along the bottom circumference (see Figure 4-47).

Parameters for the linear plastic Drucker Prager analysis
The three values of material strength were taken from Bhattacharjee and Léger (1994) and the Drucker Prager parameters were calculated using Equation 3-36 and Equation 3-37.

f_{t1} = 0.1 MPa and f_{c1} = 20 MPa
$\alpha = 0.2865$
$\sigma = 0.1496$

f_{t2} = 0.3 MPa and f_{c2}= 20 MPa
$\alpha = 0.2822$
$\sigma = 0.4466$

f_{t3} = 1.0 MPa and f_{c3} = 20 MPa
$\alpha = 0.2673$
$\sigma = 1.4621$

The symbols are same as previously and the subscripts 1, 2 and 3 refer to the material type.

Load conditions
The loads acting on the dam were applied in load steps and ramped from zero to the maximum value for each load condition to obtain the correct convergence for each load step in the analysis.

Eight load steps were used to provide for the different water levels. The first level was at full supply level and thereafter the overflow was stepped up in three increments of 5 m. The values in Table 4-7 are the inputs used in the FE program to produce the different overflow depths.

Table 4-7: Stepped load conditions

Time step	0	1	2	3	4	5	6	7
Self-weight	0	0 to 1.0	1.0	1.0	1.0	1.0	1.0	1.0
Pressure level = 0	0	0	0-0.78	0.78-0.88	0.88-1.03	1.03-1.08	1.08-1.13	1.13-1.15
Pressure level = 78	0	0	0	0-0.1	0.1-0.25	0.25-0.3	0.3-0.35	0.35-0.4
Pressure level = 103	0	0	0	0	0	0-0.05	0.05-0.1	0.1-0.15

Note: The pressure values in the table are the pressures at the specified water levels in MPa.
Self-weight = 1.0 up to full weight.

Figure 4-47 and Figure 4-48 illustrate the geometry, boundary conditions and the FE model used for the Drucker Prager analysis. The higher mesh density was chosen to be similar to that used by Bhattacharjee and Léger (1994), although Gioia et al. (1994) used a coarser mesh.

No uplift pressure and temperature load conditions were considered in this analysis.

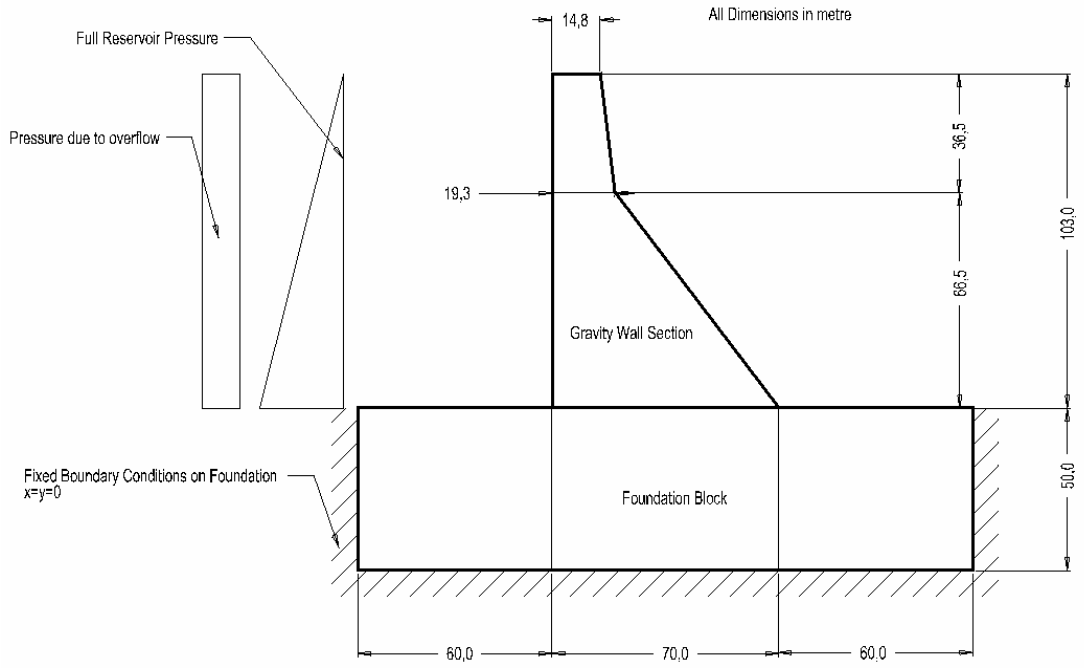

Figure 4-47: Geometry, dimensions and load conditions of the Koyna Dam (from 'Bhattacharjee and Léger, 1994)

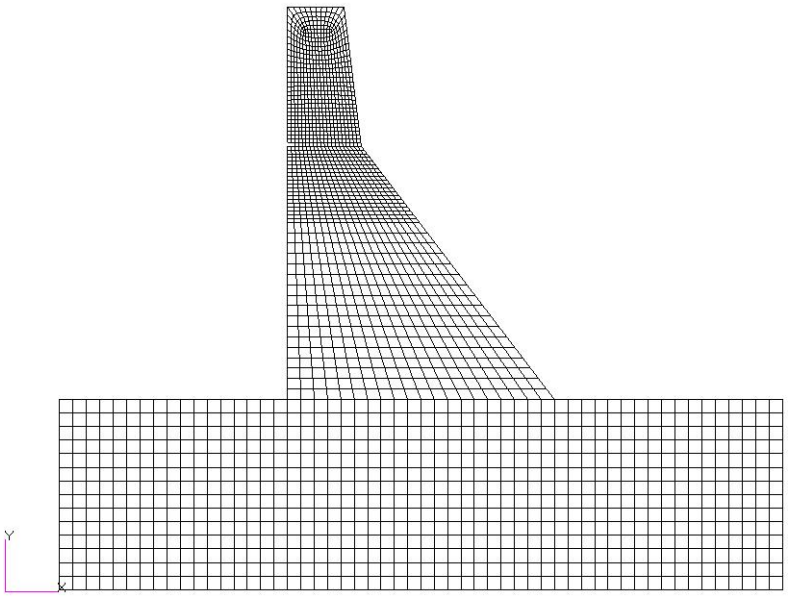

Figure 4-48: FE mesh for Koyna Dam illustrating the position of the notch

4.7.6.1 Discussion of results

Due to the many load cases analysed it is not practical to create contour plots of each case and only the analysis with the material strength of $f_t = 0.1$ MPa will be illustrated, although all the load cases were analysed. A summary of the results of all the load cases is given in graphical format see Figure 4-49 to Figure 4-53.

The first set of contour plots in Figure 4-49 illustrate the deformations through the different load steps, i.e. self-weight, full supply hydrostatic pressure and high flood condition, and the last plot shows the stage at which the analysis became unstable and stopped.

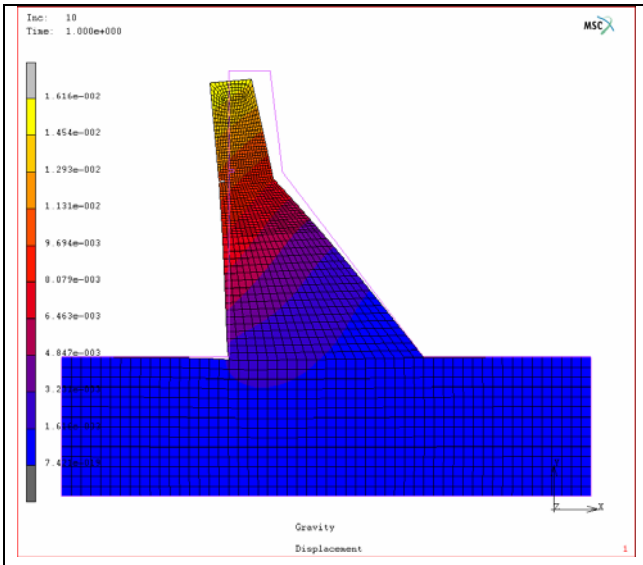

Time Step 0-2: Ramp gravity 0 to full

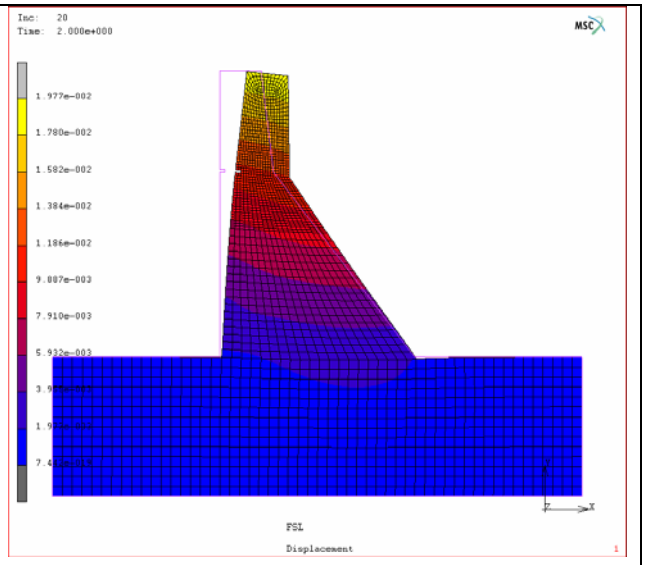

Time Step 2-4: Ramp pressure from 0 to full supply level

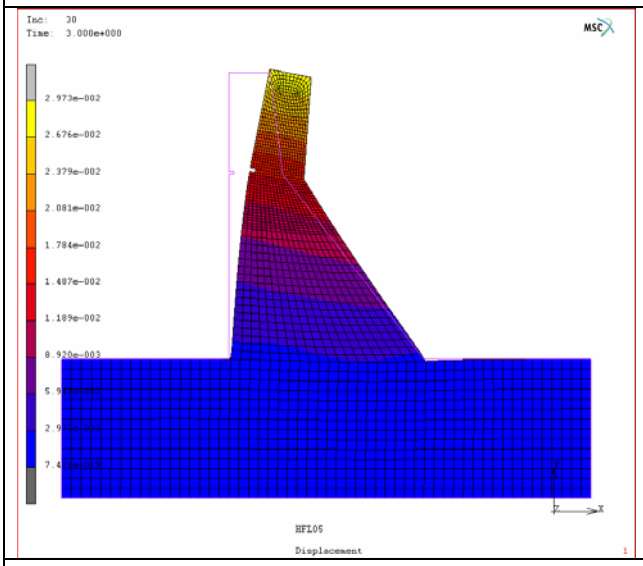

Steps 5 to 7: Ramp overflow to 5 and 10 m

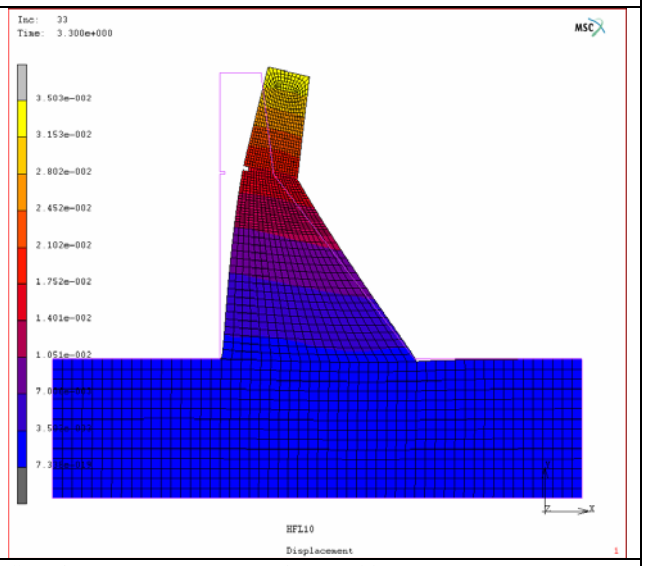

Step 8: Ramp to max. overflow to 11.5 m, collapse

Figure 4-49: Time steps for different load conditions from Table 4-7: Resultant displacement (Ur) and deformed shapes (Mentat post-processing program)

Figure 4-50 is prepared to show the failure areas in the wall at the point where the analysis became unstable.

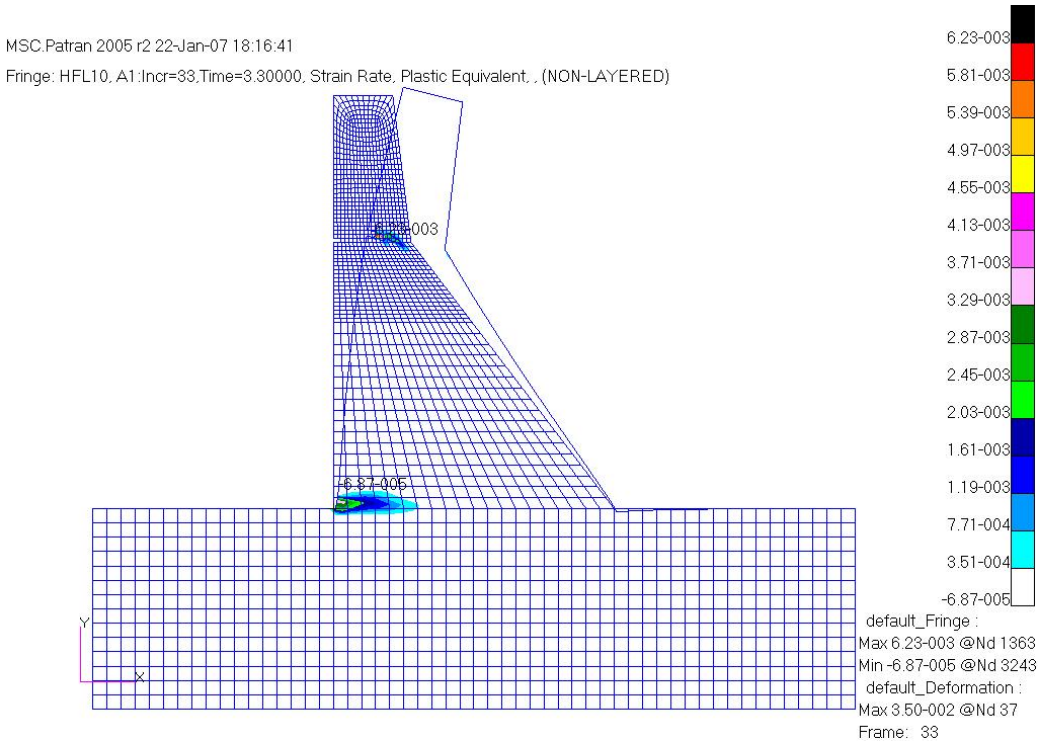

Figure 4-50: Equivalent plastic strain at 11.5 m overspill: 'collapse point'

The equivalent plastic strain in Figure 4-50 illustrates that the Drucker Prager model can generate yielding simultaneously at different positions. In this case yielding occurs at the crest notch and heel, although the yielding started at the notch. In practical terms, this would mean that the dam would probably fail first at the crest level.

4.7.7 Graphical results of the three material strengths according to Gioia et al. (1992)

The results of the analysis are presented and compared with the results of Gioia et al. (1994).

This benchmark exercise was useful because Gioia et al. (1994) also used the non-linear plastic yield FE model. The results are thus more comparable than with the fracture mechanics results. The curves representing the Drucker Prager model are titled *Marc FEM* in the figures and were compiled by the author.

Figure 4-51 to Figure 4-53 present the overspill versus the crest displacement of the Koyna Dam for the material strength $f_t = 0.1$, $f_t = 0.3$ and $f_t = 1.0$. The curves for the author's Drucker Prager model and that of Gioia et al. (1994) are shown in the same graphs.

The curves representing crest displacement were computed for overspill up to 15 m. Only the analysis of the material strength of 1.0 MPa was stable up to the maximum overspill.

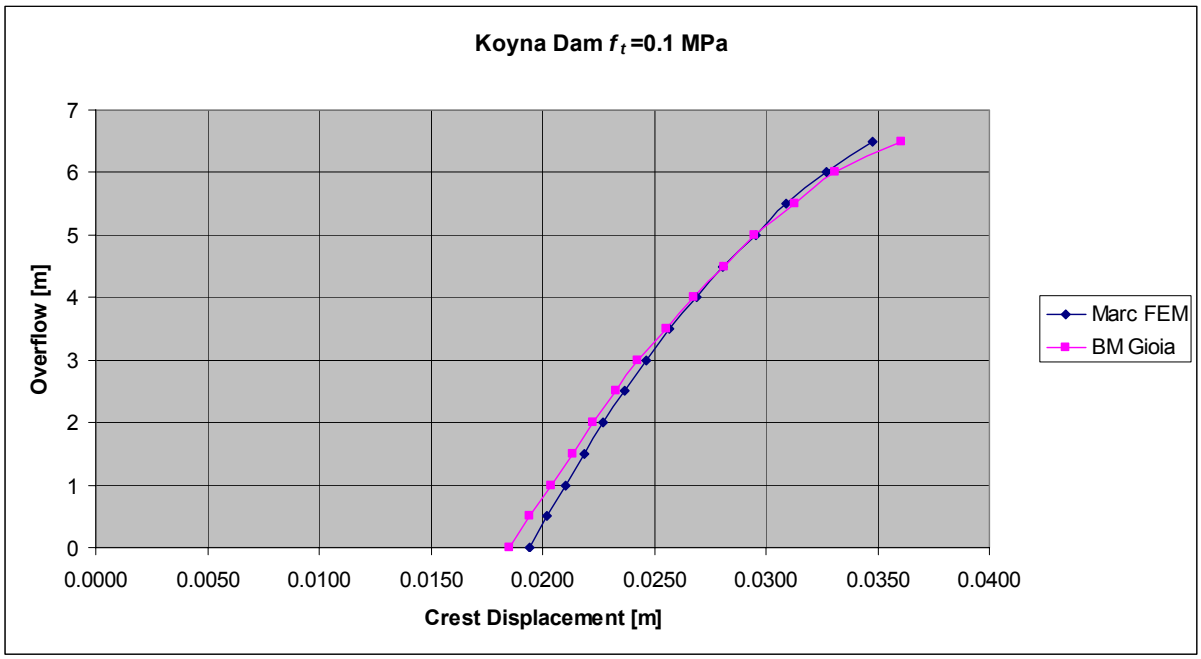

Figure 4-51: Benchmark comparison (Gioia et al., 1994) and Drucker Prager for f_t =0.1 MPa

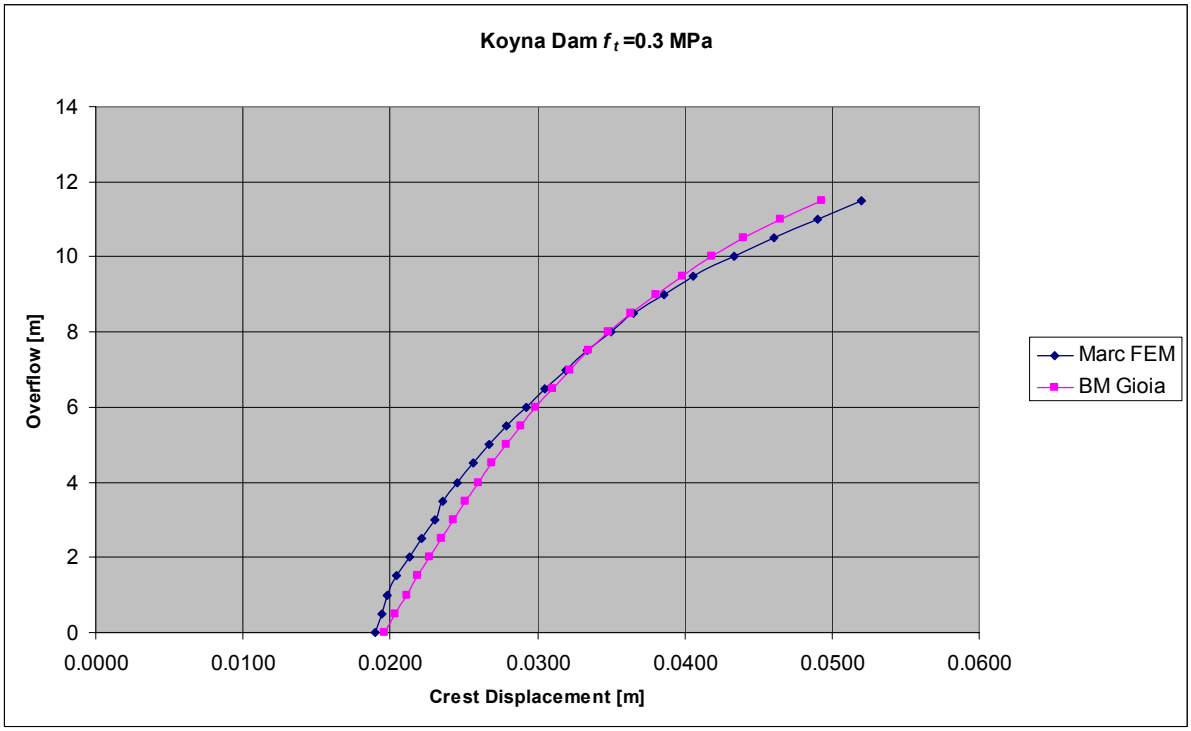

Figure 4-52: Benchmark comparison (Gioia et al., 1994) and Drucker Prager for f_t = 0.3 MPa

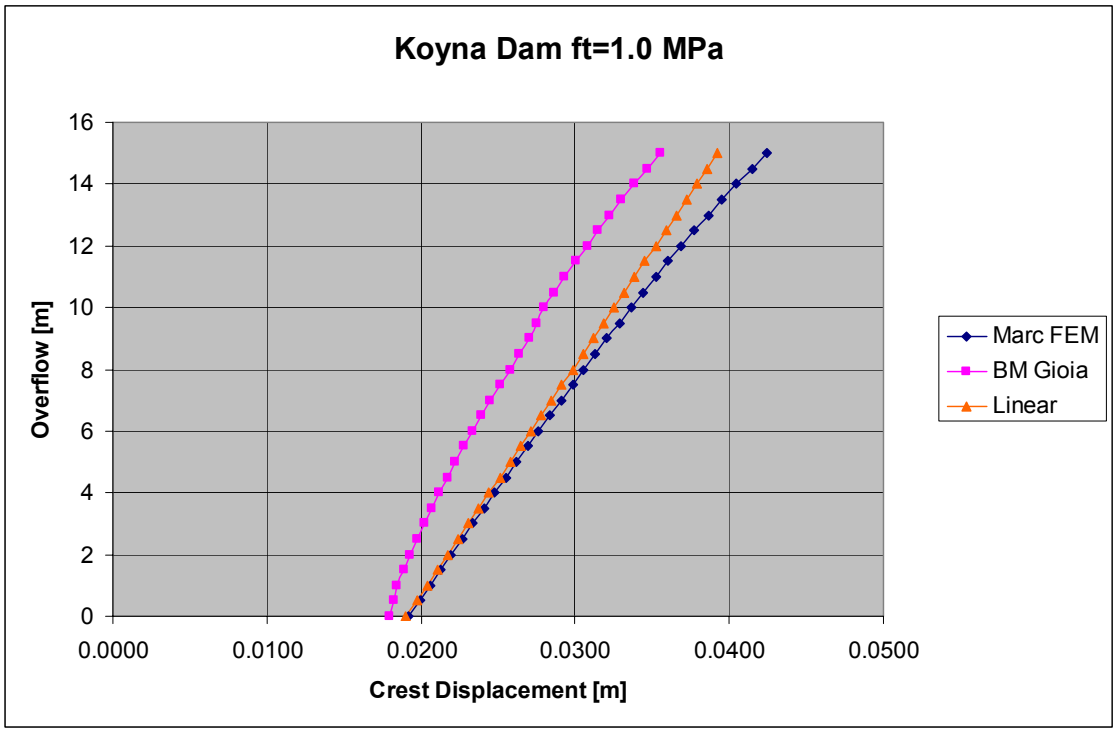

Figure 4-53: Benchmark comparison (Gioia et al., 1994) and Drucker Prager for f_t = 1.0 MPa

4.7.7.1 Discussion of results

Figure 4-49 illustrates the deformation and resultant displacement of the Koyna Dam during the different time steps. The time steps are necessary for the non-linear material to yield correctly. If the time steps are not introduced, the program will ramp all the load cases from zero to maximum, including the gravity. This is not a problem with a purely linear static analysis, but for a non-linear material analysis this would give incorrect results and the dominant load conditions would influence the results.

The region of plastic failure is shown in Figure 4-50 and in this case represents the last load increment before the analysis becomes unstable. Figure 4-51 to Figure 4-53 illustrate the Drucker Prager analysis results for the three material strengths and the results compared excellently with the results of Gioia et al. (1992), although different non-linear FEM yield models were used. The last material strength of 1.0 MPa showed some variations from Gioia et al.'s (1992) results, but the author is of the opinion that Drucker Prager results should tend more to the linear distribution, for a stronger material, because less yielding is expected. The curve for a linear elastic analysis was included in Figure 4-53 to examine the previous statement. It can be seen that the MSC Marc FEM curve is closer to the linear curve and the author is satisfied that this analysis gave acceptable results.

It can be concluded that the linear plastic Drucker Prager yield model is able to forecast accurately the yielding point of concrete with a wide variation of yielding strength. Especially the last model of Koyna Dam gave realistic results for an actual full-size gravity dam. The scale factor is still a matter of concern because the 2.4 m model of the gravity dam demonstrated that the Drucker Prager model could handle forces beyond the point where the experimental model failed.

At this stage of the study it is prudent to examine the actual concrete strengths of South Africa dams.

4.8 Concrete Strengths of DWAF Dams

The concrete strengths of some dams constructed by the DWAF were investigated. There are complete material strength laboratory reports for many of these dams. However, to explore all the detail in these reports is beyond the scope of this dissertation and it was decided to summarise the material strengths of the dams in table format. The material property values in Table 4-8 are the average values for the individual dams. The tensile yield stress, modulus of elasticity and Poisson's ratio values are from the standard split-cylinder strength test, ASTM C496 (2004). The compressive strength and density were tested by the standard SABS SM 865 (1994) method. The concrete of the dams was tested more than a year after construction, usually for the five-year dam safety inspection and evaluation. It should be noted that the average strength and material properties are for different types of concrete and construction methods as given in the second column. The aim of the table is to give an indication of the average material properties.

Table 4-8: Concrete properties of DWAF dams

Name of dam	**Concrete type**	f_c **[MPa]**	f_t **[MPa]**	E **[GPa]**	**υ**	**ρ [kg/m³]**	**Permeability [m/s]**
Boegoeberg	Mass	27.6	4.19	18.56	0.32	2476	1.82×10^{-11}
Clanwilliam	Mass	33.1	2.81	21.9	0.26	2326	2.8×10^{-10}
De Mistkraal	RCC	17.8	4.37	32.46	0.22	2691	5.9×10^{-10}
Kamanassie	Mass	22.0	2.85	20.3	0.18	2351	7.65×10^{-10}
Neusberg	RCC	29.4	3.4	36.2	0.15	2444	9.42×10^{-11}
Pietersfontein	Mass	41.1	3.41	13.4	NA	NA	NA
Pongolapoort	Mass	25.9	4.8	35.1	0.23	2555	8.6×10^{-12}
Poortjieskloof	Mass	41.2	3.32	20.2	NA	2360	NA
Roode Elsberg	Mass	66.9	4.2	30.3	0.2	2464	8.4×10^{-11}
Stompdrift	Mass	37.7	5.35	34.09	0.19	2472	2.48×10^{-11}
Van Ryneveld's Pass	Mass	30.19	3.065	28.38	0.20	2455	4.7×10^{-10}
Wolwedans	RCC	27.0	3.53	29.4	NA	2448	4.0×10^{-10}
Average **Std Deviation**		33.32 12.76	3.77 0.80	26.69 7.51	0.22 0.05	2458 102	2.73×10^{-10}

Not many of the DWAF's dams have been fully tested for material properties, but the 12 dams listed in Table 4-8 give an indication of the range that can be expected. The standard deviation is relatively high because different types of dams, with a large age difference and with their unique types of concrete are all included in the table. The author found that, on average, the material properties, as found in the literature from round the world, do correlate with the values in the table. The ratio of f_t / f_c for mass concrete is 11.3%, which also correlates well with the traditional value of 10% used in the DWAF. The average compression and tensile strength are higher than those normally used for design in the DWAF, but the reason for this is that during the design stage a conservative approach is followed. See Section 5.3.3 for the properties of the material used at the DWAF's De Hoop Dam.

In choosing material properties it should be borne in mind that during construction a very wide variation in mass concrete can eventually occur due to the numerous external factors influencing concrete quality, such as temperature, batching control, type of aggregate and consistency thereof, water cement ratio, etc. For this variation in material properties a safety factor is built in.

4.9 Discussion

In the this chapter an attempt was made to calibrate the Drucker Prager yield model by benchmarking the method with a variety of published benchmark examples found in the literature study. In some cases the results were taken from fracture mechanics papers and the results had to be compared on general structural behaviour. But overall, good correlation was found for a yield model that was originally developed in the 1950s. Although the non-linear material yield model has some shortcomings which can nowadays be overcome by the more modern fracture mechanics FE models, the Drucker Prager model has the advantage that it was developed from a relatively unsophisticated theory, has been studied by many researchers and is well documented. It has been shown in this chapter that the parameters are quite simply derived from the tensile and compression yield strength of the material, which can be determined by standard laboratory tests.

The advantage of this model is that it can be easily converted into the parabolic Drucker Prager model, which is a very useful model for soil type of material. With a small adjustment it can be converted into a concrete model as presented by Buyukozturk (1977) (see Chapter 7 of the MSC Marc User's Guide). The Drucker Prager model is also well developed in 3-D and can thus be used to analyse 3-D models for various types of dam structures that cannot be simply analysed in 2-D. This research can therefore also be used later for more complex 3-D analyses, such as those of arch dams.

The next phase of the study is examine some gravity dams with the Drucker Prager model and draw some conclusions about the object of this dissertation, i.e. to determine whether this method can be utilised to analyse a gravity dam without the help of the classical method.

5 SELECTED CASE STUDIES

Up to this point the basic tools and theories needed to perform a finite element analysis of a concrete gravity dam have been examined and discussed. As previously mentioned, the design and optimisation of gravity dams are done using the so-called classical method, which is based on the Bernoulli-Euler theory of elastic shallow beams. The shortcomings and advantages of this method were discussed in Section 3.1 and the results obtained by the two methods were compared.

The aim of this chapter is to perform analyses on different gravity dams using the non-linear Drucker Prager FEM and to examine the results under certain static load conditions.

An important question that that needs to be investigated is whether a gravity dam can be optimised and designed merely by using the FEM? If the uncertainties of the finite element singularities and the evaluation method could be resolved, then FEM could be used with more confidence to design gravity dams.

However, there are still many uncertainties regarding the reliability of roller-compacted mass concrete exposed to water and long-term hydraulic loading. Researchers at universities are studying the material properties of poro-elastic and poro-plastic concrete. The calculation of the internal pressure of porous material is an important field of study for dam engineers. The permeability of concrete is in the order of 3×10^{-10} m/s (see Table 4-8) and it can take several decades for water to saturate a concrete dam wall. It is thus very important to have accurate information about the long-term concrete strength. By means of the non-linear FE method more accurate long-term predictions can be made to determine what the structural safety of a dam is.

It is important to incorporate correctly the pore pressures in a gravity dam analysis. Watermeyer (2006) recently published a paper on the subject of uplift under gravity dams. With the non-linear FEM the continuous process of loading is important to determine the correct yielding of the material throughout the whole analysis. This chapter will demonstrate this process. However, it is difficult to add the pore pressure to the reactive pressure in the FE model because this will cause an incorrect stress condition and thus influence the yield process. In the non-linear FEM, the loads are therefore stepped in the correct load order throughout the analysis in order to simulate the correct stresses for each time step.

The units used in this chapter are given in the Table 5-1:

Table 5-1: Units used for the analysis

System of units	INPUT					OUTPUT		
	Length	**Force**	**Elastic Modulus**	**Mass**	**Mass density**	**Displace-ment**	**Force**	**Stress**
SI	m	MN	MPa	$kg.10^{-6}$	$kg.\ 10^{-6}/m^3$	m	MN	MPa

Note: The following stress convention is used:
Tensile stress is (+) and compressive stress is (-).

5.1 Case History: Hypothetical Triangular Shaped Gravity Dam

For the first case study the FEA results for a triangular gravity dam with a mesh density of 80 elements are compared with the results of the classical method. It must be restated that the theory of the finite element method and that of the classical method do not necessarily correlate with each other.

This model was chosen because it was extensively used by Chemaly (1995) for his research on fracture mechanics. In Chapter 8 of his dissertation, a calculation is done to determine the crack length of a triangular dam 100 m high. Chemaly used the theory of Gálvez et al. (1994) to calculate the crack length of this triangular dam. The aim of this paragraph is to investigate the relationship between the yield length calculated by the Drucker Prager nonlinear finite element method and the crack length calculated by the two methods used by Chemaly (1995) in his dissertation i.e. crack length calculated by the classical method and the fracture mechanics method presented by Gálvez et al. (1994).

An FE model was prepared with a relatively fine mesh in order to include a set of elements representing a joint along the base of the wall. The material of the joint was of lower strength than that of the dam and foundation to create a virtual crack path at the same position used in the fracture mechanics crack path study. The material of the joint was also varied to allow a sensitivity study to be done on what material strength would correspond to Chemaly's fracture mechanics calculations. This type of analysis could also be done with non-linear contact elements, but the aim was to examine how the DP NL FE model would perform within such an unusual condition where the non-linear elements are slotted in between the wall and the foundation.

The geometry of the triangular dam is illustrated in Figure 5-1.

5.1.1 Classical method

The classical method was included in this case study to obtain a general impression of the safety of this structure. The standards of the classical method are well known and this will help to validate the results of the FE model.

The input parameters are similar to those used by Chemaly (1995) for the classical method and are as follows:

For the mass concrete:

Density of the mass concrete is (ρ)	2 400 kg/m³

For the base joint material:

Friction angle of contact (φ)	43º
Cohesion (*c*)	1.2 MPa

Load conditions for the classical method

The load conditions are restricted to three cases:

1) Service load with water level at 100 m
2) Abnormal load with water level at 106.65 m (from a trial-and-error calculation to obtain a 32.5 m crack at the base, using the CADAM software of Leclerc and Léger, 2004)

Uplift conditions were included in all the load cases.

5.1.2 Finite element model

The FE mesh of the wall and the foundation was modelled monolithically with second-order isotropic quadrilateral elements. A plane strain model was used with 2 579 elements (see Figure 5-2). The model was created with a high-density mesh to illustrate the high stress concentrations and to observe to what extent the Drucker Prager model will redistribute this stress.

5.1.2.1 Assumptions

No tail-water pressure due to flood conditions was used on the downstream side of the wall so as to correspond to the model used by Chemaly (1995).

A 10 m horizontal virtual crack starting at the heel was assumed for calculating the uplift pressure and this stayed constant during the analysis. The size of the elements of the joint is approximately 1 m^2 at the heel of the wall.

No pressure-relief facilities were included, i.e. full uplift was assumed.

No temperature and seismic loadings were included.

The load condition can thus be seen as a severe hydrostatic load condition.

The loads were ramped up through the time steps and the stresses were then summed to present the final stress at the end of the analysis. See Table 5-3 for the time steps.

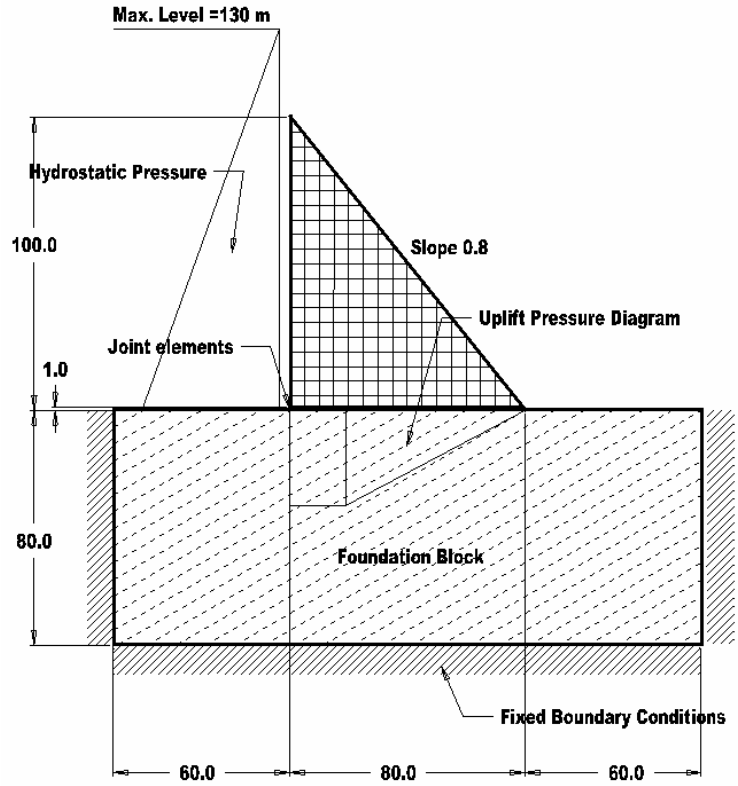

Figure 5-1: Geometry of triangular dam (from Chemaly, 1995)

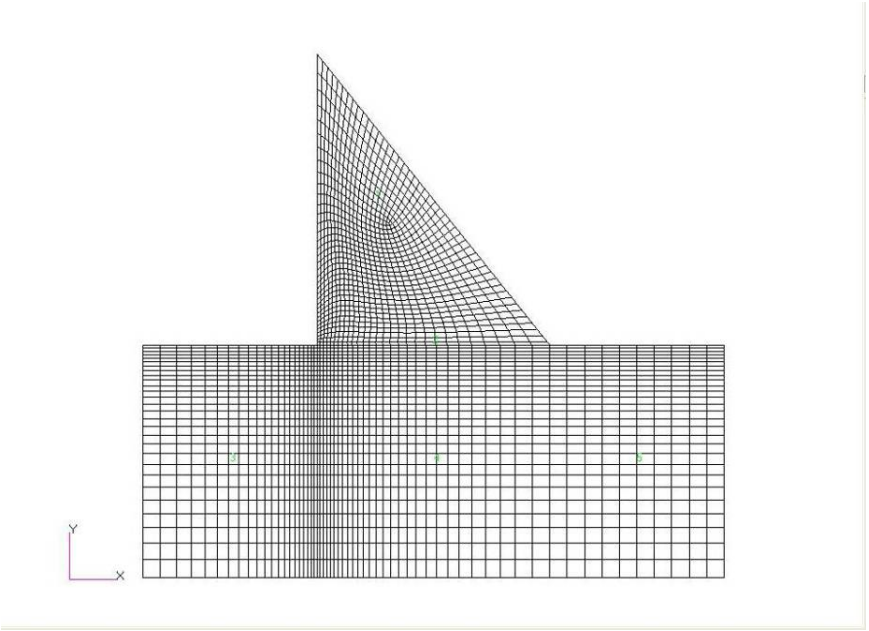

Figure 5-2: Illustration of plane strain FE mesh

5.1.2.2 Material properties

The following material properties were assumed for the finite element analysis.

Concrete parameters

E_c = 20.0 GPa
υ_c = 0.22
ρ_c = 2 400 kg/m³

Rock parameters

E_r = 30.0 GPa
υ_r = 0.25
ρ_r = zero kg/m³ (usual practice in dam analysis to simulate an infinitive foundation mass)

Drucker Prager parameters

Mass concrete strength:

f_t = 3.0 MPa
f_c = 30.0 MPa

The concrete in the joint is assumed to be of lower value to simulate a crack path (see Table 5-2).

To simulate a crack path, a set of elements was sandwiched between the wall and the foundation (see Figure 5-1). The interface elements were given brittle material properties. Four different analyses were done for four material sets, as given in Table 5-2.

Table 5-2: Material strength in joint for crack propagation exercise

Drucker Prager parameters	**Crack simulation: material strength in MPa**			
	1st material set	**2nd material set**	**3rd material set**	**4th material set**
f_t	0.0	0.1	0.5	1.0
f_c	5.0	10	10	20

Parameters for calculating the factors of safety (FOS) against sliding

The same parameters were used in the FEM as used by Chemaly (1995, p. 43) so that the factors of safety against sliding could be compared.

Friction angle is 43º and $\tan \varphi = 0.932$
Cohesion $c' = 1.2$ MPa

5.1.2.3 Boundary conditions

The model was fixed at the circumference of the foundation block in the *x*- and *y*-directions. (see Figure 5-1).

Table 5-3 shows the time steps used for the different static load conditions at the given time steps. The load cases represent the self-weight, the hydrostatic pressure up to FSL, the uplift pressure and then the final high flood conditions in three steps of 10 m, with a maximum overspill of 30 m.

Table 5-3: Time steps for load conditions for the NL FEM

Load cases	**Service load**				**Abnormal**		**Extreme**
Time step	**0**	**1**	**2**	**3**	**4**	**5**	**6**
Self-weight factor	0.0	1.0	1.0	1.0	1.0	1.0	1.0
Pressure at level at 0	0.0	0.0	1.0	1.0	1.1	1.2	1.3
Pressure at level at 100	0.0	0.0	0.0	0.0	0.1	0.2	0.3
Uplift at x = 0	0.0	0.0	0.0	1.0	1.0	1.0	1.0
Uplift at x = 10	0.0	0.0	0.0	1.0	1.0	1.0	1.0
Uplift at x=80	0.0	0.0	0.0	0.0	0.0	0.0	0.0

Note: Level 0 is at the heel of the wall.
x = 0 is at the heel and x = 80 is at the toe of the wall.

5.1.3 Analysis

The model was analysed for the six time steps with four different material properties in the 'crack interface' elements. The aim was to evaluate the different virtual crack lengths that the Drucker Prager linear plastic analysis would compute for the different material strengths. It should be noted that the analysis is not a contact or fracture mechanics analysis and the results should be read as a non-linear Drucker Prager output.

5.1.4 Results

5.1.4.1 Classical method

The results of the classical method are first presented for validation purposes.

Table 5-4 gives the results of the classical method for the three load conditions. The value of S_y is zero at the heel due to the crack on the upstream side which means that no tensile stress can exist at this point.

Table 5-4: Results of the classical method for three load conditions

Load case	**Crack length (m)**	**$FOS_{Sliding}$**	**S_y at heel (MPa)**	**S_y at the toe(MPa)**
Service	9.3	2.77	0.0	-1.554
Abnormal	32.5	1.9	0.0	-2.200
Extreme	80 (Unstable)	0.5	0.0	-2.900

Note: The S_y is zero because the wall cracked at the heel position.
The extreme load condition was included for the FEM, but the classical method resulted in the crack propagating through the full base length and the analysis is thus unstable. The FOS against overturning was calculated as 1.35 for the service load case and 0.98 for the extreme load case.

5.1.4.2 Finite element model

Linear FEA

The results of the static linear elastic FE analysis are given for four load conditions, i.e. for a service condition (100 m & uplift) and three abnormal load conditions with water heights of 110, 120 and 130 m.

Table 5-5: Maximum (S1) and minimum principal (S3) stress in MPa for the linear analysis

Load case	**Service load**		**Abnormal**		**Extreme**
Water level	**100 m**	**100 m & Uplift**	**110m**	**120 m**	**130 m**
S1	4.36	7.18	10.01	13.1	16.1
S3	-3.55	-3.51	-4.34	-5.17	-5.99

The maximum principal stress S1 varies from 4.36 MPa to 16.1 MPa from the service to the extreme condition. This indicates that yielding will occur in the joint elements for all the material properties given in Table 5-2.

Due to the many load cases, the results are best being exhibited in graphical format. For clarity, Figure 5-3 is given to demonstrate the displacements for the different time steps. The illustration in the bottom right-hand corner of this figure shows the final hydrostatic pressure state with the total pressure at 130 m, i.e. high flood level (HFL).

Non-linear Drucker Prager (DP) analysis
The values of the virtual crack distance along the base of the wall are given in Table 5-6. These distances are measured in the program's post-processor and are the distances that the equivalent plastic strain has spread along the joint line, i.e. the distance the material has yielded along this line.

Figure 5-4 and Figure 5-5 represent the maximum and minimum principal stresses at the heel of the wall for the last load condition, i.e. when the water elevation is at 130 m. As mentioned previously, this is an extreme load condition and with the high mesh density used the maximum principal stress S1 for the linear case is a high 16.1 MPa in tensile stress (see Table 5-5 and Figure 5-4). It is important to observe how the Drucker Prager yield model redistributes the tensile stress to compressive stress throughout the model.

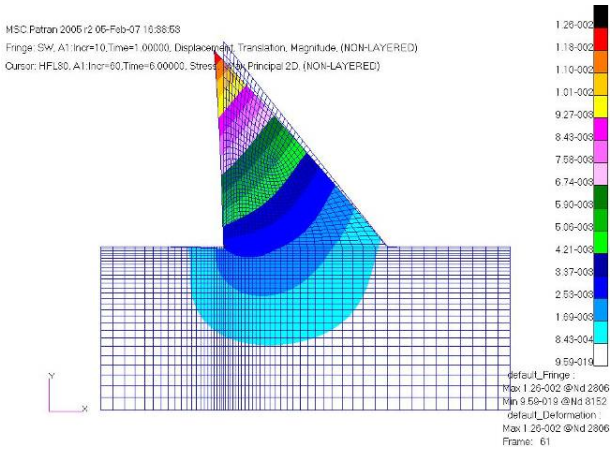

Time 0-1 Self-weight

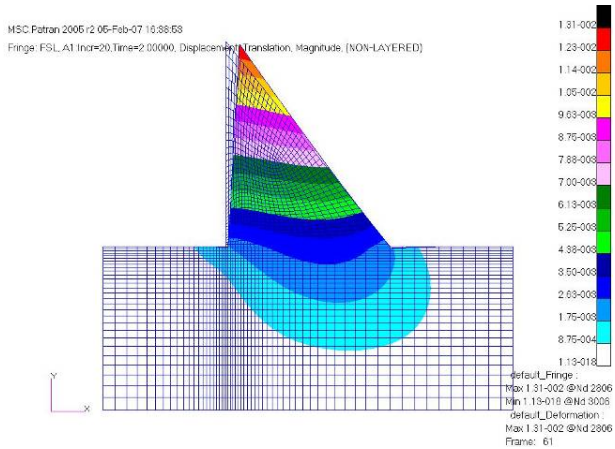

Time 1-2 Hydrostatic pressure 0 to FSL

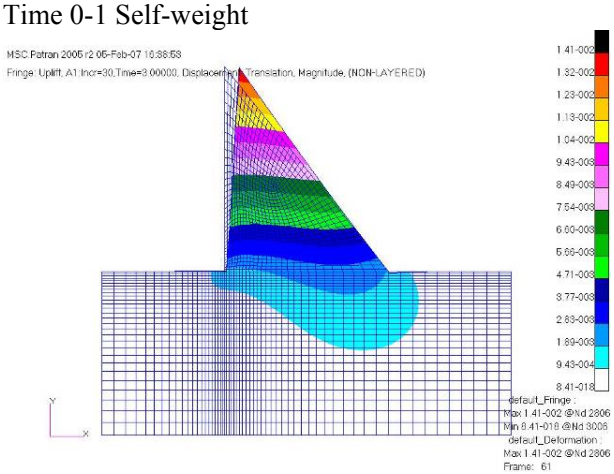

Time 2-3 Uplift pressure 0 to FSL

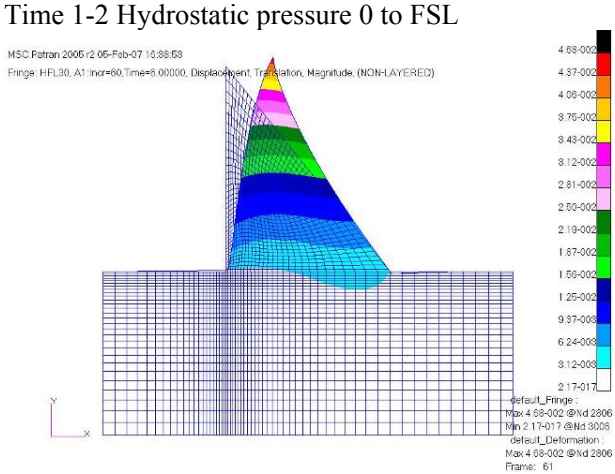

Time 3-6 Hydrostatic pressure FSL to max. HFL

Figure 5-3: Linear elastic analysis: Contour plots of resultant displacement Ur and deformation of the six load steps given in the above tables

The maximum principal stresses S1 of the four joint material strengths of 0.0, 0.1, 0.5 and 1.0 MPa are illustrated in. The characteristic curve for a linear plastic analysis can be seen in Figure 5-7 where the yield stress cut-off values stay constant with rising load condition.

Table 5-6 : Virtual crack length in metres (plastic region) calculated by the NL DP FEM

Virtual horizontal crack length, i.e. area in plastic region				
Strength f_t (MPa)	**FSL & Uplift**	**FSL + 10**	**FSL +20**	**FSL + 30**
1.0	2.1	4.5	5.87	8.7
0.5	5.1	9.5	17.0	23.9
0.1	8.0	10.3	15.2	29.5
0.0	11.2	11.2	Unstable	Unstable

All load cases include uplift pressures. The calculated crack length at FSL, for the LEFM (Chemaly), was 24.3 m for a K_{Ic}=1.0.

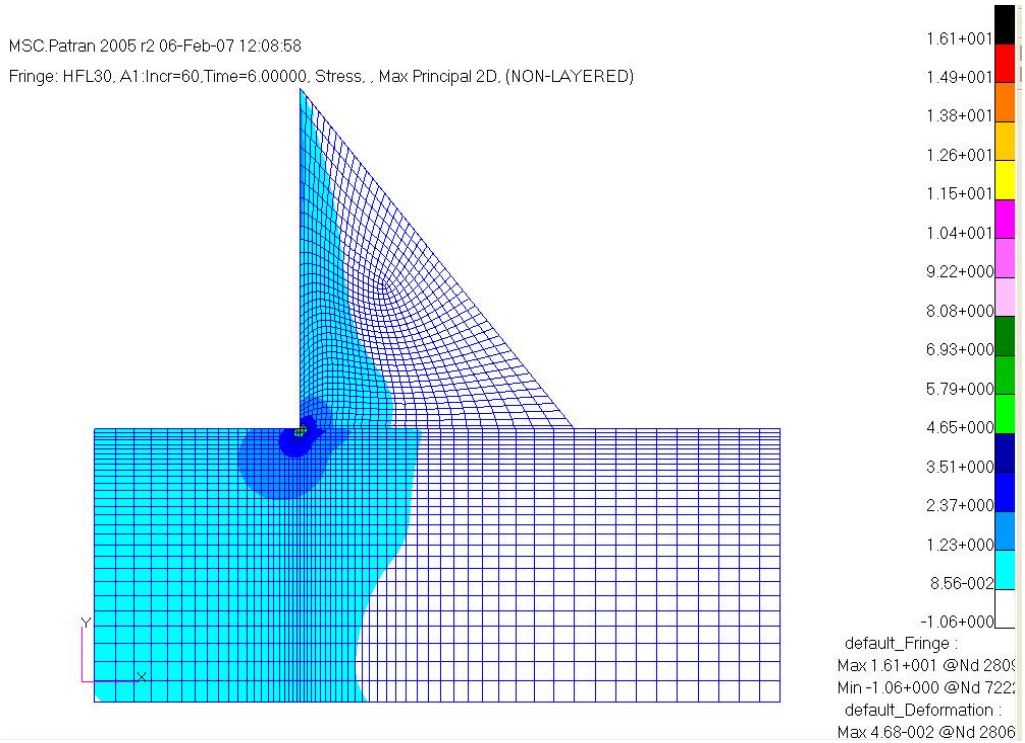

Figure 5-4: Linear static: Water load at 30 m above crest level: Maximum principal stress S1 (MPa)

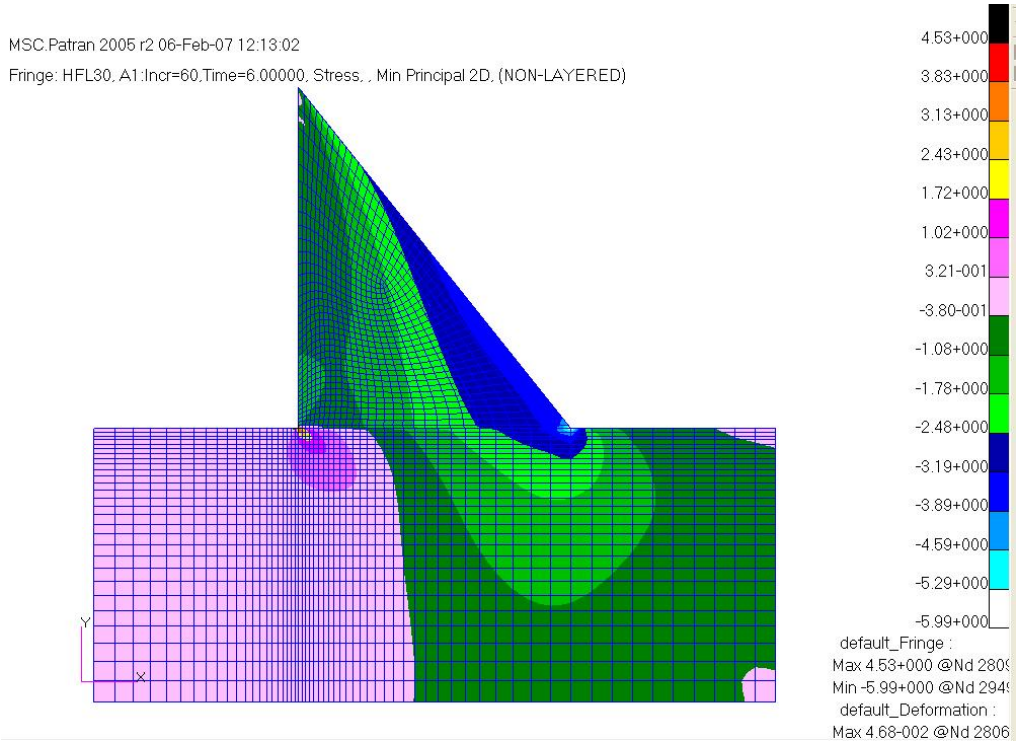

Figure 5-5: Linear static: Water load at 30 m above crest level: Minimum principal stress S3 (MPa)

Figure 5-6 presents the maximum principal stress at the heel of the wall to indicate how the non-linear yield model reduced the high stress at the heel caused by the singularity. The material strength drastically reduces the stress at the heel and reduces the singularity effect. The vertical section of the linear curve at water level 100 is due to the time step when the uplift pressure is applied to the structure.

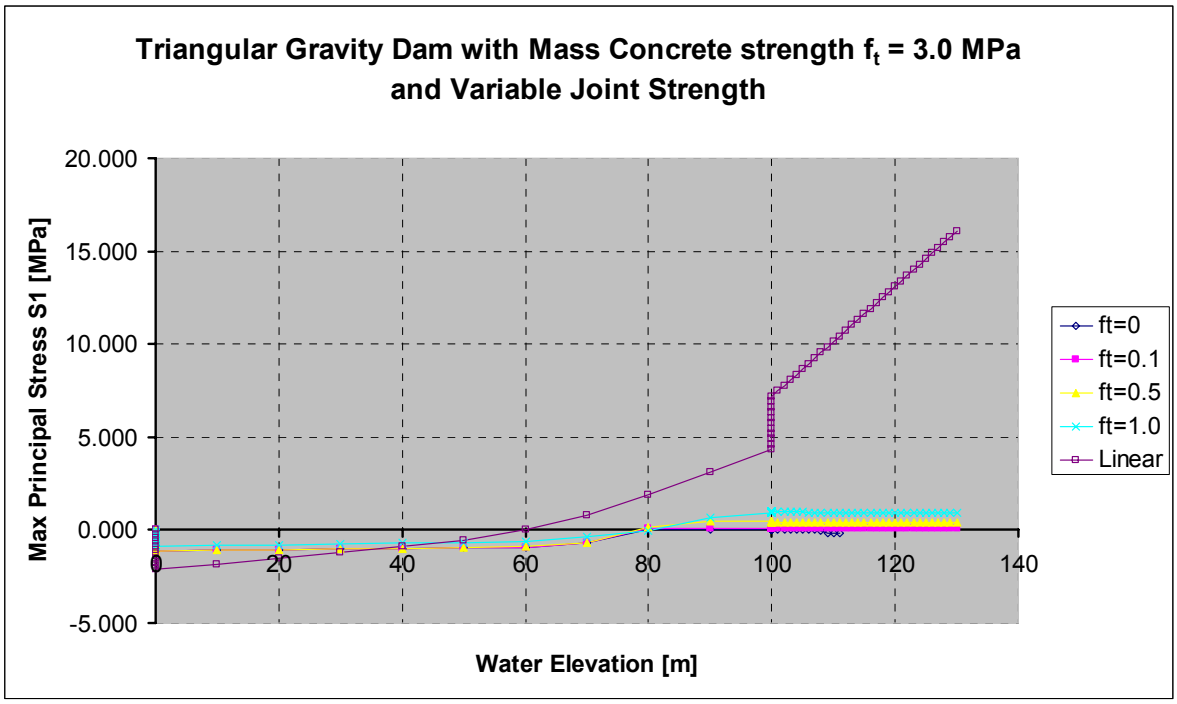

Figure 5-6: Maximum principal stress S1 for five material strength values at the heel of the wall

Figure 5-7 is a graphical presentation of the virtual crack length in relation to the values of material strength and water height given in Table 5-6.

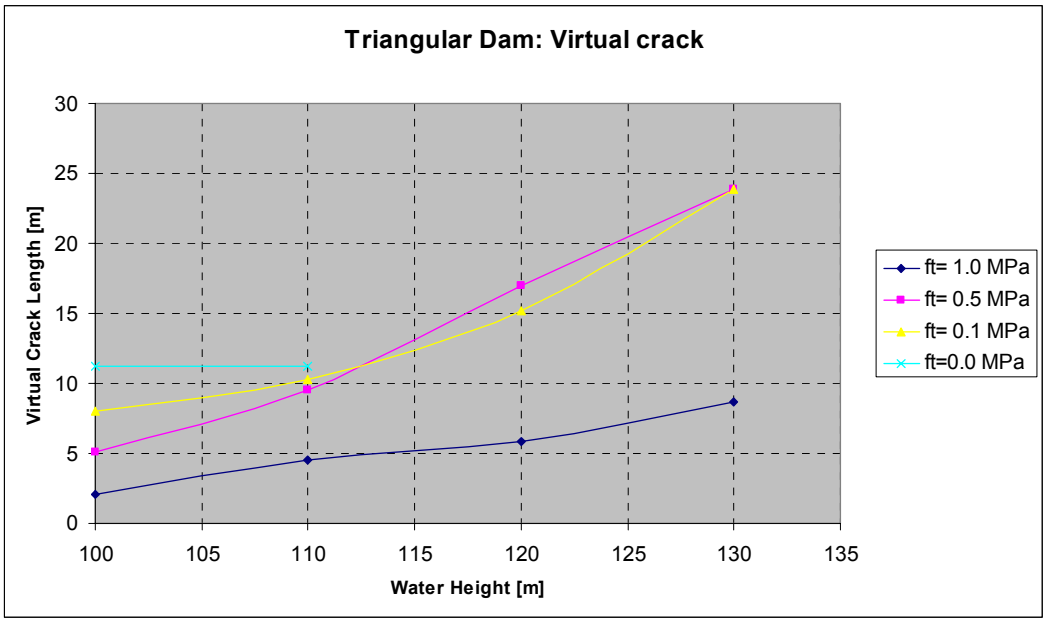

Figure 5-7: Horizontal virtual crack length for a Drucker Prager analysis with different f_t values

The curve for the f_t = 0.0 MPa analysis stopped at water height and the value basically stayed constant at 11.2 m because the FEM became unstable (see Table 5-6).

The virtual crack lengths were measured from the equivalent plastic strain (EQPS) plots in the joint elements of the Drucker Prager yield method and these were compared with the calculated crack lengths from the classical method (Chemaly, 1995). It was found that the area in plastic yielding or virtual crack length was significant smaller. One reason for this is that the formulation of the classical method is independent of the elasticity of the material (Young's modulus *E*). In other words, the stiffness of the material used in the classical method can be assumed to be rigid and therefore a crack would propagate more rapidly. See Section 3.1.3 on the theory of the classical method.

For academic interest, the material properties of the wall and foundation in the FE model were changed to a very high stiffness (E = 10^{12} GPa) relative to the stiffness in the joint elements and the analysis was run again. This was done to examine the influence of elasticity because the classical method does not account for elasticity in the material. The results of the non-linear model changed significantly: the elements in the joint would yield more quickly and the wall would displace downstream with yielding throughout the whole joint, e.g. for a total water height of 110 m, the virtual crack length has now progressed to 39 m along the base. From this analysis it can be concluded that the modulus of elasticity of both the wall and foundation can have a significant influence on the computed results of the virtual crack. However, this is not a realistic model as the variation in stiffness is too large and the crack would also propagate rapidly through the wall with a rise in water height.

The results of the Drucker Prager model illustrated that for a dam with a realistic modulus of elasticity as given above, the virtual crack is significantly smaller than with the analytical fracture mechanics method. For the FSL load case the maximum crack length for a zero material strength in the joint was 11.2 m (Figure 5-7) compared with the 24.3 m of the fracture mechanics method (Chemaly, 1995, p. 89).

To calculate the crack length in a stiff wall (E = 10^{12} GPa), with the FEM triangular wall, a trial-and-error process was used to determine the water height under which a crack length of 24.3 m would propagate (Chemaly, 1995). The FEM computation showed that 108 m of water was necessary to propagate the 24.3 m crack. The material strength in the joint was f_t = 0.5 and there was high *E* stiffness (E_c and E_r = 10^{12} GPa).

This sensitivity study proved that the modulus of elasticity is an important parameter in the calculation of crack length. In the formulation of the classical method no modulus of elasticity is included and the structure should be considered as a rigid body. The FEM with a very high stiffness, to simulate a rigid body, illustrated that a long yield path was found for high stiffness values. As the classical method represents a rigid body a long crack length can be expected.

However the fracture mechanics method as illustrated by Chemaly (1995) uses the method of Gálvez el al (1994) and this method incorporates the FEM to calculate the fracture toughness and thus includes the stiffness modulus in its formulation. This method gives a slightly shorter crack length but still not in the same order as the FEM length.

To do a direct assessment between the fracture mechanics method and the FEM a relationship between the fracture energy, fracture toughness and the DP parameters should be determined which falls beyond the scope of this dissertation. Further research on this aspect is recommended.

When the FEM is modelled as an elastic structure and the stiffness will have a significant influence on the crack length.

The factor of safety (FOS) against sliding was calculated for the FSL and the HFL (30 m spill), with a material strength in the joint of f_t =1.0 MPa. No tail-water pressure was included. The S_y stress distribution is shown in Figure 5-8.

Figure 5-8 was used to calculate the vertical friction component in the Coulomb formulae. The figure illustrates the normal stress S_y distribution along the base of the wall. This distribution was used to calculate the FOS against sliding for an FSL condition and a high flood level (HFL) spilling depth of 30 m.

This graph in Figure 5-8 does not represent the calculated crack length and the FOS against sliding is calculated for the portion where the normal stress S_y in compression.

The FOS calculation is illustrated in Appendix G of this dissertation.

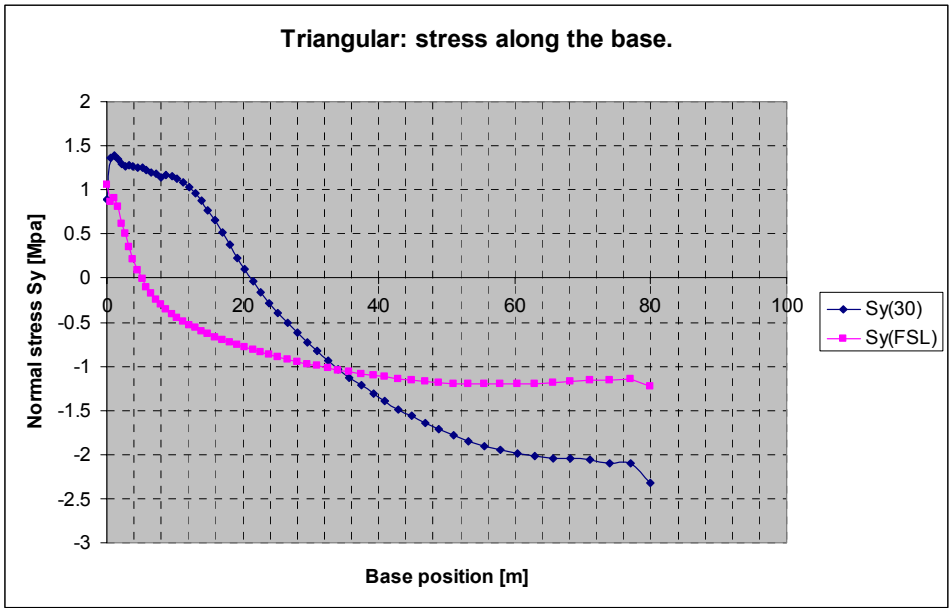

Figure 5-8: Triangular dam: Normal stress S_y versus base position: Load case is HFL 30 m overspill and FSL

The FOS was calculated by spreadsheet and is given in Appendix G.

The material properties for this analysis were:

Friction angle is 43º and	tan φ= 0.932
Cohesion	c' = 1.2 MPa

Table 5-7: Factors of safety against sliding for the triangular dam: Comparison of the classical and FE methods

Factor of safety against sliding	Service 100 m (FSL)	Extreme 130 m (HFL)
Classical method	2.82	1.26
FEM	3.18	1.93

It can be concluded that the crack length computed with the non-linear FEM differed significantly from those obtained from the classical method and the fracture mechanics model of Gálvez et al. (1994), as used by Chemaly (1995).

This case study illustrated that the classical method is significantly more conservative that the FEM. The predicted FOS was also more conservative as illustrated in Table 5-7.

5.2 Case History: Eighty-year-old Van Ryneveld's Pass Dam

The Van Ryneveld's Pass Dam was chosen because it has been in operation for more than 80 years and was designed without an under-drainage system (Figure 5-10). It also has a relatively steep downstream slope which caused some concern about its stability safety factors. The concrete of this dam was thoroughly tested in the laboratory for strength and other properties during the previous dam safety evaluations. Two sets of material properties will be used to analyse the dam to examine the sensitivity to failure criteria. The first set of concrete properties was taken from test results on a collection of cores that were drilled from the wall for a dam safety evaluation report by Van der Spuy (1992). The second set was from the material properties generally used for small dam design in the DWAF where the material properties are not readily available.

The dam is downstream of a large catchment area and the calculated Regional Maximum Flood (RMF) is 6 000 m³/s which means that high flood levels will occur during such extreme flood conditions. This extreme flood condition also causes a very high tail water on the downstream face of the wall due to the high backwater, which has a stabilising effect on the dam during high flood conditions.

Figure 5-9: Van Ryneveld's Pass dam spilling during March 2008 (Photo courtesy of A Chemaly)

It is an ideal academic case study because of the large amount of information available.

This gravity mass concrete dam was built by the DWAF and completed in 1925. The crest level is 46 m above the lowest foundation level and the spillway level is approximately 30 m above the riverbed surface. The silt level is 21.3 m above the riverbed. The downstream slope varies between 0.5, 0.65 and 1.0 from the crest downwards to the base level. The average slope is thus 0.626:1, which is considered a very steep slope in today's terms and makes it a unique dam to analyse. See Figure 5-10.

5.2.1 Finite element model

The geometry was taken from the DWAF dam safety report by Van der Spuy (1992).

The geometry used for the FEA is illustrated in Figure 5-10. The levels of the water pressures are also given in reduced level (RL) above sea level for clarity. The dotted lines represent the load pressures.

The model was created in the pre-processor and a relatively high-density mesh was generated to model the stress concentrations at the heel of the wall.

A foundation block was also modelled to soften the stress concentrations at the base of the wall.

The FE model was constructed with 5 509 second-order plane strain isoparametric elements. The whole structure is monolithic.

Figure 5-11 illustrates the finite element mesh of the Van Ryneveld's Pass Dam, the boundary conditions and some pressure loads in vector format.

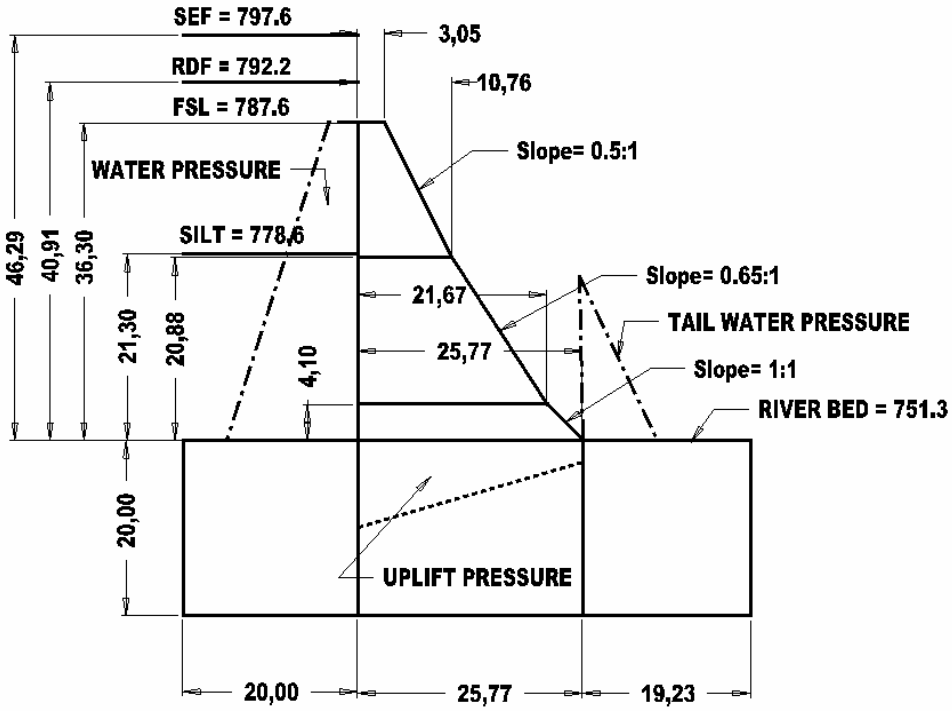

Figure 5-10: Geometry used to model the FEM of Van Ryneveld's Pass Dam

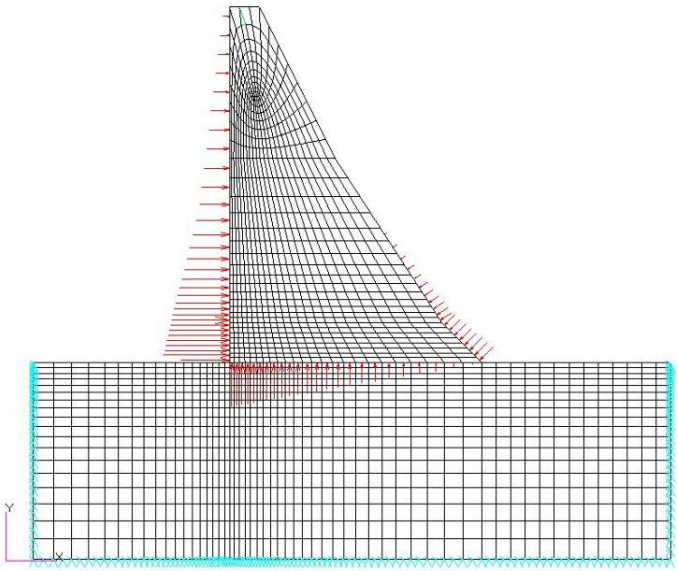

Figure 5-11: Finite element mesh of the Van Ryneveld's Pass Dam and schematic illustrating the load conditions

5.2.2 Load and boundary conditions

Load conditions

The load conditions for this exercise are limited to two cases only to illustrate the Drucker Prager material behaviour and not all load conditions as illustrated in Table 3-1 (page 26) are performed. No temperature and seismic loads were considered.

The following load conditions were applied to the model: self-weight, hydrostatic water pressure and silt pressure on the upstream face, uplift pressures at the base of the wall and tail-water pressure on the downstream face.

As there is no provision for drainage under this dam, a full triangular uplift pressure distribution was assumed. See Figure 5-10.

Figure 5-12 was prepared using the classical method program CADAM (2001) to illustrate the hydrostatic load conditions.

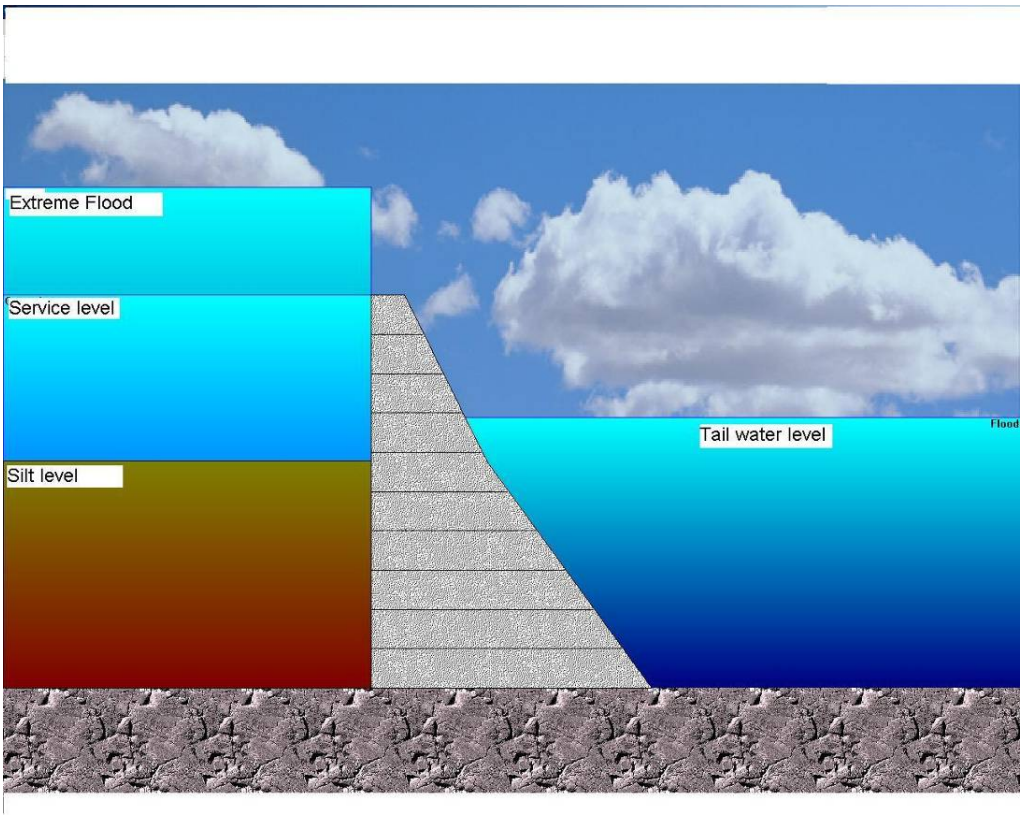

Figure 5-12: Hydrostatic and silt conditions (CADAM 2001)

From Figure 5-12 can be seen that the tail-water level will have a significant impact on the extreme load condition in that the tail-water pressure will counteract the high upstream pressure.

As for the previous examples, the load cases are ramped up through the loading from zero to maximum safety evaluation flood (SEF). Loads are stepped as follows:

1st time step – only the gravity load was ramped up.
2nd time step – the pressure was ramped up from empty to full supply level (FSL).
3rd time step – the uplift pressure and the silt load were applied.
4th time step –the water overspill was ramped up from FSL to SEF, and in addition the corresponding tail-water pressure and additional uplift pressures were applied.

Table 5-8 shows the two load conditions to be analysed. It should be noted that the dam has no under-drainage and that full pore pressure as determined from the FSL is assumed for both load conditions. The tail-water pressure was modified for the SEF condition on the downstream side of the wall.

Table 5-8: Load conditions for the Van Ryneveld's Pass Dam

Load combination	Hydrostatic loads							Other loads	
	MOL	FSL	RDF	SEF	TW	Silt	Gravity	Pore pressure	
								Partial	Full
Service -1		X			X	X	X		X
Extreme - 2				X	X	X	X		X

The water heights for the FSL and SEF floods, as well as the silt level, are given in Figure 5-10.

The FSL was considered to be the service condition and the SEF was considered to be the extreme condition.

The loads are as follows:

Full supply level (FSL) RL is	787.60 m
Hydrostatic upstream water level (SEF) RL is	797.6 m (10 m spill)
Tail-water level for SEF RL is	777.0 m (maximum is 25.7 m)
Silt level RL is	778.6 m

RL is the reduced level above sea level.

Restrictions in this analysis
No earthquake and temperature load conditions are examined as the emphasis of this dissertation is on the static Drucker Prager yield model.

Boundary conditions
The foundation block was fixed in the U_x and U_y directions along the circumference, as illustrated in Figure 5-11.

5.2.3 Material properties

Two types of material strength are examined to test the sensitivity of the yield model on this dam (subscripts 1 and 2).

The material properties used are taken from Van der Spuy (1992).

$E_{concrete(1)}$ =	28.4 GPa	$E_{concrete(2)}$ =	20 GPa
E_{rock} =	30 GPa	E_{rock} =	30 GPa
$\upsilon_{concrete}$ =	0.22	υ_{rock} =	0.22
$\rho_{concrete}$ =	2 450 kg/m³	ρ_{rock} =	0
f_{t1} =	3.0 MPa	f_{t2} =	1.5 MPa
f_{c1} =	30 MPa	f_{c2} =	15 MPa

$\alpha_1 =$	0.2466	$\alpha_2 =$	0.2466
$\bar{\sigma}_1 =$	4.271	$\bar{\sigma}_2 =$	2.1356

Residual friction angle (tan Φ) =1.43 (friction angle of 55º)
Cohesion (c`) = 2.41 MPa

5.2.4 Results

The results of the two load case analyses are given in Table 5-9 and represent a service load and an extreme load condition for comparison.

Table 5-9: Results of Van Ryneveld's Pass Dam for the service and extreme load cases

Load case	Displacement Ur [mm]	Max. principal stress S1 [MPa]	Min. principal stress S3 [MPa]	Normal stress Sy at the heel [MPa]
Service 1 Linear	2.46	2.98	-1.30	1.75
Extreme 2 Linear	6.32	4.76	-2.05	3.11
Service 1 NL (f_{t1}=3.0)	2.46	2.85	-1.33	1.68
Extreme 2 NL (f_{t1}=3.0)	6.23	3.30	-1.99	2.70
Service 1 NL (f_{t2}=1.5).	2.47	1.58	-1.30	1.16
Extreme 2 NL (f_{t2}=1.5).	6.31	1.63	-2.02	1.39

Notation: f_{t1} = 3 represents the average concrete tensile strength physically tested from cores drilled out of the wall and f_{t2} = 1.5 represents the standard concrete tensile strength (see Sub-section 5.2.3 on material properties.

Figure 5-13 was created to illustrate the convergence history plot of the S1, S_y and S_x stresses. From this plot the stress history plot can be seen whether the conversion of the analysis was completed correctly.

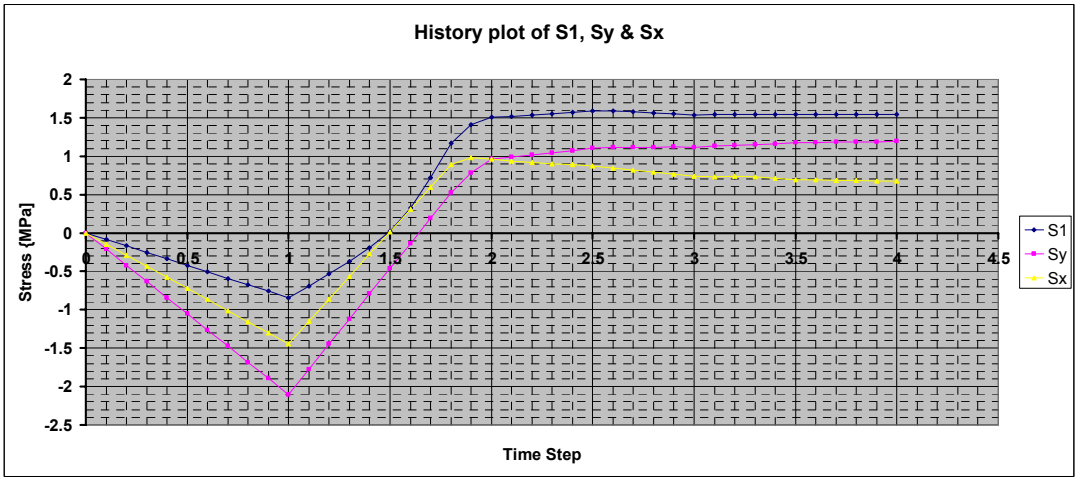

Figure 5-13: History plot of the S1, S_y and S_x stresses in MPa

From the history plot in Figure 5-13 the different convergences can be seen. The S_x stress declines most in the yield model. This decline in the S_x stress is probable due to the high tail-water pressure which is applied to the structure during the last phase.

Figure 5-14 illustrates the deformation contour plots for the four load steps given in Sub-section 5.2.2 for the lower material strength condition, i.e. f_t = 1.5 MPa. As previously mentioned, these time steps are important to simulate the correct stress conditions in the DP yield model.

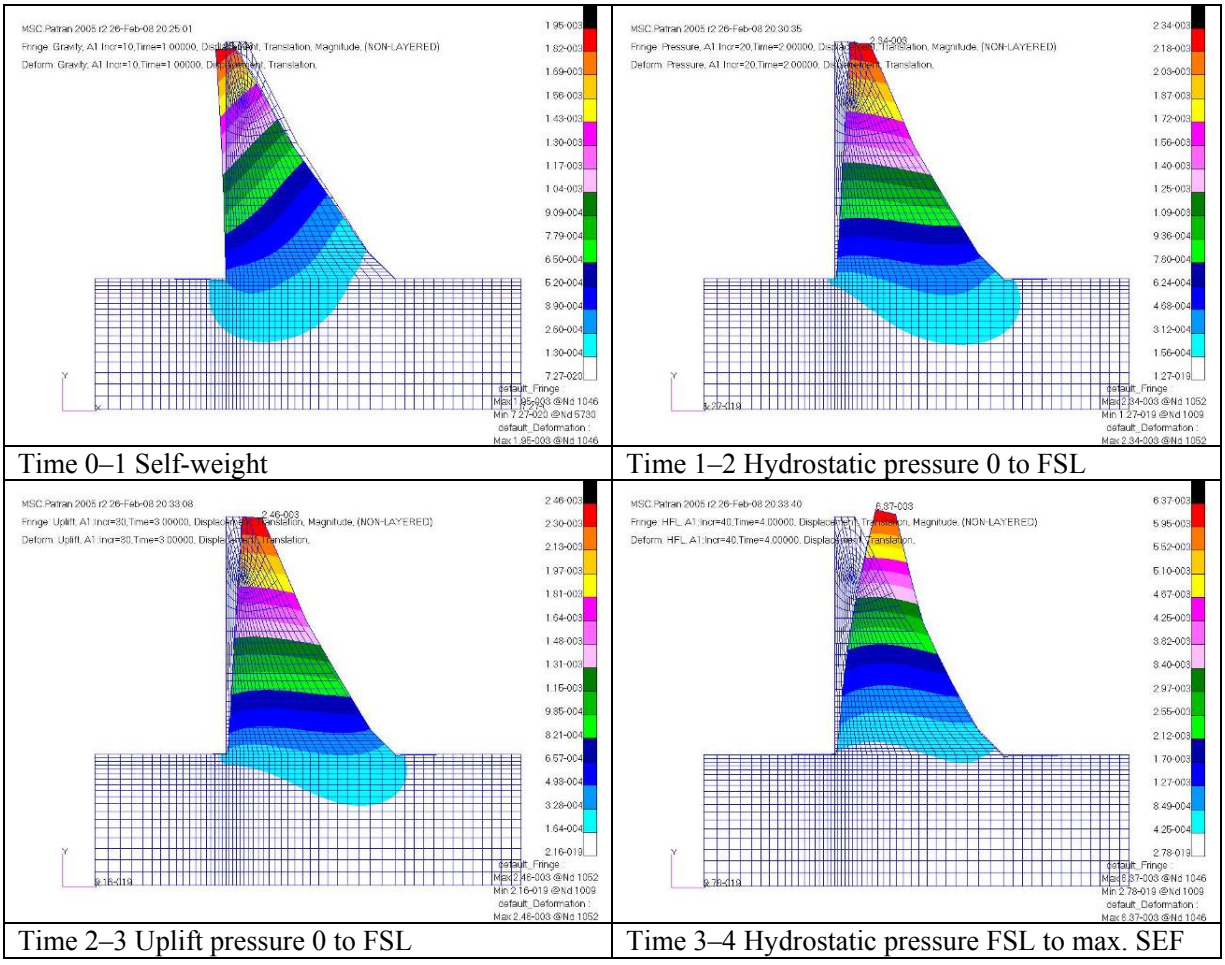

Time 0–1 Self-weight | Time 1–2 Hydrostatic pressure 0 to FSL

Time 2–3 Uplift pressure 0 to FSL | Time 3–4 Hydrostatic pressure FSL to max. SEF

Figure 5-14: Deformation contour plots of the four load steps for the ft = 1.5 MPa material strength

From the displacement figures of Figure 5-14 the different time steps can be seen. During the first time step, the wall deforms in an upstream direction. The next step is when the hydrostatic pressure is loaded from zero to FSL. Time step 3 represents the phase in which the full uplift pressure is applied. During the last time step, the high flood level is ramped up from the FSL to the SEF water level. Simultaneously, the tail-water level is also applied on the downstream face.

Figure 5-15 to Figure 5-17 illustrates the maximum principal stress (S1) for the Van Ryneveld's Pass Dam; they are for the linear material and the two DP material properties for f_{t1} and f_{t2} so as to illustrate the sensitivity of the material yield strength in the DP yield model.

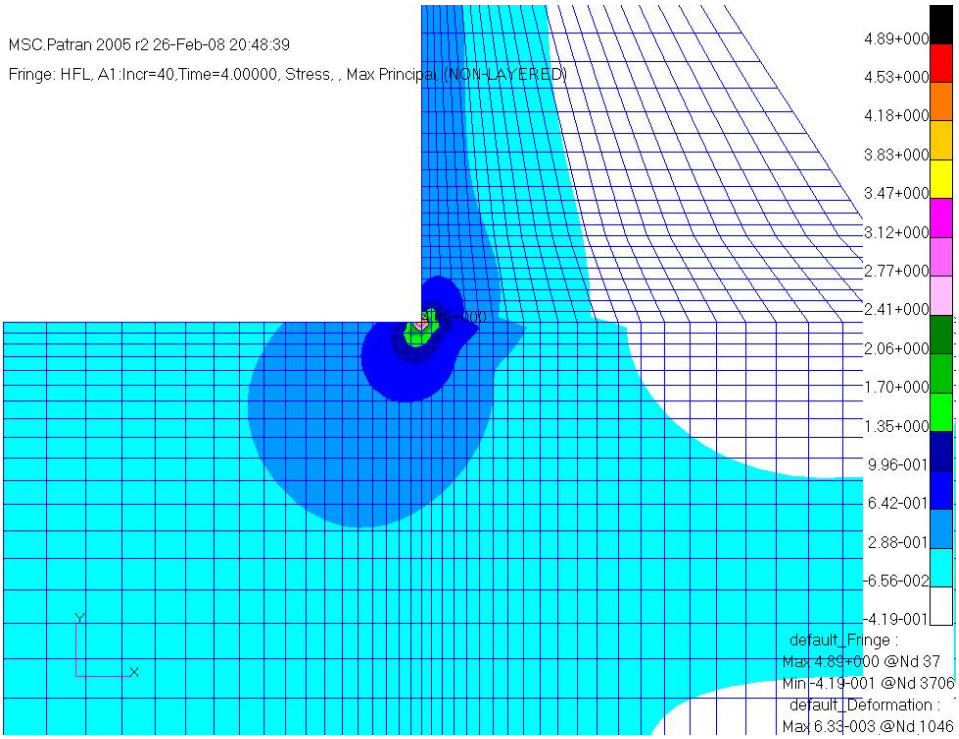

Figure 5-15: Van Ryneveld's Pass Dam max. principal stress S1: LC = Extreme 2, Linear case

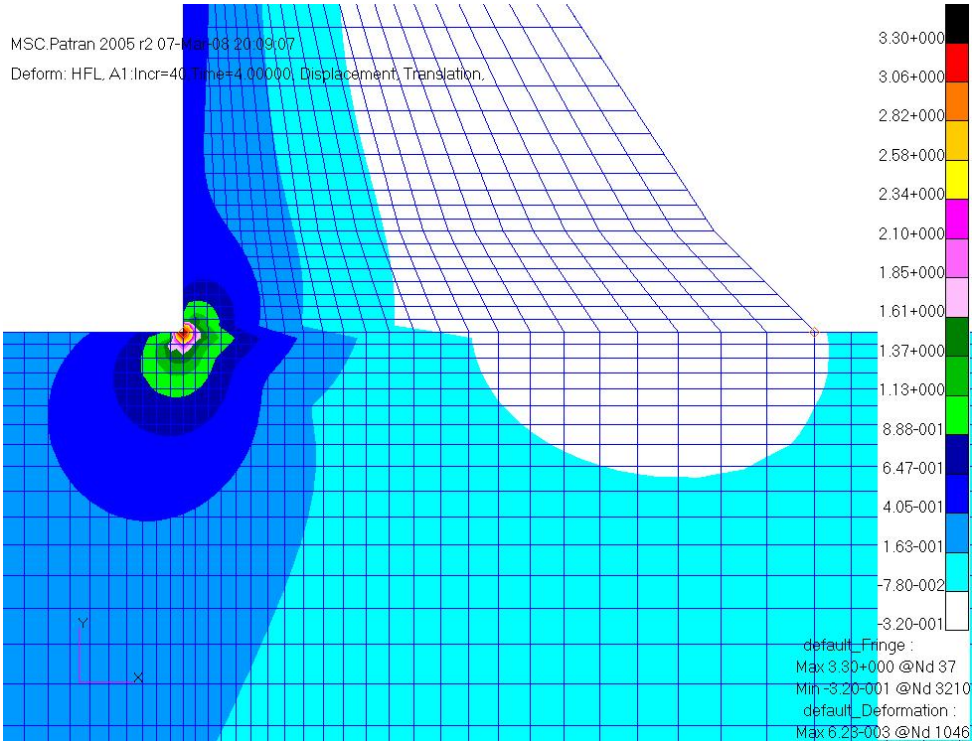

Figure 5-16: Van Ryneveld's Pass Dam max. principal stress S1: LC = Extreme 2, DP NL FEM f_{t1}=3.0

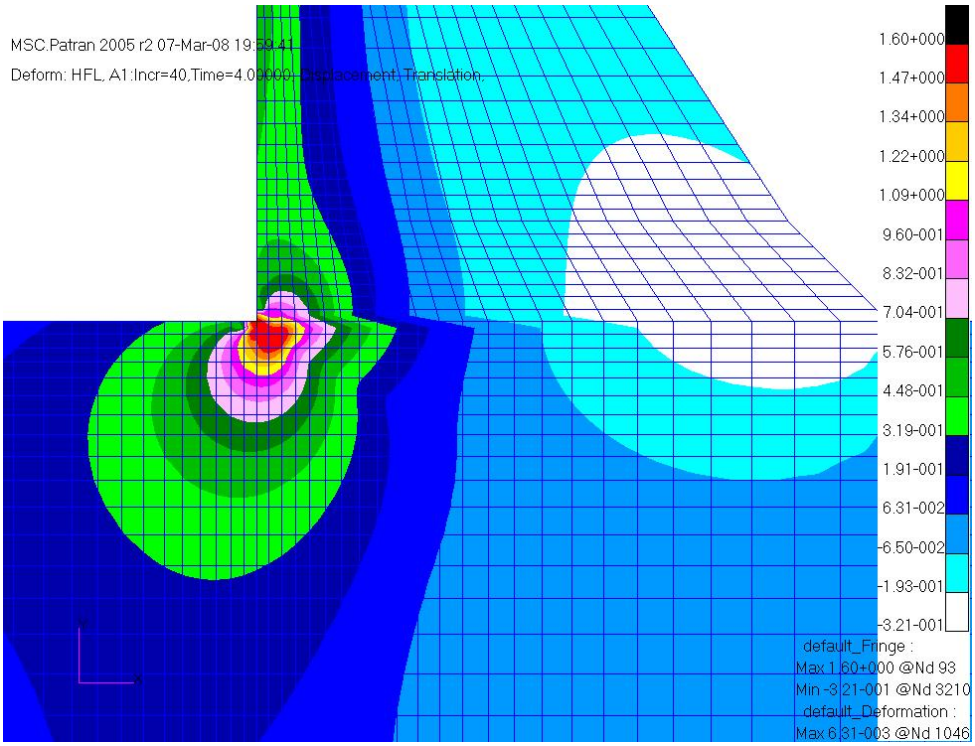

Figure 5-17: Van Ryneveld's Pass Dam max. principal stress S1: LC = Extreme 2, DP NL FEM f_{t2}=1.5

It can be seen from Figure 5-15 that the stress for the linear case is very high (since a high mesh density was used) and that local yielding of the concrete can be expected in the DP model.

Figure 5-16 and Figure 5-17 illustrate the maximum principal stress (S1) as calculated by the DP yield model analysis and indicate that the area where the stress distributes from the heel downstream is sensitive to the material yield strength. A much larger area is in red for the lower material strength of 1.5 MPa.

Figure 5-18 and Figure 5-19 are given to illustrate the equivalent plastic strain (EQPS) area of the DP yield model analysis for the two material properties.

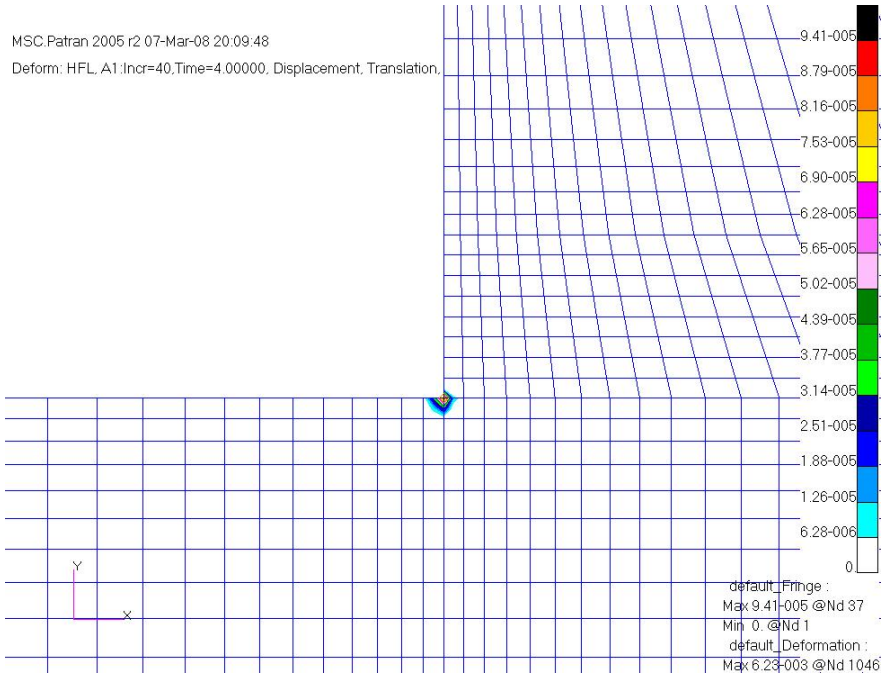

Figure 5-18: Van Ryneveld's Pass Dam: Equivalent plastic strain: LC = Extreme 2, DP NL FEM $ft2$=3.0

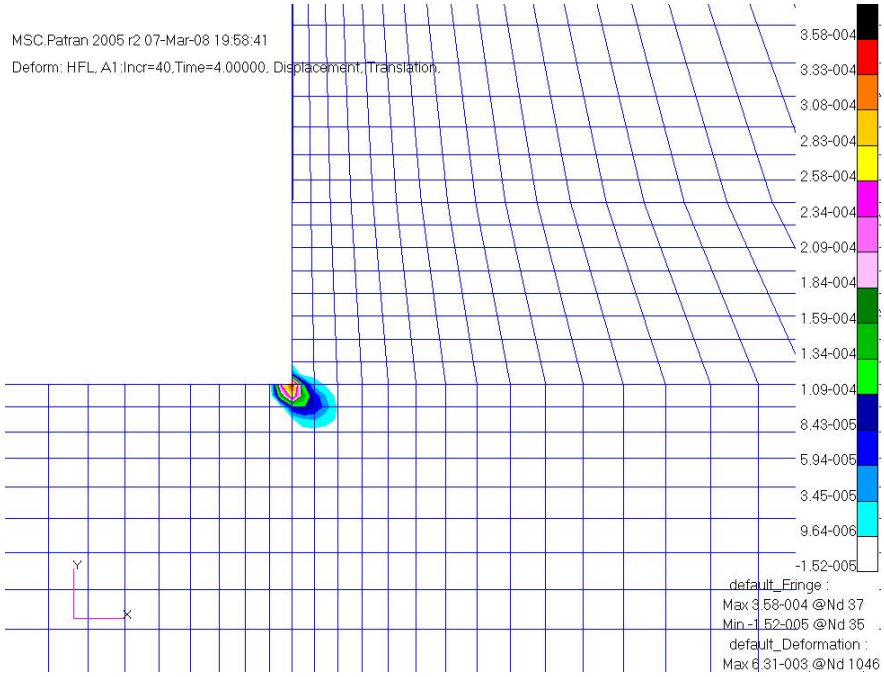

Figure 5-19: Van Ryneveld's Pass Dam: Equivalent plastic strain : LC = Extreme 2, DP NL FEM $ft2$=1.5

Figure 5-18 and Figure 5-19 illustrate the EQPS for the non-linear DP model with concrete strengths of f_{t1} = 3.0 MPa and f_{t2} = 1.5 MPa, and gives an indication of the yielding that occurred in the two different materials. From the stress and EQPS contours it can be seen that the EQPS is higher for the f_{t2} = 1.5 MPa than the 3.0 MPa material. The EQPS for equal material strength for the concrete and rock, i.e. f_{tc} and $f_{tr,}$ tends to dip at a 45º into the rock foundation and that little of the base length is reduced due to predicted cracking. The EQPS is also relatively localised at the heel of the wall for the extreme load condition and this predicts that the material can withstand the load condition.

Calculation of factor of safety against sliding ($FOS_{sliding}$)

A spreadsheet was used to calculate the factor of safety against sliding ($FOS_{sliding}$) by using the Coulomb friction theory similar to the one used for the classical method (Equation 3-3 from Sub-section 3.1.3). However, the normal stress (S_y) of the non-linear DP model was used to determine the vertical stress for Equation 3-3.

$$FOS_{sliding} = \frac{c`.A + (\sum V - \sum U).\tan\Phi}{\sum H} \qquad \textbf{Equation 3-3}$$

The formula used in the spreadsheet was modified as follows:

$$FOS_{sliding} = \frac{\sum c`.A + \sum (R_y.\tan\Phi)}{\sum H} \qquad \textbf{Equation 5-1}$$

where all the symbols are the same as previously defined for Equation 3-3, with the exception that R_y represents the vertical reaction force derived from $R_y = S_y\ A$ and the area A here is defined as the area of the base width of each individual element that is summated along the base of the wall. S_y is the vertical normal stress calculated in the FEA.

In the dam safety report (Van der Spuy, 1992) the values for the laboratory-tested material properties were given in Table 6.1 as:

- Residual shear coefficient (tan Φ) = 1.43, which represents a friction angle of 55º
- Cohesion (c`) = 2.41 MPa

(In the author's opinion, these values are very liberal and high FOS are expected.)

Figure 5-20 was created to illustrate the normal stress S_y for an extreme load condition at the contact level between the wall and the foundation, and these stresses were used to calculate the resultant vertical force ΣV for the Coulomb friction resistance.

An assumption was made in the spreadsheet calculation of the $FOS_{sliding}$ that the virtual crack length is the total length where the S_y stress is in tension. This is a conservative approximation as the actual virtual crack length is usually smaller, as illustrated in Figure 5-18, Figure 5-19 and Figure 5-20. In the last figure can be seen that the compression zone starts at

approximately 5 m from the heel of the wall. The area is thus reduced according to the area in tension.

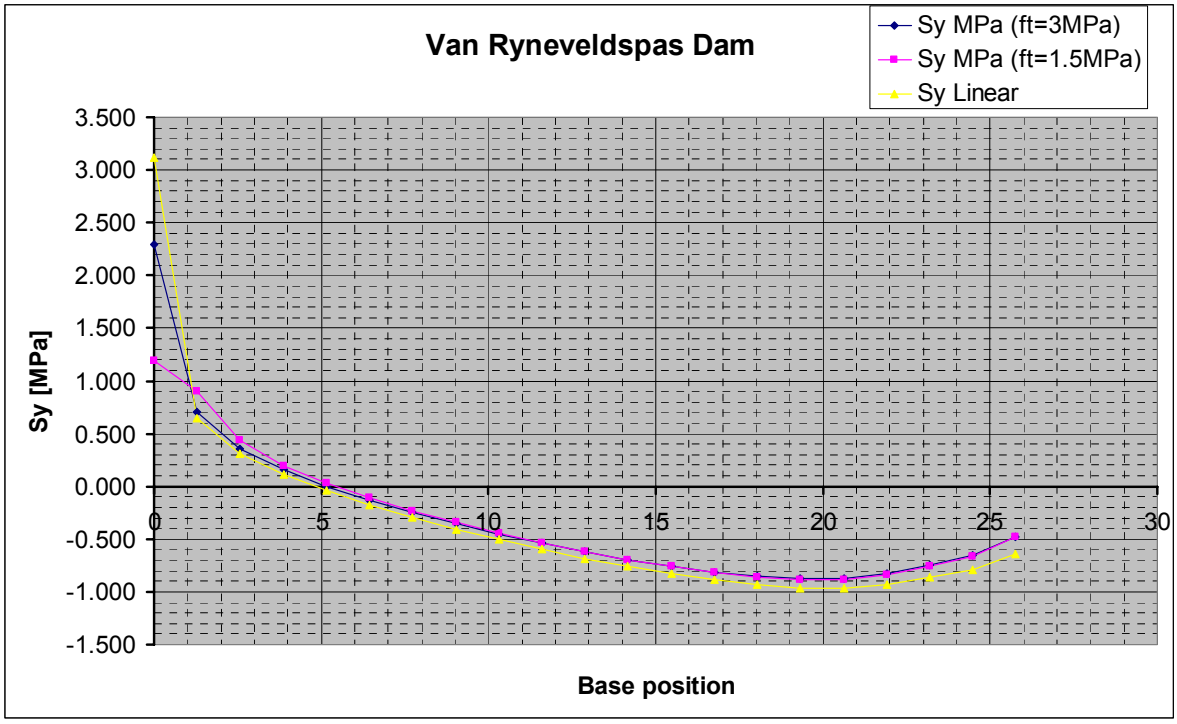

Figure 5-20: Normal stress Sy versus base position for two material properties for the extreme load case

The spreadsheet calculations for the $FOS_{sliding}$ were performed for two tensile strength values, $f_t = 1.5$ MPa: and $f_t = 3.0$ MPa (see Table 5-10). Included in Table 5-10 are the results for the classical method (CM) as calculated by the CADAM (2001) program. The parameters for the CM were taken from Van der Spuy (1992) and are c' = 2.41 MPa and tan φ = 1.43 or 55º

The loading condition for the $FOS_{sliding}$ was restricted for the '*Extreme 2'* condition (see Table 5-8).

Table 5-10: $FOS_{sliding}$ for the two material properties at the base level.

NL Drucker Prager FEM			Classical method CADAM (2001)
Load condition	**FOS for $f_t = 1.5$ MPa**	**FOS for $f_t = 3.0$ MPa**	**No cracking**
Service	8.66	8.66	7.9
Extreme	8.03	8.32	5.7

The Van Ryneveld's Pass Dam was examined in this dissertation as it is a dam that was originally designed without considering the pore pressure under the dam. Without uplift pressure, a dam could be designed with a steep downstream slope. The results of the classical method for this dam illustrate that the dam is safe on condition that the strong material properties (c' and φ) of Van der Spuy (1992) are used.

The classical method was followed with and without the crack facility. With the material values given by Van der Spuy (1992), no crack propagated. However, the allowable tensile stress has to be reduced to 0.66 MPa (660 kPa) to activate the cracking and this was found to be very sensitive in the CADAM program. A variation of 200 kPa was sufficiently significant to change the results from a fully cracked to an uncracked condition and the author decided to reject the results of the cracked analysis. The classical method also indicated that the dam was unstable for the extreme flood condition and that the overtopping FOS was approximately 0.82 for both the cracked and uncracked conditions.

The author's opinion is that the c' and φ values of Van der Spuy (1992) are too high to be used for the classical method and also too high for the FEM when the Coulomb friction equation is used. The FOS for sliding as given in Table 5-10 is very high for all load cases. To examine the FOS boundary limits ('failure domains', see Oosthuizen, 1985) a set of curves was created – Figure 5-21 and Figure 5-21 – which represent $FOS_{sliding}$ = 1.0, 1.5 and 2.0. The value of the cohesion was calculated by an iterative process by keeping tan φ =0 constant and iterating the values of c' until the required FOS was obtained. The opposite was also calculated, i.e. the cohesion (c') was kept constant at zero and the values of tan φ were iterated until the required FOS was found. The cures were only created to represent a material strength of f_t = 1.5 for the FSL and SEF conditions. The f_t = 3.0 MPa material strength was not included to prevent the graphs from becoming too cluttered. The FOS was taken to represent the service condition and an extreme flood condition.

For purposes of comparison, the curves for the classical method are also shown. These are illustrated in the same colour so that the reader can distinguish the range between the two FOSs.

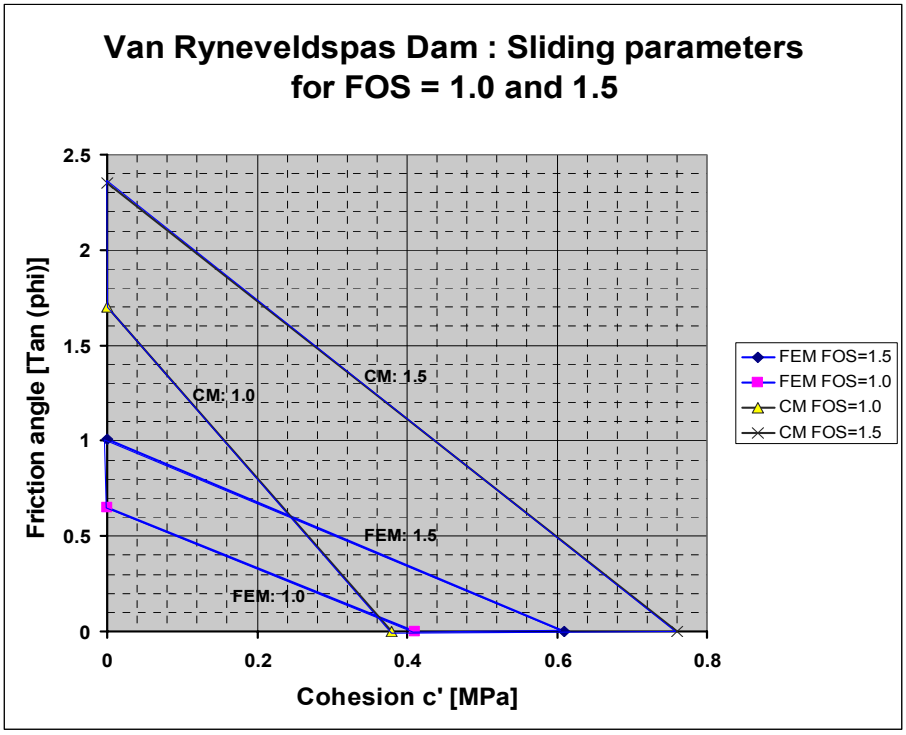

Figure 5-21: Failure and safe domain for $FOS_{sliding}$ for extreme flood and f_t=1.5 MPa

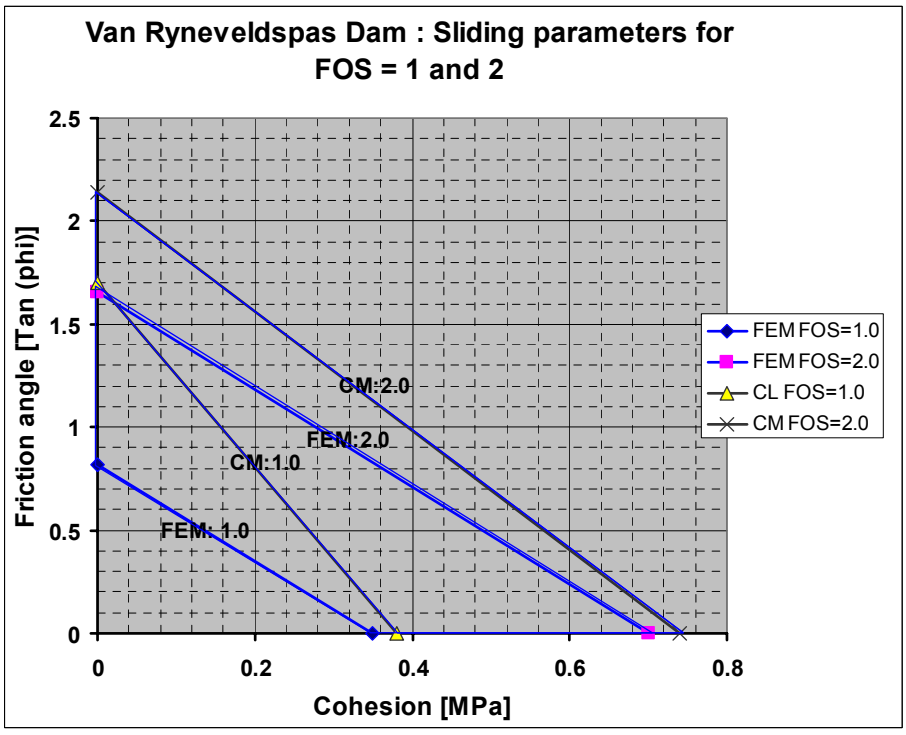

Figure 5-22: Failure and safe domain for $FOS_{sliding}$ for FSL and f_t=1.5 MPa

From the above figures the region below the FOS = 1.0 curves is the unsafe region where the $FOS_{sliding}$ is smaller than 1 and represents the boundary condition at which sliding can be

expected for an extreme flood or service condition. Sets of curves are plotted for other factors of safety 1.5 and 2.0 which will then represent the area where the dam will be safe for an extreme load condition.

The graphs also show that the classical method gives a more conservative result for the FOS than does the FEM, in other words larger φ and c' values are necessary to stabilise the structure when the classical method is used.

The calculations for the FOS were done using the material properties of Van der Spuy (1992). It can be seen that the results for the FOS are very high (see Table 5-10), and these material properties are thus seen as very liberal for this dam. For this dam lower values for the input parameters are recommended for the classical method, in line with the values represented in Figure 5-21 and Figure 5-22, due to the inconsistency of the Bernoulli theory as previously discussed in relation to the thin beam theory.

If the normal standards for maximum allowable tensile stress as given in Table 3-2 for the classical method were used as the criterion, the dam would be classified as unsafe because the tensile stress exceeds the norm.

This dam was later evaluated by an independent engineer, Seddon (1998), from the consulting firm Ninham Shand by means of the classical method. He states in his report: "*Stability analyses which have been carried out show that the Van Ryneveld's Pass Dam does not comply with the stability criteria currently applicable to new dams. When analysed as an existing structure, however, it was found to be just stable with the reservoir at full supply level. Under Safety Evaluation Flood (SEF) conditions or in the event of a flood equal to the Recommended Design Flood (RDF) it was found to be unstable even when analysed as an existing structure…".*

As an alternative method, the FEA was used to evaluate the safety of this dam in terms of material strength. The non-linear Drucker Prager yield model is the better approach for studying this problem because the actual material strength can be used to simulate the yielding behaviour of the wall.

Figure 5-18 and Figure 5-19 display the contour plots of the equivalent plastic strain and thus indicate the area where failure is expected. The influence of the material strength can be seen and both materials gave relatively little material yielding. However, one should bear in mind that a homogeneous material is used and that no internal cracks of the concrete were incorporated into the model. Therefore, before one can make a proper evaluation of the dam, it is necessary to clarify the condition of the concrete; this is best done by drilling cores at strategic positions.

From these calculations it can be concluded that the dam would not fail due to material yielding even if the material strength were to be as low as 1.5 MPa. The calculations also reveal that the risk of the dam suffering a vital crack that could cause failure is relatively small. For this dam the critical risk of failure is sliding.

It should be kept in mind that this dissertation concentrates on DP material strength and yielding behaviour, and not on a comprehensive dam safety evaluation. In dam safety evaluations, several other safety factors should be considered. For example, the high silt level in the dam has a significant influence on the pore-water pressure at the base of the wall. As already mentioned, the position of possible cracks in the concrete is important. The existing geology and foundation condition and the material properties play an important role in determining the FOS against sliding. Seismic analysis and temperature loads are also important aspects to consider in the final evaluation of the stability, but were not performed for this analysis.

5.3 Case History: Proposed De Hoop Dam

The proposed De Hoop Dam used as a case study in this section was chosen because it is a recently designed dam, designed in accordance with the latest design criteria, and was reviewed by a panel of internal and external dam specialists in South Africa. The shape of the dam was, however, optimised by the classical method in agreement with the recommended design memorandum (RDM) of the De Hoop Dam Professional Design Team (2005). Figure 5-23 is an artist's impression of the proposed De Hoop Dam which includes a small-scale plan view at the top and a photo impression of the downstream view of the wall at the bottom.

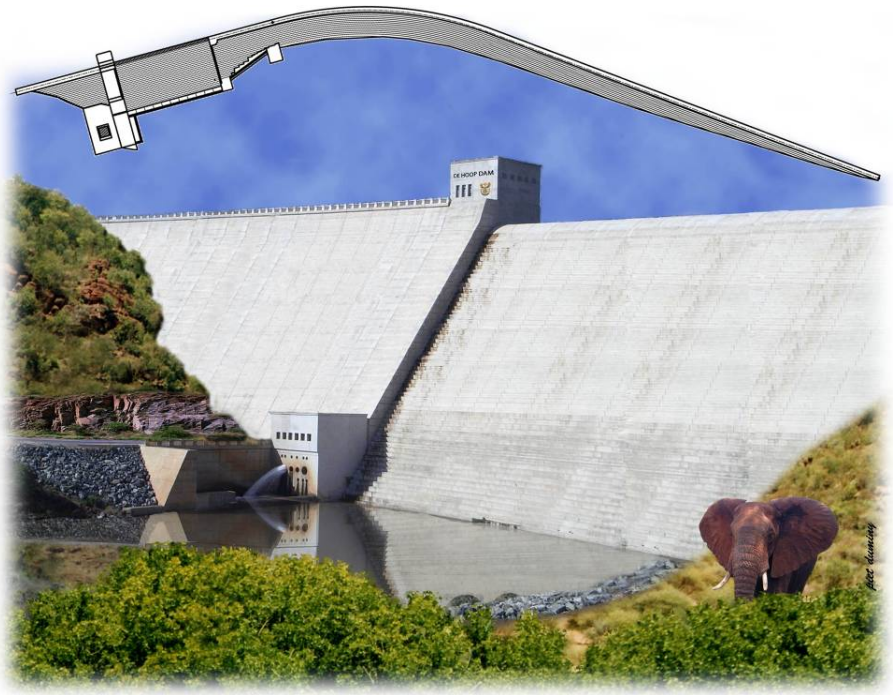

Figure 5-23: De Hoop Dam: artist's impression of the proposed gravity dam

The information of this dam relating to the design of an RCC wall is readily available. The object was to see how the results of the NL DP yield model would appear for this dam's geometry and material parameters. A comparison can also be made with the standards of the

classical method as they are available from the internal design reports for the dam (De Hoop Dam Professional Design Team, 2007a,b).

What is unique about this study is that the normal or short-term material properties were used as well as the residual or long-term material properties to analyse this dam. The residual material properties were taken directly from De Hoop Dam Professional Design Team's (2007a). They were actually intended for use in the classical method and are thus very conservative values for the FEM.

Both linear and non-linear DP FEA was done. For the purpose of this dissertation, not all the load conditions are included that were used in the original design of the dam, but only those that are related to the topic of this dissertation, i.e. the NL DP material yield model.

The geometry was created at the deepest section of the riverbed, where the wall was 75.0 m high, and the spillway section was chosen as it would illustrate the position of the maximum stresses. The geometry of the gallery was left out for the purpose of this study as it will have very little effect on the stresses at the heel of the wall created by the hydrostatic pressures. Figure 5-24 shows the basic geometric shape and dimensions.

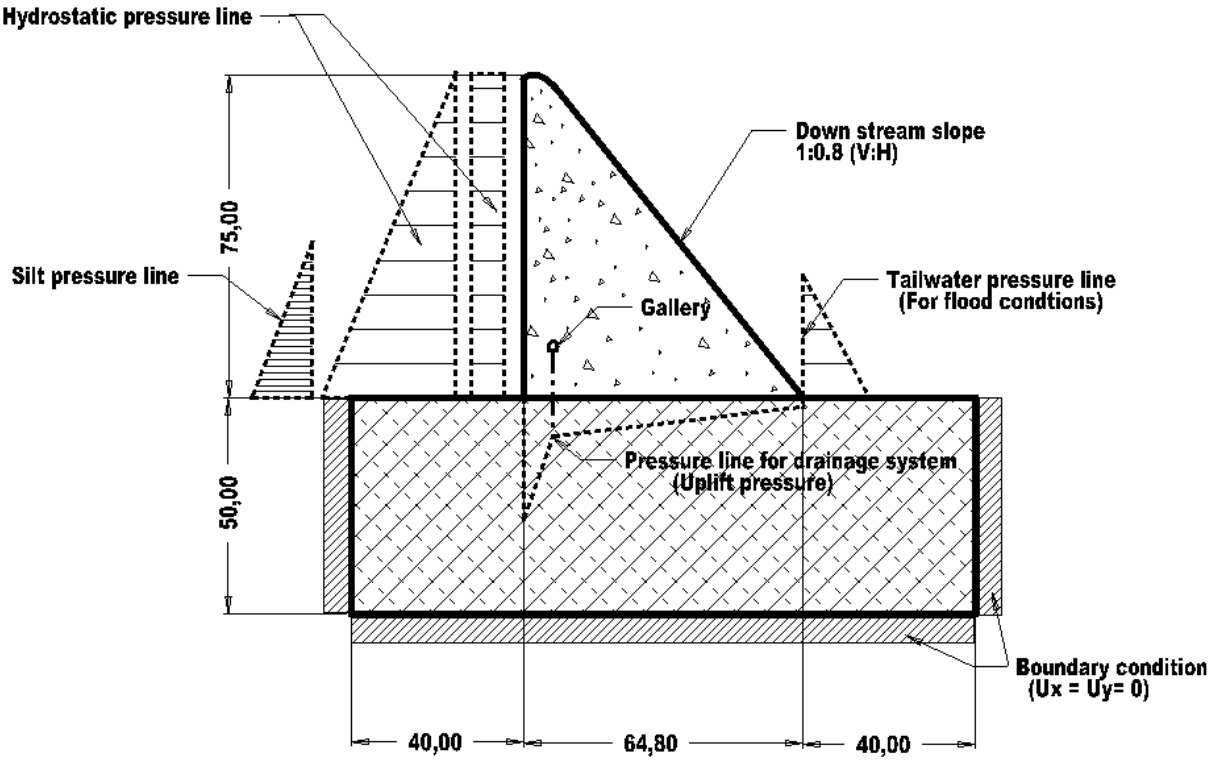

Figure 5-24: Geometry, boundary conditions and pressure loads of the De Hoop Dam

5.3.1 Finite element mesh

The finite element mesh was created with a high mesh density to illustrate the NL DP material behaviour. Two-dimensional plane strain, second-order, isotropic quadrilateral elements were used to model the spillway section. The element size at the heel of the wall is approximately 0.5 m and this was scaled up away from the heel where the tensile stresses fade away. High stresses and singularity effects are expected at the heel of the wall and the object is to see how the NL DP analysis will deal with this problem.

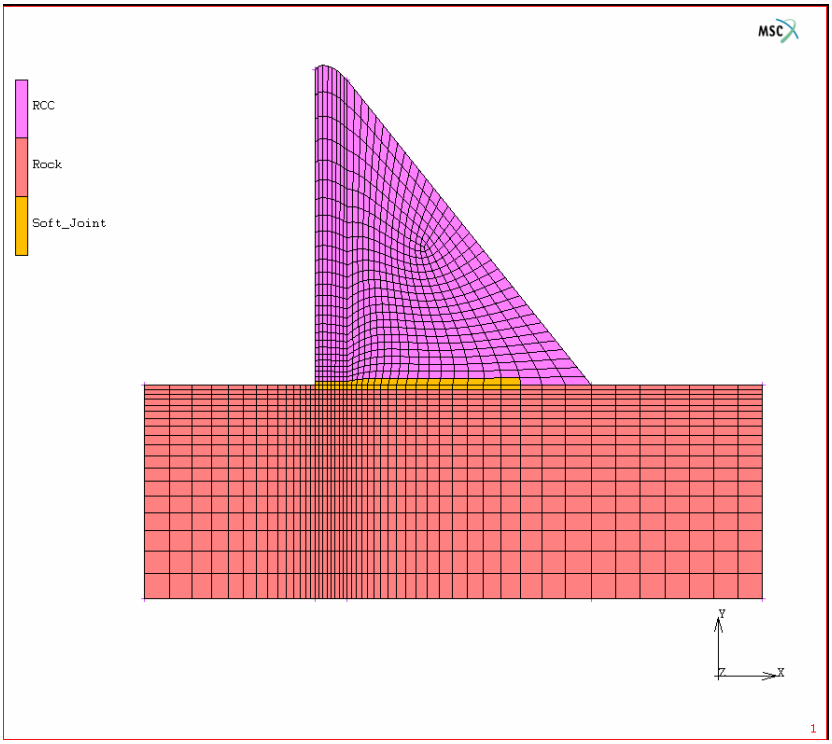

Figure 5-25: Finite element mesh of the wall, foundation block and soft joint

A foundation block was modelled so that the material yielding that could be expected in the rock material could also be examined. This aspect of the study was included to evaluate the stress along the concrete rock interface which has a significant influence on the sliding resistance of the wall. A horizontal baseline was chosen here because the actual dam will be constructed on a straight mass concrete foundation base. The base thickness varies between 2 and 4 m and follows the solid rock line. The analysis by means of the classical method was also performed on a horizontal line.

5.3.2 Boundary conditions

The structure was restricted on the circumference of the foundation block in the x and y directions, i.e. $U_x = U_y = 0$ (see Figure 5-24).

5.3.3 Material properties

The following comparisons of material strength were conducted for this exercise:

For the concrete in the wall:

- Normal (short term or peak)
- Residual (or long term)

Foundation:

- Hard
- Fractured foundation material effects

The material properties for the non-linear Drucker Prager analyses were defined for normal (also called peak) strength, as well as for long-term (also called residual) strength. Similar to the classical method, the residual material strength analysis is done to examine the long-term stability, i.e. for material properties of concrete that have withstood water pressure for 50 years and longer with a fully developed phreatic line from the upstream to the downstream side.

At this stage little information is available on these material properties. However, a first approximation was done by choosing a very low tensile residual stress of $f_t = 0.2$ MPa after personal communication with Dr Oosthuizen (2007) on acoustics emission laboratory tests on long-term saturated concrete strength. One of the objects of this analysis was to observe the behaviour of the structure under such extremely low material strength. Statistics of tensile stress from drilling samples on old DWAF dams have, though, shown relatively high tensile stresses (between 2 and 3 MPa). See Section 4.8, which demonstrates that this is a very conservative assumption.

The concrete material properties were taken from the Material Laboratory Report (De Hoop Dam Professional Design Team, 2007a) in which the concrete mix designs are specified. A concrete of an average strength of 15 MPa was specified. The maximum allowable tensile stress was calculated from the ratio given in Sections 4.7.2 and 4.8, i.e. an average ratio of 1:10 (tensile: compression).

Concrete:

Non-linear static material properties:

Modulus of elasticity (E_c)	20 000 MPa
Poisson's ratio (υ)	0.22
Density (ρ)	2 450 kg/m³

Properties for sliding stability:

This information is taken from the De Hoop Dam Professional Design Team's (2007b) report on the stability of the wall. The properties are only for the contact zone.

Friction angle (φ)	40º
Cohesion (c')	0.6 MPa

Drucker Prager parameters:

Normal and long-term compression stress f_{cc} = 15.0 MPa
Normal (peak) tensile stress f_{tc} = 1.5 MPa
Long-term (residual) tensile stress f_{tc} = 0.2 MPa

From Equation 3-36 and Equation 3-37 the material parameters are calculated:

f_{tc} = 1.5 MPa: Drucker Prager parameters α_c = 0.2466 and $\overline{\sigma}_c$ = 2.1356 MPa
f_{tc} = 0.2 MPa: Drucker Prager parameters α_c = 0.2829 and $\overline{\sigma}_c$ = 0.2980 MPa

Rock foundation:

For the purpose of this dissertation a slightly weathered rock material property was chosen. The value selected for the deformation modulus of rock was taken from the geology report for De Hoop Dam by Davies (2006), as well as from the author's personal experience of previous dam analyses in the Department of Water Affairs and Forestry.

The modulus of elasticity for unweathered hard rock is approximately 25 GPa. For weaker rock conditions, however, this can vary between 5 and 15 GPa, depending on the fracture condition of the rock. An average value of 10 GPa was used.

For the sensitivity study two limits were chosen, i.e. for a solid type of rock and a fractured type of rock. The aim of the exercise was to investigate the progression of the yielding.

Foundation properties:

Modulus of elasticity (fractured) (E_r)	10 000 MPa
Poisson's ratio (υ)	0.25
Density (ρ_r)	Zero

Drucker Prager parameters:
f_{tr} = 1.5 MPa: Drucker Prager parameters α_r = 0.2466 and $\overline{\sigma}_r$ = 2.1356 MPa were calculated from Equation 3-36 and Equation 3-37.

Joint at the base of the wall:
A joint was made with different materials along the base of the wall to examine the effect of a limited zone made of a weak material. The reason a joint was also modelled was so as not to have a whole wall structure with a weak material of f_{tc} = 0.2 MPa, which would not be a realistic representation of the actual structure. Approximately half the base was made with a row of two elements in the vertical direction to simulate a weak material joint. The f_{tc} = 0.2 MPa material strength was used in the joint and the rest of the wall was modelled with the same material properties as the RCC, i.e. a f_{tc} = 1.5 MPa.

5.3.4 Assumptions for the non-linear analysis

The material strength (f_t) of the concrete and rock are assumed to be the same for the purpose of this study (although the stiffnesses vary) and will illustrate how the non-linear yielding will act in both materials simultaneously and how the stress will dictate the direction that the yielding will follow.

From the equivalent plastic strain contour plots the area where material yielding will occur can be visualised. This gives an indication of where cracking could be expected. The reader should note that this is not a fracture mechanics crack analysis, but an ideal elastic plastic non-linear yield analysis.

Section 3.6.7 gives the theory of the DP method used. An Excel spreadsheet was programmed to calculate the parameters for the different DP material flow models. These flow models were benchmarked and calibrated previously in this dissertation for mass concrete materials.

The factor of safety (FOS) against sliding was calculated from the Coulomb friction theory and adapted for the Van Ryneveld's Pass Dam (see Equation 5-1 in the previous section).

$$FOS_{sliding} = \frac{\sum c`.A + \sum (R_y . \tan \Phi)}{\sum H}$$ **Equation 5-1**

5.3.5 Load cases for the non-linear analysis

With the non-linear analysis, the load conditions are applied in time steps. This is necessary to obtain the correct stress distribution throughout the structure for the material yielding. The time steps are as follows:

1st time step – the gravity load is ramped up.
2nd time step – the hydrostatic pressure is ramped up from empty to FSL.
3rd time step – the uplift pressure is applied as well as the silt load.
4th time step –the water overspill is ramped up from FSL to SEF and the corresponding tail-water pressures are applied.

See Table 5-13 for the load steps in tabular format.

Table 5-11 was prepared to illustrate all the relative water elevations for the different load conditions.

Table 5-11 should be read with Figure 5-24 and gives the water height for each flood condition for the upstream and downstream sides. The information is taken from the De Hoop Dam Professional Design Team's report (2007b).

Table 5-11: Water height for flood conditions (De Hoop Dam Professional Design Team, 2007b)

Flood condition	Upstream water height [m]	Tail-water height [m]
FSL	75.0	0.0
RDF	77.9	17.0
SEF	81.5	23.4

Silt load:

The silt level is 40 m above the foundation level and represents the 300-year long-term operation (De Hoop Dam Professional Design Team, 2007b).

Table 5-12 represents the load cases for the Drucker Prager material elastic plastic yield model. All these load cases are incorporated in the single non-linear FE analysis because the loads are ramped up from zero to maximum during the individual time steps as described above. A minimum operating level was also included to examine an empty dam condition.

Table 5-12: Load cases for the Drucker Prager model

Load category	Load case	Hydrostatic loads							
		FSL	RDF	SEF	TW	Silt	Gravity	Uplift pressure	
								Partial uplift	Full uplift
MOL	**NL-0**						x		
Service	**NL-1**	x			x	x	x	x	
	NL-2		x		x	x	x	x	
Abnormal	**NL-3**	x			x	x	x		x
	NL-4		x		x	x	x		x
	NL-5			x	x	x	x	x	
	NL-6			x	x	x	x		x
Long term (residual)	**NL-7**	x				x	x	x	
	NL-8		x		x	x	x	x	
	NL-9			x	x	x	x	x	

Note. MOL = Minimum operating level
Partial uplift is with drainage and
Full uplift is without drainage.

(Although load cases NL5 and NL9 have the same load conditions, they have different material properties in order to compare the sensitivity of material strength to the stress results in the wall.)

Table 5-13: Time step loading for the non-linear analysis

Time step	Water level	Activity (ramp up load condition from min to max.)
0-1	Zero	Gravity
1-2	0 to FSL	Water pressure
2-3	Constant FSL	Pore water pressure and silt load
3-4	FSL to SEF	Water pressure and corresponding tail water

Note: The pore pressure and silt are kept constant during steps 2-3 and 3-4.

For comparison, to illustrate the high stresses caused by the singularity effects, a linear analysis was also prepared.

5.3.6 Results

The results of the NL FEA are presented in Table 5-14 and the most relevant contour plots are shown in Appendix D. The results are presented in the same order as the load cases in Table 5-12

The results of the non-linear analysis are very useful for examining the structural behaviour and material integrity for normal and long-term (residual) material properties. The non-linear analysis also reduces the stress peaks at critical positions where singularities are a problem in high-density meshes.

The results are presented for the both the hard and soft foundations (see discussion in Sub-section 5.3.3 on foundation rock).

The results presented in Table 5-14 are the final stress values of the time steps representing the hydrostatic pressure conditions. This is for the hard rock foundation properties.

Table 5-14: Results of the DP analysis with f_t = 1.5 MPa and solid foundation E_r = 25 GPa

Load case	Resultant displacement at crest [mm]	Normal stress at the heel of the wall: Sx [MPa]	Normal stress at the heel of the wall: Sy [MPa]	Principal stress at the heel of the wall: S1 [MPa]	Principal stress at the toe of the wall: S3 [MPa]
NL-0 (MOL)	-7.43	0.282	-5.40	0.360[1)]	-6.39
NL-1 (FSL_{PU})	5.63	1.46	1.21	1.60	-2.42
NL-2 (RDF_{PU})	7.02	1.49	1.27	1.60	-2.42
NL-3 (FSL_{FU})	5.63	1.46	1.21	1.59	-2.41
NL-4 (RDF_{FU})	7.30	1.46	1.42	1.63	-2.41
NL-5 (SEF_{PU})	10.59	1.50	1.56	1.66	-2.92
NL-6 (SEF_{FU})	11.03	1.56	1.70	1.72	-2.93

Notes. 1) The maximum principal stress S1 of the MOL conditions is not at the heel of the wall but approximately 1.5 m upstream on the foundation level.
+ Stress value is tension.
- Stress value is compression.
The subscript PU is partial uplift, i.e. with underdrainage, and
FU is full uplift, i.e. without underdrainage.
Negative displacement refers to an upstream movement for the MOL load condition.

Table 5-15 represents the same load conditions as in the previous table but for a fractured foundation material. This analysis was conducted to see what influence the foundation stiffness would have on the general stress distribution.

Table 5-15: Results of the Drucker Prager analysis with f_t = 1.5 MPa and fractured foundation properties

Load case	Displacement at the crest [mm]	Normal stress at the heel of the wall: Sx [MPa]	Normal stress at the heel of the wall: Sy [MPa]	Principal stress at the heel of the wall: S1 [MPa]	Principal stress at the toe of the wall: S3 [MPa]
NL-1 (FSL_{PU})	8.70	1.51	0.73	1.55	-3.44
NL-2 (RDF_{PU})	11.25	1.49	1.14	1.60	-3.68
NL-3 (FSL_{FU})	9.21	1.48	1.08	1.58	-3.33
NL-4 (RDF_{FU})	11.25	1.50	1.34	1.59	-3.65
NL-5 (SEF_{PU})	16.40	1.46	1.43	1.63	-4.53
NL-6 (SEF_{FU})	16.38	1.47	1.43	1.63	-4.53

The S_x stress in Table 5-15 load cases 2 and 6 decreased slightly with an increase in the hydrostatic load. This was controlled by doing a history plot through the time steps. It was also seen that the S_x stresses vary by a small amount. The only reason for this could be identified that during the last phase the tailwater was applied on the downstream side of the wall. The S_y stress, however, increases and his would indicate that the tailwater had insignificant effect on the S_y stress.

The values in Table 5-16 represent the stresses of a very weak material to simulate a very old structure with a fully developed phreatic pressure distribution. This is an extreme condition and is included to examine a long-term (residual) material property relating to the behaviour of the structure. Three load cases are represented to illustrate the structural behaviour.

Table 5-16: Results of the Drucker Prager analysis with *ft* = 0.2 MPa throughout the whole structure

Load case	Displacement at the crest [mm]	Normal stress at the heel of the wall: Sx [MPa]	Normal stress at the heel of the wall: Sy [MPa]	Principal stress at the heel of the wall: S1 [MPa]	Principal stress at the toe of the wall: S3 [MPa]
NL-7 (FSL_{PU})	6.125	0.321	-0.215	-0.350	-2.45
NL-8 (RDF_{PU})	7.87	0.347	-0.193	-0.330	-2.75
NL-9 (SEF_{PU})	12.88	0.300	-0.272	-0.330	-3.60

It was observed that the Sx and S1 values in load case 9 decreased with an increase in the hydrostatic load. A history plot was made to check the stresses in the load cases as given in Table 5-16 and it could be seen that the stresses varied through the time steps. These variations in stress are due to the tailwater that was applied on the downstream side of the wall. The stresses S1, S3 and Sy were included in Figure 5-26 for comparison. It should also be noted that the stresses S1 and Sy were taken at the heel of the wall and the S3 stress was measured at the toe of the wall.

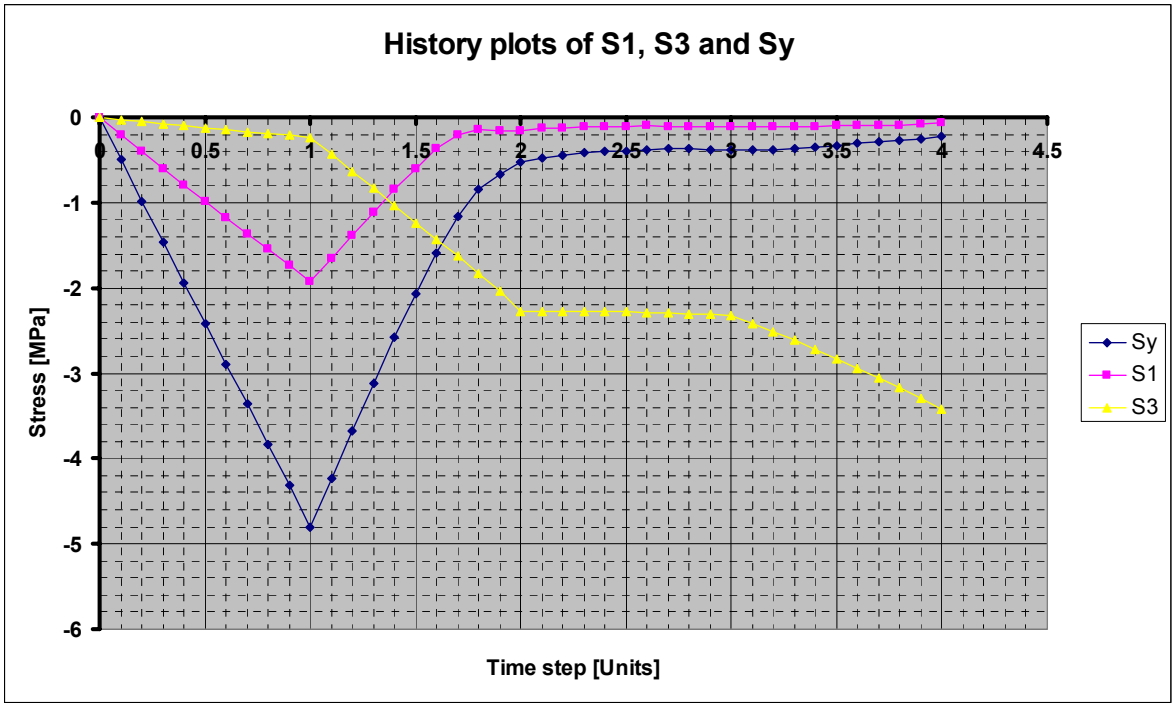

Figure 5-26: History plot of the S1, Sy and S3 stresses for f_{tc} and f_{tr} = 0.2 MPa

In interpreting the curves in Figure 5-26 it should be noted that all the stresses, including the principal stress S1, are in compression. The value of f_{tc} = 0.2 MPa represents such a weak material that failure started already in time step 2, which represents the uplift pressure stage. The DP NL FE model has the ability to redistribute the tensile stress to compression stress as the material yields through the time steps. Later in this section the S_y stress distribution along the base of the wall will be illustrated and used to calculate the $FOS_{sliding}$.
Figure 5-27 illustrates the displacement of the crest to examine the effect of the load conditions at each time step. The curves represent the short- and long-term (residual) material strengths. The curves were plotted for a low-strength wall and a soft joint. The joint was included to model a more realistic state of the residual material distribution because the contact zone is more likely to deteriorate with time and there is a possibility of water penetration in this area.

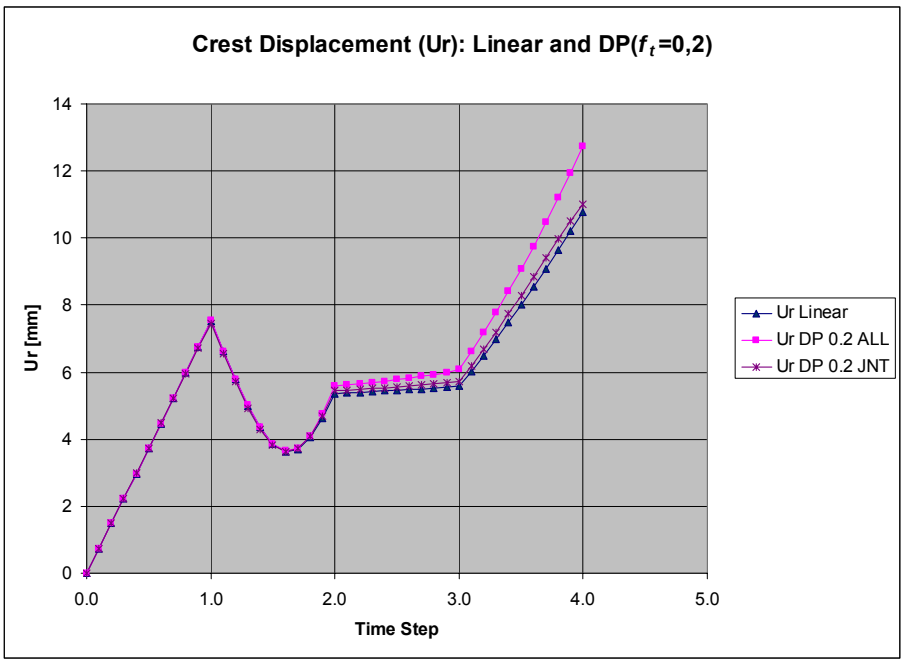

Figure 5-27: Time steps versus resultant crest displacement (Ur) for linear and Drucker Prager f_t = 0.2 MPa

The difference between the long-term and normal material strengths gives a resultant displacement of approximately 2.1 mm at the crest of the wall.

Figure 5-28 presents the same information as Figure 5-27, but relates to the water level in the dam. Note that the first time step is for an empty dam condition where the structure's displacement progresses in an upstream direction, with a displacement of 5 mm as the gravity load is ramped up. See Table 5-13 for an explanation of the load steps.

The results for the three load cases are shown in Figure 5-28, i.e. linear, NL (f_t = 1.5 MPa) and NL (f_t = 0.2 MPa). The linear analysis was included for comparison with the non-linear analysis to examine the influence of the different yielding models of the concrete.

The aspect pore pressure or uplift pressure under the dam is discussed in response to the recent paper by Watermeyer (2006) on uplift pressure and gravity dams. In this dissertation the uplift pressure was added to the base of the wall during a specific time step following the upstream hydrostatic pressure. The alternative was also examined: subtracting the pore pressure from the resultant stress (S_y) caused the hydrostatic pressure. This, however, caused the material to yield incorrectly because the stress was relieved at an earlier point. With the FEM the more correct procedure is to use poro-plastic elements that deal automatically with pore pressures and predict the correct material yielding. This theory is complex and falls outside the scope of this dissertation. The author is of the opinion that the load-stepping method is an acceptable approximation for most dam analyses. The effect of pore pressure could also be simulated by varying the density in the wall to represent the uplift effect. However, little research has been done in this field to date. With very old dams in which a fully phreatic condition has progressed, the poro-plastic elements should be considered.

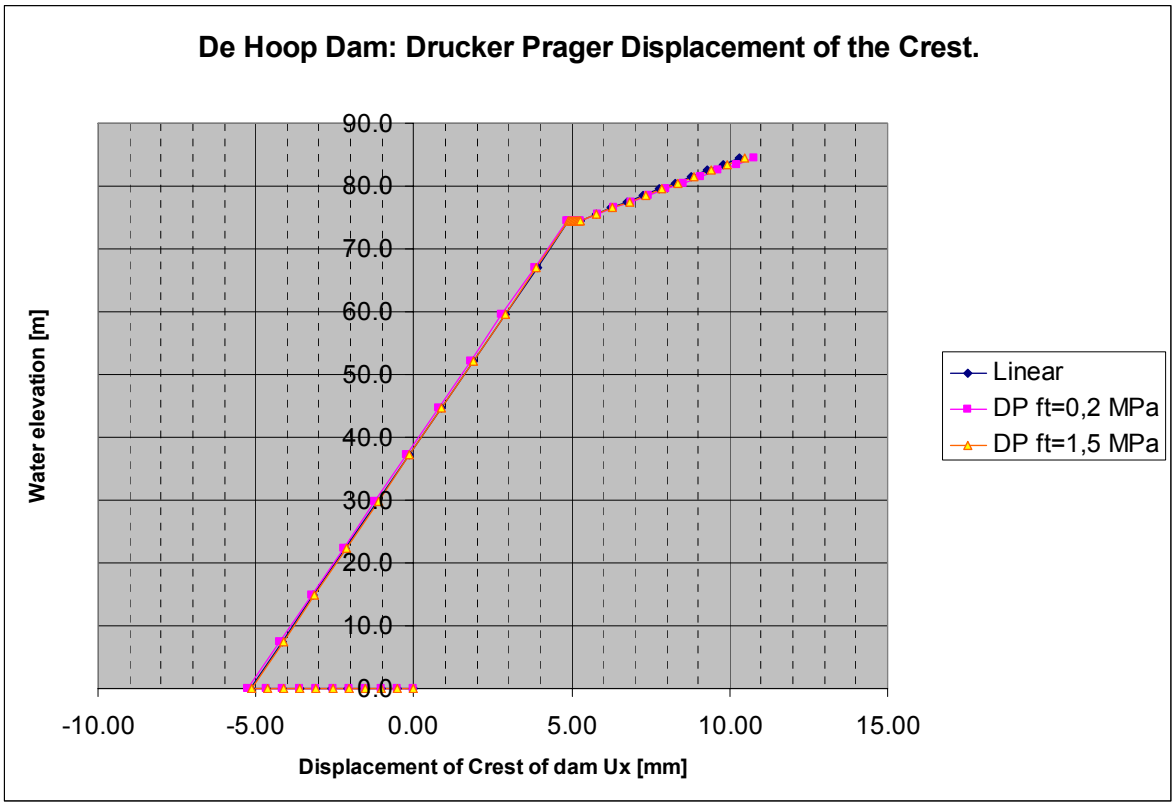

Figure 5-28: Displacement of the crest versus water level in dam for short- and long-term material strength

Very little variation is seen between the displacement of the linear and non-linear (f_t = 1.5 MPa) cases. No material creep is included in the non-linear analysis and the additional displacement for the long-term condition is based purely on the yielding of the material.

The results in Figure 5-26 to Figure 5-28 can be interpreted as follows:

The first two figures are related to the time steps and are types of history plot for the displacement of the crest and stress at the heel and toe of the wall. It can be seen that the yielding of the material has a stabilising effect on the stress plot and that the stress increase stabilises. However, the displacement tends to increase as the material yields and also the displacement of the weaker material increases more rapidly than the other material. The deviation between the linear and DP curves is an indication of the material failure.

Figure 5-28 gives more or less the same information as the previous figure but is plotted against the water level. During the first step, only the self-weight is applied to the wall and the displacement decreases with no increase of water. During the second step, the upstream water load is applied and the displacement increases with the water load. It can be seen that no or very little material yielding occurs for the curves that follow the linear analysis curve. When the uplift pressure is applied, the water level stays constant, with a small increase in displacement. During the high flood level (HFL) loads, the effect of the material yielding can be seen.

Factor of safety (FOS) against sliding:
The FOS was calculated on a spreadsheet and based on Equation 3-3 in Sub-section 3.1.3. For each value of S_y for each element along the base of the wall, the shear resistance was calculated and added together to obtain the total resistance:

$$FOS_{sliding} = \frac{\sum c`.A + \sum (R_y . \tan \Phi)}{\sum H} \qquad \text{Equation 5-1}$$

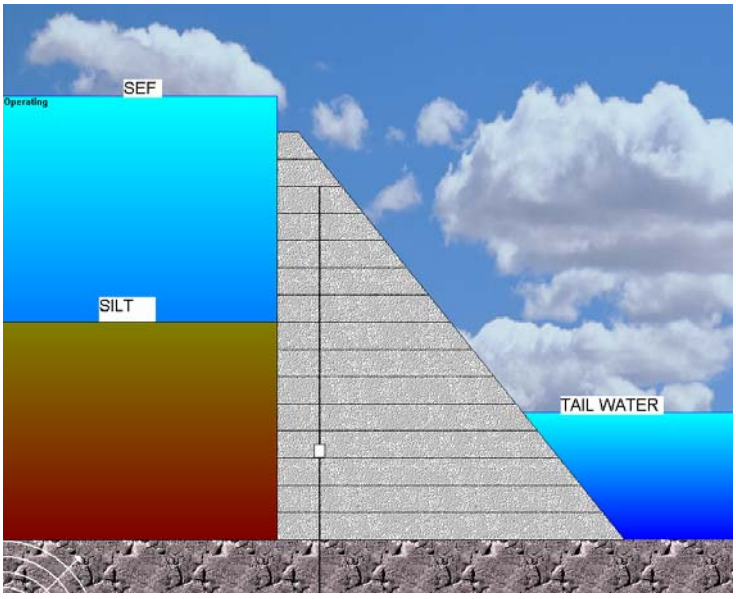

Figure 5-29: Presentation of the gravity dam load conditions (CADAM User's Manual, 2001)

The FOS against sliding was calculated for the non-linear (f_t = 1.5 MPa) material strength and for a severe load condition, i.e. the safety evaluation flood (SEF) condition, and the partial uplift condition.

$$FOS_{sliding} = 2.25 \ (f_t = 1.5 \text{ MPa})$$

The influence of the friction parameters can best be illustrated by using the so-called 'failure domain principle'. This graph was created using a similar method to that used for the failure domain graph in Figure 5-30 for the Van Ryneveld's Pass Dam, i.e. by iterating the values of c' and φ to achieve FOSs of 1.0 and 2.0 by keeping one of the parameters constant at zero. The coloured zone is the safety domain of the classical method.

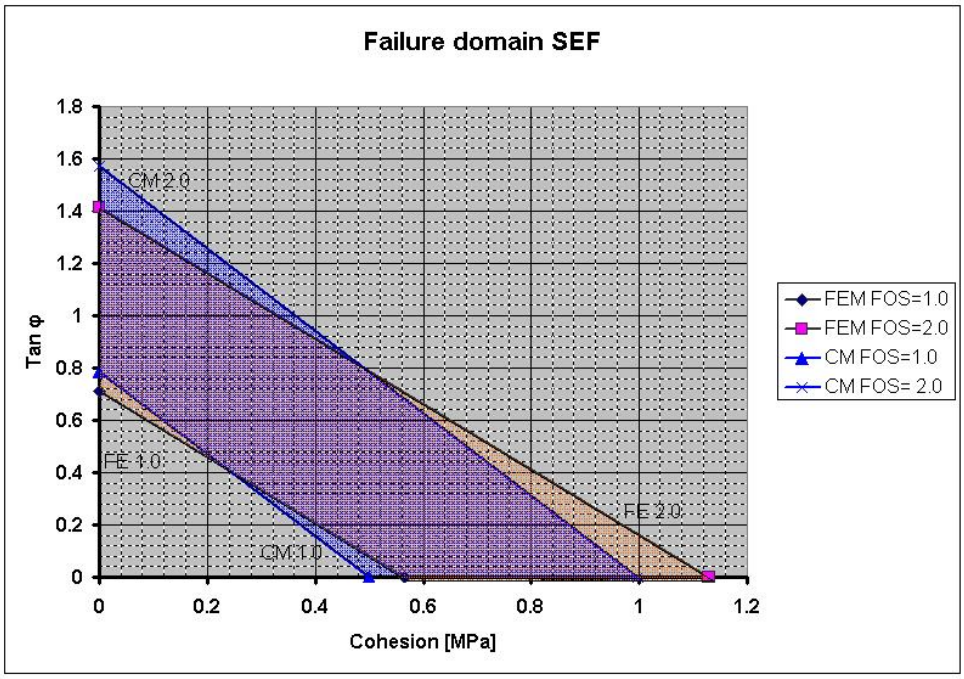

Figure 5-30: Failure and safe domain for the f_{tc} = 1.5 material for $FOS_{sliding}$ = 1.0 and 2.0 for the SEF load condition

This failure domain graph is useful in that if there is uncertainty about the values for φ and c', the graph in Figure 5-30 can be used to do a sensitivity study to see whether the dam is safe. This is especially useful with back analyses for dam safety evaluations where the parameters are not available. For the De Hoop Dam, the values of tan φ = 0.84 and c'= 0.60 MPa are used for the design and from Figure 5-30 it can be concluded that the $FOS_{sliding}$ falls beyond the 2.0 curve and can therefore be considered as safe.

From Figure 5-31 it can be seen that the maximum principal stress (S1) is 6.0 MPa for the linear case and that this high stress is reduced to 0.2 MPa by the DP yield model for the SEF

load case. The equivalent plastic strain indicates the area where the material failed (see Figure 5-33, NL (SEF_{PU}): equivalent plastic strain for the f_{tc} = 1.5 MPa).

In Figure 5-31 the three different material models are plotted together for comparison purposes. They are all extracted from the high-density mesh, hence the high stress value of 6 MPa for the linear case.

The long-term stress S_y is almost constant and only ties in with the other cases after a chainage distance of 20 m, while the other two cases match up after about 5 m.

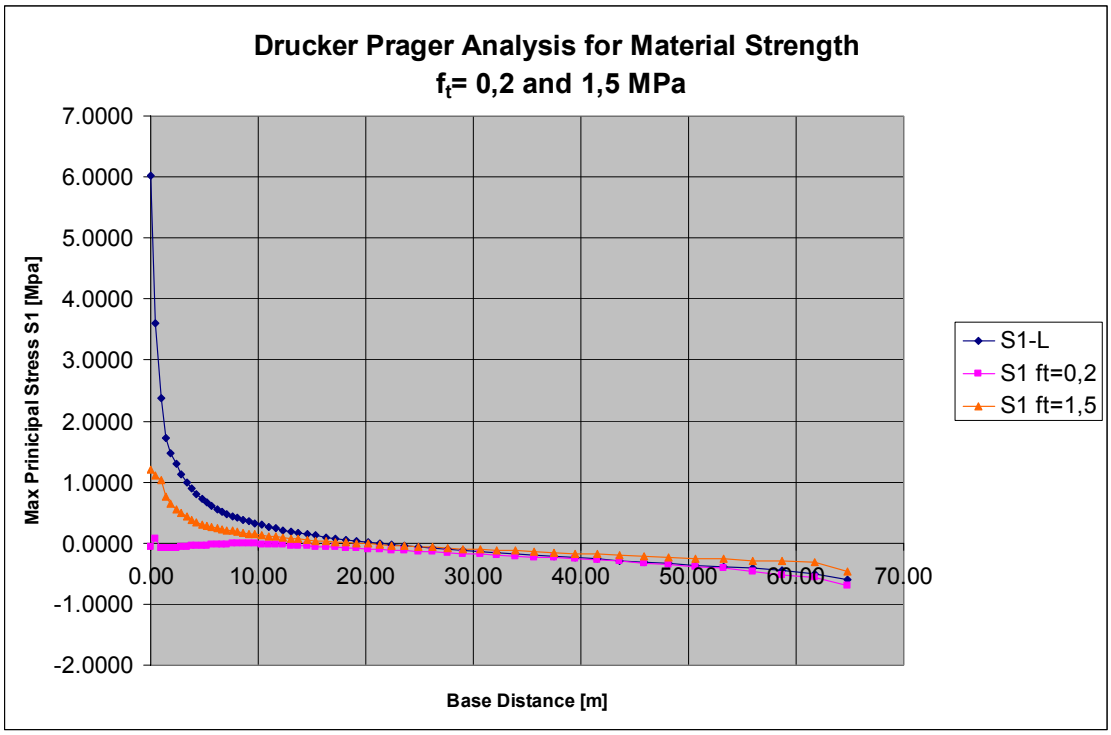

Figure 5-31: Comparison of the results of the max. principal stress (S1) of three material models for the load conditions SEF and partial uplift

Figure 5-32 to Figure 5-35 are included to illustrate the material yielding of the DP material model.

Figure 5-32 and Figure 5-33 represent the EQPS for a material strength of f_{tc} = 1.5 MPa, which is the design strength of the dam.

Figure 5-34 represents the EQPS for a residual strength of f_{tc} = 0.2 MPa, which can be regarded as the worst-case scenario when the concrete is totally depleted. The author is of opinion that the value is realistic for the classical method but is too conservative for the FEM. It was, however, included because the acoustic emission results of some specimens gave such low strength values (Oosthuizen, 2007).

Figure 5-35 was included to represent a condition where only the material at the contact point between the concrete and the foundation deteriorates heavily to a very weak material with a strength of f_t = 0.2 MPa.

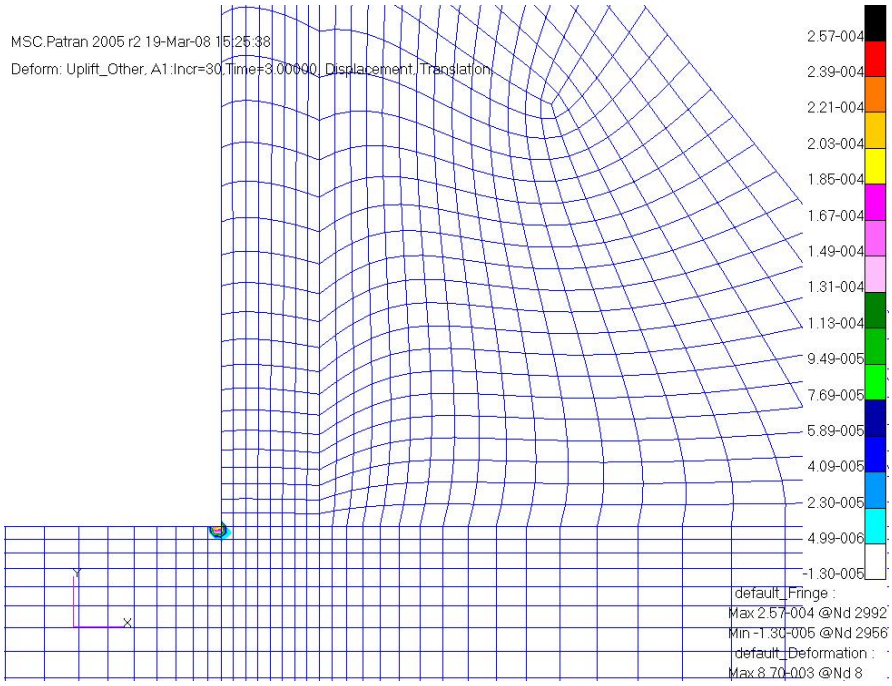

Figure 5-32: Equivalent plastic strain for the FSL condition with partial uplift. (f_t=1.5 MPa)

Figure 5-32 shows the equivalent plastic strain for an FSL with partial uplift service load condition. The yield path is very much localised, approximately 1.5 m long and dipping into the foundation rock.

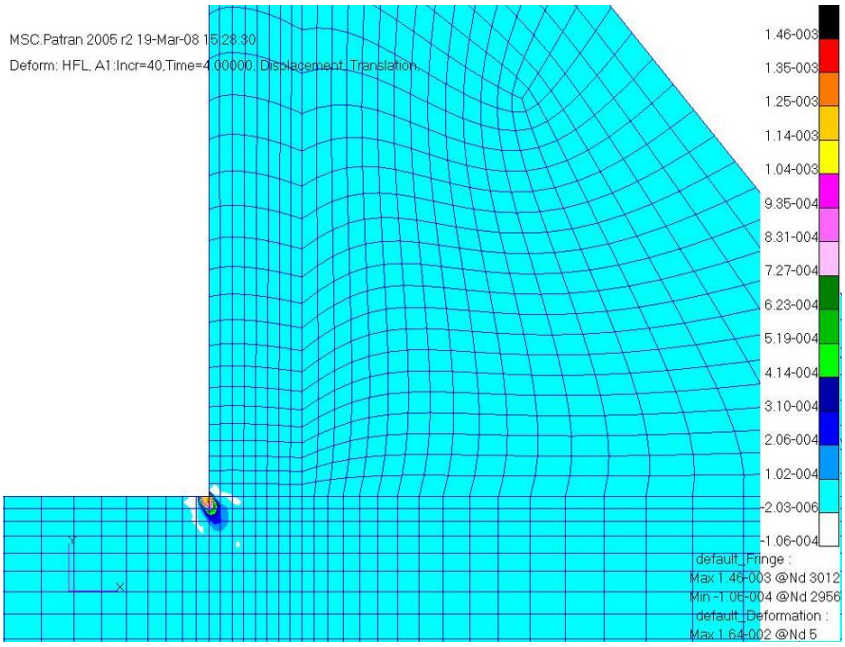

Figure 5-33: Equivalent plastic strain for the SEF condition with partial uplift. (f_t=1.5 MPa)

Figure 5-33 illustrates the equivalent plastic strain for an SEF with partial uplift, for a severe load condition. The yield path is still very much localised and approximately 2.5 m long, which represents approximately 3.8% of the base length.

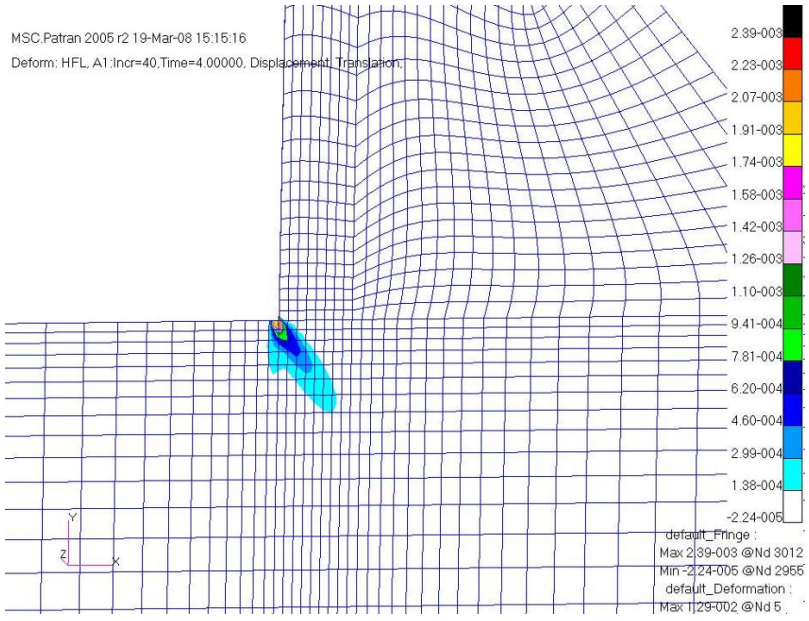

Figure 5-34: Equivalent plastic strain for the SEF condition with partial uplift (f_t=0.2 MPa)

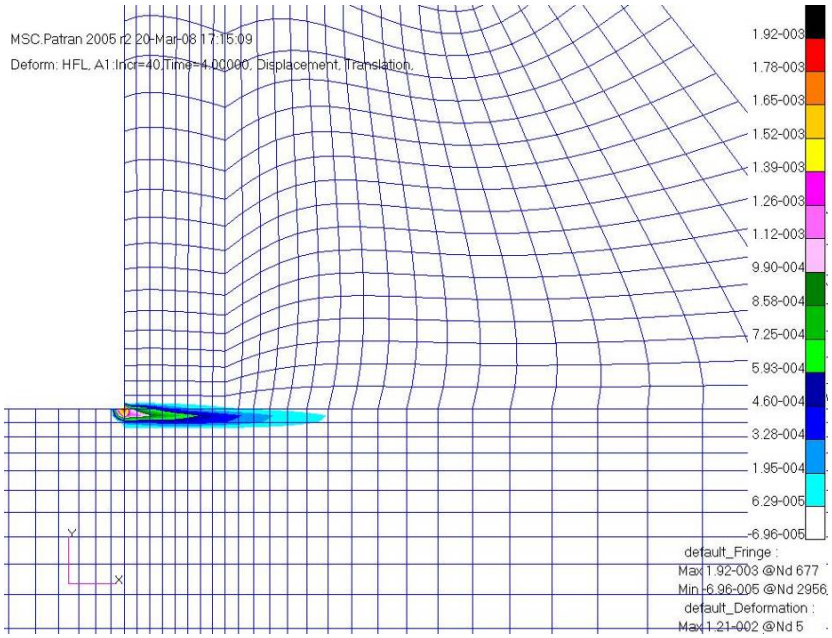

Figure 5-35: Equivalent plastic strain for a weak joint for the SEF condition with partial uplift (f_t = 0.2 MPa)

The progression of DP material yielding model from Figure 5-32 to Figure 5-35 is clear. The residual material is a worst-case scenario.

In this analysis the concrete and foundation materials were the same and it can be seen that the EQPS dips in the foundation at an angle of 45º (see Figure 5-34). For the worst-case scenario it can thus be concluded that the cracks would dip into the foundation for approximately 15 m. However, because the cracks dip into the foundation, this would not endanger the wall structure. The last scenario where the residual material is localised in a joint region is a more realistic approach and will give a conservative $FOS_{sliding}$ because the effective length of the contact base will be reduced by the predicted virtual crack length.

5.4 Conclusion

Various FEM tools have been illustrated in the case study of the De Hoop Dam. In this study it has been illustrated that the FEM can be utilised as a design tool and is superior to the classical method in that a more accurate indication of the stress distributions is obtained. A method has also been illustrated for determining the FOS against sliding. A graph of the failure domain has also illustrated and the finite element method has compared with the classical method. In this case the two methods compared well with each other, although the classical method gave a more conservative failure range.

6 PROPOSED METHODOLOGY

On the basis of these studies, a methodology for the analysis of gravity dams is proposed. The methodology consists of the following steps:

- **Step: General information to be considered in order to perform an FEA**

Chapter 4 gives some useful hints and guidelines on preparing an FE model. Some of the guidelines relate to understanding the engineering problem:

- ❖ Get the overall picture of the approximations and assumptions made to simulate the problem; this will include the choice of elements and mesh size.
- ❖ Understand the structural behaviour of the wall to be able to evaluate the results of the FEM.

- **Step: Geometric modelling**

Modern FE programs have powerful pre-processors which link with a range of sophisticated CADD programs and these days the geometry of solid models can easily be translated into the pro-processor to create FE meshes.

- **Step: FE mesh density or mesh size**

Different mesh densities should be created for linear or non-linear analysis. For a gravity dam it is advisable to model a high-density mesh for a non-linear analysis. However, if there are restrictions such as limited disk space, long processing time or a limited FE program, a linear FE model could be created. When linear FEA is used, care should be taken to deal with the stress peaks caused by singularities, as dealt with in Section 4.5. For linear static analysis it is advisable to create a coarser mesh in order to eliminate stress peaks due to singularities. It is preferable to use quadrilateral (rectangular) elements shapes in the model as they give more accurate results.

- **Step: Material properties**

The most convenient method of determining the non-linear yield model parameters is to use the material stresses and formulation by Chen (1982), as given in Sub-section 3.6.7.

The material properties could be obtained from the following sources:

- o Concrete mix design, as for new dams, or alternatively if the historic data is available from the original construction reports.
- o Actual measured material properties, gathered from core drilling and laboratory samples. (Preferred option for back analyses)
- o Standardised material properties taken from literature or available data base.
- o Calculating the Drucker Prager input parameters, i.e. the σ and α from f_t and f_c as given in paragraph 3.6.7.

- **Step: Benchmark check**

Unless the analyst is experienced, it is recommended that a simple benchmark check be run beforehand to clarify uncertainties concerning the analysis. For example, type and order of elements to be used, element distortion allowable, correct mesh density, type of analysis (plane strain or 3-D), sensitivity of material properties, convergence criteria and tolerances to be used, etc. The benchmarks used in this dissertation or alterative benchmarks available from the literature could be followed. Many serious errors can be avoided by doing the correct benchmark checks and valuable time can be saved.

- **Step: Selection of load conditions**

For linear analysis the load conditions are usually easy to combine because everything is in a linear proportion. The loading order is usually not critical. In most cases the loads can be added to the structure in a single load step. With non-linear analysis the loading order, number of time steps and intervals are significant. It is necessary to ramp up the loads in time steps and load combinations to get realistic yielding conditions. The case studies in Chapter 5 are practical guidelines in this regard.

- **Step: Analysis**

It is useful to do a linear analysis first in order to scrutinise the model and get a first impression of the deformations and stresses caused by the given load cases.

When the input data have been carefully scrutinised in each section of the non-linear FE program and the analysis has been successfully completed, it is necessary to check the output results carefully. An inspection should be done to see whether the analysis has been through all the load steps and whether the convergence has run correctly through the given tolerances.

- **Step: Validate results**

Benchmarking can be useful to compare the convergence steps. The author has learned that although the results may look correct in the beginning, after careful inspection convergence errors are still picked up. It is sometimes useful to run deformation and stress animations through the load steps to interpret the results. The results should be compared with those of previous analyses of a similar nature, if available.

The results should be interpreted in terms of the performance expected from the structure. The structure must be understood and aspects that are critical for examining the safety of the structure must be identified. For example, where will the first critical failure occur and what is the significance of this? Positions where failure occurs are best identified by making contour plots of the equivalent plastic strain (this is where the structure deforms in the plastic zone and is the area where yielding occurs.).

- **Step: Evaluation against safety standards**

During the evaluation of the structure using the classical method, the maximum tensile and compression stresses at the heel and toe of the dam were considered and compared with the permissible stress and FOS against sliding (see Sub-section 3.3.1). To a certain extent the evaluation done with a linear FEA is done in a similar manner, but the permissible stresses are usually much higher. However, no standard has been set because the mesh density has a major influence on the magnitude of the stress and the evaluation of the structure is very much a process of using engineering judgement.

Evaluating the structure by means of the non-linear plastic FEM is different from evaluating it by means of the classical method. The stresses are controlled by the yielding values of the DP NL FE model and in this way the structure is examined for material failure. The material failures in gravity dams are found at the heel of the wall and in the foundation block just upstream of the wall. The failure path is sensitive to the relative stiffness moduli of the wall and foundation. For example, if a high stiffness modulus is accepted for the foundation block in relation to the wall stiffness, the failure path will tend to follow the contact line. On the other hand, if the stiffness of the foundation block is relatively low, the failure path will tend to dip into the foundation. The author has found that if the yield path falls between 5% and 10% of the base width, a special investigation should be done to evaluate the integrity of the structure. This is not a rule but an approximate indication that the structural safety may fall outside the norm. The failure path in relation to the material strength chosen is therefore now the norm for deciding on the safety of the structure.

The FOS against sliding is calculated from the well-known Coulomb theory and the shear resistance is calculated for the portion of the base length where the stresses are in compression, i.e. excluding the virtual crack as exhibited by the EQPS. It is important to do a few trial runs to incorporate the correct pore pressures in the cracked zones of the base. At this stage an iteration process is suggested to compute the virtual crack length and then the full uplift pressure in the cracked zone should be applied. The iteration process should be continued until the crack length stays constant. Usually this is not very sensitive and only a few iterations are necessary.

The contact line between the wall and the foundation can also be modelled to include shear keys and the natural rock profile to arrive at a more realistic shear resistance.

It is advisable to use some alternative methods to check the correctness of the analysis. Since it is a conservative measurement tool, the classical method can be useful as an overall check on the stability of a gravity dam if actual material parameters are used.

6.1 Way forward: 3-D

For many gravity dams the total stability is a result of 3-D structural interaction and the non-linear FEM can be used to model foundation layers with various material properties. In this regard a recent article *3-D Analysis of Gravity Dams* by Lombardi (2007) is very informative.

7 CONCLUSIONS AND RECOMMENDATIONS

The object of this research was aimed to investigating the implications of using the finite element method to design a gravity dam.

7.1 Dam Building Considerations and Practice

In Chapter 2 a basis was laid to illustrate the merit of this research. Dam building practice is a very old science and the evolution of dam design methods has progressed with time. During the last century the design of gravity dams was based on the theory of the classical method.

Dams are very expensive structures to construct and the longevity of a dam is an important consideration. Many dams are utilised for very extensive periods and it is therefore important to evaluate the safety of these structures regularly. In most countries, including South Africa, legislation on dam safety has been introduced to safeguard the public against catastrophic dam failures which are usually disastrous events due to the high hazard potential of the stored water behind the structure. This research on the Drucker Prager non-linear finite element method (DP NL FEM) was done to determine whether the FEM can be used successfully as an alternative method to analyse the behaviour of gravity dams in order to evaluate the safety of the structures. Before an alternative design method can be introduced, however, there should be evidence that the proposed method is reliable.

The risks involved and the cost of safeguarding a dam were also briefly discussed and it was pointed out that these factors have to be played off against each other in terms of the risk a developer is willing to take within the standards laid down by the dam safety legislation. The proposed DP NL FEM can also be utilised to optimise the shape of a gravity dam more accurately.

It was argued that the classical method had to some extent served its time for large gravity dams. The theory of this method is an approximation of the actual structural response of a gravity dam and there are now more advanced techniques available, such as the FEM, for analysing gravity dams. It was shown that the FEM can be utilised as a reliable design tool.

7.2 Limitations and Advantages of the Classical Method

At this stage the so-called classical method or conventional method is used by many dam building organisations to design gravity dams. The limitations and advantages of the classical method were described and it was demonstrated that the limitations overshadow the advantages of this method (Section 3.1) although in many countries informal design codes have been developed around the theory of the classical method, this method is still accepted as a design standard for small gravity dams.

It has been shown in this dissertation that two separate formulas are used to calculate the vertical stress and shear resistance along the base of the wall.

The limitations of the classical method for analysing certain load conditions on a gravity dam are:

- Gives only approximate stress distribution along the baseline of a gravity dam
- Unable to incorporate material properties in the model
- Unable to determine the stresses induced by temperature variations
- Can model only limited foundation conditions
- Can model only very basic seismic loadings (pseudo-static).

The emphasis of this dissertation is on the DP NL FEM material behaviour and thus the temperature and seismic load conditions were not considered.

7.3 Literature Study on the NL FEM

In order to obtain a sound background knowledge of dam design, the relevant literature on the evolution of gravity dam design was studied (Fahlbusch 2001). It is interesting to see how the theory developed up to the existing classical method and how different countries developed dam design codes based on Bernoulli's theory of a shallow beam.

The literature study covered the theory of the classical method (CADAM User's Manual, 2001; USBR, 1976; US Army corps 1995, etc.) as well as some of the old applications in DWAF. A DWAF classical method for raising a gravity dam was also presented which illustrated the proposed load cases and design process. This method could also be utilised in the FEM.

The literature study of the FEM and the NL FEM was compiled mainly from different handbooks on FEM and the more descriptive portions were used to compile the theoretical sections of this dissertation. Some useful FEM formulations of the plane strain elastic matrix are included. In the textbook on FEM by Rockey et al. (1975) the authors give a useful and understandable method to illustrate the basic steps in deriving a finite element stiffness matrix for different types of elements and this was also included.

In order to evaluate and calibrate the DP NL FEM the literature study focused on finding of useful information on NL FEM and yield models. Although much literature was found on the theory, few researchers actually calibrated and benchmarked the DP NL FEM on dams using standardised benchmarks. However, some benchmarks were found in the literature in the fracture mechanics field that could be utilised to calibrate the DP NL FE yield model. Some of these benchmarks were used in Section 4.7 to benchmark the DP NL FEM.

Research results obtained by Reinhardt and Tassilo (1998) on a tension specimen were used to calibrate the basic tensile specimen that illustrated the DP linear plastic behaviour in the model.

Raw laboratory data on the Palawan Dam in Zimbabwe were obtained from Chemaly (2006) with regard to the BS 1881 standard concrete tests. These data were used to do the second calibration which was on a standard beam in bending mode and based on actual laboratory sample results.

The handbook by Chen (1982) allowed a more exact FEM benchmark to be performed on a soil-type material. The results obtained by Chen and by means of the Marc FE program compared well for the DP flow rules.

It was possible to use the research done by Bhattacharjee and Léger (1994) in the fracture mechanics field indirectly to benchmark a similar DP NL FEM on a notched shear beam. The results compared well, although different failure theories were used.

A model gravity dam, 2.4 m high, by Carpinteri et al. (1992) was used to benchmark the first gravity dam. Crack mouth opening displacement (CMOD) in the notch compared well with the experimental values.

The well-known Koyna dam was also benchmarked by Bhattacharjee and Léger (1994) and the FEM used in this dissertation was modelled with the same mesh configuration. Gioia et al. (1994) also benchmarked the Koyna Dam with an NL FEM yield model which correlated well with the DP NL FEM.

In Section 3.6.8 a summary was given of other research work done on the NL FEM. The focus in new research is on fracture mechanics and dynamic analysis. Some related research was found on the internet on the NW-IALAT website, on benchmarks done on dams. From an article by Wieland (2005) it could be seen that the stress peaks caused by singularities are still a problem for dam designers.

In order to calibrate the DP NL FEM material parameters properly, the author did a literature study of gravity dams designed and constructed by the DWAF. Twelve dams were identified with useful information on their concrete properties. The material parameters were analysed statistically and are presented in Section 4.8.

The author is of the opinion that the DP NL FEM can be developed to a more accurate standard with proper benchmarking. The advantage of the DP NL FEM is that the input parameters are relatively simple to determine by laboratory tests. The DP should be developed to include the results of proper research into the strain hardening and softening domain so that crack propagation can be predicted more accurately. The NL DP can also be used in 3-D NL dynamic FEM because of its relatively simple constitutional equations.

7.4 Application of Linear Elastic FEM to Demonstrate the Effect of Stress Peaks Caused by Singularities at Points of Sharp Edges and Re-entrant Corners

Linear elastic FE was applied to demonstrate the high stresses caused by singularities at the sharp edges at the base of a vertical positioned rectangular cantilever and a triangular shaped

dam, and this is illustrated in graphical format Figure 4-2. A brief explanation of the cause of singularities is given. Some techniques for overcoming this problem were presented and compared with each other. Examples were given to illustrate the results of the solutions and the non-linear FEM was found to be the most suitable solution for overcoming the singularity problem. This dissertation was limited to the linear plastic Drucker Prager model, although there are other non-linear material yield models and fracture mechanics methods that could also be applied to solve the problem.

7.5 Establishment of a Method to Determine Appropriate Parameters for the DP NL FEM Yield Model

From the literature study a method was developed by combining the formulation from the handbook by Chen (1982) and the user manual for the Marc program (MSC Marc User's Guide, 2003) to establish the parameters of the DP NL FEM plastic yield model. It was shown that only two material characteristics were necessary, i.e. the tensile (f_t) and compression (f_c) strength of the concrete which can be determined from basic material laboratory tests.

7.6 Strategy for Applying the DP NL FEM to Gravity Dams

By experimenting with different mesh densities using the DP NL FEM, it was established that a relatively fine mesh is necessary to get correct stress distribution at the positions where singularity problems occur, such as at the heel of the wall. It is also important to subdivide the dam wall into its different material zones because each material will have a unique behaviour during the analysis.

The DP NL FEM must also be analysed using time steps to obtain the correct yielding conditions. In most analyses of gravity dams the following time steps were used: self-weight, hydrostatic pressure, silt pressure, uplift pressure, high flood pressures and tail-water pressure on the downstream face. It is important that the non-linear yielding (if it occurs) should converge correctly and that the stress is correctly redistributed. (For a definition of convergence see Section 3.6.2). For example, tensile stress at the heel of the wall is usually redistributed to compression stress to a position downstream of the heel.

7.7 Benchmark Comparisons with Published Results

All mathematical models have their limitations and various models were chosen that would be appropriate for benchmarking the linear plastic Drucker Prager model for gravity dams.

The benchmarks were selected progressively from relatively plain models to more advanced models. Most of the benchmarks considered were from recognised international researchers, obtained from the literature survey.

The conclusions from the benchmarking exercise will be discussed only briefly.

Tension specimen: The model performed well and the results were in agreement with the begin time of the Reinhardt and Tassilo (1988) graph. The typical curve for a linear plastic material model was observed.

Benchmark of a beam in bending according to BS 1881: The standard beam as presented in BS 1881 was modelled, with a few modifications to prevent material failure at roller contact positions. The model was stable and converged correctly. The beam yielded at the correct yielding stress. The linear plastic material yielding pattern could be observed from the stress-strain curve.

Benchmark of Drucker Prager yield theory and flow rules by Chen (1982): This was a very useful benchmark to validate the software and to examine the different Drucker Prager flow models. A graph of the three Drucker Prager flow models compared with the author's results was prepared. The curves for the DP NL FEM calculated by the author correlate well with those presented by Chen. A computer post-processor animation (not presented in the dissertation) illustrated accurately the displacement flow patterns of the material through all the time steps.

Benchmark of a shear beam (Bhattacharjee and Léger, 1994): The results of the author's linear plastic Drucker Prager model compared well, although slightly higher displacement was recorded with the FE model of Bhattacharjee and Léger. The shear beam from the reference was originally modelled for a fracture mechanics study. The equivalent plastic strain (EQPS) contour plots exhibited very similar failure patterns to the benchmark model. Failure occurred at the correct stress value. The author was satisfied with the performance of the model.

Benchmark of a 2.4-m-high model gravity dam (Bhattacharjee and Léger, 1994): Although only the tensile stress was provided in the paper, the compressive strength was calculated by the 10% ratio. The FE results were benchmarked against actual experimental data. This was originally a paper on a fracture mechanics model, but most of the information could be used to benchmark this model. The DP NL FEM computations compared well with the experimental crack mouth opening displacement (CMOD) measurements in the notch. It was interesting to see that the DP NL model followed the experimental crack pattern accurately, although the DP model was not intended to be a fracture mechanics model. The material yielded correctly and it was illustrated that the DP model could handle multiple yielding, i.e. first yielding at the notch and then yielding during later time steps at the heel of the model dam.

Non-linear analysis of a full-size concrete dam (Koyna Dam – Gioia et al., 1992): Many researchers in the literature used this model and it has been well documented by them.
The results of the crest displacement versus the overflow, in the non-linear analysis, compared well with the published FEM benchmark results, except for the last material strength of 1.0 MPa which showed some variations. The author's opinion is that the displacement curve for the DP NL FEM 1.0 MPa material should correlate to a linear distribution because it was a stronger material and the yielding would have to be lower.

7.8 Realistic Concrete Properties from Existing Dams

The laboratory sample results on the material properties of 12 DWAF dams were statistically evaluated.

The average concrete strength and standard deviation for tensile and compression stress were calculated and it was concluded that the ratio of f_t/f_c= 0.109 relates well to the typical 10% ratio used in the DWAF. It could be concluded from this small sample that the strength ratio for mass concrete use in DWAF dams is 10%. The average tensile stress f_t is 3.77 MPa and the compressive stress f_c is 33.32 MPa. Other mass concrete properties are given in Table 4-8.

7.9 Comparison of the DP NL FEM with the Results of the Classical Method and the Proposed LEFM Method of Chemaly (1994)

Hypothetical triangular shaped gravity dam

The object of this exercise was to see whether there is any relationship between the fracture mechanics models of Gálvez et al. (1994) and Chemaly (1995). A DP NL FEM was created with a set of elements that could represent a joint between the wall and the foundation.

The outcome of the FEM for the low-strength material, i.e. the worst-case scenario, was that the equivalent plastic strain area simulated a virtual crack length of 11.2 m. Chemaly's model gave a 24.3 m crack for the same load condition, which is double the length. Because the classical method used by Chemaly is based on empirical input data, the author is of opinion that the FEM gives a more realistic result.

For academic interest, the material properties of the wall and foundation in the FE model were changed to a very high stiffness (E = 10^{12} GPa), while the stiffnesses in the joint elements were left unchanged. The results of the non-linear model changed significantly and the virtual crack progressed to 39 m at water level 110 m. From this analysis it can be concluded that the moduli of elasticity of both the wall and the foundation can have a significant influence on the computed results of the virtual crack. It is thus important to use realistic stiffness parameters in the FEM in order to get realistic virtual crack length results.

The $FOS_{sliding}$ for the DP NL FEM with a service load (FSL) was found to be 2.55 and for the classical method it is 2.77. Here it can be seen that the $FOS_{sliding}$ for the DP NL FEM is more conservative. With the extreme load condition (30 m spill) the classical method showed that the dam became unstable, but the FEM model gave a $FOS_{sliding}$ of 1.34. In this case the FOS result of the classical method was the more conservative one. From the results it can be concluded that the $FOS_{sliding}$ is more critical than the risk of having a material failure. The FOS for overturning is dependent on the material strength at the contact between the concrete and the rock. The $FOS_{overturning}$ for the classical method for the extreme load case was 0.98, calculated at the base of the triangular wall.

7.10 Case Study of the Van Ryneveld's Pass Dam – A Sensitivity Study and Evaluation of the Stability

This dam was chosen because of the relatively steep downstream slopes (1 vert.: 0.65 hor.) of the wall and because no underdrainage was included.

The classical method showed that the design of this dam falls beyond the standards used for modern gravity dams.

The DP NL FEM showed that the material yielding of this dam was not the critical consideration, but that the FOS against sliding is critical. Previous dam safety evaluations used very liberal sliding parameters, which exhibited high factors of safety. Another reason for the high FOS was that the dam has high tail water during extreme flood conditions, which has a stabilising effect on the wall during such load conditions.

The foundation conditions and the material properties at the contact between the concrete and the foundation thus determine what the actual FOS will be on this dam. Failure domain graphs of critical values for the friction angle (φ) and cohesion (c') for $FOS_{sliding}$ = 1.0 and 2.0 are given (Figure 5-21and Figure 5-22). These graphs are useful for giving an engineering opinion on the safety more readily. They pertain to different material strengths and illustrate the sensitivity of material strength to the $FOS_{sliding}$.

7.11 Case Study of the Proposed De Hoop Dam – Including Long-term (Residual) Material Properties

In comparison to the previous case study, this dam is still to be constructed, but the design has been completed. The dam was designed by the DWAF under the supervision of internal and external review panels. A Recommended Design Memorandum (RDM) determined the design standards.

The shape of the dam was optimised by the classical method, which resulted in a conservative shape. The downstream slope of 1:0.8 is well known as a modern design standard for gravity dams.

By means of the NL DP FEM it was illustrated that dams designed by means of the classical method are over-designed from the point of view of material strength. The NL DP FEM illustrated that with a very weak material having a tensile stress of f_t = 0.2 MPa, the material still has limited failure. The critical failure mode of these dams is thus the resistance against sliding.

A graph of the failure domain for this gravity dam was created to measure the sensitivity of the sliding parameters, i.e. friction coefficient tan φ and cohesion (Figure 5-30). It demonstrates the usefulness of the failure domain, especially for back analysis for dam safety

evaluations because the analyst can immediately distinguish the range of the parameters where the dam is considered to be unsafe.

8 CONCLUDING REMARKS

This dissertation has focused on the linear plastic Drucker Prager model to first gain an understanding of the behaviour of the yield model by benchmarking it against recognised benchmarks from the literature. Now that a good understanding of the NL DP FEM yield model is available, it can be expanded to the DP yield models that also incorporate strain hardening and strain softening, and to the parabolic models to simulate the material yielding more accurately. Basically, the same benchmarks could be used to calibrate the other models.

The scope of this dissertation was limited to hydrostatic loads, but seismic and temperature loads are very important in the shape optimisation and design of gravity dams. Non-linear material models can be used for seismic load conditions by applying transient dynamic analysis to simulate these yield conditions accurately. For this type of analysis high-end computers are necessary due to the enormous amount of number crunching these analyses require.

In this dissertation pore pressure was modelled as uplift pressures in the FEM. A more accurate means of analysing pore pressure is by utilising special poro-plastic elements that can successfully address the material yielding. This is an important field for further study.

It was illustrated that the NL DP FEM is a reliable method of analysing large gravity dams and has many additional advantages. The benchmarks were progressed in stages of complexity to demonstrate the performance of the NL DP FEM in finally analysing a full-size gravity dam. The NL DP has the advantage that it can be used successfully for 3-D analysis and thus its usefulness can be extended to other types of analysis and other types of dam, such as arch dams.

8.1 The Way Forward

Case history studies can now be extended by utilising this model for the 3-D analysis of gravity dams (see Lombardi's paper on the 3-D analysis of gravity dams (Lombardi, 2007). Arch dams can be analysed in 3-D and the NL DP FEM can also be utilised to evaluate these structures.

8.2 Additional Studies Required

The Drucker Prager parabolic model was developed for soil and rock material, and further studies should be done to develop a methodology for accurately modelling rockfill dams. Large deformations occur in these dams that could be addressed with the NL DP FEM. Important research should be done to find the appropriate material properties for rockfill dams from scaled-down and graded rock material tested in large-diameter oedometer equipment.

8.3 Foundations and their Discontinuities

Dam failure statistics indicate that most dams that fail have poor foundation conditions. At this stage there is a large technology knowledge gap between the structural engineering and the geology fields. Very little work has been done to model foundation conditions properly with complex joints and faults. The non-linear finite element method can be utilised to model such conditions with combined contact and non-linear material properties.

9 REFERENCES

Austin Dam, 2005. Website: http://www.coudy.com/Austin/Austin-dam.htm. (Accessed: 28 August 2005)

ANCOLD (Australia) 1991. Guidelines on design criteria for concrete gravity dams. Australian National Committee on Large Dams (ANCOLD).

Arrea, M. and Ingraffea, A.R. 1981. Mixed-mode crack propagation in mortar and concrete. Report 81-13, Department of Structural Engineering, Cornell University, Ithaca, NY, USA.

ASTM C496. 2004. Splitting tensile strength of cylindrical concrete specimens. ASTM International, PA, USA.

Bathe, K-J. 1982. Finite Element Procedures in Engineering Analysis. Prentice-Hall: Englewood Cliffs, USA.

Bažant, Z P. 1990. A critical appraisal of 'no tension' design: A fracture mechanics viewpoint. *Dam Engineering,* 1(4): 237-247.

Berg, CL 1985. Die toepassing van die eindigelementmetode op beton swaartekragdamme. MEng dissertation, University of Pretoria, South Africa.

Bhattacharjee, S.S. 1993. Smeared fracture analysis of concrete gravity dams for static and seismic loads. PhD Thesis, McGill University of Montreal.

Bhattacharjee, S.S. and Léger, P. 1993. FEM of the tensile strain softening behaviour of plain concrete structures. *Engineering Computations*, 10: 205-221.

Bhattacharjee, S.S. and Léger, P. 1994. Application of NLFM models to predict cracking in concrete gravity dams. *Journal of Structural Engineering*, 120, Paper No. 4766.

BS 1881. 1983. British Standard for Testing Concrete. Part 118: Method for determination of flexural strength. British Standards Institution, London, UK.

Buyukozturk, O. 1977. Nonlinear analysis of reinforced concrete structures. *Computers and Structures*, 7: 149-156.

CADAM User's Manual 1.4.3. 2001. Department of Civil, Geological and Mining Engineering, University of Montréal (Québec), Canada

Cai, Q. (2007). Finite element modelling of cracking in concrete gravity dams. PhD thesis, University of Pretoria, South Africa.

Carpinteri, A, Valente, S.V., Farrara, D., and Imperato, L. 1992. Experimental and numerical fracture modelling of a gravity dam. In: Fracture Mechanics of Concrete Structures, Elsevier: Amsterdam, 351-360.

CDSA (Canadian Dam Safety Association) 1999. Dam safety guidelines. Revision January 1999. Website: http://www.cda.ca/ (Accessed: February 2007)

Chemaly, A.G. 1984. Gravity dams and fracture mechanics. MEng dissertation, University of Pretoria, South Africa.

Chemaly, A.G. 1995. Gravity dams and fracture mechanics. MEng dissertation, University of Pretoria, South Africa.

Chemaly, AG. 2006. Personal communication on concrete properties of the Palawan Dam built in Zimbabwe and the raw laboratory data he was willing to share with the author for the purpose of this research.

Chen, W.F. 1982. Plasticity in Reinforced Concrete: McGraw-Hill: New York, NY, USA.

Chopra, A.K. and Chakrabarti, P. 1972. The earthquake experience at Koyna Dam and stresses in concrete gravity dams. *Earthquake Engrg & Struct. Dynamics*, 1: 151-164.

Davies, G. 2006. De Hoop Dam. Engineering geological report. Council for Geoscience.

DBA (Design by Analysis) Undated. Draft CEN prEN 13445-3. Website: http://www.mpa-lifetech.de/EPERCTP/ped/jrc/design_by_analysis/annex2-c.pdf (Accessed: 22 February 2007)

Desai, C.S. and Abel, J.F. 1972. Introduction to the FEM. A Numerical Method for Engineering Analysis. Van Nostrand Reinhold: New York, NY, USA.

De Hoop Dam Professional Design Team. 2005. Design criteria memorandum for comparative dams. Internal report, Dept of Water Affairs and Forestry (DWAF), South Africa.

De Hoop Dam Professional Design Team. 2007a. Material Laboratory report on concrete materials and trial mixes. Internal report, Dept of Water Affairs and Forestry (DWAF), South Africa.

De Hoop Dam Professional Design Team. 2007b. Stability of the non-overspill section and spillway with internal gallery. Internal report, Dept of Water Affairs and Forestry (DWAF), South Africa.

Evergreen. 2007. Website: http://www.evergreen.loyola.edu/~cxenophontos/pubs/wccm1.pdf (Accessed: 7 February 2007)

Fahlbusch, H. 2001. Historical dams. ICID CIID 48, Nyaya Marg, Chanakyapuri, New Delhi, India.

Federal Energy Regulatory Commission (FERC). 2002. Gravity dam design. Chapter III. Website: http://www.ferc.gov/industries/hydropower/safety/guidelines/eng-guide/chap3.pdf (Accessed: 22 February 2007)

Forbes, BA. (Manager, GHD (Pty) Ltd, Australia). 2006. Presentation on major dam projects and personal discussions with engineers of the Dept of Water Affairs and Forestry, South Africa, during his visit to South Africa in March 2006.

Franke, P. and Frey, W. 1987. Talsperren in der Bundesrepublik Deutshland. National Komitee fur Grobe Talsperren in der Bundesrepublik (DVWK), Gluckstrabe 2, 5300, Bonn 1, Germany.

Fulton FS 1977. Concrete technology. A South African handbook. Portland cement institute. Kew road, Richmond, Johannesburg.

Gálvez. J., Llorca, J., Elices, M. 1994. Stability of concrete gravity dams: A fracture mechanics approach. Proceedings of the International Workshop on Dam Fracture and Damage, Chambercy; France, March 1994, pp 31-40.

Geoengineer. 2007.
Website: http://www.geoengineer.org/gallery/main.php?g2_view=core.ShowItem&g2_itemId=944 (Accessed: 11 May 2007)

Gioia, G., Bažant, Z.P. & Pohl, B.P. 1994. Is no-tension dam design always safe? – A numerical study. *Dam Engineering,* III(1).

Guanglun, W., Pekau, O.A., Chulan, Z. & Shaomin, W. 2000. Seismic fracture analysis of concrete gravity dams based on non linear fracture mechanics. Engeneering fracture mechanics 65 (2000) 67-87

Hansen KD. 1988 Roller compacted Concrete II. Procedings of the conference. San Diego, California USA, February 29 – March 2, 1988

Hansen HD. 1992. Roller compacted Concrete III. Procedings of the conference. San Diego, California USA, February 2-5 1992

Heilmann, A.K., Hilsdorf, H. & Finsterwalder, K. 1976. Festigkeir und Verformung von Beton unter Zugspannungen. DAfstb Heft203, Ernst & Sohn, Berlin, Germany.

Herman, R. & Ausubel, J.H. 1988. Cities and their vital systems: Infrastructure past, present and future. Website: http://www.nap.edu/openbook/0309037867/html/313.html (Accessed: 28 August 2005)

Hollingworth, F. 1970. Internal DWAF working document on classifying loading conditions on dams. Dept of Water Affairs and Forestry, South Africa.

ICOLD. 1994. Bulletin 94: Computer software for dams. Validation. Commission Internationale des Grands Barrages, Paris.

ICOLD. 2000. Bulletin 117: The gravity dam: A dam of the future. Commission Internationale des Grands Barrages, Paris.

Jansen R.B. 1988. Advanced dam engineering for design, construction and rehabilitation. Van Nostrand Reinhold, New York.

Jefferson, A.D. & Hee, S.C. 2003. NW-IALAD: Workshop WP2/TG4: Analysis of Concrete Gravity Dams using the Finite Element Program LUSAS. Cardiff University, UK.

Jordaan, J.M. 1949. Water Control and Utilisation in the United States of America. Government Printer: Pretoria, South Africa.

Köksal, H.O., Karakoc, C. & Yildirim, H. 2005. Compression behaviour and failure mechanisms of concrete masonry prisms. Jounal of materials, ASCE February 2005.

Kroon, J. 1984. Gravity dam structures. MEng dissertation, University of Pretoria, South Africa.

Leclerc, M. & Léger P. 2004. CADAM: Version 1.4.13: Computer analysis of concrete gravity dams. École Polytechnique de Montréal, Canada.

Lombardi, G. 2007. 3-D analysis of gravity dams. *Hydropower and Dams*, 1.

MSC Marc User's Guide. 2003. MSC Software GmbH, München, Germany.

Nisar, A., Dollor, D., Jacob, P., Chu, D., Logie, C. and Li, G. 2008. Non-linear incremental thermal stress-strain analysis for Portuguese dam, an RCC gravity arch dam. Website: http://www.mmiengineering.com/pdf/Nisar2008USSD.pdf

NW-IALAD. 2001. Integrity and safety assessment. European Working Group on Large Dams. Website: http://nw-ialad.uibk.ac.at (Accessed: 20 September 2007)

O'Connor, J.P. 1985. The static and dynamic analysis of arch dams. PhD thesis, University of Bradford, UK.

Oliver, J., Huespe, A. & Blanco, S. 2004. NW-IALAD Benchmark 3: TG3 Scalere Dam. Civil Engineering School, Technical University of Catalonia, E-08034, Barcelona. Website: http://nw-ialad.uibk.ac.at. (Accessed: 20 September 2007)

Oosthuizen, C. 1985. Methodology for the probabilistic evaluation of dams (part of a PhD thesis, University of Columbia Pacific, USA). Department of Water Affairs and Forestry.

Oosthuizen, C 2006. Director Civil Engineering; Department: Water Affairs and Forestry. Design guidelines: Pretoria, RSA.

Oosthuizen, C. 2007. Personal communication related to the results of concrete material strength tested by the acoustic emission process for concrete loaded for long time periods.

Ottosen, N.S.1977. A failure criterion for concrete. *Journal of Engineering Mechanics*, ASCE, 103: 527-535.

Owen, D.R.J. & Hinton, E. 1980. Finite Elements in Plasticity. Pineridge Press: Swansea, UK.

Plowman, J.M. 1951. Maturity and the strength of concrete. *Magazine of Concrete Researc*h, 2(6): 13-22.

Prukl, R. 2007. MFT Computing. Website: http://www.FiniteElements.net (Accessed 2007)

Reinhardt, H-W & Tassilo, R. 1998. High strength concrete under sustained tensile loading: *Otto Graf-Journal,* 9.

Rockey KC, Evans HR, Griffiths DW and Nethercot DA. 1975. The Finite Element Method. Granada Publishing, Technical Books Division: Frogmore, St Albans, UK

Roller Compacted Concrete II and III. 1992. Proceedings of the Conference sponsored by the Geotechnical Engineering and Materials Engineering Divisions of the ASCE, ASCE, New York, NY, USA.

SABS (South African Bureau of Standards). 1994. SM 865 1994 (or SANS 5865) Concrete tests, Edition 2. The drilling, preparation and testing for compressive strength of cores taken from hardened concrete. Pretoria, South Africa.

SANCOLD. 1991. Safety Evaluations of Dams: Report No 4: SANCOLD, Pretoria, South Africa.

SANCOLD. 2007. Proceedings of Short Course: Hydropower and Environmental Aspects of Dam Design, June, University of Stellenbosch, South Africa.

Schnitter, J. 1994. A History of Dams – The Useful Pyramids. AA Balkema: Rotterdam/Brookfield.

Seddon, C.V. 1998. Ninham Shand Consulting Engineers: Report on the safety inspection of the Van Ryneveld' s Pass Dam. Report No. 2835/7938, Cape Town, South Africa.

Smith, G.N. 1971. Introduction to Matrix and Finite Element Methods in Civil Engineering. Applied Science Publishers: Barking, Essex, UK.

Smith, N. 1971. A History of Dams. Peter Davies: London, UK.

St Francis Dam. 2006. University of California at Berkeley. Website: http://www.ce.berkeley.edu/~sitar/ce281/Introduction.pdf (Accessed: 11 May 2007)

US Army Corps, 1995. Gravity dam design. EM 1110-2-2200: Depot, 2803 52nd Avenue, Hyattsville, MD 20781-1102 USA

USBR. 1976. Design of gravity dams. US Government Printing Office: Denver, Colorado, USA.

USBR. 1987. Design of small dams. US Government Printing Office: Denver, Colorado, USA.

Van der Berg, L. 1985. The application of the finite element method on concrete gravity dams. MEng dissertation, University of Pretoria, South Africa.

Van der Spuy, D. 1992. Van Ryneveldspas Dam: Alternatiewe vir die verbetering: Risiko-gebaseerde ontleding. Dam Safety Report, Dept of Water Affairs and Forestry (DWAF), South Africa.

Watermeyer, C.F. 2006. A review of the classical method for medium-height gravity dams and aspects of base shortening with uplift. *Journal of the South African Institute of Civil Engineering* (SAICE), Volume 48 Page 2-11 paper 598

Wieland, M. 2005. Seismic analysis; tensile stress: Stress management. *International Journal of Water Power & Dam Construction.* March.

Zienkiewicz, O.C. 1977. Finite Element Method. 3rd edition, McGraw-Hill Book Co: UK.

10 APPENDICES

APPENDIX A SOUTH AFRICAN DAM SAFETY LEGISLATION

This information was taken from the South African Water Act, 1956, as published on 25 July 1986 in Government Gazette No.10366 and the Regulations in terms of Section 9C of the Water Act, 1956, relating to dams with a safety risk.

CLASSIFICATION OF DAMS:

Every dam with a safety risk shall be classified in accordance with Regulation 2.4 on the basis of its size and hazard potential to determine the level of control over the safety of such structure that is applicable in terms of these Regulations.

The size classification of a dam with a safety risk shall be based on the maximum wall height in accordance with the following table:

Table 10-1: Size and classification

Size class	**Maximum wall height in metres**
Small	More than 5 but less than 12 m
Medium	Equal to or more than 12 but less than 30 m
Large	Equal to or more than 30 m

The classification of a dam with a safety risk by hazard potential shall be effected in accordance with the following table:

Table 10-2: Hazard potential classification

Hazard potential rating	**Potential loss of life**	**Potential economic loss**
Low	None	Minimal
Significant	Not more than 10	Significant
High	More than 10	Great

USE OF THE CLASSIFICATION OF DAMS WITH A SAFETY RISK:
The requirements to be compiled relating to a dam with a safety risk in respect of the design, construction, putting into operation, operation, maintenance and abandonment of any such dam shall be determined in accordance with the category classification in the following table:

Table 10-3: Category classification of dams with a safety risk

Size class	**Hazard potential rating**		
	Low	**Significant**	**High**
Small	Category I	Category II	Category II
Medium	Category II	Category II	Category III
Large	Category III	Category III	Category III

More details can be obtained from the website of the Department of Water Affairs and Forestry: www.dwaf.gov.za under the subtitle: Dam Safety Office. The entire Water Act, Regulations, as well as the Summary of Legal Requirements for prospective and existing dam owners, are available at this website.

APPENDIX B EVOLUTION OF GRAVITY DAMS

Throughout history, dams have been closely related to the development of civilisation and it is interesting to see how ancient civilisations utilised dams, e.g. for irrigation, water supply for domestic use, flood control, combined with bridges (bridge weirs), as driving power for water mills and even as venues for entertainment.

Some of these structures were most impressive and are preserved today as monuments because they are well known for their architectural styles demonstrating interesting construction techniques.

In the book by Fahlbusch (2001) the oldest known dam, of which there are still remains left, is the Sadd-el kafara Dam. The ruins of the dam were discovered in approximately 1982 in the Nile valley. The historians dated the dam to around 2600 BC, i.e. at the beginning of the Pyramid age. The basic dimensions were 14 m in height and 113 m in crest length. The reservoir capacity was approximately half a million cubic metres and the purpose was the retention of the rare but violent floods in the valley.

According to the Fahlbusch, the dam had a grossly overdesigned cross-section, which was probably due to lack of experience. Fahlbusch states: "*This is particularly true for the central impervious core of silty sand and gravel between two shells of rockfill. The volume of fill was approximately 87 000 m³ and was constructed over a period of some 8 to 10 years. The placement of the 17 000 blocks for the slope protection, each weighing approximately 300 kg, must have been an interesting construction technique.*"

Time line of gravity dams (information taken from Fahlbusch, 2001)

The historical evolution of gravity dams dates back far in history and literature on the historical development of gravity dams dates as far back as 750 BC. Many of these dams were constructed in Turkey, Iran and Russia. Gravity dam construction skills were handed down from generation to generation, from Achaemenidan to the Macedonian, Alexander the Great, to the Seleucidae and Parthians to the Sassanidae. Around 260 AD, there was a merger of Persian and Roman hydraulic engineering, and in Persia the age of building weirs began.

Here the first recorded manmade reservoirs were built in the time of Aristotle, 384-322 BC, and Archimedes, 287-212 BC, who contributed to hydraulic engineering by developing theorems of the mechanics of dam design. These and Gallileo's discoveries were generally accepted up to the Renaissance period.

With the rise of industrialisation in the 19th century, there was a strongly increasing demand for mechanical machinery driven by water power. This was quickly developed to transform mechanical energy into the generation of electricity, with the concomitant expansion of large systems of overhead transmission lines to supply large amounts of electricity to the vicinities of the industrial centres.

The French and the Germans were the forerunners in the development of larger dams during this period and the historical development of dams in these countries was documented. It is interesting to observe that the present-day shape of gravity and arch dams dates far back in history and that during the 19th century very few new shapes were developed. However, an attempt was made to try and construct these large and expensive structures as cheaply as possible, hence the development of the modern, rapid-spreading, roller-compacted concrete (RCC) dams.

An interesting comparison and outline of the Intze gravity dams constructed in central Europe and their dates is given in Figure 10-1.

Intze, a German engineer, designed gravity dams by a unique approach using a lime, trass and sand mixture in the proportion 1.0:1.5:1.75. Cement as a binding material was rejected in order to keep the hydration temperatures low to ensure a crack-free structure of low permeability.

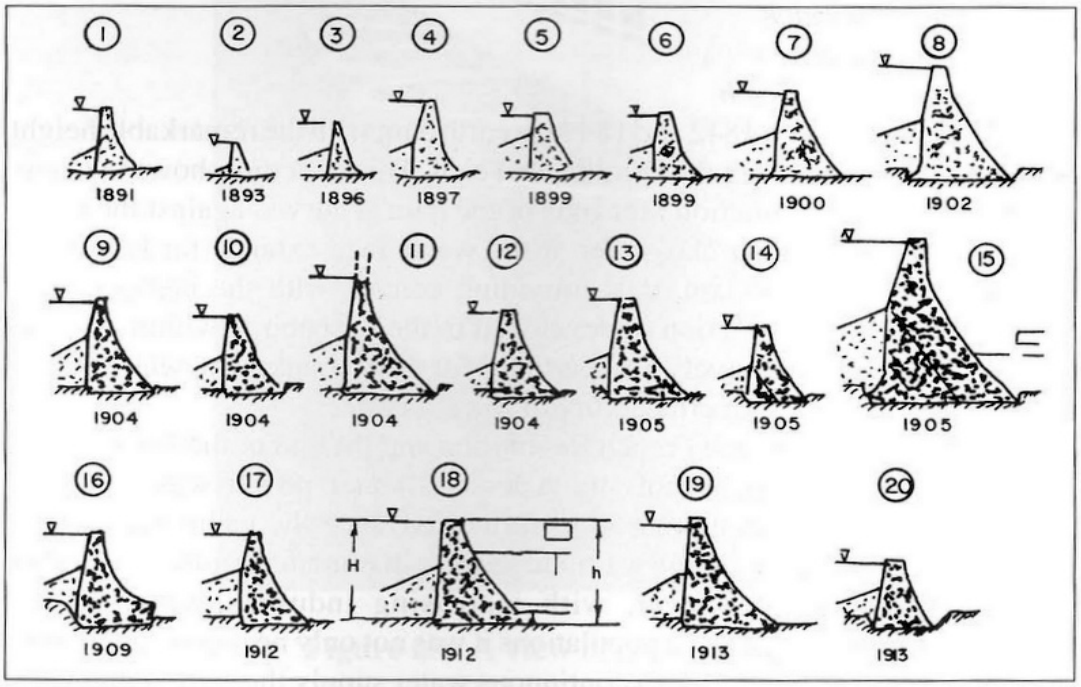

Figure 10-1: Comparative outline of the Intze dams (from Fahlbusch, 2001)

The design principles of Intze were as follows (summarised from Fahlbusch, 2001)

- The dams were curved in plan with a radius approximately corresponding to the width of the valley at the crest. For the stability of the wall, the curved profile was not considered. The curved structure was assumed to cater for elastic movement due to variations in water pressure and temperature.

- The stability of the wall was calculated for a water load up to the crest level of the dam.

- The upstream side of the dam was provided with a cement membrane as an impervious layer to prevent water entering the wall as these structures were relatively pervious. The sealed layer was then protected by a rock/stone fill on the upstream side to approximately one third of the height of the wall.

- Behind the protective sealing layer, a drainage system was introduced to collect the drainage water into a pipe system leading to a drainage tunnel.

- The structure was designed for full uplift pressure and no under-drainage was provided.

- The cross-section of the wall was calculated in such a way that the resultant acting forces remained in the middle third of the cross-section for both an empty and fully loaded structure. Thus tensile stresses were prevented, although no under-drainage was considered. (It is interesting to note that the 'middle third principle' is still used today, but with under-drainage taken into consideration.)

Figure 10-1 shows a typical example of one of the Intze Dam designs. The Ennepe Dam was constructed with the Intze mixture and the wall is approximately 50 m high (Franke and Frey, 1987).

Many of the dams built in the late 1800s and early 1900s were designed without under-drainage. Although the German dams in the Intze period had some form of drainage behind the impervious upstream membrane, most of the dams built in this period had to undergo some form of refurbishment to stabilise the structures. Refurbishment included grouting the dam to reduce the seepage in the dam and foundation and, in some cases, stabilisation with downstream rockfill, e.g. Tenay Dam built in 1864.

The dams built in this period were chosen because they were problematic and valuable lessons can be learned from these analyses.

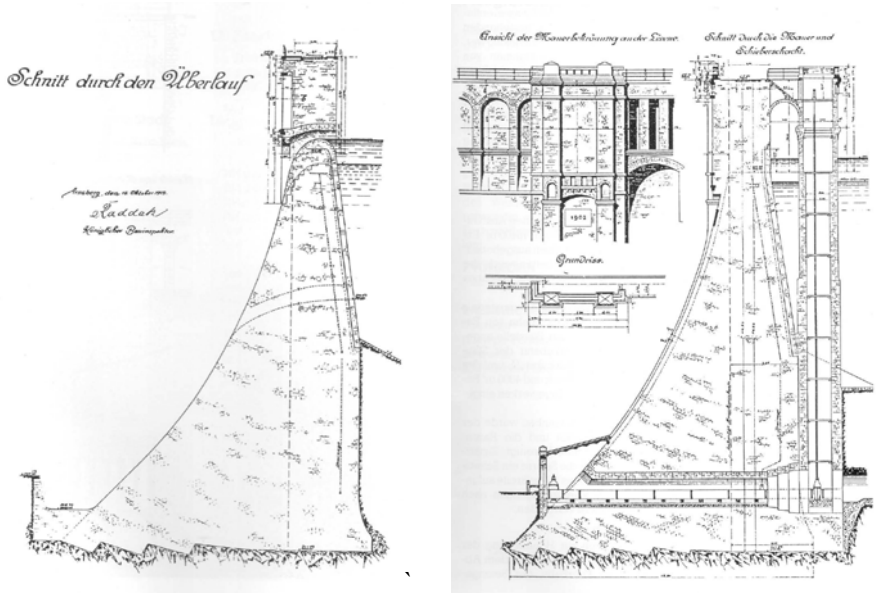

Figure 10-2: Ennepe Dam (Germany): Constructed 1902-1904: Cross-sections

The Ennepe Dam was one of the dams attacked and hit by the Royal Air Force (in May 1943), but it survived the attack.

Some interesting French dam profiles of the early post-De Sazillian period and Delocre. (1853-1900) compared with the German dams of the same era as Intze

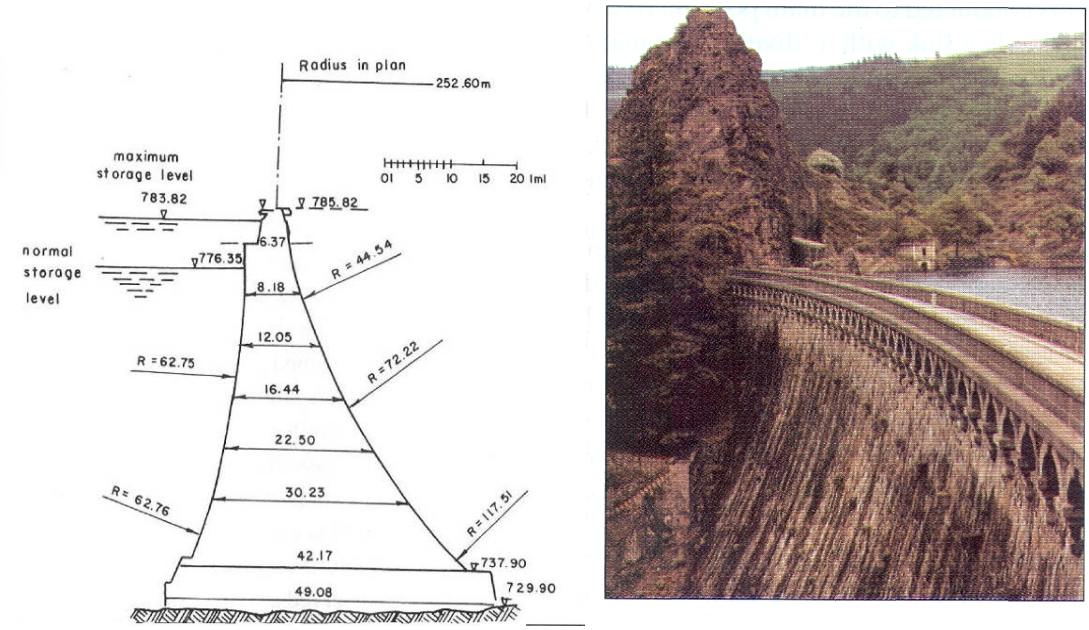

Figure 10-3: Cross-section of the Gouffre d'Enfer Dam 1886. This is a gravity-arch type of dam built in France (from Fahlbusch, 2001)

Louis Navier (1785-1836), a French engineer, formulated the first stress analysis on structures in their elastic conditions with a modulus of elasticity and with safe stress conditions. Thereafter Torerne de Sazilly (1812-1852) demonstrated in 1850 that the most advantageous profile for a gravity dam is a triangular shape with a vertical upstream face, the shape that is still considered valid today.

De Sazilly's findings were put into practice by Emile Delocre (1828-1908) under the supervision of Auguste Graeff (1812-1884), both members of the French Corps of Bridge and Highway Engineers, and they built the Gouffre d'Enfer Dam (1861-1866) on the Furan River. The purpose of this dam was flood control and water supply. Despite the narrow gorge of the Furan River (length to height ratio of 1:7), the base width of the wall ratio was still 82% of the height of the wall because the maximum compressive stress was limited to 0.6 MPa.

The dam was designed as a gravity dam, although it was constructed with a slight curve in plan, a provision made on Delocre's recommendation. This concept was later adopted in some modern roller-compacted concrete (RCC) 'arch gravity' dams. The shape of these dams was checked for safety with the then-modern finite element methods, e.g. Blyderivierspoort, Knellpoort and Wolwedans Dams which were constructed in South Africa.

The following illustrations give some idea of the evolution of gravity dams as designed by French engineers. The handbook on the history of dams by Smith (1971) gives an important description of the evolution of gravity dams and helps us to understand where the shape of gravity dams is derived from. De Sazilly adopted the theory of the so-called 'profile of equal resistance', which formulated that for each horizontal section, the maximum vertical compressive stress of an empty dam shall be equal to the maximum vertical compressive stress of a full dam. Due to the complex differential equation involved, he simplified the problem by using a profile that was stepped on both faces and therefore yielded elements of finite size which could be calculated one at a time (see Figure 10-4). It is interesting to note that de Sazilly makes no formal mention of the design conditions that a gravity dam should meet, i.e. no tensile stress should be allowed and the dam should be safe in resisting overturning about the toe of the wall. This theory was available during de Sazilly's time and was formulated by B.F. de Belidor, 1750. In fact, the profile of equal resistance was later discovered to cover these requirements automatically, but it is not clear whether de Sazilly realised this.

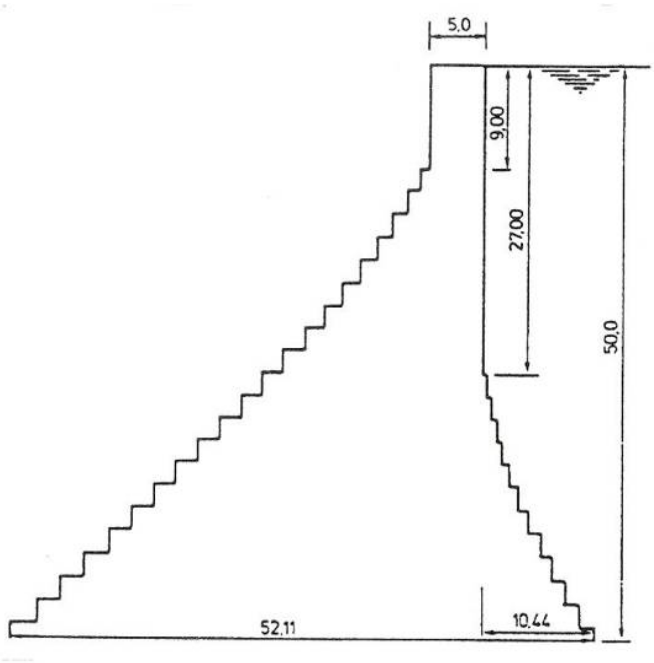

Figure 10-4: De Sazilly Dam: Gravity wall, 1853 (sketch taken from Fahlbusch, 2001)

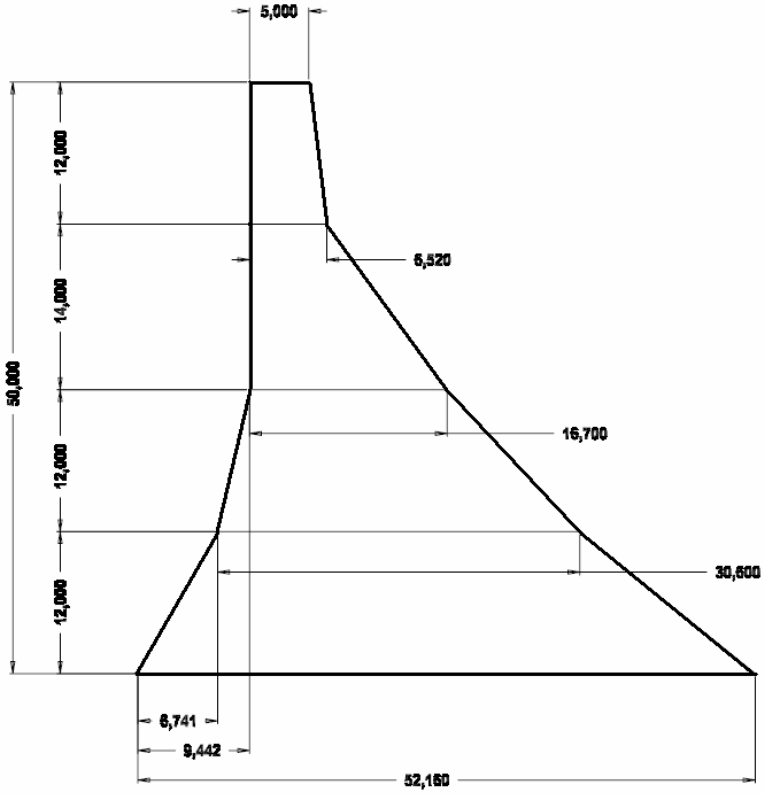

Figure 10-5: Delocre Dam: Gravity wall, 1858 (dimensions taken from Fahlbusch, 2001)

Delocre later utilised de Sazilly's principles in his dam designs, but did away with the profile of stepped faces. He argued that this was a waste of expensive concrete and therefore proposed a profile of polygonal faces by which he could save significant volumes of concrete (see Figure 10-5). The designs were done without any under-drainage and full pore pressure was assumed. From the literature it seems that the uplift problem was first addressed in 1895, although the principle was known at the time.

The evolution of gravity dam design (Fahlbusch, 2001)

The design of gravity dams was mainly a trial-and-error process in the early days. The Navier stress distribution approach or stability analysis was the more important methodology, followed by the concept of pore pressure developed by Maurice Levy after the failure of the Bouzey Dam in 1895. The classic triangular profile of later-designed gravity dams is derived directly from the Navier approach and the pore pressure concept. It is the minimum-volume profile with the so-called 'no-tension' at the heel of the dam.

In the last 30 years, dam engineers have been focusing on the behaviour of gravity dams during earthquakes. They have pointed out that the 1:0.8 gravity dam was not necessarily an appropriate cross-section in highly seismic areas. The strong tensile stresses that develop at the heel during an earthquake are likely to initiate horizontal cracks, introduce pore pressure beneath the dam and compromise dam stability. Inclination of the upstream face, at least at the base, lessens this risk and also limits the shear stresses at the contact with the foundation. Japanese RCC dams illustrate this trend (see Figure 10-6).

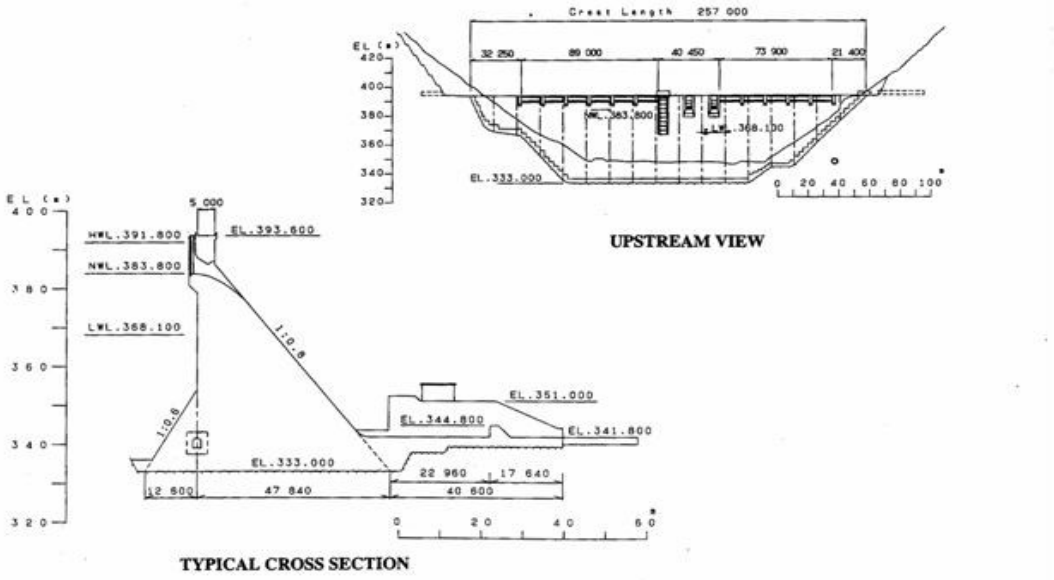

Figure 10-6: Sakaigawa Dam illustrating the inclination of the upstream face (ICOLD South Africa, 1994, brochure on Japanese dams)

The Americans have also used the so-called 'trial load method', which is based on the interaction of vertical cantilevers representing the wall. The interacting cantilevered elements cause torsional moments, or twists, which materially affect the manner in which the water load is distributed between the cantilevers of the wall. This changes the stress distribution from that found by the ordinary gravity analysis in which the effects of twist, as well as deformation of the foundation rock, are neglected. This method analyses the straight gravity dam as a 3-D structure (USBR, 1976, p. 44).

A new trend in the design of gravity dams, popular in seismic regions, is to investigate the so-called 'faced symmetrical hardfill dams' (FSHD). From an earthquake point of view, a 0.5:1 to 0.8:1 upstream slope allows the dam to withstand strong seismic events without cracking, the upstream face remaining under compression. However, the dynamic finite element method seems to demonstrate that the traditional pseudo-static earthquake method can be very conservative and that the response spectrum method can exemplify a completely different picture (ICOLD Bulletin 117, 2000).

Some recent studies reported in the literature have called for caution in that when using the classical method, with regard to crack simulation, it can be concluded that in certain conditions the so-called 'no-tension method' on which the classical method is based is not guaranteed to be safe (Bazant, 1990).

APPENDIX C FIGURES OF THE DAMS ANALYSED BY THE CLASSICAL METHOD

For the CADAM results the stress is in kPa and the tensile stress has a negative value.

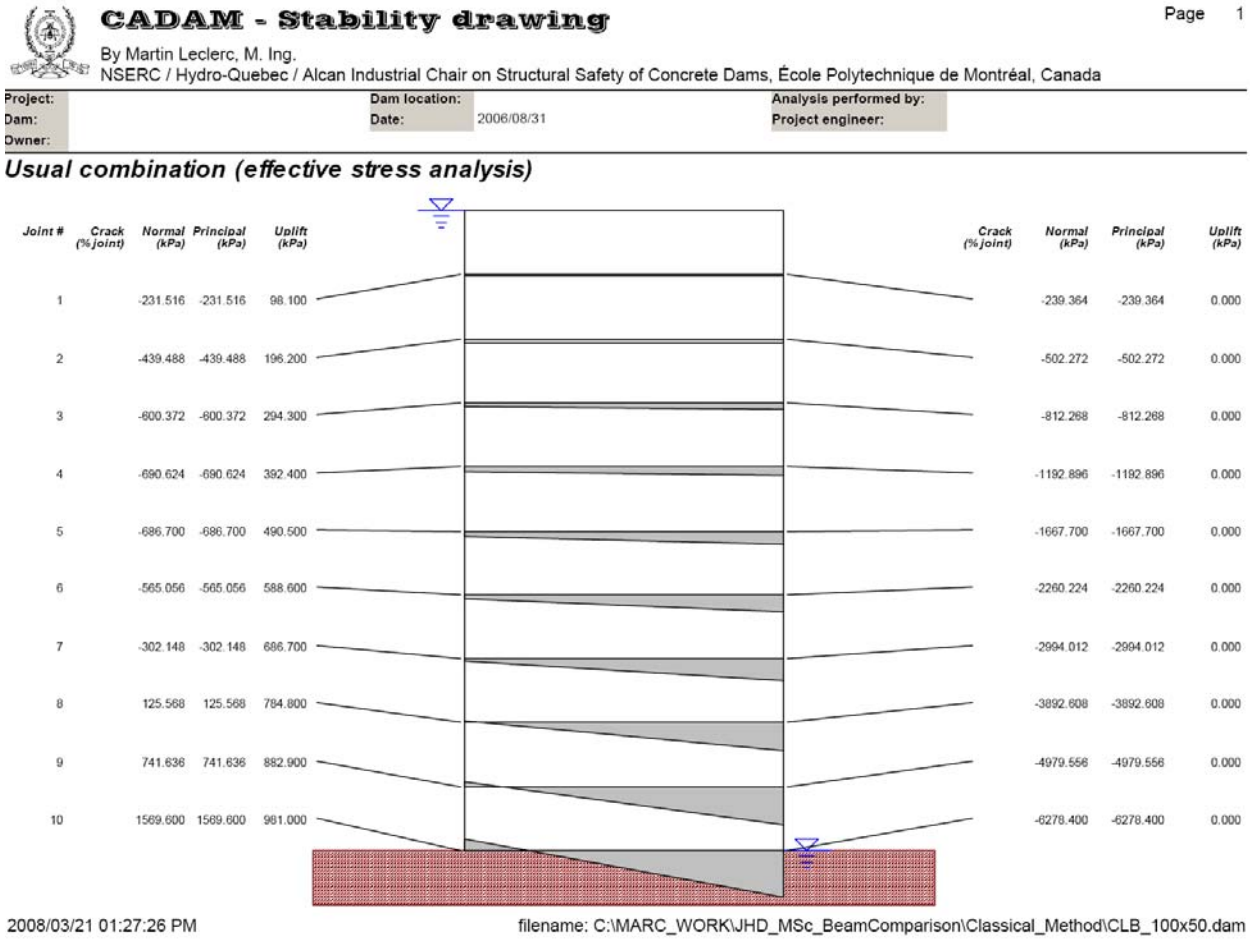

CADAM - Stability drawing Page 1

By Martin Leclerc, M. Ing.
NSERC / Hydro-Quebec / Alcan Industrial Chair on Structural Safety of Concrete Dams, École Polytechnique de Montréal, Canada

Project: Dam location: Analysis performed by:
Dam: Date: 2006/08/31 Project engineer:
Owner:

Usual combination (effective stress analysis)

Joint #	Crack (% joint)	Normal (kPa)	Principal (kPa)	Uplift (kPa)	Crack (% joint)	Normal (kPa)	Principal (kPa)	Uplift (kPa)
1		-231.516	-231.516	98.100		-239.364	-239.364	0.000
2		-439.488	-439.488	196.200		-502.272	-502.272	0.000
3		-600.372	-600.372	294.300		-812.268	-812.268	0.000
4		-690.624	-690.624	392.400		-1192.896	-1192.896	0.000
5		-686.700	-686.700	490.500		-1667.700	-1667.700	0.000
6		-565.056	-565.056	588.600		-2260.224	-2260.224	0.000
7		-302.148	-302.148	686.700		-2994.012	-2994.012	0.000
8		125.568	125.568	784.800		-3892.608	-3892.608	0.000
9		741.636	741.636	882.900		-4979.556	-4979.556	0.000
10		1569.600	1569.600	981.000		-6278.400	-6278.400	0.000

2008/03/21 01:27:26 PM filename: C:\MARC_WORK\JHD_MSc_BeamComparison\Classical_Method\CLB_100x50.dam

Figure 10-7: Stress distribution of a rectangular beam using the classical method

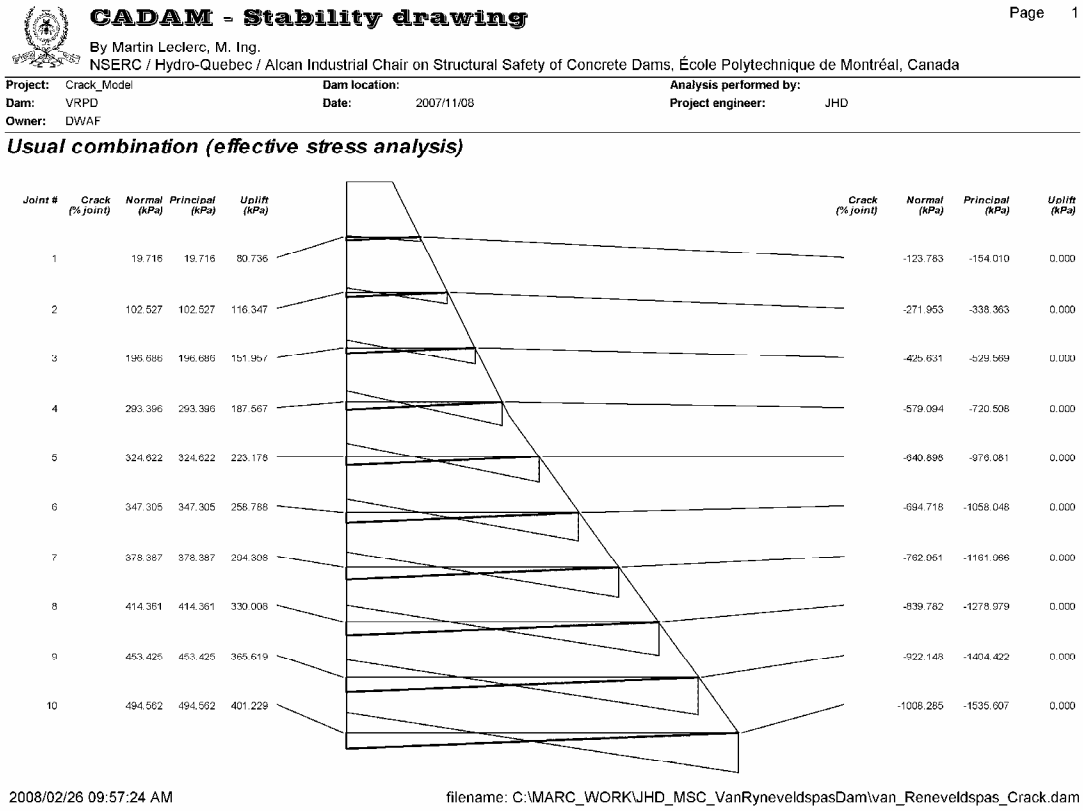

Figure 10-8: Van Ryneveld's Pass Dam: HFL = 40.9 m and no crack propagated

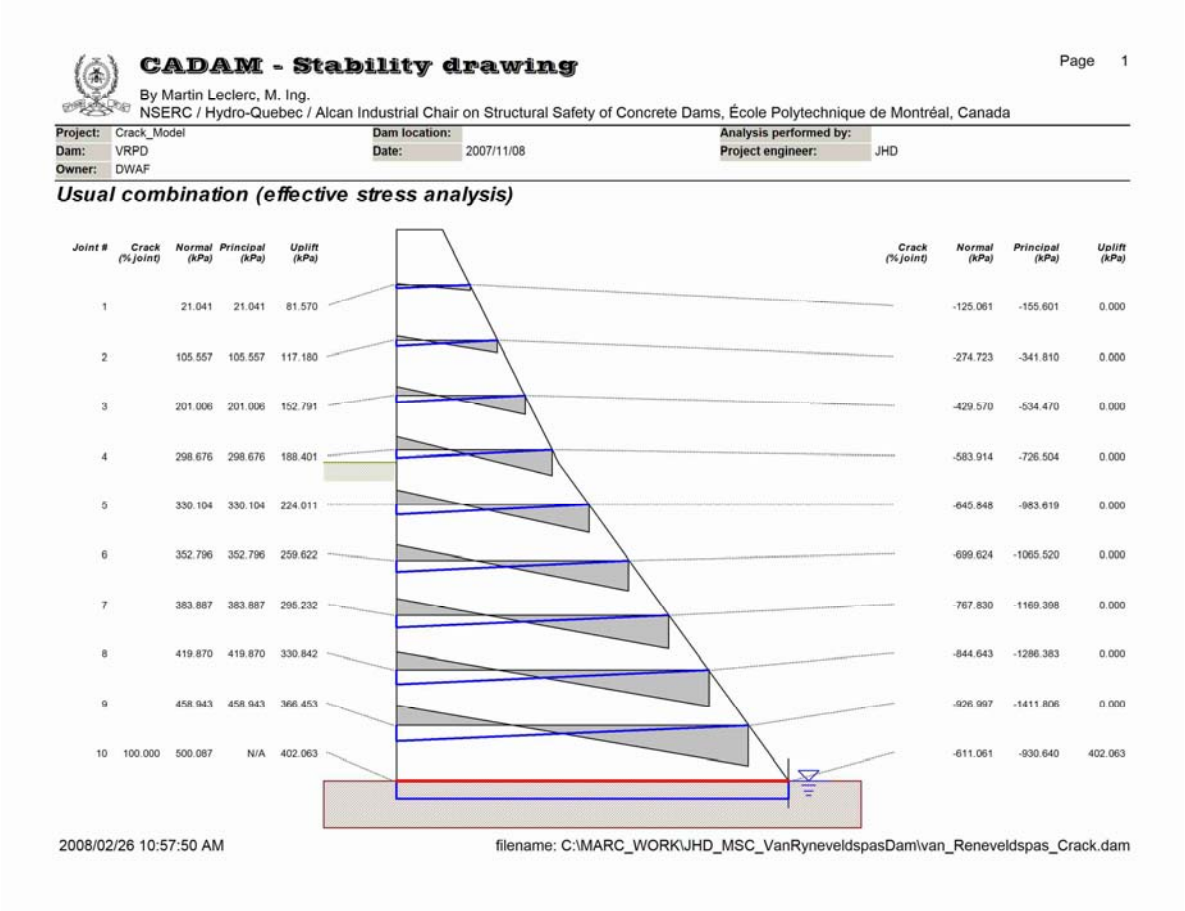

Figure 10-9: Van Ryneveld's Pass Dam: HFL = 40.98 m and a full crack propagated

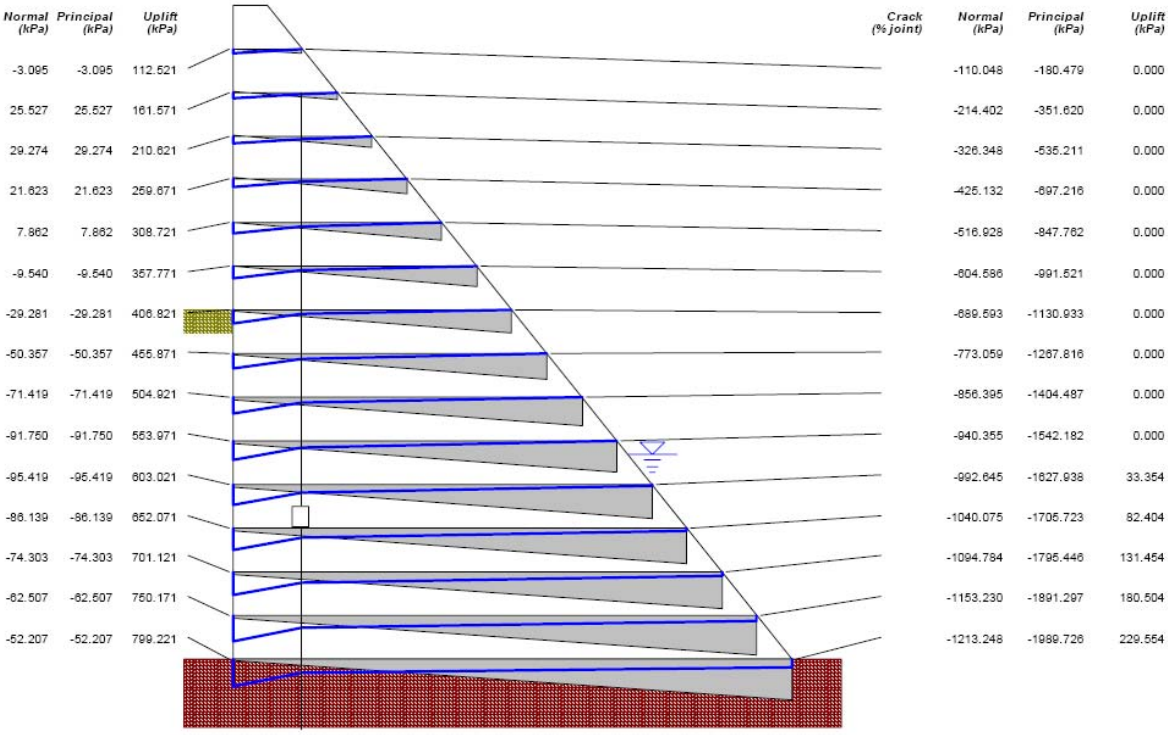

Figure 10-10: De Hoop Dam: Stress distribution of the SEF load condition (CADAM 2001)

APPENDIX D CONTOUR PLOTS OF THE FEM.

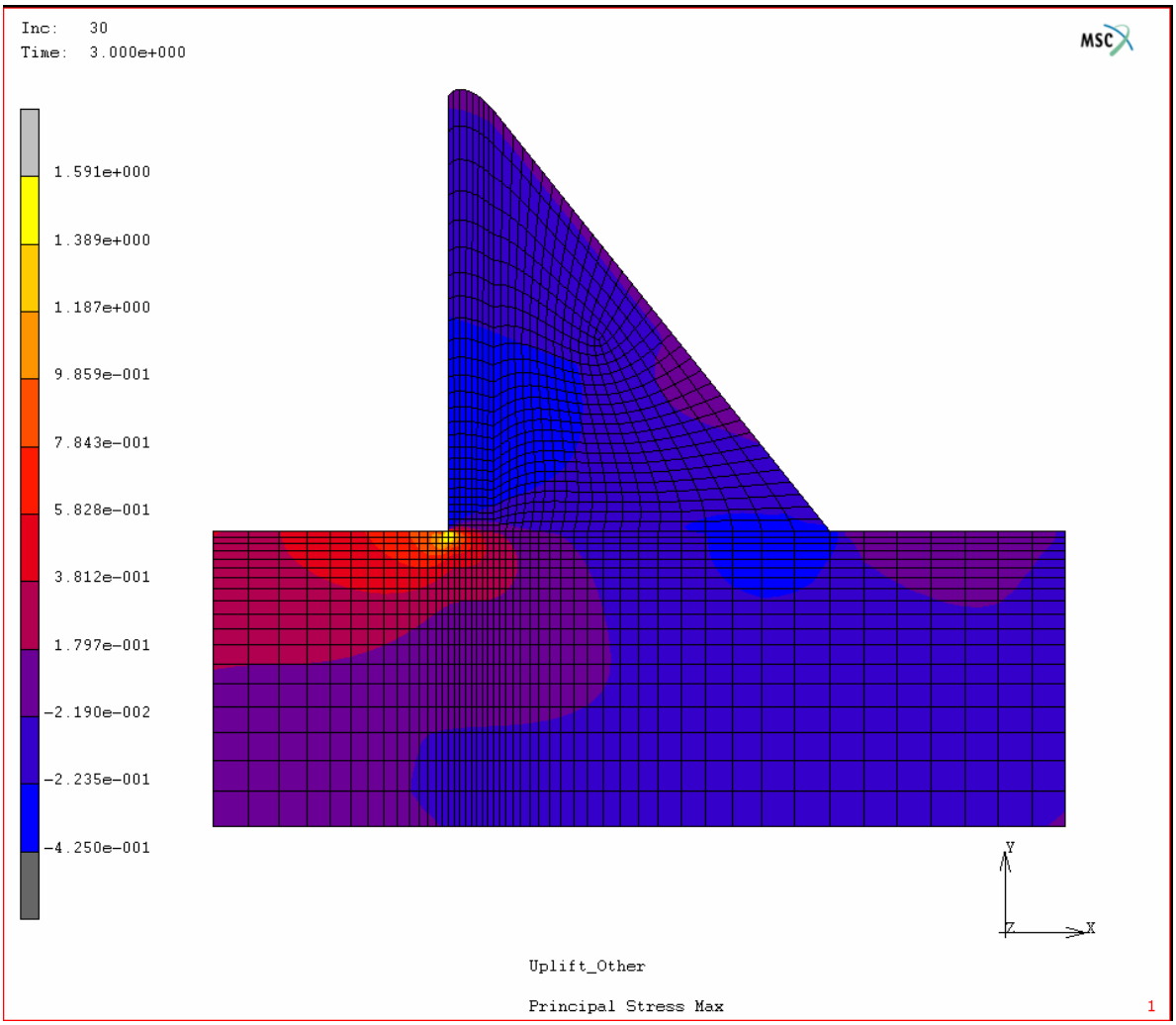

Figure 10-11: De Hoop Dam: Load case NL1 (FSL $_{PU}$): S1 stress in MPa (Mentat preprocessor)

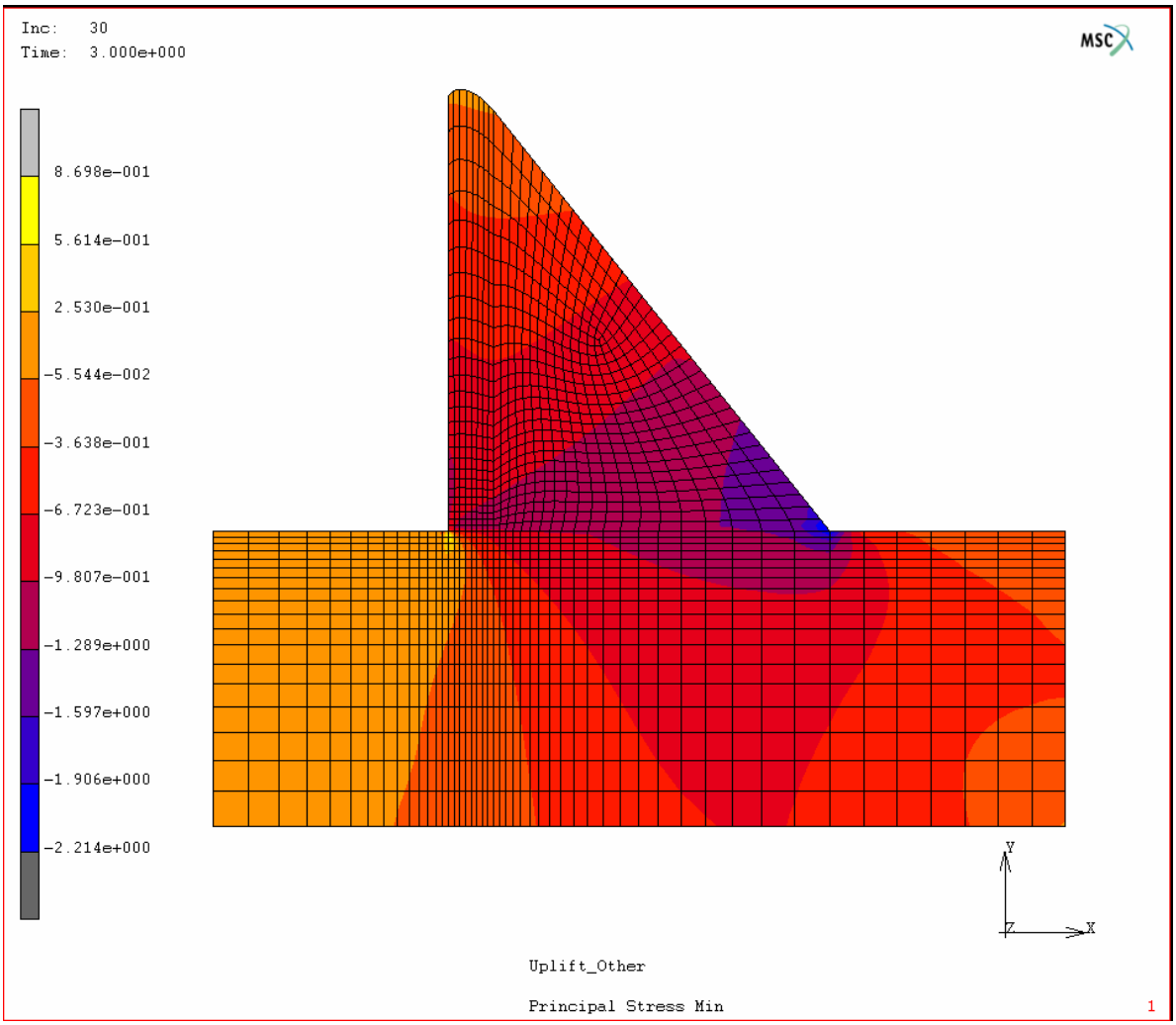

Figure 10-12: De Hoop Dam: Load case NL1 (FSL $_{PU}$): S3 stress in MPa (Mentat)

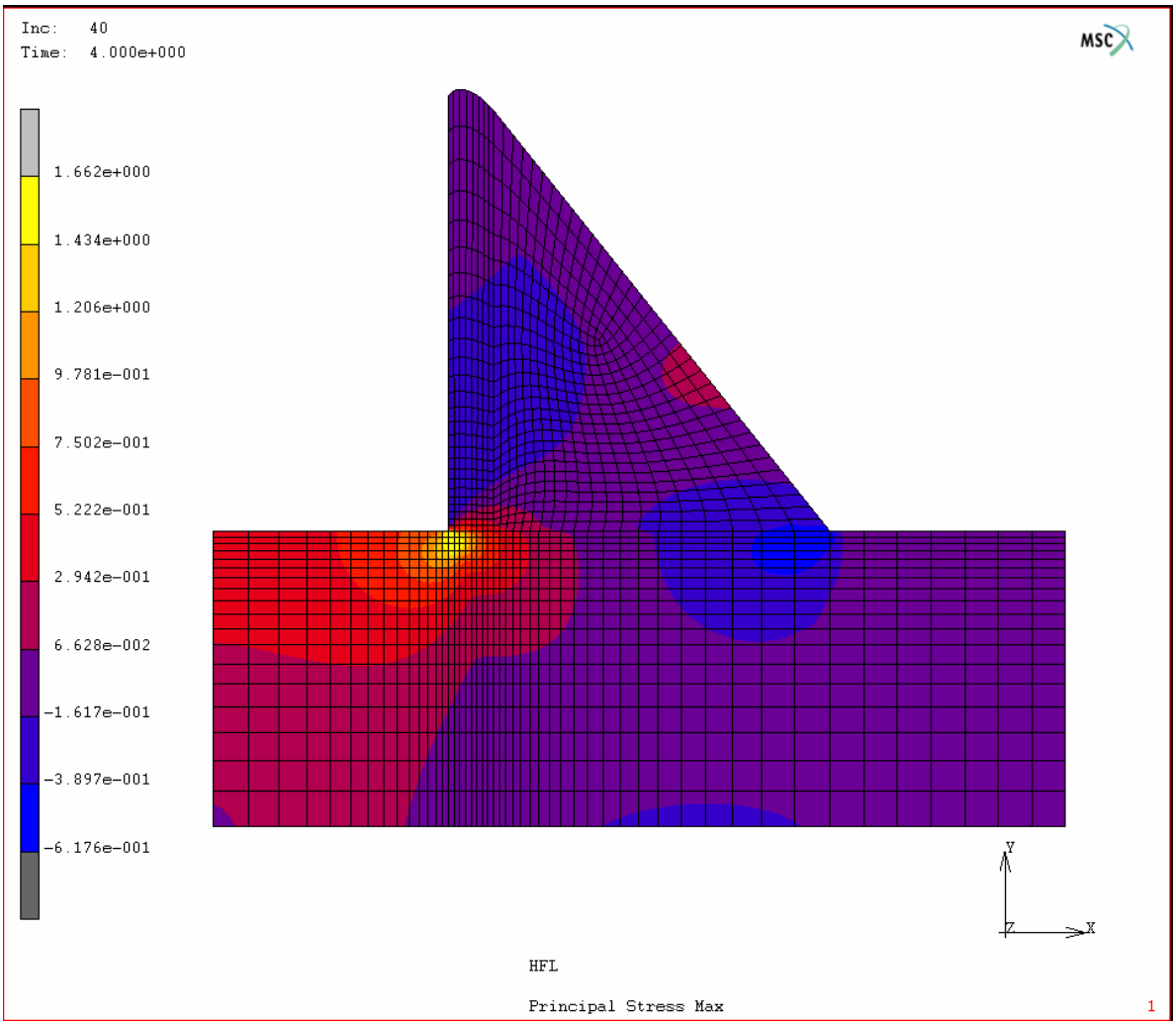

Figure 10-13: De Hoop Dam: Load case NL5 (SEF $_{PU}$): S1 stress in MPa (Mentat)

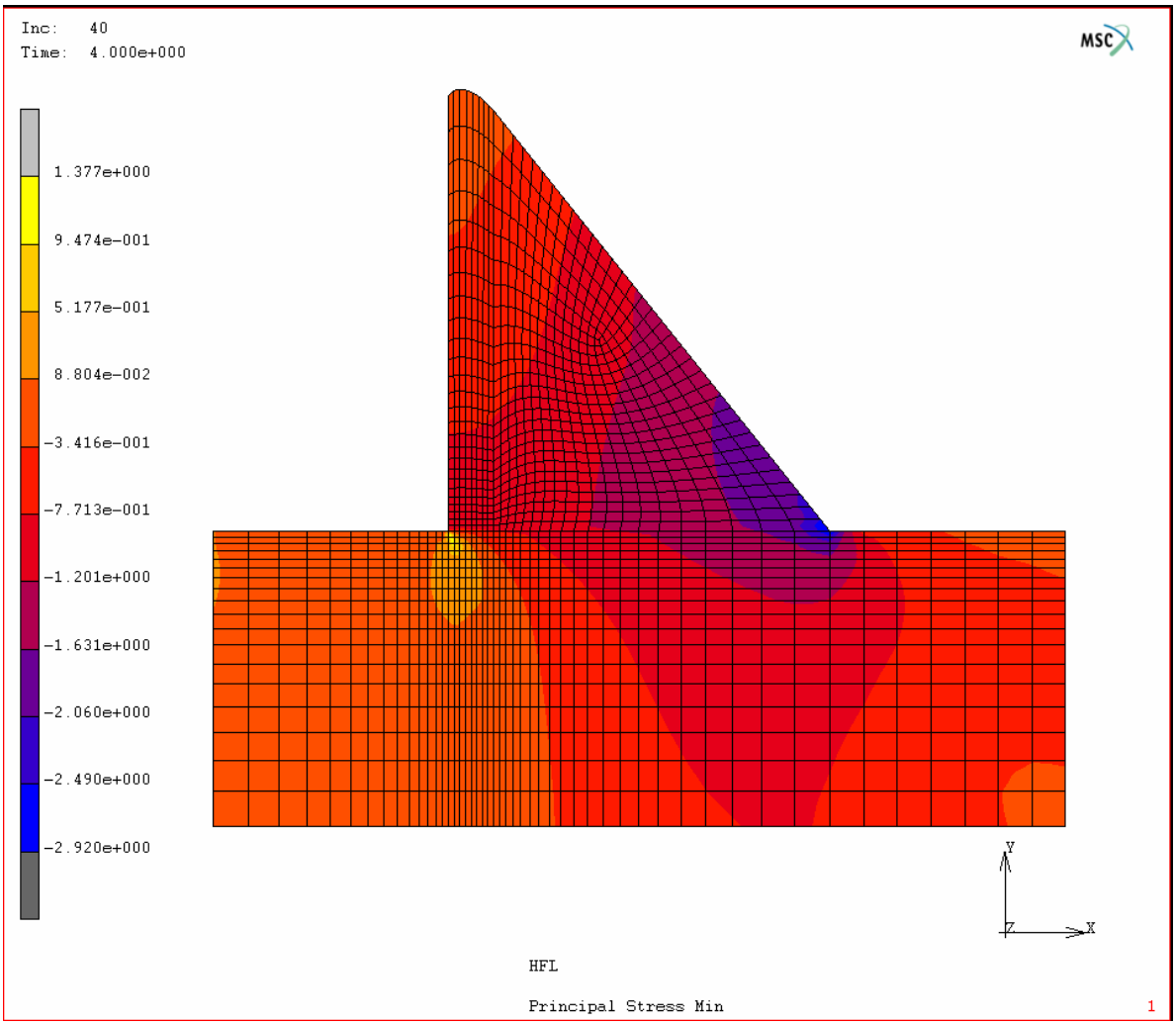

Figure 10-14: De Hoop Dam: Load case NL5 (SEF $_{PU}$): S3 stress in MPa (Mentat)

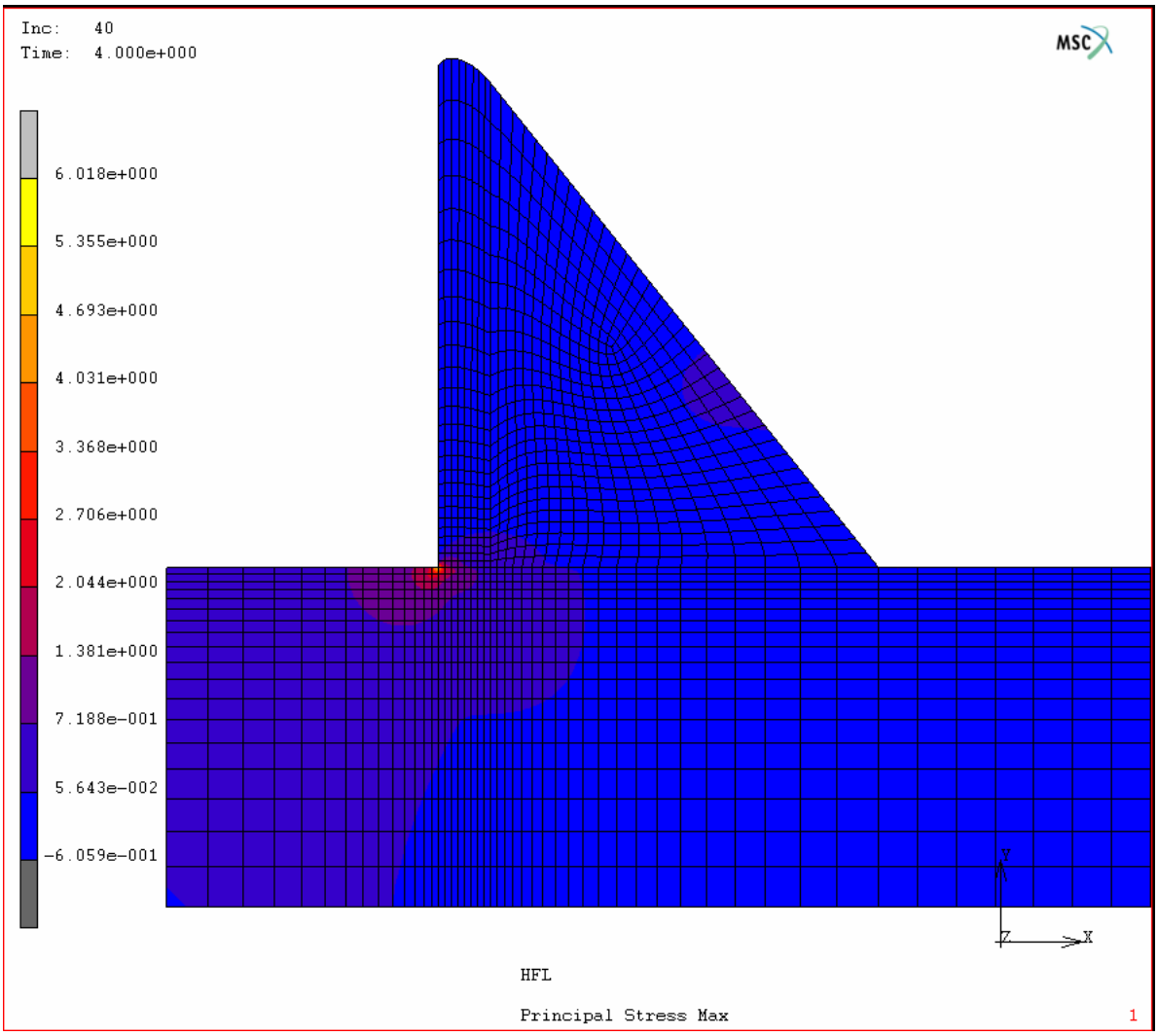

Figure 10-15: De Hoop Dam: Linear analysis (SEF $_{PU}$): S1 stress in MPa (Mentat)

APPENDIX E BASIC THEORY OF THE STIFFNESS MATRIX OF A RECTANGULAR ELEMENT FOR PLANE ELASTICITY (SEVEN STEPS)

The seven basic steps for deriving the stiffness matrix of rectangular plane strain stiffness are illustrated. The equations were taken from the textbook by Rockey et al. (1975).

Step I: Choose a suitable co-ordinate system for the node numbers

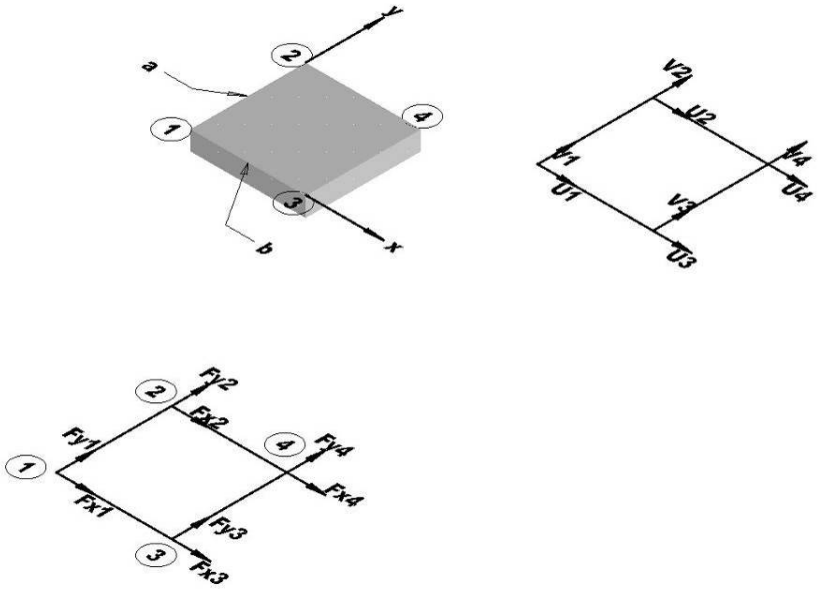

Figure 10-16: Nodal displacements and nodal forces for a plane strain stiffness matrix

The rectangular element in Figure 10-16 has sides of length ***a*** and ***b*** and a unit thickness. Since the element is derived for a plane strain configuration, each node has two degrees of freedom. Thus the element has eight degrees of freedom.

In matrix notation the displacement is given as:

$$\{\delta_1\} = \begin{Bmatrix} u_1 \\ v_1 \end{Bmatrix}$$

Likewise, the forces at node 1 can be written:

$$\{F_1\} = \begin{Bmatrix} F_{x1} \\ F_{y1} \end{Bmatrix}$$

The complete displacement and force vectors for the element are given as:

$$\{\delta^e\} = \begin{Bmatrix} \{\delta_1\} \\ \{\delta_2\} \\ \{\delta_3\} \\ \{\delta_4\} \end{Bmatrix} = \begin{Bmatrix} u_1 \\ v_1 \\ u_2 \\ v_2 \\ u_3 \\ v_3 \\ u_4 \\ v_4 \end{Bmatrix} \qquad \textbf{Equation 10-1}$$

$$\{F^e\} = \begin{Bmatrix} \{F_1\} \\ \{F_2\} \\ \{F_3\} \\ \{F_4\} \end{Bmatrix} = \begin{Bmatrix} F_{x1} \\ F_{y1} \\ F_{x2} \\ F_{y2} \\ F_{x3} \\ F_{y3} \\ F_{x4} \\ F_{y4} \end{Bmatrix} \qquad \textbf{Equation 10-2}$$

Each of these vectors contains eight terms so that the element stiffness matrix $[K^e]$ is now an 8 x 8 matrix.

$$\{F^e\}=[K^e]\{\delta^e\} \qquad \textbf{Equation 10-3}$$

Equation (I)

Step II: Choose a displacement function [f(x,y)] that defines displacement {δ(x,y)} at any point in the element

In the plane elastic problem, the state of the displacement at any point (x,y) within the element may be presented by two components:

$$\{\delta(x,y)\} = \begin{Bmatrix} u \\ v \end{Bmatrix}$$

The element has eight degrees of freedom and thus eight unknown coefficients must be involved in the polynomial representing the displacement pattern:

$$u = \alpha_1 + \alpha_2 x + \alpha_3 y + \alpha_4 xy$$

Equation 10-4

$$v = \alpha_5 + \alpha_6 x + \alpha_7 y + \alpha_8 xy$$

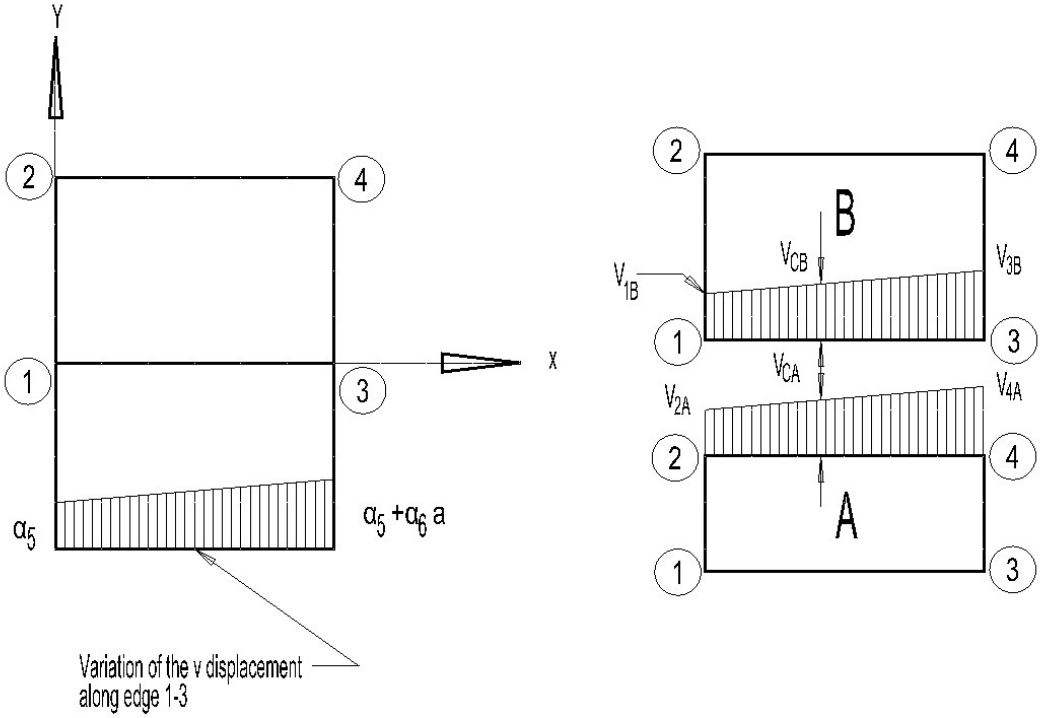

Figure 10-17: Representation of the nodal forces for a plane strain problem

It should be noted that the displacements vary linearly along each side of the rectangular element, e.g. along edge $1 > 3 y = 0$, so that $u = \alpha_1 + \alpha_2 x$ and $v = \alpha_5 + \alpha_6 x$. The displacement thus varies linearly along this edge from a value of α_5 at node 1 (where x = 0) to the value of $\alpha_5 + \alpha_6 a$ at node 3 (where $x = a$) (see Figure 10-17).

From Figure 10-16 and considering the two adjacent elements A and B, the solution is specified that:

$$v_{2A} = v_{1B} \qquad \textit{and} \qquad v_{4A} = v_{3B}$$

Consequently,

$$v_{cA} = v_{cB}$$

In matrix notation:

$$\begin{Bmatrix} u \\ v \end{Bmatrix} = \begin{bmatrix} 1 & x & y & xy & 0 & 0 & 0 & 0 \\ 0 & 0 & 0 & 0 & 1 & x & y & xy \end{bmatrix} \begin{Bmatrix} \alpha_1 \\ \alpha_2 \\ \alpha_3 \\ \alpha_4 \\ \alpha_5 \\ \alpha_6 \\ \alpha_7 \\ \alpha_8 \end{Bmatrix} \qquad \textbf{Equation 10-5}$$

This can be summarised as Equation II:

$$\{\delta(x,y)\} = [f(x,y)]\{\alpha\} \qquad \textbf{Equation (II)}$$

Step III: Express the state of displacement {δ(x,y)} at any point within the element in terms of nodal displacements {δ^e}

By substituting the values of the nodal co-ordinates [*f(x,y)*] into Equation II and then solving for {α}:

At node 1, $x_1 = 0$ and $y_1 = 0$.

$$[f(x_1, y_1)] = \begin{bmatrix} 1 & 0 & 0 & 0 & 0 & 0 & 0 & 0 \\ 0 & 0 & 0 & 0 & 1 & 0 & 0 & 0 \end{bmatrix}$$

At node 2, $x_2 = 0$ and $y_2 = b$.

$$[f(x_2, y_2)] = \begin{bmatrix} 1 & 0 & b & 0 & 0 & 0 & 0 & 0 \\ 0 & 0 & 0 & 0 & 1 & 0 & b & 0 \end{bmatrix}$$

At node 3, $x_3 = a$ and $y_3 = 0$.

$$[f(x_3, y_3)] = \begin{bmatrix} 1 & a & 0 & 0 & 0 & 0 & 0 & 0 \\ 0 & 0 & 0 & 0 & 1 & a & 0 & 0 \end{bmatrix}$$

At node 4, $x_4 = a$ and $y_4 = 0$.

$$[f(x_4, y_4] = \begin{bmatrix} 1 & a & b & ab & 0 & 0 & 0 & 0 \\ 0 & 0 & 0 & 0 & 1 & a & b & ab \end{bmatrix}$$

Thus using Equation 10-5,

$$\{\delta^e\} = \begin{Bmatrix} \{\delta_1\} \\ \{\delta_2\} \\ \{\delta_3\} \\ \{\delta_4\} \end{Bmatrix} = \begin{Bmatrix} \{\delta(x_1, y_1)\} \\ \{\delta(x_2, y_2)\} \\ \{\delta(x_3, y_3)\} \\ \{\delta(x_4, y_4)\} \end{Bmatrix} = \begin{bmatrix} [f(x_1, y_1)] \\ [f(x_2, y_2)] \\ [f(x_3, y_3)] \\ [f(x_4, y_4)] \end{bmatrix} \{\alpha\} \qquad \textbf{Equation 10-6}$$

On substituting for $\lfloor f(x\ , y\ \rfloor$ etc., Equation 10-6 results in Equation 10-7:

$$\{\delta^e\} = \begin{bmatrix} 1 & 0 & 0 & 0 & 0 & 0 & 0 & 0 \\ 0 & 0 & 0 & 0 & 1 & 0 & 0 & 0 \\ 1 & 0 & b & 0 & 0 & 0 & 0 & 0 \\ 0 & 0 & 0 & 0 & 1 & 0 & b & 0 \\ 1 & a & 0 & 0 & 0 & 0 & 0 & 0 \\ 0 & 0 & 0 & 0 & 1 & a & 0 & 0 \\ 1 & a & b & ab & 0 & 0 & 0 & 0 \\ 0 & 0 & 0 & 0 & 1 & a & b & ab \end{bmatrix} \{\alpha\} \qquad \textbf{Equation 10-7}$$

This can be summarised as:

$$\{\delta^e\} = [A]\ \{\alpha\} \qquad \textbf{Equation 10-8}$$

where {α} is the vector of the unknown coefficients of the polynomial expression given in Equation 10-4. Thus Equation 10-8 defines the [*A*] matrix for the particular case of a rectangular element in plane elasticity problems.

The unknown coefficient {α} is obtained by pre-multiplying both sides of Equation 10-8 by the inverse of [A], yielding Equation 10-9.

$$\{\alpha\} = [A]^{-1}\{\delta^e\} \qquad \textbf{Equation 10-9}$$

The inverse of [*A*] is done on computer numerically by a subroutine program.

The process of the inversion is a method of solving eight simultaneous equations so that the values of the eight unknown α coefficients can be expressed in terms of the u and v displacements of the nodes. The simultaneous equations represented in Equation 10-7 are:

$$u_1 = \alpha_1$$
$$v_1 = \alpha_2$$
$$u_2 = \alpha_1 + b\alpha_3$$
$$v_2 = \alpha_5 + b\alpha_7$$
$$u_3 = \alpha_1 + a\alpha_2$$
$$v_3 = \alpha_5 + a\alpha_6$$
$$u_4 = \alpha_1 + a\alpha_2 + b\alpha_3 + ab\alpha_4$$
$$v_4 = \alpha_5 + a\,\alpha_6 + b\,\alpha_7 + a\,\alpha_8$$

The algebraic solution of these equations is obtained by solving Equation 10-9 and may be written in full as:

$$\begin{bmatrix} \alpha_1 \\ \alpha_2 \\ \alpha_3 \\ \alpha_4 \\ \alpha_5 \\ \alpha_6 \\ \alpha_7 \\ \alpha_8 \end{bmatrix} = \begin{bmatrix} 1 & 0 & 0 & 0 & 0 & 0 & 0 & 0 \\ -1/a & 0 & 0 & 0 & 1/a & 0 & 0 & 0 \\ -1/b & 0 & 1/b & 0 & 0 & 0 & 0 & 0 \\ 1/ab & 0 & -1/ab & 0 & -1/ab & 0 & 1/ab & 0 \\ 0 & 1 & 0 & 0 & 0 & 0 & 0 & 0 \\ 0 & -1/a & 0 & 1/b & 0 & 0 & 0 & 0 \\ 0 & 1/ab & 0 & -1/ab & 0 & -1/ab & 0 & 1/ab \\ 0 & 1/ab & 0 & -1/ab & 0 & -1/ab & 0 & 1/ab \end{bmatrix} \begin{Bmatrix} u_1 \\ v_1 \\ u_2 \\ v_2 \\ u_3 \\ v_3 \\ u_4 \\ v_4 \end{Bmatrix}$$

The algebraic matrix $[A]$ is multiplied by $[A]^{-1}$ and the product is the identity matrix $[I]$ and can be used as a check to see if the calculation has been done correctly.

Equation II can then be rewritten to express

$$\{\delta(x,y)\} = [f(x,y)]\,[A]^{-1}\{\delta^e\} \qquad \textbf{(Equation III)}$$

Step IV: Relate the strains $\{\varepsilon(x,y)\}$ at any point to the displacements $\{\delta(x,y)\}$ and hence to the nodal displacements $\{\delta^e\}$

The relationship between strain and displacement at a point in a plane elasticity solution is independent of the shape of the element chosen. In the normal notation:

$$\{\varepsilon(x,y)\} = \begin{Bmatrix} \varepsilon_x \\ \varepsilon_y \\ \varepsilon_{xy} \end{Bmatrix} \qquad \textbf{Equation 10-10}$$

From the elasticity theory:

$$\varepsilon_x = \frac{\partial u}{\partial x}$$

$$\varepsilon_x = \frac{\partial v}{\partial y}$$

$$\gamma_{xy} = \frac{\partial u}{\partial y} + \frac{\partial v}{\partial x}$$

Substituting for *u* and *v* from Equation 10-4, the following expressions are obtained for the strains at any point within the element.

$$\varepsilon_x = \frac{\partial}{\partial x}(\alpha_1 + \alpha_2 x + \alpha_3 y + \alpha_4 xy) = \alpha_2 + \alpha_4 y$$

$$\varepsilon_y = \frac{\partial}{\partial y}(\alpha_5 + \alpha_6 x + \alpha_7 y + \alpha_8 xy) = \alpha_7 + \alpha_8 x$$

$$\gamma_{xy} = \frac{\partial}{\partial y}(\alpha_1 + \alpha_2 x + \alpha_3 y + \alpha_4 xy) + \frac{\partial}{\partial x}(\alpha_5 + \alpha_6 x + \alpha_7 y + \alpha_8 xy)$$

$$= \alpha_3 + \alpha_4 x + \alpha_6 + \alpha_8 y$$

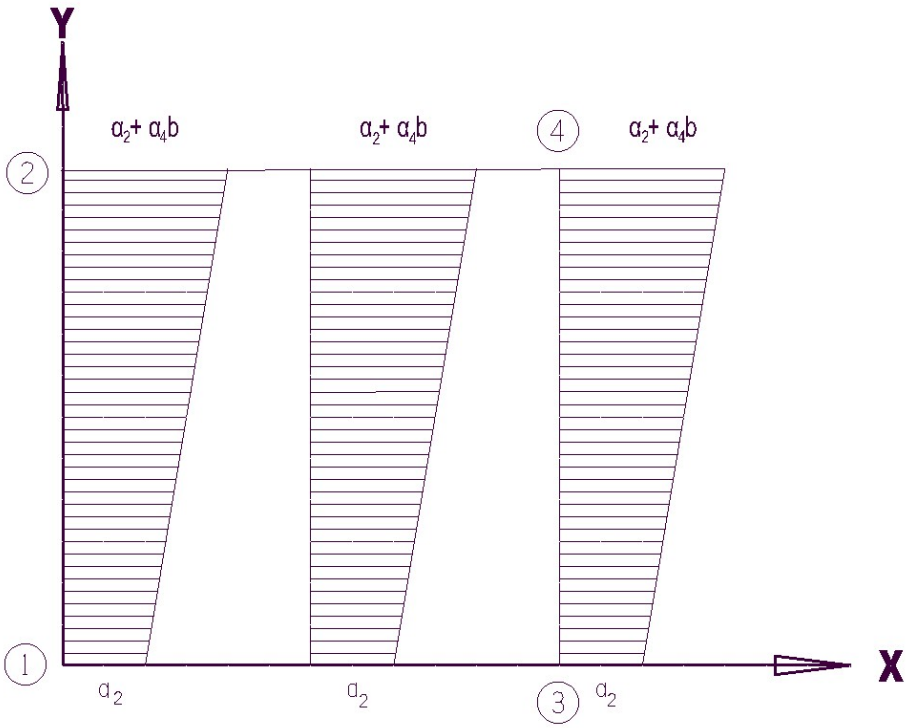

Figure 10-18: Variation of strain in a plane strain element

The strains in the element are illustrated in Figure 10-19 and vary linearly over the element considering the variation of ε_x which is linearly independent of x but linearly dependent on y and thus varies over the element in the manner shown in Figure 10-19. Similarly, ε_y is independent of y and linearly dependent on x, whereas γ_{xy} varies linearly with both x and y.

Substituting these expressions for the strains into Equation 10-10:

$$\{\varepsilon(x,y)\} = \begin{Bmatrix} \varepsilon_x \\ \varepsilon_y \\ \varepsilon_{xy} \end{Bmatrix} = \begin{Bmatrix} \alpha_2 + \alpha_4 y \\ \alpha_7 + \alpha_8 x + \\ \alpha_3 + \alpha_4 x + \alpha_6 + \alpha_8 y \end{Bmatrix} \qquad \textbf{Equation 10-11}$$

$$= \begin{bmatrix} 0 & 1 & 0 & y & 0 & 0 & 0 & 0 \\ 0 & 0 & 0 & 0 & 0 & 0 & 1 & y \\ 0 & 0 & 1 & x & 0 & 1 & 0 & y \end{bmatrix} \begin{Bmatrix} \alpha_1 \\ \alpha_2 \\ \alpha_3 \\ \alpha_4 \\ \alpha_5 \\ \alpha_6 \\ \alpha_7 \\ \alpha_8 \end{Bmatrix}$$

Therefore

$$\{\varepsilon(x,y)\} = [C]\{\alpha\} \qquad \textbf{Equation 10-12}$$

on substituting for $\{\alpha\}$ using Equation 10-9

$$\{\varepsilon(x,y)\} = [C][A]^{-1}\{\delta^e\} \qquad \textbf{Equation 10-13}$$

or $\{\varepsilon(x,y)\} = [B]\{\delta^e\}$

Where $[B] = [C][A]^{-1}$

The matrix $[B]$ has the typical form of a stiffness matrix in other general FE literature.

The matrix $[C]$ is defined in Equation 9-11 and the $[A]^{-1}$ matrix in Equation 10-9. The matrix $[B]$ is obtained as:

$$\begin{bmatrix} -\frac{1}{a}+\frac{y}{ab} & 0 & \frac{-y}{ab} & 0 & \frac{1}{a}-\frac{y}{ab} & 0 & \frac{y}{ab} & 0 \\ 0 & \frac{-1}{b}+\frac{x}{ab} & 0 & \frac{1}{b}-\frac{x}{ab} & 0 & -\frac{x}{ab} & 0 & \frac{x}{ab} \\ -\frac{1}{b}+\frac{x}{ab} & -\frac{1}{a}+\frac{y}{ab} & \frac{1}{b}-\frac{x}{ab} & -\frac{y}{ab} & -\frac{x}{ab} & \frac{1}{a}-\frac{y}{ab} & \frac{x}{ab} & \frac{y}{ab} \end{bmatrix}$$

Step V: Relate the internal stresses $\{\sigma(x,y)\}$ **to the strains** $\{\varepsilon(x,y)\}$ **and to the nodal displacements** $\{\delta^e\}$

The relationship between stresses and strains given by the equation $\{\sigma(x,y)\}= [D]\ \{\varepsilon(x,y)\}$ is independent of the shape of element taken

from $\{\sigma(x,y)\} = \begin{Bmatrix}\sigma_x \\ \sigma_y \\ \sigma_z\end{Bmatrix}$ and $\{\sigma(x,y)\} = [D]\ \{\varepsilon(x,y)\}$ for a rectangular element

The matrix [D] required in general Equation V is:

$$\{\sigma(x,y)\}=[D][B]\{\delta^e\} \qquad \textbf{(Equation V)}$$

which gives the required relationship between stresses at any point and nodal displacements, and is thus as defined in Equation VI in the next step. This can be rearranged to the following format to simplify the large matrix.

$$[D] = \begin{bmatrix} d_{11} & d_{12} & 0 \\ d_{21} & d_{22} & 0 \\ 0 & 0 & d_{33} \end{bmatrix} \qquad \textbf{Equation 10-14}$$

Where for plane strain element:

$$d_{11} = d_{22} = \frac{(1-\nu)E}{(1+\nu)(1-2\nu)}$$

$$d_{21} = d_{12} = \frac{\nu E}{(1+\nu)(1-2\nu)}$$

$$d_{33} = \frac{E}{2(1+\nu)}$$

Step VI: Replace the internal stresses $\{\sigma(x,y)\}$ **with statically equivalent nodal forces** $\{F^e\}$; **relate the nodal forces to the nodal displacements** $\{\delta^e\}$ **and obtain the element stiffness matrix** $[K^e]$

The general equation is derived from the principle of virtual work to determine the set of nodal loads statically equivalent to the internal stresses. The 'principle of virtual work' is not described in detail here but is given as:

$$\{F^e\} = \left[\int [B]^T [D][B] d(vol)\right] \{\delta^e\}$$

(see Equation VI below) and can be derived basically from Chapter 3 of Rockey et al. (1975) as follows:

An arbitrary set of nodal displacements represented by the vector $\{\delta^{*e}\}$ is selected, where:

$$\{\delta^{*e}\} = \begin{Bmatrix} \{\varepsilon_1^{*e}\} \\ \{\varepsilon_2^{*e}\} \\ . \\ . \\ \{\varepsilon_n^{*e}\} \end{Bmatrix}$$

The external work done by the nodal loads W_{ext} is given by:

$$W_{ext} = \{\delta_1^{*e}\}\{F_1^e\} + \{\delta_2^{*e}\}\{F_2^e\} + ... + \{\delta_n^{*e}\}\{F_n^e\}$$

$$= \{\delta^{*e}\}^T \{F^e\}$$

The internal work done per unit volume is:

$$W_{int} = \{\varepsilon(x,y)^*\}^T \{\sigma(x,y)\}$$

The total internal work is obtained by integrating over the volume of the element:

$$\int^v W_{int} d(vol) = \int^v \{\varepsilon(x,y)^*\}^T \{\sigma(x,y)\} d(vol)$$

From Equation IV, $\{\varepsilon(x,y)\}=[B]\{\delta^e\}$. When the nodal displacements are imposed, the corresponding strains may be written as:

$$\{\varepsilon(x,y)^*\} = [B]\{\delta^{*e}\}$$

Then $$\{\varepsilon(x,y)^*\}^T = \{\delta^{*e}\}^T[B]^T$$

Furthermore, from Equation V, the actual stresses in the element are known to be related to the actual nodal displacements as:

$$\{\sigma(x,y)=[D][B]\{\delta^e\}$$

These expressions are substituted into the virtual work equation for the internal work to obtain:

$$\int^v W_{\text{int}} d(vol) = \{\delta^*\}^T \int^v [B]^T [D][B]\{\delta^e\} \quad d(vol)$$

$$W_{ext} = \{\delta^{*e}\}^T\{F^e\}$$

The final operation is to equate the internal and external work done during the system of virtual displacements $\{\delta^{*e}\}$. Since the basic principle of virtual displacements is valid for any system of applied displacements, the system of virtual nodal displacements may be chosen at will. For the present purposes, it is convenient to assume that unit values of the nodal displacements are applied. Then equating the internal and external work gives:

$$[F^e] = [\int [B]^T [D][B] d(vol)] \quad \{\delta^e\} \qquad \textbf{(Equation VI)}$$

On comparing Equation VI with Equation I, this is restated as below:

$$\{F^e\}=[K]\{\delta^e\}$$

It is clear that the required element stiffness matrix $[K^e]$ is given by the expression in the large square brackets in Equation VI. Therefore:

$$[K^e] = \int [B]^T [D][B] \quad d(vol) \qquad \textbf{Equation 10-15}$$

For an element with constant thickness:

$$[K^e] = t\iint [B]^T [D][B] dxdy \qquad \textbf{Equation 10-16}$$

The product $[B]^T[D][B]$ has to be evaluated first and the terms of the resulting matrix have to be integrated over the area of the element.

For first-order elements, the integration can still be done algebraically, but for second-order isoparametric elements these integrations become too complex and are carried out by means of numerical integration processes. In the handbook by Bathe (1982, Chapter 5.8) the different methods of numerical integration are derived. The popular methods are the Newton-Cotes and Gauss methods. Figure 10-19 illustrates the location of the Gauss integration points for a rectangular element. This figure is included for an understanding of the so-called Gauss points and where their relative positions are on the element. Most current FE programs have the option to print the Gauss point stresses of a model. In the modern FE post-processing programs, the Gauss point stresses are interpolated to the different nearest nodal points to give a contour stress plot of the average nodal point stresses. The FE work done in this dissertation is on second-order, eight-node isoparametric elements and these are utilised in the plane strain elements; usually, 2 x 2 or 3 x 3 Gauss integrations are used. Because certain function values are calculated at the integration points and the same function values are required to calculate the stresses, it is customary in modern programs to calculate the stresses at the integration points.

Bathe (1982) proves in his handbook that the stresses are best calculated at the integration points to get the most accurate results. If stresses are to be calculated at other points on the element, such as the nodal points, they are then usually extrapolated from the Gauss points.

For a 2 x 2 Gauss point integration, the equation is given as:

$$\int f(r,s)dsdr = \alpha_1 F(r_1,s_1) + \alpha_2 F(r_2,s_2) + \alpha_3 F(r_3,s_3) + \alpha_4 F(r_4,s_4) \qquad \textbf{Equation 10-17}$$

with $s_1 = r_1 = -\frac{1}{\sqrt{3}}$

$s_2 = r_2 = +\frac{1}{\sqrt{3}}$

and $\alpha_1 = \alpha_2 = \alpha_3 = \alpha_4 = 1$

Integration order	Degree of precision	Location of integration points
2 × 2	3	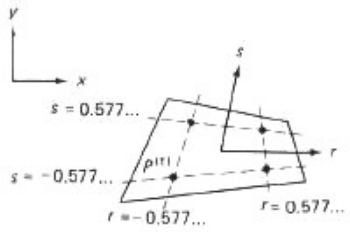
3 × 3	5	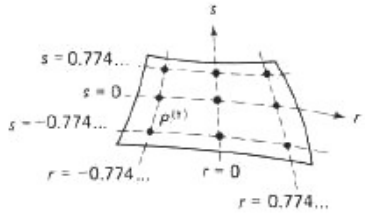
4 × 4	7	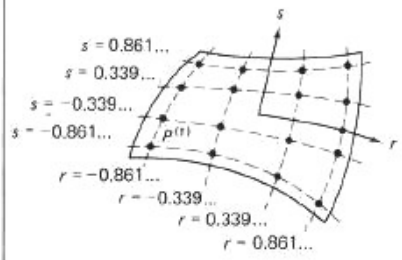

(1) The location of any integration point in the x–y coordinate system is given by : $x_p = \Sigma_i h_i(r_p, s_p)x_i$ and $y_p = \Sigma_i h_i(r_p, s_p)y_i$

TABLE 5.3 Gauss numerical integrations over rectangular domains. The integration weights are given in Table 5.2 using (5.132).

Figure 10-19: Location of Gauss integration points (from Bathe, 1982)

The final value of the [K^e] matrix obtained from these calculations is given in Equation 10-18 which is the matrix from Rockey et al. (1975). This equation is derived where $p = a/b$ to simplify the matrix.

Step VII: Establish the stress-displacement matrix [H]

The required relationship is given in general Equation VII as:

$$\{\sigma(x,y)\}=[D][B]\{\delta^e\} \qquad \textbf{(Equation VII)}$$

or $$\{\sigma(x,y)\}=[H]\{\delta^e\} \qquad \textbf{(Equation VIII)}$$

where [H] = [D][B] is the required stress-displacement matrix.

The following matrices have been scanned in from Rockey et al. (1975):

$$[K^e] = \frac{t}{12}\begin{bmatrix}
4d_{11}p^{-1} + 4d_{33}p & & & & & & & \\
3d_{21} + 3d_{33} & 4d_{22}p + 4d_{33}p^{-1} & & & & & & \\
2d_{11}p^{-1} - 4d_{33}p & 3d_{21} - 3d_{33} & 4d_{11}p^{-1} + 4d_{33}p & & & \text{symmetric} & & \\
-3d_{21} + 3d_{33} & -4d_{22}p + 2d_{33}p^{-1} & -3d_{21} - 3d_{33} & 4d_{22}p + 4d_{33}p^{-1} & & & & \\
-4d_{11}p^{-1} + 2d_{33}p & -3d_{21} + 3d_{33} & -2d_{11}p^{-1} - 2d_{33}p & 3d_{21} + 3d_{33} & 4d_{11}p^{-1} + 4d_{33}p & & & \\
3d_{21} - 3d_{33} & 2d_{22}p - 4d_{33}p^{-1} & 3d_{21} + 3d_{33} & -2d_{22}p - 2d_{33}p^{-1} & -3d_{21} - 3d_{33} & 4d_{22}p + 4d_{33}p^{-1} & & \\
-2d_{11}p^{-1} - 2d_{33}p & -3d_{21} - 3d_{33} & -4d_{11}p^{-1} + 2d_{33}p & 3d_{21} - 3d_{33} & 2d_{11}p^{-1} - 4d_{33}p & -3d_{21} + 3d_{33} & 4d_{11}p^{-1} + 4d_{33}p & \\
-3d_{21} - 3d_{33} & -2d_{22}p - 2d_{33}p^{-1} & -3d_{21} + 3d_{33} & 2d_{22}p - 4d_{33}p^{-1} & 3d_{21} - 3d_{33} & -4d_{22}p + 2d_{33}p^{-1} & 3d_{21} + 3d_{33} & 4d_{22}p + 4d_{33}p^{-1}
\end{bmatrix}$$

Equation 10-18

and

$$[H] = \frac{1}{ab}\begin{bmatrix}
-d_{11}(b-y) & -d_{21}(a-x) & -d_{11}y & d_{21}(a-x) & d_{11}(b-y) & -d_{21}x & d_{11}y & d_{21}x \\
-d_{21}(b-y) & -d_{22}(a-x) & -d_{21}y & d_{22}(a-x) & d_{21}(b-y) & -d_{22}x & d_{21}y & d_{22}x \\
-d_{33}(a-x) & -d_{33}(b-y) & d_{33}(a-x) & -d_{33}y & -d_{33}x & d_{33}(b-y) & d_{33}x & d_{33}y
\end{bmatrix}$$

Equation 10-19

In order to obtain the stresses at a specific point, the co-ordinates of that point are substituted into terms of the [H] matrix. In this way, the stresses at each of the four nodes of the element can be determined. These may be represented by $\{\delta^e\}$ where:

$$\{\sigma^e\} = \begin{Bmatrix} \{\sigma(x_1, y_1)\} \\ \{\sigma(x_2, y_2)\} \\ \{\sigma(x_3, y_3)\} \\ \{\sigma(x_4, y_4)\} \end{Bmatrix} = \begin{bmatrix} [H(x_1, y_{1)}] \\ [H(x_2, y_{2)}] \\ [H(x_3, y_{3)}] \\ [H(x_4, y_{4)}] \end{bmatrix} \{\delta^e\}$$

Equation 10-20

The value of [H(x_1,y_1)], for example, is obtained simply by substituting the co-ordinates of node 1 into the expression for [H] given in Equation 10-20 **A similar procedure is then followed for each of the other three nodes,** thus defining the [H^e] matrix for a rectangular element in the plane elasticity solution.

Since the strains vary linearly over this rectangular element, as discussed earlier, the stresses also vary linearly across the element for constant values of x and y:

$$\{\sigma^e\} = \frac{1}{ab}\left[\begin{array}{cccccccc}
-d_{11}b & -d_{21}a & 0 & d_{21}a & d_{11}b & 0 & 0 & 0 \\
-d_{21}b & -d_{22}a & 0 & d_{22}a & d_{21}b & 0 & 0 & 0 \\
-d_{33}a & -d_{33}b & d_{33}a & 0 & 0 & d_{33}b & 0 & 0 \\
\hline
0 & -d_{21}a & -d_{11}b & d_{21}a & 0 & 0 & d_{11}b & 0 \\
0 & -d_{22}a & -d_{21}b & d_{22}a & 0 & 0 & d_{21}b & 0 \\
-d_{33}a & 0 & d_{33}a & -d_{33}b & 0 & 0 & 0 & d_{33}b \\
\hline
-d_{11}b & 0 & 0 & 0 & d_{11}b & -d_{21}a & 0 & d_{21}a \\
-d_{21}b & 0 & 0 & 0 & d_{21}b & -d_{22}a & 0 & d_{22}a \\
0 & -d_{33}b & 0 & 0 & -d_{33}a & d_{33}b & d_{33}a & 0 \\
\hline
0 & 0 & -d_{11}b & 0 & 0 & -d_{21}a & d_{11}b & d_{21}a \\
0 & 0 & -d_{21}b & 0 & 0 & -d_{22}a & d_{21}b & d_{22}a \\
0 & 0 & 0 & -d_{33}b & -d_{33}a & 0 & d_{33}a & d_{33}b
\end{array}\right]
\begin{array}{l}
\left.\begin{array}{l}\text{node 1}\\ x=0\\ y=0\end{array}\right\} \\
\left.\begin{array}{l}\text{node 2}\\ x=0\\ y=b\end{array}\right\} \\
\{\delta^e\} \\
\left.\begin{array}{l}\text{node 3}\\ x=a\\ y=0\end{array}\right\} \\
\left.\begin{array}{l}\text{node 4}\\ x=a\\ y=b\end{array}\right\}
\end{array}$$

Equation 10-21

Equation 10-20 may thus be rewritten as shown in Equation 10-22. This equation may be summarised as:

$$\{\sigma^e\}=[H^e]\{\delta^e\}$$ **Equation 10-22**

APPENDIX F THEORY OF LINEARISATION TO MINIMISE SINGULARITY EFFECTS

This method is based on the theory used in the pressure vessel code. The theory is given in the *ASME Vol. III: Pressure Vessels*. The theory was also found on a internet site: *DBA (Design by Analysis) Draft CEN prEN 13445-3.* See the reference for the internet address.

Portions of the lengthy design process are taken from this reference and have been extracted to describe the concept.

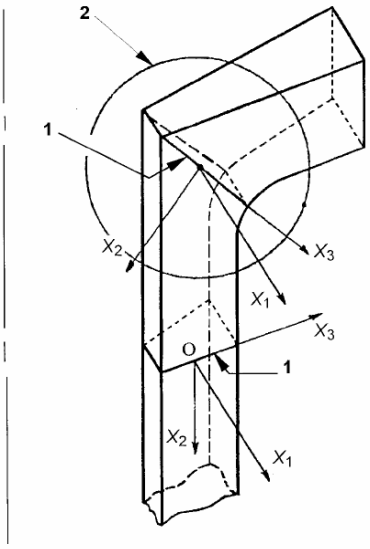

Figure 10-20: Segment of a pressure vessel in which elementary stresses are expressed

The linearisation of stresses is a decomposition of the membrane and bending stresses. The bending stress component is usually non-linear and is then linearised to reduce the high peak stresses at the boundaries. Figure 10-21 illustrates the different stress components

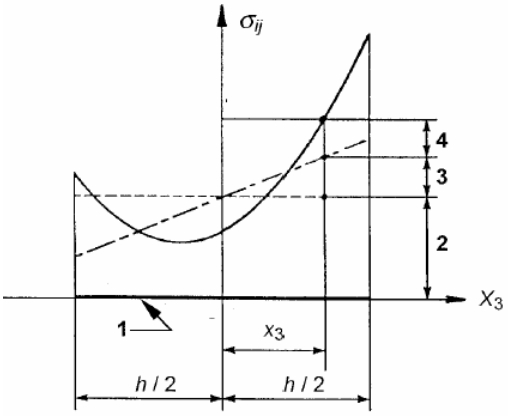

1 : supporting line segment
2 : membrane stress $\sigma_{ij,m}$
3 : bending stress $\sigma_{ij,b}$
4 : nonlinearity stress $\sigma_{ij,nl}$

Figure 10-21: Decomposition of elementary stresses

A cylindrical shell pressure vessel subjected to an external bending moment is illustrated in Figure 10-22.

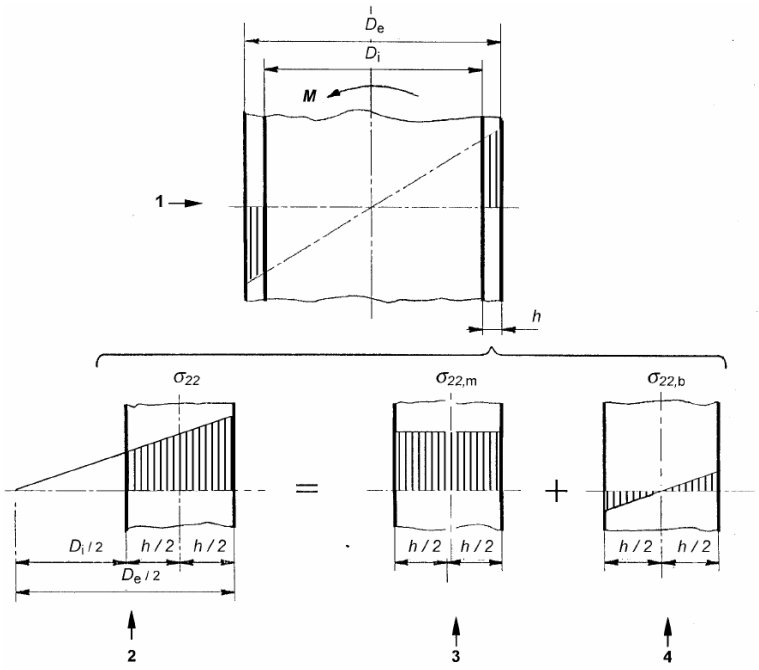

Figure 10-22: Decomposition of the longitudinal stress for a cylindrical shell subjected to external bending moment M

1. Longitudinal stress distribution along the shell cross-section.
2. Longitudinal stress distribution along the thickness of the wall
3. Membrane stress: $\sigma_{22,m}$
4. Bending stress: $\sigma_{22,m}$

Linearisation by means of the FEM is done by dividing the normal stresses into the membrane and bending stresses. In the example of a arch dam, there are no membrane stresses and the bending stresses are then linearised. In the case of a gravity dam, the cantilever stress (syy) is the only stress caused by bending and this stress can thus be linearised.

The author attempted to do such a linearisation on the 100 m triangular gravity dam, but was of opinion that this method is sensitive to mesh density and the answers are very uncertain. The theory was developed for circular shell pressure vessel structures and the geometry of a gravity dam is far from that of a shell structure. The theory might be useful for thin arch dams, but should then be benchmarked and calibrated.

However, the results for this particular mesh density were remarkable, giving a stress very close to zero which coincides with the results one would expect for the classical method. For interest's sake, a triangular gravity dam – 100 m high with a 0.8 downstream slope and full uplift condition – was analysed with the classical method program CADAM (2004). This provided an upstream tensile stress result of 0.159 MPa and a downstream compression stress result of 1.533 MPa. Figure 10-23 illustrates the linearisation of this dam.

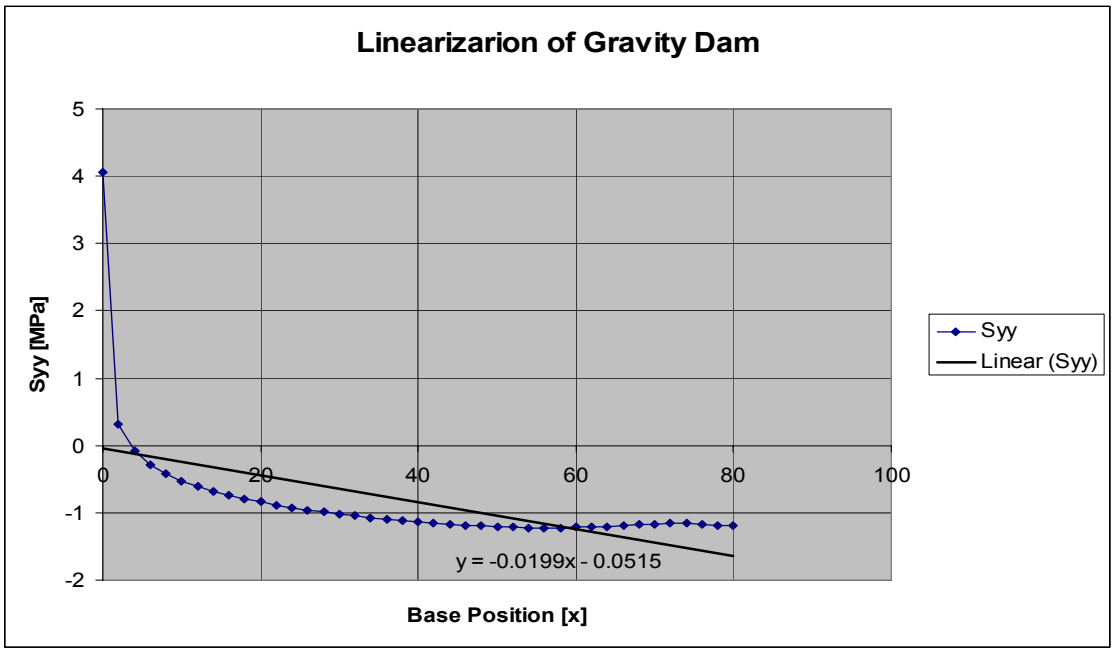

Figure 10-23: Linearisation of a 100 m triangular gravity dam with an 80 element mesh density; the linearised Syy stress is -0.052 MPa

APPENDIX G FACTORS OF SAFETY CALCULATED FOR A TRIANGULAR DAM WITH THE RESULTS OF AN FEA

The Factors of Safety against sliding were calculated on an MS Excel spreadsheet.

FOS of triagular dam 100m (0.8) & ft=1.0 Mpa FSL

Tan Φ=	0.932
C=	1.2

Σ Shear Resit	Σ Water Load	FOS Shear
158.76	50.00	3.18

	Base	FSL Syy		Del L	Avg Syy	Pore Pres	-R	R.tanΦ	C.A	CA + RTanΦ	Σ Shear
0	0.000	1.052									
1	0.507	0.869		0.507	0.961		-0.487	-0.454	0.609	0.155	
2	1.014	0.908		0.507	0.888		-0.450	-0.420	0.609	0.189	
3	1.556	0.808		0.542	0.858		-0.465	-0.433	0.650	0.217	
4	2.098	0.618		0.542	0.713		-0.387	-0.360	0.650	0.290	
5	2.677	0.498		0.579	0.558		-0.323	-0.301	0.695	0.394	
6	3.256	0.349		0.579	0.423		-0.245	-0.229	0.695	0.466	
7	3.875	0.217		0.619	0.283		-0.175	-0.163	0.743	0.580	
8	4.494	0.088		0.619	0.152		-0.094	-0.088	0.743	0.655	
9	5.155	-0.015		0.661	0.037		-0.024	-0.023	0.794	0.771	
10	5.817	-0.101		0.661	-0.058		0.038	0.036	0.794	0.829	0.829
11	6.524	-0.177		0.707	-0.139		0.098	0.092	0.848	0.940	1.769
12	7.230	-0.244		0.707	-0.210		0.149	0.139	0.848	0.987	2.756
13	7.985	-0.303		0.755	-0.273		0.206	0.192	0.906	1.099	3.854
14	8.741	-0.356		0.755	-0.329		0.249	0.232	0.906	1.138	4.992
15	9.548	-0.404		0.807	-0.380		0.307	0.286	0.968	1.254	6.246
16	10.355	-0.449		0.807	-0.426		0.344	0.321	0.968	1.289	7.535
17	11.217	-0.491		0.862	-0.470		0.405	0.378	1.035	1.413	8.948
18	12.079	-0.531		0.862	-0.511		0.441	0.411	1.035	1.446	10.394
19	13.001	-0.568		0.922	-0.550		0.506	0.472	1.106	1.578	11.972
20	13.923	-0.604		0.922	-0.586		0.540	0.503	1.106	1.609	13.581
21	14.907	-0.638		0.985	-0.621		0.611	0.570	1.182	1.751	15.332
22	15.892	-0.670		0.985	-0.654		0.644	0.600	1.182	1.782	17.115
23	16.944	-0.702		1.052	-0.686		0.722	0.673	1.263	1.936	19.051
24	17.997	-0.732		1.052	-0.717		0.755	0.703	1.263	1.966	21.017
25	19.121	-0.762		1.125	-0.747		0.840	0.783	1.350	2.133	23.149
26	20.246	-0.790		1.125	-0.776		0.873	0.813	1.349	2.163	25.312
27	21.448	-0.819		1.202	-0.804		0.967	0.901	1.442	2.343	27.655
28	22.649	-0.846		1.202	-0.832		1.000	0.932	1.442	2.374	30.029
29	23.933	-0.872		1.284	-0.859		1.103	1.028	1.541	2.569	32.598
30	25.218	-0.898		1.284	-0.885		1.137	1.060	1.541	2.601	35.199

31	26.590	-0.924		1.372	-0.911		1.250	1.165	1.647	2.812	38.011
32	27.962	-0.948		1.372	-0.936		1.285	1.197	1.647	2.844	40.854
33	29.429	-0.973		1.466	-0.961		1.409	1.313	1.760	3.072	43.927
34	30.895	-0.996		1.466	-0.984		1.444	1.345	1.760	3.105	47.032
35	32.462	-1.019		1.567	-1.008		1.579	1.472	1.881	3.352	50.384
36	34.029	-1.041		1.567	-1.030		1.615	1.505	1.880	3.385	53.770
37	35.704	-1.063		1.675	-1.052		1.762	1.642	2.010	3.652	57.422
38	37.378	-1.084		1.675	-1.073		1.798	1.675	2.010	3.685	61.106
39	39.168	-1.104		1.789	-1.094		1.957	1.824	2.147	3.971	65.077
40	40.957	-1.122		1.790	-1.113		1.991	1.856	2.147	4.003	69.081
41	42.869	-1.140		1.912	-1.131		2.162	2.015	2.295	4.310	73.391
42	44.782	-1.156		1.912	-1.148		2.195	2.045	2.295	4.340	77.731
43	46.825	-1.170		2.043	-1.163		2.376	2.214	2.452	4.666	82.397
44	48.868	-1.182		2.043	-1.176		2.403	2.240	2.452	4.692	87.089
45	51.052	-1.193		2.184	-1.187		2.593	2.417	2.620	5.037	92.126
46	53.236	-1.200		2.184	-1.196		2.613	2.435	2.620	5.055	97.182
47	55.569	-1.205		2.334	-1.203		2.806	2.615	2.800	5.415	102.597
48	57.903	-1.206		2.334	-1.205		2.813	2.621	2.800	5.422	108.019
49	60.396	-1.204		2.494	-1.205		3.004	2.800	2.992	5.792	113.811
50	62.890	-1.198		2.494	-1.201		2.994	2.790	2.992	5.783	119.594
51	65.555	-1.184		2.665	-1.191		3.174	2.958	3.198	6.155	125.749
52	68.219	-1.166		2.665	-1.175		3.132	2.919	3.198	6.117	131.865
53	71.067	-1.154		2.848	-1.160		3.304	3.079	3.417	6.496	138.362
54	73.914	-1.153		2.848	-1.154		3.285	3.061	3.417	6.478	144.840
55	76.957	-1.141		3.043	-1.147		3.490	3.252	3.651	6.904	151.744
56	80.000	-1.233		3.043	-1.187		3.612	3.366	3.651	7.018	158.762